



Delft University of Technology

Finite-dimensional approximation and control of shear flows

Tol, Henry

DOI

[10.4233/uuid:68de92fd-0185-4e08-b911-253358708a9c](https://doi.org/10.4233/uuid:68de92fd-0185-4e08-b911-253358708a9c)

Publication date

2018

Document Version

Final published version

Citation (APA)

Tol, H. (2018). *Finite-dimensional approximation and control of shear flows*. [Dissertation (TU Delft), Delft University of Technology]. <https://doi.org/10.4233/uuid:68de92fd-0185-4e08-b911-253358708a9c>

Important note

To cite this publication, please use the final published version (if applicable).
Please check the document version above.

Copyright

Other than for strictly personal use, it is not permitted to download, forward or distribute the text or part of it, without the consent of the author(s) and/or copyright holder(s), unless the work is under an open content license such as Creative Commons.

Takedown policy

Please contact us and provide details if you believe this document breaches copyrights.
We will remove access to the work immediately and investigate your claim.

Finite-dimensional approximation and control of shear flows

Finite-dimensional approximation and control of shear flows

Proefschrift

ter verkrijging van de graad van doctor
aan de Technische Universiteit Delft,
op gezag van de Rector Magnificus prof.dr.ir. T.H.J.J. van der Hagen,
voorzitter van het College voor Promoties,
in het openbaar te verdedigen op maandag 4 juni 2018 om 10:00 uur

door

Hendrikus Johannes TOL

Ingenieur Luchtvaart en Ruimtevaart,
Technische Universiteit Delft, Nederland
geboren te Volendam, Nederland.

Dit proefschrift is goedgekeurd door de promotor en de copromotoren.

Samenstelling promotiecommissie:

Rector Magnificus,	voorzitter
Prof. dr. F. Scarano,	Technische Universiteit Delft, promotor
Dr. ir. C.C. de Visser,	Technische Universiteit Delft, copromotor
Dr. M. Kotsonis	Technische Universiteit Delft, copromotor

Onafhankelijke commissieleden:

Dr. S. Bagheri,	KTH Royal Institute of Technology, Sweden
Prof. dr. S. Hickel,	Technische Universiteit Delft
Prof. B. Bamieh,	University of California, Santa Barbara
Prof. dr. ir. B. Koren,	Technische Universiteit Eindhoven
Prof. dr. ir. L.L.M. Veldhuis	Technische Universiteit Delft, reservelid

Prof.dr.ir. M. Mulder heeft in belangrijke mate aan de totstandkoming van het proefschrift bijgedragen.



Keywords: Flow instability and control

Printed by: Rijnja Repro Delft

Copyright © 2018 by H.J. Tol

ISBN 978-94-6186-926-5

An electronic version of this dissertation is available at
<http://repository.tudelft.nl/>.

Contents

Summary	ix
Samenvatting	xiii
1 Introduction	1
1.1 Flow instability and control	3
1.1.1 Stability equations	3
1.1.2 Global instabilities and limit cycle oscillations	4
1.1.3 Convective instabilities and transition.	6
1.1.4 The flow control problem.	8
1.2 Research motivation and objectives	11
1.2.1 Motivation	12
1.2.2 Research objectives and scope	13
1.3 Research approach, contributions and dissertation outline	15
2 Model reduction of parabolic PDEs using multivariate splines	17
2.1 Introduction.	18
2.2 Class of systems under consideration	20
2.3 Preliminaries on multivariate splines	23
2.4 Boundary conditions as side constraints.	25
2.5 Model reduction of linear parabolic PDEs.	29
2.6 Controller synthesis.	33
2.7 Demonstration	34
2.7.1 Boundary feedback stabilisation of a reaction-diffusion equation 35	
2.7.2 In-domain control of a reaction-convection-diffusion equation .	37
2.8 Conclusions	40
3 Localised estimation and control of instabilities in shear flows	43
3.1 Introduction.	44
3.1.1 Distributed control and localised computations.	44
3.1.2 Model reduction and localised control.	45
3.1.3 Scope and outline of the present study	46
3.2 Dynamic modelling and problem formulation.	48
3.2.1 Governing equations	49
3.2.2 Inputs and outputs	50
3.2.3 Inflow disturbance model.	51
3.2.4 State-space formulation	56
3.2.5 Finite-dimensional system	59
3.2.6 Formulation of the \mathcal{H}_2 control problem	60

3.3	Controller design and synthesis	63
3.3.1	Analysis of the uncontrolled system	64
3.3.2	Reduced-order controller	66
3.3.3	Closed-loop frequency response	71
3.4	Closed-loop simulations	72
3.4.1	Case A: single-frequency disturbance	73
3.4.2	Case B: multiple-frequency disturbance	76
3.4.3	Case C: stochastic in-domain forcing	79
3.5	Conclusions	82
4	Estimation and control of TS waves in Falkner-Skan boundary layers	85
4.1	Introduction.	86
4.2	Governing equations	89
4.3	State-space formulation	92
4.3.1	Abstract form.	92
4.3.2	finite-dimensional approximation	94
4.4	Inflow disturbances	94
4.5	Pressure output equation.	97
4.6	\mathcal{H}_2 /LQG reduced-order control design	99
4.7	Results	103
4.7.1	Nominal performance.	104
4.7.2	Effect of domain truncation	107
4.7.3	Robustness	108
4.8	Conclusions	110
5	Experimental estimation and control of natural TS waves	113
5.1	Introduction.	114
5.2	Experimental set-up	116
5.2.1	Flow facility and PIV set-up	116
5.2.2	Control system elements	117
5.2.3	Base flow and stability	119
5.3	The linear compensator	120
5.3.1	State estimator	121
5.3.2	Controller	124
5.4	Experimental control performance.	126
5.5	Conclusions	128
6	Conclusions and outlook	131
6.1	Conclusions	131
6.1.1	Finite-dimensional approximation	131
6.1.2	Modelling, estimation and control	132
6.1.3	Actuators, sensors and experimental demonstration	133
6.1.4	Final discussion	134
6.2	Outlook and open problems	134

A	A state-space representation for incompressible fluid flows	139
A.1	Numerical method	139
A.2	Verification	145
B	Solution of the \mathcal{H}_2/LQG optimal control problem	147
C	A null space algorithm for linear systems	149
C.1	Algorithm	150
C.2	An illustrative example.	152
	Bibliography	155
	Acknowledgements	167
	Curriculum Vitæ	169
	List of Publications	171

Summary

Dynamical systems theory can significantly contribute to the understanding and control of fluid flows. Fluid dynamical systems are governed by the Navier-Stokes equations, which are continuous in both time and space, resulting in a state space of infinite dimension. To incorporate tools from systems theory it has become common practise to approximate the infinite-dimensional system by a finite-dimensional lumped system. Current techniques for this reduction step are data driven and produce models which are sensitive to the simulation/experimental conditions. This dissertation proposes a rigorous and practical methodology for the derivation of accurate finite-dimensional approximations and output feedback controllers directly from the governing equations. The approach combines state-space discretisation of the linearised Navier-Stokes equations with balanced truncation to design experimentally feasible low-order controllers. The approximation techniques can be used to design any suitable linear controller. In this study the reduced-order controllers are designed within an \mathcal{H}_2 optimal control framework to account for external disturbances and measurement noise. Application is focused on control of laminar wall-bounded shear flows to delay the classical transition process initially governed by two-dimensional convective perturbations, to extend laminar flow and reduce skin friction drag. The effectiveness and practical feasibility is demonstrated in both simulation and experiment. The research performed in this dissertation can be divided in three main parts respectively dealing with finite-dimensional approximation, modelling & control design and experimental validation.

The first part is concerned with the development of mathematical tools and procedures to derive finite-dimensional state-space descriptions from the governing equations. A new methodology is presented to derive state-space systems for a class of linear parabolic partial differential equations (PDEs). Multivariate splines of arbitrary degree and arbitrary smoothness are used in combination with Galerkin's method to spatially discretise the system. A novel null-space projection method is proposed to incorporate the smoothness conditions and boundary conditions and to transform the discrete system of equations to state-space format. This projection also reduces the order of the system and naturally produces a system that is free of non-physical spurious eigenmodes. The method can be applied to general geometries and any actuator/sensor configuration. The effectiveness is demonstrated for two benchmark PDE control problems, a one-dimensional unstable reaction-diffusion equation and a two-dimensional unstable reaction-convection-diffusion equation. It is shown that the models quickly converge for increasing mesh resolution and degree of splines. Furthermore, it is shown that the order of the model only has to be sufficiently large to achieve an effective feedback stabilisation.

In the second part, the developed tools are applied for modelling and control of convective perturbations in two-dimensional wall-bounded shear flows. The velocity-

pressure form of the linearised incompressible Navier-Stokes equations is used to derive the state-space system. To avoid singularities, the pressure is eliminated from the governing equations by using a space of velocity fields that is divergence free and a suitable choice of the Galerkin variational formulation of the equations. This also gives a significant model-order reduction as the divergence-free constraint space of functions is much smaller than the unconstrained space. Wall-bounded flows dominated by convective processes are highly sensitive to external upstream disturbances. Accurately modelling the influence of external disturbances is crucial as it forms the basis for the measured unsteadiness. A new perturbation modelling approach is proposed that effectively balances spatio-temporal resolution with respect to the external disturbances and the order of the system. Very large systems are avoided by synthesising the controller within a localised computational domain that encapsulates the actuators/sensors. The modelling is combined with balanced truncation to reduce the order of the controller and the truncated dynamics is taken into account in the order selection and in the control design. A fast convergence of the \mathcal{H}_2 closed-loop system norms, which characterise the control performance, is demonstrated. It is shown that between one and two orders of magnitude amplitude reduction of the perturbations can be achieved with low-order controllers, also in the case of unmodelled disturbances and sensor inaccuracies.

The third and final part involves the experimental implementation of the controller. Motivated by their practical advantages, a plasma actuator and a microphone that measures the pressure fluctuations at the wall are used as actuator/sensor pair to control the flow. The chosen control objective is the suppression of natural two-dimensional convective perturbations in a boundary layer flow over a flat plate under an externally imposed adverse pressure gradient. New output operators are derived that relate the flow perturbations with the pressure fluctuations at the wall and an experimentally derived body force model of the actuator is integrated in the control design. The estimates obtained from the Kalman filter, which is part of the optimal controller, are compared with the experimental data obtained from PIV. The results show that the Kalman filter is able to filter the measurements and to estimate the spatio-temporal behaviour of naturally occurring perturbations in the presence of unknown external disturbances. The nominal performance as well as the robust performance in off-design conditions of the controller is evaluated in comparison with open-loop continuous forcing. In nominal designed conditions a maximum additional reduction of 60% in the r.m.s. of the pressure fluctuations is measured 9 cm downstream of the plasma actuator, which corresponds to approximately four times the wavelength of the dominant perturbations. A reduction between 30-60% is measured for a range of off-design conditions.

The main advantages of the proposed approach are low costs for obtaining the model, fast convergence of the model and the availability of a high fidelity truth model. The truth model can be used to assure that the reduced-order controllers are naturally robust to the truncated dynamics. The main limitation of the proposed approach is that it is currently practically limited to two-dimensional linear flow configurations. As the matrices are explicitly formed, this approach may be closely tied to the available computational resources for more complex and three-dimensional

flow configurations. The main open problem is guaranteeing both robust stability and robust performance in the presence of model uncertainties. Several possible directions of research are proposed that extend the results in this dissertation and address the open problems.

Samenvatting

Systeem theoretische regeltechnieken kunnen aanzienlijk bijdragen aan zowel het begrijpen en het besturen van luchtstromingen. Aerodynamische systemen worden beschreven door de Navier-Stokes vergelijkingen welk continu zijn in zowel de tijd als ruimte wat resulteert in systemen met een oneindige dimensie. Voor het toepassen van regeltechniek is het de gewoonte om de oneindige dimensie te benaderen wat resulteert in een eindig systeem. Huidige technieken voor deze reductie-stap zijn empirisch wat resulteert in modellen die gevoelig zijn voor de experimentele of simulatie condities. Dit proefschrift presenteert een nieuw raamwerk voor zowel de eindige benadering en de besturing van aerodynamische systemen op basis van alleen de vergelijkingen. De aanpak bestaat uit spatiale discretisatie van de vergelijkingen met *balanced truncation* voor het ontwerpen van lage orde regelaars die gebruikt kunnen worden in experimenten. De benaderingstechnieken kunnen worden gebruikt om elke geschikte lineaire regelaar te ontwerpen. In deze studie zijn de regelaars ontworpen met behulp van \mathcal{H}_2 optimale regeltechnieken om rekening te houden met externe verstoringen en meetruis. Het raamwerk is toegepast op gelaagde stromingen over vlakke platen om transitie naar turbulente stroming te vertragen en de weerstand te verlagen. De prestaties van het regelsysteem zijn geëvalueerd in zowel simulaties als experimenten. Het werk in dit proefschrift kan verdeeld worden in drie aspecten: eindige benadering, modeleren & het ontwerp van regelaars en het implementeren van regelaars in experimenten.

Het eerste deel van dit werk betreft de ontwikkeling van nieuwe technieken voor het afleiden van eindige state-space systemen die gebruikt kunnen voor het ontwerpen van regelaars. Een nieuwe methode is gepresenteerd voor een generieke klasse van parabolische systemen die worden beschreven door partiële differentiaalvergelijkingen. Multivariate splines van arbitraire orde en arbitraire gladheid worden gebruikt in combinatie met Galerkin's methode voor de spatiale discretisatie van het systeem. Een nieuwe nul ruimte projectie is voorgesteld voor het inbrengen van de randvoorwaardes en continuïteits condities en het transformeren van het discrete systeem naar *state-space* formaat. Deze projectie reduceert ook de orde van het discrete systeem en produceert een systeem dat de stabiliteitseigenschappen van het oneindige systeem behoudt. De methode kan worden toegepast op generieke geometrieën en elke actuator/sensor configuratie. De methode is toegepast op twee bekende onstabiele regelproblemen. Een snelle convergentie van het model wordt aangetoond. Het wordt ook aangetoond dat voor een effectieve besturing de orde van het model en de regelaar laag kan zijn.

In het tweede deel van dit werk worden de nieuwe technieken toegepast voor het modelleren en besturen van verstoringen in luchtstromingen rondom vlakke platen. De vectoriële snelheid-druk formulering van de Navier-Stokes vergelijking is gebruikt voor het afleiden van het *state-space* systeem. Om singulariteiten te voorkomen is

de druk geëlimineerd van de vergelijking door het gebruiken van een ruimte waar het snelheidsveld divergentie vrij is en een geschikte keuze van de Galerkin variatie formulering van de vergelijkingen. Deze eliminatie geeft ook een significante orde verlaging omdat de divergentie-vrije beperkte ruimte een stuk kleiner is dan de niet beperkte ruimte. Stromingen rond vlakke platen zijn heel gevoelig voor verstoringen van buitenaf. Het accuraat modeleren van het effect van deze verstoringen is cruciaal, omdat het de basis vormt van de gemeten verstoringen met de sensors. Een nieuw model is voorgesteld dat effectief balanceert tussen spatiale en temporale resolutie van de verstoringen en de orde van het model. Hele grote systemen worden voorkomen door de regelaars te synthetiseren in een gelokaliseerd domain dat de actuatoren en sensoren inkapselt. De methodologie is gecombineerd met *balanced truncation* om de orde van de regelaar verder te reduceren en de verwaarloosde dynamica wordt meegenomen in het ontwerp. Een snelle convergentie van de \mathcal{H}_2 systeem normen die de besturingsprestaties karakteriseren wordt aangetoond. Een amplitude reductie van een a twee orders in magnitude van de verstoringen wordt gedemonstreert, ook in het geval van niet gemodelleerde externe verstoring en gevoeligheden in de sensoren.

Het derde en laatste deel betreft de experimentele implementatie van de regelaar. Gemotiveerd door hun praktische voordelen wordt een plasma actuator en een microfoon die de drukschommeling meet aan de wand gebruikt als actuator/sensor paar om de luchtstroming te regelen. Het gekozen besturingsdoel is het onderdrukken van convectieve verstoringen in een grenslaag stroming over een vlakke plaat. Nieuwe operatoren zijn afgeleid die de verstoringen relateren aan de druk fluctuaties aan de wand en een experimenteel afgeleid krachtmodel van de actuator is geïntegreerd in het ontwerp van de controller. De schattingen die zijn verkregen met het Kalman-filter, die deel uitmaakt van de optimale controller, zijn vergeleken met experimentele meting gemaakt aan de hand van PIV. De resultaten laten zien dat het Kalman-filter de metingen kan filteren op basis van het model en het spatiale-temporale gedrag van het natuurlijke verstoringenveld kan schatten in de aanwezigheid van onbekende externe verstoringen. De nominale prestaties en de robuuste prestaties in buiten ontwerp omstandigheden van de regelaar zijn geëvalueerd in vergelijking met continue open-lus besturing. In nominale ontwerp omstandigheden is een maximale extra reducering van 60% in de r.m.s van de drukfluctuaties gemeten 9 cm stroomafwaarts van de plasma actuator. Een reducering tussen 30-60% is gemeten voor een reeks van of-ontwerp condities

De belangrijkste voordelen van het voorgestelde raamwerk zijn lage kosten voor het verkrijgen van het model, snelle convergentie van het model en de beschikbaarheid van een hoge orde kwaliteitsmodel. Het hoge orde model kan gebruikt worden om te verzekeren dat de regelaars van gereduceerde orde van nature robuust zijn voor de verwaarloosde dynamica. De voornaamste beperking van de voorgestelde raamwerk is dat deze momenteel praktisch beperkt is tot tweedimensionale gelineariseerde luchtstromingen. Omdat de matrices expliciet worden gevormd, kan het raamwerk nauw verbonden zijn met het beschikbare computer vermogen voor meer complexere en driedimensionale luchtstromingen. Het belangrijkste open probleem is het garanderen van zowel robuuste stabiliteit als robuuste prestaties in de aanwe-

zigheid van modelonzekerheden. Verschillende mogelijke richtingen van onderzoek worden voorgesteld die de resultaten in dit proefschrift uitbreiden en de open problemen mogelijk kunnen oplossen.

1

Introduction

Currently, active flow control (AFC) is considered a viable route to further push the performance boundaries of aerodynamic bodies such of transport aircraft and ground vehicles. A recent demonstration of AFC technologies and concepts is the joint NASA/Boeing effort to enhance the aerodynamic efficiency of the vertical tail of a Boeing 757 ecoDemonstrator [1]. The vertical tail was equipped with 31 sweeping jet actuators to increase the effective side-force generated by the rudder. They achieved to maintain an attached flow and to delay flow separation on a highly deflected rudder. This increased the effective side force and may enable a smaller vertical tail to provide the required control authority. This study indicated that the AFC-enhanced vertical tail could lead to an overall drag reduction of 1%, which in turn could save billions when applied worldwide. This example illustrates how the delay of separation can lead to an increased control effectiveness and eventually overall drag reduction. Common control objectives in AFC are

- Delaying/preventing separation
- Delaying/preventing transition from laminar to turbulent flow
- Suppressing turbulence and flow relaminarisation
- Suppressing vortex shedding
- Suppressing cavity induced oscillations

The benefits that can be gained from these objectives include drag reduction, lift enhancement, noise suppression and reducing structural vibrations. For example, bluff body flows, such as flow past cars or aircraft, are characterised by a recirculating flow behind the body, called the wake. When the flow is unstable the phenomenon of vortex shedding occurs in the wake causing structural vibrations, acoustic noise and an increase in the mean drag. The application of flow control is aimed at modifying the flow behaviour around the structure such that vortex shedding is suppressed [2, 3]. Another example is a flow over a cavity, such as flow over

wheel wells, weapons bays and junctions on aircraft wings, which results in pressure induced oscillations inside the cavity. These oscillations produce strong resonant tones which can reach 170 dB sound pressure level and quickly lead to structural fatigue issues inside aircraft. The cavity drag is significantly higher under resonant conditions and controlling acoustic tones is also coupled with the safe departure and accurate delivery of stores (store separation) from internal weapon bays [4, 5].

Aircraft drag reduction is one of the main motivators of AFC. A primary source of aircraft drag is surface skin friction. The effect of skin friction on the flow is limited to a thin adjacent region to the body surface called the boundary layer. Within this boundary layer the velocity is dominated by viscous effects and varies from zero at the surface to the external freestream velocity. On an aircraft wing profile, the boundary layer close to the leading edge is usually laminar. Laminar boundary layers are characterised by parallel shear layers moving in a smooth, regular and deterministic way. Laminar flows are usually unstable and highly receptive to perturbations, e.g. generated by wall surface roughness. These perturbations, will unless controlled, evolve into turbulent flow. Turbulent boundary layers are characterised by small scale velocity components with a chaotic, non-deterministic behaviour and have a considerable higher skin friction drag. A control system that delays/prevents transition or relaminarises the flow in the turbulent regime can therefore significantly reduce the skin friction drag [6–8]. Laminar boundary layer transition delay is the main objective considered in the present work.

These examples illustrate the benefits of applying flow control. Flow control technologies have been extensively studied the past decades and the concepts of flow control come with a wide variety of technical and theoretical disciplines. The ecoDemonstrator concept is an example of open-loop active control in which the actuator settings have been determined a priori and do not depend on measurements. Open-loop AFC dates back to the discovery of the boundary layer by Prandtl, who used steady suction flow control to remove the boundary layer on the walls, enhancing their stability. Open-loop control involves changing the mean flow conditions to achieve stabilisation of the flow. Closed-loop control strategies on the other hand aim at targeting the inherent instability mechanism by means of unsteady actuation, without changing the mean flow properties. Such systems use real-time sensor information to devise controls that alter the flow in its desired state. The benefit of closed-loop control is the ability to achieve large scale changes in flow behaviour with low levels of energy input, resulting in an improved performance and lower power consumption.

The present study focusses on a more narrow definition of AFC that has attracted much attention from both the control community and fluid dynamic community: the application of systems and control theory to fluid dynamical systems. Such model-based techniques provide important insights into the instability mechanisms that have to be addressed and potentially lead to the best possible performance with stability guarantees. Systems and control theory is an established field dealing with the analysis and control of continuous-time dynamical systems. However, the Navier-Stokes equations, which govern the dynamics of fluid dynamical systems, are continuous in both space and time, giving rise to infinite dimensional systems. This

dissertation proposes a practical methodology for the derivation of finite-dimensional approximations and controllers for fluid dynamical systems. Before giving the research motivation and objectives of the present work, first an introduction is given to the integrated discipline.

1.1. FLOW INSTABILITY AND CONTROL

Control strategies are structured around the understanding of the flow instabilities and their role in the physical phenomena (transition, wakes, etc.) to be controlled. The main hypothesis in the present work is that these flow phenomena can be properly described and controlled within a linearised framework. There is now a vast amount of literature on flow stability theory and control supporting this hypothesis. The interested reader is referenced to excellent reviews in this field recently published in [7–9]. Clearly linear models do not capture the nonlinear couplings of instability modes that support turbulence with multi-scale characteristics. Therefore, linear control is often referred to as *laminar flow control* and focusses on the stabilisation of equilibrium points existing in laminar transitional flows. This section introduces the governing equations, the instability mechanisms commonly addressed using control theory and the control design problem.

1.1.1. STABILITY EQUATIONS

The starting point in both hydrodynamic stability theory and linear control design is to linearise the incompressible Navier-Stokes equations around the steady laminar solution. The viscous incompressible Navier-Stokes are given by the momentum equations

$$\frac{\partial \mathbf{U}}{\partial t} = -(\mathbf{U} \cdot \nabla) \mathbf{U} + \frac{1}{Re} \Delta \mathbf{U} - \nabla P, \quad (1.1)$$

and the incompressibility constraint

$$\nabla \cdot \mathbf{U} = 0, \quad (1.2)$$

which describe the evolution of the three components of velocity field $\mathbf{U}(\mathbf{x}, t) = (U, V, W)$, and the pressure field $P(\mathbf{x}, t)$ in space $\mathbf{x} = (x, y, z)$ and time t . To have a mathematically well posed solution and to solve the system, the equations have to be complemented with boundary conditions depending on the physical domain and initial conditions. The equations are non-dimensionalised with a velocity scale U^* and a length scale L^* . The reference variables are lumped in the Reynolds number $Re = L^* U^* \rho / \mu$ where ρ is the density and μ the dynamic viscosity of the fluid. The non-dimensional form is more convenient for analysis, since any flow with the same Reynolds number are identical once scaled properly. Stability theory is concerned with the dynamics of small amplitude perturbations $\mathbf{u}(\mathbf{x}, t)$ to an equilibrium solution $\mathbf{U}_0(\mathbf{x})$ for (1.1) called the base flow. The base flow can be obtained either as a steady (numerical) solution to (1.1) or as a time-averaged solution obtained from a snapshot ensemble of the flow field under the assumption that Reynolds stresses are negligible. An example of a base flow over a cylinder and

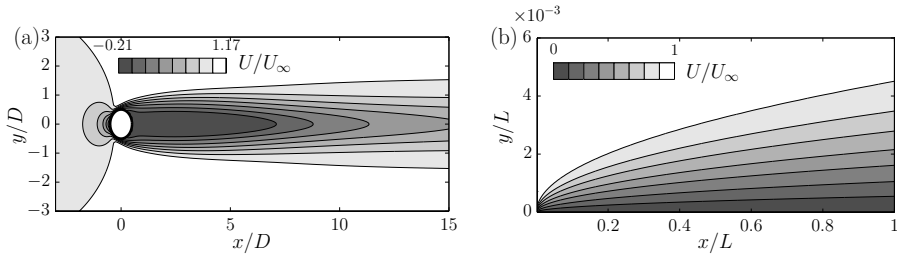


Figure 1.1: Base flow \mathbf{U}_0 for a flow over circular cylinder for $Re_D = 100$ (a) and for a Blasius flow over a flat plate for $Re_L = 513 \times 10^3$ (b) visualised by the contours of the streamwise velocity

over a flat plate (Blasius flow) is shown figure 1.1. Let $\mathbf{U} = \mathbf{U}_0 + \mathbf{u}$ and $P = P_0 + p$ be the velocity field and pressure field of a slightly perturbed flow. Inserting these expressions in (1.1), subtracting the steady equations and neglecting the nonlinear term gives the linearised Navier-Stokes equations (LNSE)

$$\frac{\partial \mathbf{u}}{\partial t} = -(\mathbf{U}_0 \cdot \nabla) \mathbf{u} - (\mathbf{u} \cdot \nabla) \mathbf{U}_0 + \frac{1}{Re} \Delta \mathbf{u} - \nabla p, \quad \nabla \cdot \mathbf{u} = 0. \quad (1.3)$$

For incompressible flows the pressure is instantaneously determined by the velocity field due to the divergence-free constraint, resulting in a singular system of equations. To avoid singularities, (1.3) is commonly formulated in a divergence-free basis, thereby eliminating the pressure from the equations. For example, using the streamfunction formulation, or the wall-normal velocity-vorticity formulation of the equations [10]. This can be viewed more abstractly as the projection of (1.3) on a divergence-free subspace resulting in the following initial value problem

$$\partial_t \mathbf{u} = \mathcal{A} \mathbf{u}, \quad \mathbf{u}(0) = \mathbf{u}_0. \quad (1.4)$$

The linear operator \mathcal{A} is called the linearised Navier-Stokes evolution operator around the base flow \mathbf{U}_0 . The calligraphic notation is used to denote a spatial differential operator, rather than a matrix. Equation (1.4) describes the evolution of initial small amplitude perturbations to the base flow \mathbf{U}_0 . It is the starting point for studying the spatio-temporal behaviour of the instabilities and the onset of the physical phenomena to be controlled. In turn, controllers which stabilise (1.4), stabilise the original system (1.1) around the base flow. The term instability refers to a single fundamental eigensolution or mode to (1.4) and a perturbation refers to a full solution, which can be decomposed into a range of instabilities. From a physical point of view we have to distinguish between global instabilities and convective instabilities according to their role as transition is approached [11]. These two instability mechanisms also have different implications for the control design [9].

1.1.2. GLOBAL INSTABILITIES AND LIMIT CYCLE OSCILLATIONS

Open shear flows or free shear layer flows such as open cavity flows and bluff body flows behave as oscillators displaying characteristics of resonant systems. These flows are commonly referred to as oscillator flows and are characterised by a large-scale energetic structure that oscillates at a particular frequency. The spatial structure,

oscillation frequency and the initial growth of the perturbation can be contributed by the presence of linear global instabilities, called the *global modes*. If the flow is unstable, the global modes amplify in time and for a sufficiently large amplitude, the global modes will eventually saturate into limit cycle oscillations. This nonlinear saturation results in a periodic flow pattern around the base flow. For example, for a flow past a 2-D circular cylinder, which is commonly considered as benchmark for studying vortex shedding, vortices are shed from the upper and lower sides of the cylinder, subjecting the cylinder to periodic forcing. This periodic forcing leads in turn to structural vibrations and acoustic noise.

Characterising the properties of global modes requires a global linear stability analysis [12]. The term global refers to the instability of the entire flow field and finding the complete eigenspectrum of \mathcal{A} . This is to find fundamental solutions for the global modes of the form

$$\mathbf{u} = \tilde{\mathbf{u}}e^{-i\omega t}. \quad (1.5)$$

The spatial structure of the global modes is characterised by the eigenvector $\tilde{\mathbf{u}}$ and the temporal behaviour by the eigenvalue $\omega = \omega_r + i\omega_i$. Here ω_i is the exponential amplification rate and ω_r the frequency of the oscillation. Substituting the fundamental solution in (1.4) transforms the initial value problem to an eigenvalue problem

$$\mathcal{A}\tilde{\mathbf{u}} = -i\omega\tilde{\mathbf{u}}. \quad (1.6)$$

Equation (1.6) is also known as the spatial differential operator eigenvalue problem, which can be solved numerically for the eigenvectors $\tilde{\mathbf{u}}$ and eigenvalues λ . Equation (1.6) is a large scale eigenvalue problem. In fact, an infinite number of eigensolutions exist and to resolve a large window of the eigenspectrum for complex flows, requires subspace iterations and massive parallelisation [13]. Fortunately, nature is forgiving and only a few (commonly one complex pair at low Re) result in unstable dynamics. The dominant eigensolutions are the physical global modes which are observed in practical applications. It has therefore become common practice to only extract the physically important modes. For example by obtaining converged solutions for the unstable modes using (1.6) or by means of a modal decomposition of an experimental or numerical dataset of the flow field [14]. As an example, the unstable global mode for the cylinder flow at $Re_D = 100$ is shown in figure 1.2. Vortices of alternating sign can be observed in the wake and are advected downstream. An effective control system targets the global modes, while accounting for the nonlinear saturation of the modes. A pertinent example showing the potential of linear control theory is the wake stabilisation recently achieved by Flinois and Morgans [15]. They designed robust linear controllers, which were robust enough to stabilise the wake behind a bluff body, even from the nonlinear vortex shedding state at off-design Reynolds numbers.

In this work, a class of linear parabolic PDEs will be used as benchmark for globally unstable systems, for the development of tools to find a finite-dimensional representation of the operator \mathcal{A} that can be used for control design. The eigenspectrum of the spatial differential operator \mathcal{A} for globally unstable flows shows a clear separation between the finite-dimensional slow/unstable part and an infinite-dimensional stable complement. This is a typical property of parabolic PDE systems

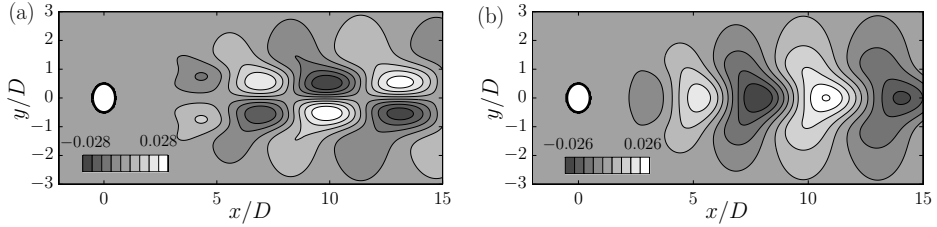


Figure 1.2: The dominant global mode for a flow around a circular cylinder characterised by shedding frequency $\omega = 0.72$. Shown is the real part of the streamwise perturbation component (a) and the wall-normal perturbation component (b). (axis not to scale)

which will be extensively treated in chapter 2. The global mode in figure 1.2 is also obtained using the methods presented in chapter 2.

1

1.1.3. CONVECTIVE INSTABILITIES AND TRANSITION

Wall-bounded shear flows or boundary layer flows such as flows over a flat plate, aerofoils and channel flows behave as amplifiers of external disturbances. These flows are commonly referred to as amplifier flows and support convective instabilities in a frequency broadband that amplify in both space and time as they propagate downstream. These instabilities are driven by non-deterministic (unknown) upstream disturbance sources, such as freestream turbulence, and are the precursor of laminar boundary layer transition. Different transition scenarios may occur depending on the intensity of the external disturbances acting on the flow [16]. Disturbances in the freestream, such as sound or vorticity, enter the boundary layer via receptivity mechanisms as unsteady fluctuations around the base flow. In case of weak levels of freestream turbulence ($<1\%$) linear instabilities are triggered, called Tollmien-Schlichting (TS) waves, in the form of nearly two-dimensional wavepackets that propagate downstream. The initial streamwise growth of the TS waves is exponential. As the amplitude of the wavepacket grows above a critical level, three-dimensional and nonlinear interactions occur. In this stage the instabilities grow rapidly, break down to smaller length scales and a transition to turbulence occurs. This is referred to as the *classical route*, or weak route, to turbulence [17]. TS waves are the main reason for transition on unswept wings or moderate swept wings in low freestream turbulence conditions, as for example encountered in clean cruise flight conditions.

In case of higher levels of freestream turbulence, the perturbations can experience a large transient energy growth bypassing the exponential growth of the TS waves. This can be contributed to the non-normality of the linearised operator, that is the eigenmodes of the operator are not mutually orthogonal and their influence on each other may result in a large amplification of the disturbance [18]. In case of boundary layers this results in three-dimensional lift-up of streamwise aligned vortices, creating elongated regions of alternating accelerated and decelerated flow, called streaks [19, 20]. After the primary energy growth due to the lift-up effect, the flow is in a more complex nonlinear state and eventually breaks down to turbulence.

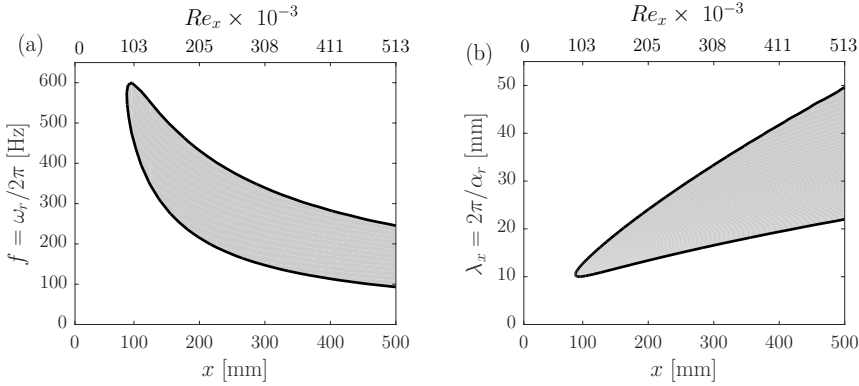


Figure 1.3: Spatial-temporal neutral stability curve for a Blasius boundary layer for $U_e = 15$ m/s. (a) Frequency bandwidth which gives spatial growth. (b) Spatial wavelengths which results in temporal growth. Gray region indicates unstable TS waves.

This is referred to as streak breakdown or *bypass transition* since the transition occurs bypassing the exponential growth of the TS waves.

This work particularly focusses on the weak turbulence scenario, where the TS waves can initially be described by the two-dimensional linearised equations. The properties of TS waves can be analysed by means of a local linear stability analysis [21]. The term local refers to the stability properties of a local velocity profile by making the assumption of a locally parallel flow. This assumption is valid in fully developed flows where the base flow does not significantly varies in the streamwise direction (e.g. channel flows) and is approximately valid in spatially developing boundary layers. This assumption permits a Fourier decomposition in both time and the streamwise coordinate resulting in fundamental solutions of the form

$$\mathbf{u} = \tilde{\mathbf{u}}(y)e^{i(\alpha x - \omega t)}. \quad (1.7)$$

This transforms the initial value problem (1.4) into a spatio-temporal eigenvalue problem

$$-i\omega\tilde{\mathbf{u}}(y) = \mathcal{A}(\alpha)\tilde{\mathbf{u}}(y), \quad (1.8)$$

with α the spatial eigenvalue that appears nonlinearly. Equation (1.8) is known as the Orr-Sommerfeld equation, which can be solved numerically for the temporal and spatial eigenvalues [22, 23]. There are an infinite number of eigenvalues satisfying (1.8). Fortunately, TS waves are only unstable in a limited frequency band in both space and time depending on the Reynolds number of the flow. The stability characteristics can be investigated by means of the exponential growth rate of the modes and the base flow is subsequently labelled unstable if an unstable eigenmode is found. In this way the locus can be computed, called the neutral stability curve, which separates the stable frequency region from the unstable frequency band. As an example, figure 1.3 shows the stability curve for a Blasius boundary layer flow computed using (1.8) and figure 1.4 shows a fully developed single frequency ($f = 200$ Hz) TS-wave computed as numerical solution to the LNSE. Figure 1.3(a) shows

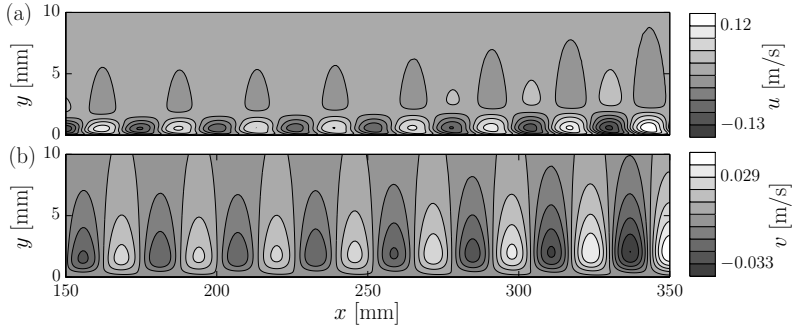


Figure 1.4: A snapshot of a fully developed single frequency $f = 200$ Hz Tollmien-Schlichting wave for the Blasius boundary layer flow over a flat plate with freestream velocity $U_e = 15$ m/s.

1

the temporal frequencies which result in spatial amplification. Similarly figure 1.3(b) shows the spatial wavelengths of the TS waves which result in temporal amplification as they convect downstream. For example, the single frequency (200 Hz) TS-wave in figure 1.4 has a wavelength of approximately 25 mm and amplifies after $x = 200$ mm, which matches the predictions in figure 1.3.

As a final observation, note that boundary layers are frequency selective and behave as spatio-temporal bandpass filters of upstream perturbations; the spectrum at some given downstream location reflects the broadband noise present in the upstream flow. This observation will form the basis for efficiently modelling the effect of the upstream disturbance environment and capturing the relevant flow physics in chapter 3 and chapter 4.

1.1.4. THE FLOW CONTROL PROBLEM

The instability mechanisms described in the previous two sections form the basis for the design of controllers using linear systems theory. The control design not only includes choosing the control strategy, but also includes choosing suitable actuators/sensors, placement of the actuators/sensors and modelling of the external noise environment. This section formulates the control problem typically considered for flow control applications.

ACTUATORS AND SENSORS

Linear systems theory provides a natural extension of stability theory by including actuators and sensors in equation (1.4). The input-output dynamics can be described by a linear *state-space* system as

$$\begin{aligned}\partial_t \mathbf{u} &= \mathcal{A}\mathbf{u} + \mathcal{B}\phi, \\ \mathbf{y} &= \mathcal{C}\mathbf{u} + \mathcal{D}\phi,\end{aligned}\tag{1.9}$$

where \mathcal{B} models the influence of the actuator input ϕ on the flow and with \mathcal{C} the output operator that relates the flow perturbation field to the measured quantities \mathbf{y} . In some cases the control input may affect the measured output instantly modelled by the feedthrough \mathcal{D} . Actuators used for flow control include plasma actuators

[24], fluidic actuators such as synthetic jets and moving surfaces such as morphing surfaces. The reader is referred to Cattafesta III and Sheplak [25] for a detailed review on actuators for flow control. The most common sensors for flow control are velocity measurements using hot-wires, shear stress ($\partial u/\partial y$) measurements using hot-film sensors and pressure measurements using microphones. The choice and number of actuators and sensors has a decisive effect on the maximum attainable performance. The actuator must be chosen such that it has sufficient bandwidth in both space and time to effectively control the instabilities; it should comply with the time and length scales of the instabilities. Similarly, the sensor must have a sufficient signal to noise ratio in order to detect the instabilities. While the actuator/sensor location can in some cases be optimised [26], the placement is often based on the state-space properties [27, 28] and physical insight. For example, for control of global instabilities that never leave the laboratory frame, the sensor is commonly placed where the instability (global mode) is largest and the actuator is placed where the sensitivity of the instability is largest, e.g. at the separation point of the free shear layer. For control of convectively unstable flows on the other hand there exist only a small window in time to cancel the incoming perturbations. Therefore, a feedforward actuator/sensor configuration is commonly considered in which the sensor is placed upstream of the actuator. In this case the sensor can detect the incoming perturbations as soon as possible. The actuator should in turn be placed close to the sensor to limit the effect of time delays and increase the robustness in case of model uncertainties [27].

THE COMPENSATOR

The state-space representation of the flow is the starting point for modern control design. The two most used theories for flow control design are the state-space \mathcal{H}_2 /LQG and \mathcal{H}_∞ optimal control theories [29]. These techniques automatically handle multivariable inputs/outputs and allow to rigorously account for modelling uncertainties, external environment noise and measurement noise in the control design. Optimal control refers to the synthesis of controllers by minimising a predefined cost function describing the desired features to be controlled. The control design can thus be viewed as the formulation and solution of an optimisation problem. If the state-space model of the flow is available then the optimal controller can be derived by simple state-space formulas [30]. First the structure of the optimal controller is discussed. The formulation of the optimisation problem will follow thereafter.

The optimal controller can be decomposed in a dynamic state estimator/observer for the perturbations and a static feedback control law and can be expressed in the so-called observer form

$$\begin{aligned}\partial_t \hat{\mathbf{u}} &= \mathbf{A}\hat{\mathbf{u}} + \mathbf{B}\phi + \mathcal{L}(\mathbf{y} - \mathbf{C}\hat{\mathbf{u}}), \\ \phi &= -\mathcal{F}\hat{\mathbf{u}}.\end{aligned}\tag{1.10}$$

Equation (1.10) is commonly referred to as a dynamic compensator. The idea is to design the compensator using the state-space model and to apply the result to the original flow. The complete compensated system, which includes the compensator in closed-loop with the system is shown in figure 1.5. The dynamic estimator contains a copy of the state-space system with an additional output injection term to

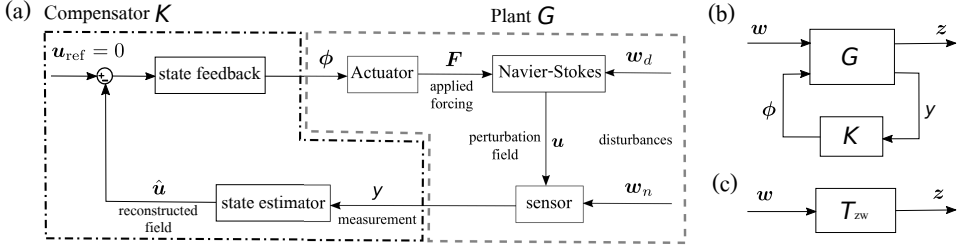


Figure 1.5: Compensated system and the input-output signals (a), the generalised plant representation of the system including control objective z (b) and the closed-loop system representation (c).

account for disturbance uncertainties. In practice, the flow is driven by (unknown) external disturbances such as sound and vorticity in the freestream. Furthermore, measurements are non-ideal (noisy) and available only in a small portion of the system, i.e the information is incomplete. In addition, the initial condition is generally unknown/uncertain due to the external perturbations. The estimator problem is to compute the gain \mathcal{L} such that the injecting term forces the estimated state \hat{u} to converge to the true state u in (1.9) in the presence of these aforementioned uncertainties. The estimator filters the available information using the governing equations itself to extract the signal $\hat{y} = \mathcal{C}\hat{u}$ and to reconstruct the state \hat{u} of the system in the process. The estimated state is subsequently used for feedback control of the perturbations. The state feedback control problem is subsequently to compute the gain \mathcal{F} to stabilise the estimated state, i.e. forces the state towards zero.

FORMULATION OF THE CONTROL PROBLEM

The control design can be viewed as the formulation and solution of an optimisation problem. The formulation involves the modelling of the external disturbances and formulating the control objective. If this information is added to equation (1.9) the latter results in the so-called generalised plant

$$\begin{aligned} \partial_t \mathbf{u} &= \mathbf{A}\mathbf{u} + \mathbf{B}_1 \mathbf{w} + \mathbf{B}_2 \phi, \\ z &= \mathcal{C}_1 \mathbf{u} + \mathcal{D}_{12} \phi, \\ \mathbf{y} &= \mathcal{C}_2 \mathbf{u} + \mathcal{D}_{21} \mathbf{w}, \end{aligned} \quad (1.11)$$

with $\mathbf{w} = (\mathbf{w}_d, \mathbf{w}_n)$ the combined vector of state disturbances \mathbf{w}_d and measurement noise \mathbf{w}_n and z the vector of control objectives to be minimised. The output $\mathcal{C}_1 \mathbf{u}$ should describe the desired features of the flow to be controlled, e.g. the wall shear stress (skin-friction drag) in wall-bounded flows or the structure of the global mode in open flows. The objective z also contains a penalty on the control input given by $\mathcal{D}_{12} \phi$ to have a desirable trade-off between performance and control effort. The input operator \mathbf{B}_1 models how the external disturbances such as sound and vorticity enter the boundary layer and is used to account for uncertainties in the control design. Globally unstable flows are rather insensitive to upstream disturbances due

to the dominance of the global mode; the instability is always there even if the flow is unforced by external disturbances. Issues related to disturbance uncertainties therefore play a subordinate role in the control design [3, 9]. However, convectively unstable flows are highly receptive to external disturbances and there exists only a small window in time to suppress convective instabilities. This poses great challenges for control design and accurately modelling the influence of upstream disturbances is crucial as it forms the basis for the measured unsteadiness. This will be treated in detail in chapter 3 of the present work.

Both the \mathcal{H}_2 and \mathcal{H}_∞ optimal control problems involve the minimisation of the effect of the external disturbances on the performance objective \mathbf{z} . The main difference is in the assumption on the external disturbances/noise. \mathcal{H}_2 control assumes white noise external disturbances, i.e. equal excitation over all frequencies. In contrast \mathcal{H}_∞ control assumes worst case disturbances that give the maximum amplification of the performance measure \mathbf{z} . Mathematically this corresponds to minimising the \mathcal{H}_2 system norm $\|\mathbf{T}_{zw}\|_2$ and the \mathcal{H}_∞ system norm $\|\mathbf{T}_{zw}\|_\infty$ of the closed-loop map \mathbf{T}_{zw} . This work focusses on white stochastic external disturbances. Note that this is physically relevant since Navier-Stokes systems are inherently frequency selective depending on the Reynolds number of the flow. The time domain interpretation of the \mathcal{H}_2 cost function is given by

$$\|\mathbf{T}_{zw}\|_2 = \sqrt{E \left\{ \int_0^\infty \mathbf{z}^T \mathbf{z} dt \right\}}. \quad (1.12)$$

In other words, the control objective is to reduce the expected root mean square value of the output \mathbf{z} when \mathbf{w} is unit variance white Gaussian noise. The synthesis problem is respectively to find a controller of the form (1.10) that minimises (1.12) subject to the system dynamics (1.11). The uniqueness conditions and the state-space formulas of the optimal solution as well as the frequency domain interpretation of the cost function are given in appendix B.

1.2. RESEARCH MOTIVATION AND OBJECTIVES

This work investigates a less explored approach to design and synthesise controllers (1.10) for fluid dynamical systems and is based on state-space discretisations of the governing equations. To place this approach in the context of the current practices and literature Wiener's modelling classification [31] is used. This classification was recently reviewed rigorously and extended to the framework of flow control by Brunton and Noack [8]. The model classification from Brunton and Noack [8] is shown in figure 1.6. This diagram is extended to include the route considered in this work, which is indicated in blue. Rather than giving a complete literature overview, this section discusses the motivation of this route and how it complements current practices. The purpose of this section is to clearly introduce the overall idea and to formulate the objectives, which formed the initial point of departure and the basis for the individual chapters. A more complete literature review will be given in the individual dissertation chapters.

1.2.1. MOTIVATION

The Navier-Stokes equations are continuous in both time and space, resulting in a state space of infinite dimension. Regardless of the control strategy employed, a finite-dimensional state-space representation is required in order to apply linear control theoretical tools. This is often considered the main challenge in the application of linear control theory [7, 9]; To find a practical mathematical model representing the flow dynamics from all the inputs (disturbance and control) to all the outputs (sensors and objectives).

Fluid dynamical systems are complex and display a wide range of temporal and spatial features. Modern computational fluid dynamics (CFD) techniques and experimental techniques can represent the detailed dynamics using a large number of degrees of freedom (i.e. 10^6 or more). For the analysis and control of fluid dynamical systems it has become common practice to use the data from CFD simulations and experiments, to extract the physically important features/modes and represent them in a simpler reduced-order model (ROM). The interested reader is referred to Rowley and Dawson [32] and Taira *et al.* [14] for recent reviews on empirical model reduction methods and modal analysis for fluid flows. Rowley and Dawson [32] also provide a complete list of successful control applications of various methods up to the year 2017. In the case of white/gray-box approaches, the governing equations are taken into account to derive the control model. This starts with a modal decomposition of the data to construct a reduced-order spatial basis that uses snapshots of the flow, for example a POD basis, describing the desirable and physically relevant features to be controlled. The governing equations are subsequently projected on this basis using Galerkin's method to obtain a so-called gray-box ROM, or empirical Galerkin model that can be used for control design.

Reduced-order models based on data from DNS or experiments provide real-time capable models. However, these models are expensive and difficult to create. They rely on the availability of a linearised solver or prior experimental data, which may not always be available. It also requires an adjoint linearised solver in order to construct the dynamically important modes and to guarantee observability/controlability of the basis [33, 34]. Furthermore, the influence of the neglected dynamics is hard to quantify and the projection basis can be sensitive to the temporal and spatial resolution of the data, initial conditions and simulation/experimental conditions [35].

These limitations and difficulties motivate the use of state-space discretisations for control design. In the case of Galerkin discretisation the state-space model is obtained by projecting the governing equations on prior selected mathematical modes. The main advantages of mathematical Galerkin models is that they are guaranteed to converge to the Navier-Stokes solution with increasing number of modes [36] and they are less sensitive to variations in the experimental/simulation conditions [35, pp. 112-149]. In other words, mathematical modes are guaranteed to be complete for the function space (state space) to be approximated, independently of the equations/flow configuration to be approximated. The main limitation is that this approach naturally leads to high order models. Fortunately, the flow to be modelled is laminar and the equations to be approximated are linear, reducing the

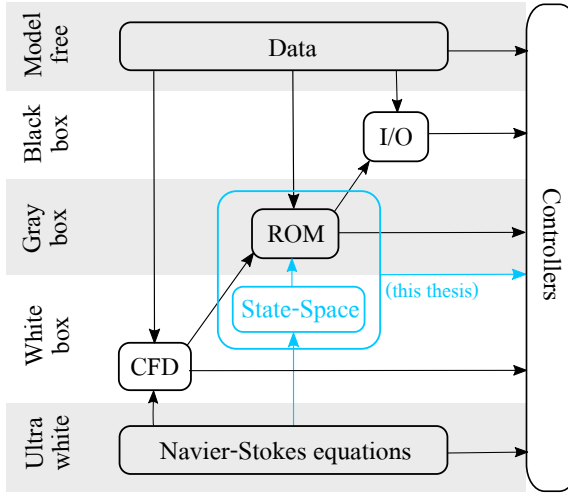


Figure 1.6: Model hierarchy for control design from Brunton and Noack [8]. The blue part indicates the extension from Brunton and Noack [8] to include the finite-dimensional approximation and control approach considered in this dissertation.

dimensional complexity. Furthermore, the instability mechanisms can be leveraged to avoid very large systems; convective instabilities appear in a bounded frequency band and the spectrum of globally unstable systems shows a clear separation between a finite-dimensional unstable part and an infinite dimensional stable complement.

The central philosophy in this dissertation is that the model should be good enough for control applications rather than numerical simulations; Modelling for control rather than modelling for simulation and control. The idea is to select an analytic basis a priori with the flexibility and accuracy required for control applications and to obtain the state-space model directly from the governing equations. The state-space model represents a white-box that effectively balances the accuracy and computational complexity required for the application of system theoretical tools for model reduction and control design. The white-box state-space model can also be used as a higher fidelity 'truth' model, which is crucial to ensure that a control does not exploit a weakness/neglected dynamics in a ROM. Therefore the controllers synthesised with this approach are indicated on the intersection between gray-box and white-box. It is anticipated that this route can open new possibilities for modelling & control design and can simplify the synthesis of controllers also for real-life applications of flow control. This is investigated in the present work.

1.2.2. RESEARCH OBJECTIVES AND SCOPE

This dissertation aims to develop systematic tools and procedures to design experimentally feasible controllers from the governing equations. A significant part of this dissertation presents a theoretical framework for modelling, finite-dimensional approximation and control design for fluid dynamical systems as motivated in the previous section. Additionally, this dissertation aims at demonstrating the practical

feasibility of the proposed approach in both simulation and experiment. Application is particularly focussed on control of linear convective instabilities in two-dimensional wall-bounded shear flows. This is encountered in many physically and engineering relevant cases, such as laminar-turbulent transition on aircraft wings in low disturbance cruise conditions. While breakdown in convectively dominated flows is preceded by nonlinear and three-dimensional development of instabilities, an efficient and cost effective control strategy has higher chances of success if applied at the initial, linear stages of growth, due to the more relaxed constraints on actuator amplitude, dynamic range, sensor-actuator lag, consumed power and dimensional complexity.

This work combines both numerical, theoretical and experimental parts. The research performed in this dissertation can be divided in three main parts, which are finite-dimensional approximation, modelling & control of convective instabilities and experimental validation. The objectives are summarised below.

1

Objective 1 *Develop a new framework to derive finite-dimensional state-space descriptions from the governing equations.* This objective links the Navier-Stokes equations with control theory. State-space modelling is not simply the spatial discretisation of the governing equations. It poses significant analytic and numerical challenges (even in a 1-D spatial domain when considering the Orr-Sommerfeld/Squire form in wavenumber space [37–39]) for irregular geometries and general actuator/sensor configurations. All computations, e.g. incorporating the boundary conditions and the divergence-free constraint, have to be done with care to have a well conditioned system matrix (i.e. with a low condition number) without spurious modes, that can be used for control design. An effort is made to make state-space modelling viable for 2-D/3-D general geometries while ensuring that fundamental properties like stability, controllability/observability of the system are not affected by the discretisation.

Objective 2 *Gain physical insight into the instability mechanisms and exploit these mechanisms for modelling, estimation and control.* This objective involves the application for control of convective instabilities. Model-based controllers rely on a priori assumptions on the external disturbance environment, particularly for effective estimation of the flow instabilities. Convective instabilities are reflections of upstream disturbances, which are not precisely known in real environments. Furthermore, wall-bounded flows have a conceptually unbounded domain. This poses great challenges for accurately capturing the effect of the upstream disturbance environment, which is crucial for an effective control design as it forms the basis for the measured unsteadiness in convectively unstable flows. An effort is made to accurately model the effect of external disturbances on the flow instabilities and the measured unsteadiness, while at the same time avoiding a disturbance specific control design and very large systems.

Objective 3 *Integrate practical actuators and sensors and evaluate the controllers in experiments.* This objective is crucial to investigate the practical feasibility. Practical demonstrations of flow control are tied to the availability of suitable sensor and actuator hardware. Desired attributes of actuators/sensors include a rapid response, high bandwidth, cheap, small and light weight devices that need to be integrated into existing hardware, such as wings. In addition an explicit description of the actuator and sensor is required. For the control design the spatial distribution of the actuator momentum forcing (\mathcal{B}) has to be estimated, which is generally difficult in experimental applications. Similarly, for dynamic flow estimation the physical model variables to be estimated have to be related with the output measurements (\mathcal{C}), which is difficult for surface integrated sensors, e.g. surface microphones. An effort is made to integrate suitable actuators/sensors in the control design methodology, while accounting for their physical constraints in order to effectively apply the controllers in an experimental framework.

1.3. RESEARCH APPROACH, CONTRIBUTIONS AND DISSERTATION OUTLINE

The research approach taken in this dissertation follows from the research objectives. Ideally, flow control research leads to practical applications. Therefore, the choice was made to work towards experimental validation in wind-tunnel experiments, rather than focussing on comparison studies to challenge the current tools and frameworks available in the community. The chosen control objective is the cancellation of TS waves for laminar boundary layer transition delay. Plasma actuators and surface microphones that measure pressure fluctuations were chosen as the actuator/sensor pair to manipulate the flow. Plasma actuators have no moving parts, have a high operating bandwidth, and a very fast frequency response. Pressure measurements can be extracted remotely from the surface by embedding the microphone within a small cavity. Furthermore, microphones have a high signal-to-noise ratio and are able to measure tiny TS waves in their early linear stage. These properties make this actuator/sensor configuration attractive for flow control also by ensuring that the associated costs of flow control are positively balanced by net power savings. With this set-up in mind a bottom-up approach was taken.

Chapter 2 presents a new framework to derive state-space descriptions from the governing equations. Multivariate splines defined on triangulations [40] were chosen as mathematical basis for the Galerkin projection. They allow for mesh, degree and smoothness refinements, which are desirable properties for control-oriented modelling. The developed tools are now part of a Matlab library and are also designed to be used in many other applications than flow control. To extend the scope of this dissertation the choice was made to initially focus on a class of linear parabolic PDEs. The literature review is also performed in the field of control of parabolic PDEs. The application of this method to derive state-space descriptions for the velocity-pressure form of the linearised Navier-Stokes equations is given in appendix A. The derivation of the state-space system relies on the availability of a null space basis matrix and a particular solution for a large sparse linear system of

equality constraints. An efficient null space algorithm is presented in appendix C, which accomplishes this goal and avoids the need for computationally expensive matrix factorisations (QR, SVD).

Chapter 3 deals with the modelling, estimation and control of convective instabilities in wall-bounded flows. The main contribution is a new perturbation modelling that effectively balances spatio-temporal resolution with respect to external disturbances and model order. The modelling is integrated with \mathcal{H}_2 optimal reduced-order control design. The state-space formulas for the controller that solves the \mathcal{H}_2 optimal control problem are given in appendix B. A two-dimensional channel flow is initially considered as application case. This is both mathematically and physically one of the best understood geometries and allowed for a rigorous verification of the modelling method and the control design using the classical local linear stability theory. This chapter also contains a detailed literature review on model-based flow control.

Chapter 4 is concerned with the application for control of Tollmien-Schlichting in laminar boundary layer flows. It provides the first step toward the implementation of controllers using pressure-based sensing for transition delay in experiments. It was found that the inclusion of pressure sensors for dynamic flow estimation was not trivial. This chapter identifies the modelling challenges and provides physical insights in how these modelling challenges affect the maximum attainable performance. In past studies, implementation of pressure sensing has not been treated in a systematic way as part of the control design methodology, which is addressed in this chapter.

Chapter 5 present an experimental study to investigate the practical feasibility of the proposed framework. The controllers have been tested in the newly constructed anechoic vertical tunnel at TU Delft. Experiments have been conducted on a natural laminar flow over a flat plate. A surface microphone that measures the fluctuating pressure and a plasma actuator are used as actuator/sensor pair to control the flow. Experimentally derived body force models of plasma actuators are integrated in the control design methodology. The control logic is implemented on a field-programmable gate array (FPGA) inside a real-time digital signal processor, which is ideal for high-speed flow control applications that require precise timing and hardware tasks. This chapter provides the first study on white-box model-based estimation and control of Tollmien-Schlichting waves naturally occurring in low freestream turbulence conditions.

Finally, **chapter 6** reflects on the objectives, summarises the main findings and recommendations for the proposed approach are given. Additionally, a list of open problems is provided and an outlook for future work/opportunities that extend the results in this dissertation are given.

2

Model reduction of parabolic PDEs using multivariate splines

A new methodology is presented for model reduction of linear parabolic partial differential equations (PDEs) on general geometries using multivariate splines on triangulations. State-space descriptions are derived that can be used for control design. This method uses Galerkin projection with B-splines to derive a finite set of ordinary differential equations (ODEs). Any desired smoothness conditions between elements as well as the boundary conditions are flexibly imposed as a system of side constraints on the set of ODEs. Projection of the set of ODEs on the null space of the system of side constraints naturally produces a reduced-order model that satisfies these constraints. This method can be applied for both in-domain control and boundary control of parabolic PDEs with spatially varying coefficients on general geometries. The reduction method is applied to design and implement feedback controllers for stabilisation of a 1-D unstable heat equation and a more challenging 2-D reaction-convection-diffusion equation on an irregular domain. It is shown that effective feedback stabilisation can be achieved using low order control models.

This chapter has been published as: H.J. Tol, C.C. de Visser and M. Kotsonis, *Model reduction of parabolic PDEs using multivariate splines*, International Journal of Control, 2016

2.1. INTRODUCTION

This chapter presents a reduced-order modelling approach for control of distributed parameter systems (DPS) on general geometries using multivariate basis splines (B-splines) defined on triangulations [40–42]. With DPS the system state, input, output and parameters vary both spatially and temporally. This chapter focuses on DPS governed by parabolic partial differential equations (PDEs) which for example arise in the context of chemical processes, thermal processes and fluid dynamic systems. PDE control theory often focuses on extending finite dimensional results such as stability and optimal control to the infinite-dimensional case (see Curtain and Zwart [43], Lasiecka and Triggiani [44] for a more complete coverage, and references therein). While mathematically precise, these results are often derived for general classes of PDEs and for systems defined on 2-D/3-D general geometries only abstract results are typically available.

This led to the attention of structure specific opportunities that exist in PDEs to produce results that are both constructive and mathematically rigorous [45, 46]. Constructive methods for solving optimal control problems for a class of spatially invariant systems with distributed sensing and actuation was first presented in Bamieh *et al.* [45]. By applying a Fourier transform to the system along the spatially invariant coordinates the system can be block-diagonalized and decoupled in terms of a frequency parameter that replaces the spatially invariant coordinate [45]. In this way, analysis and design of the controller can be carried out on a parameterised lower dimensional system and later reconstructed in the physical space [45, 47]. In Smyshlyaev and Krstic [46, 48] a closed-form continuous backstepping control/observer design method was first presented for stabilisation of a class of 1-D parabolic PDEs. The backstepping method has the powerful feature that it produces explicitly computable gains and has been extended to higher dimensional spatial domains and systems of coupled PDEs. We refer to Baccoli *et al.* [49] for a recent overview of developments of the backstepping method. In particular, by also exploiting spatial invariance this method has led to explicit solutions for 2-D and 3-D spatially invariant control problems [50] such as the Navier-Stokes channel flow [51].

Many practical engineering problems are formulated in spatially variant geometries such as irregular channels or require that the controls and sensors are spatially localised. In this case a finite-dimensional approximation of the infinite-dimensional system is often required. Model reduction is the process of reducing the infinite dimensional PDE to a finite set of ODEs that can be used for control design. We refer to Li and Qi [52] for a recent review on model reduction techniques for PDEs. Galerkin projection is most commonly applied to parabolic PDEs and in this method, one obtains a lower dimensional approximation by projecting the PDE onto a set of spatial basis functions that contain characteristics of the expected solution. The orthogonality of the projection ensures the best possible solution in the space spanned by the basis functions. The main advantage of this approach is that it is robust with respect to the truncated dynamics; a controller which exponentially stabilises the closed-loop ODE system also stabilises the closed-loop parabolic PDE system [53–55]. On the other hand it may require a large number of modes to derive an ODE system with the desired degree of accuracy. Selection of the spatial basis

functions is critical and has a great impact on the modelling performance.

A feature of most parabolic PDE systems is that the eigenspectrum of the spatial differential operator shows a clear separation between a finite-dimensional slow part and an infinite-dimensional fast complement [53]. If the eigenfunctions of the spatial differential operator are known, a suitable choice for model reduction is therefore the projection of the system on the modal subspace spanned by the dominant eigenfunctions [56–58]. This requires analytic solutions of the spatial differential operator eigenvalue problem to form the modal subspace which are often not available for systems defined on irregular domains and systems with spatially varying coefficients. Another approach is to utilise simulation data or experimental data of the PDE system to compute a set of empirical eigenfunctions through the proper orthogonal decomposition (POD) method (see e.g. Armaou and Christofides [59, 60], Baker *et al.* [61]). The POD method is a statistical technique that extracts the most energetic modes from a set of snapshots and therefore leads to low-order expansions. The POD method is applicable to a wide range of DPS, including those defined on irregular domains. However, each set of POD modes is intrinsic to a particular simulation or snapshots and its effectiveness is highly dependent on the simulation or experimental settings [34, 52]. It also has limitations for the describing input-output behaviour of the system [34].

This chapter introduces a new systematic approach for model reduction of parabolic PDEs on general geometries using multivariate B-splines defined on triangulations [40–42]. This method uses Galerkin projection with B-splines to derive a finite set of ODEs. The multivariate B-spline consists of piecewise defined polynomials of arbitrary degree called B-form polynomials. Any desired smoothness conditions between elements as well as the boundary conditions are flexibly imposed as a system of side constraints on the set of ODEs. Projection of the set of ODEs on the null space of the system of side constraints naturally produces a reduced-order model that satisfies these constraints. The multivariate B-spline has been used in the past to find numerical solutions for elliptic PDEs [62, 63] and steady Navier-Stokes equations [64, 65] based on energy methods, and to find numerical solutions for Hamilton-Jacobi-Bellman PDEs using the collocation method [66]. This work is different in the sense that it does not find explicit numerical solutions for PDEs. Instead the PDE is spatially discretised and converted to a linear state-space representation that is used for control design.

The main contribution of this chapter is a new framework to derive state-space descriptions for a class of parabolic PDEs to which standard control theoretic tools can be applied. The main advantage of this method is that it is general in the sense that it can be applied for both in-domain control and boundary control of parabolic PDEs with spatially varying coefficients defined on general geometries. It is in particular useful for parabolic PDEs for which analytic solutions of the spatial differential operator eigenvalue problem are not possible. We are also able to use multivariate spline functions of variable degrees and variable smoothness across any given domain. These properties make spline functions more user-friendly compared to standard finite elements. Splines with higher order smoothness can directly be implemented to approximate the strong solution of the PDE system

and polynomials of high degrees can be easily used to get better approximation properties [62–64]. The degree and order of continuity of splines are simply input variables for creating the state-space models which can be also tuned to achieve a desirable trade-off between the accuracy and the order of the model. Together with the mesh flexibility, this method allows the construction of reduced-order models which are both accurate and suitable for online applications. We refer to Awanou *et al.* [62] for an overview of more features of multivariate splines and references within. Compared to POD-Galerkin methods, this approach may lead to higher order models, but in return provides a systematic approach in which the input-output behaviour of the system is easily established. This method can also be used in conjunction with other open-loop truncation methods for state-space systems such as balanced truncation [67]. This combination can open a new route towards the control of more complex problems such as the three-dimensional Navier-Stokes equations.

In this chapter, we restrict our attention to a linear class of parabolic PDEs. Nonlinear parabolic PDEs are also tractable for the spline Galerkin method and, in the most general case, lead to nonlinear state-space descriptions of the PDE. To accurately capture the nonlinear couplings between the fast and slow modes without using a high-order model the Galerkin method should be used in combination with (approximate) inertial manifolds to compensate the fast modes with the slow modes [56, 61, 68]. Nonlinear model reduction and control of parabolic PDEs will therefore be considered in a forthcoming study.

The outline of this chapter is as follows. In section 2.2 the class of parabolic PDEs and control types for which the reduction method can be applied is formulated. In section 2.3 a preliminary on multivariate B-splines is given. In section 2.4 the side constraints for the boundary conditions are derived using new expressions for differential operators acting on B-splines. Section 2.5 contains the main contribution of this chapter in which the state-space descriptions are derived, and in section 2.6 the state-space models are used to synthesise the output feedback controller. Finally, in section 2.7 the reduction method is used to implement the feedback controllers for stabilisation of a 1-D unstable heat equation and a 2-D unstable reaction-convection-diffusion equation on an irregular domain, followed by conclusions in section 2.8.

2.2. CLASS OF SYSTEMS UNDER CONSIDERATION

Let Ω be an open-bounded subset of \mathbb{R}^n with a Lipschitz-continuous boundary Γ and set $\Omega_T = \Omega \times (0, T]$ for some fixed time $T > 0$. In this chapter we consider linear parabolic PDEs, with the following state-space description

$$\frac{\partial u(\mathbf{x}, t)}{\partial t} = \mathcal{L}u(\mathbf{x}, t) + \mathbf{g}(\mathbf{x})\phi(t) \quad \text{in } \Omega_T, \quad (2.1a)$$

$$\mathcal{L}_\Gamma u(\mathbf{x}, t) = \mathbf{g}_\Gamma(\mathbf{x})\phi_\Gamma(t) \quad \text{on } \Gamma_T, \quad (2.1b)$$

$$y_k(t) = \int_\Omega \delta(\mathbf{x} - \mathbf{x}_k) \mathcal{L}_y u(\mathbf{x}, t) \quad \text{for } k = 1, \dots, K, \quad (2.1c)$$

$$q_i(t) = \int_\Omega h_i(\mathbf{x}) \mathcal{L}_q u(\mathbf{x}, t) d\mathbf{x} \quad \text{for } i = 1, \dots, Q, \quad (2.1d)$$

with $u(\mathbf{x}, t)$ the state variable, $\mathbf{x} \in \Omega$ the spatial coordinate, $y_k \in \mathbb{R}$ a measured output and $q_i \in \mathbb{R}$ a controlled output, which is used to define the control objective later in this section. The vector function $\mathbf{g}(\mathbf{x}) = [g_1(\mathbf{x}), \dots, g_m(\mathbf{x})]$, $g_i \in L^2(\Omega)$ describes how the inputs $\boldsymbol{\phi}(t) = [\phi_1(t), \dots, \phi_m(t)]^T \in \mathbb{R}^m$ from m linear actuators are distributed in the domain, $\mathbf{g}_\Gamma(\mathbf{x}) = [g_{\Gamma,1}(\mathbf{x}), \dots, g_{\Gamma,m}(\mathbf{x})]$, $g_{\Gamma,i} \in L^2(\Gamma)$ describes how the inputs $\boldsymbol{\phi}_\Gamma(t) = [\phi_{\Gamma,1}(t), \dots, \phi_{\Gamma,m}(t)]^T \in \mathbb{R}^{m_\Gamma}$ are distributed over the boundary and $h_i(\mathbf{x})$ is determined by the desired performance specifications in the domain Ω . The operator \mathcal{L} is defined as a linear partial differential operator with derivatives up to order $k \geq 1$ with spatially varying coefficients

$$\mathcal{L}u = \sum_{|\alpha| \leq k} a_\alpha(\mathbf{x}) D^\alpha u = a_0(\mathbf{x})u + \sum_{1 \leq |\alpha| \leq k} a_\alpha(\mathbf{x}) D^\alpha u, \quad (2.2)$$

where we have used the well-known multi-index notation for the spatial derivative

$$D^\alpha u = \frac{\partial^{|\alpha|} u}{\partial x_1^{\alpha_1} \partial x_2^{\alpha_2} \dots \partial x_n^{\alpha_n}} \quad (2.3)$$

for a given multi-index $(\alpha_1, \alpha_2, \dots, \alpha_n)$ of order $|\alpha| = \alpha_1 + \alpha_2 + \dots + \alpha_n$ and the operators $\mathcal{L}_\Gamma, \mathcal{L}_y, \mathcal{L}_q$ are defined as partial differential operators with constant coefficients. Common boundary conditions are Dirichlet ($\mathcal{L}_\Gamma = I$), Neumann ($\mathcal{L}_\Gamma = \frac{\partial}{\partial n}$) and Robin boundary conditions ($\mathcal{L}_\Gamma = I + \frac{\partial}{\partial n}$). In this study feedback stabilisation of (2.1a) is considered where the PDE describes the error between the unsteady response and the equilibrium profile, e.g. the error between the unsteady temperature and the equilibrium profile of the temperature. It is assumed that point measurements from K boundary or in-domain sensors are used for feedback.

The objective is to reduce the infinite-dimensional state-space system (2.1) to a finite-dimensional state-space system using multivariate splines, which can be used to synthesise any suitable linear controller. In this study a classical linear quadratic optimal control problem is considered. To define the control objective, the system (2.1) is formulated as an infinite-dimensional system in a Hilbert space \mathcal{X} [43, 68]. The derivation of this system is also closely related to the derivation of the reduced-order model in section 2.5. The space of square integrable functions $\mathcal{X} = L^2(\Omega)$ with inner product $(u_1, u_2) = \int_\Omega u_1 u_2 d\mathbf{x}$ and norm $\|u_1\|_2 = (u_1, u_1)^{1/2}$ where $u_1, u_2 \in \mathcal{X}$ is chosen as the state space. The trajectory segment $u(\cdot, t) = \{u(\mathbf{x}, t), \mathbf{x} \in \Omega\}$ is chosen as the state with $u(t)|_\Gamma \in \mathcal{U}$ the value of $u(t)$ on the boundary defined in a separable Hilbert space \mathcal{U} . Defining the following operators on \mathcal{X} as

$$\begin{aligned} \mathcal{A} : D(\mathcal{A}) \subset \mathcal{X} &\mapsto \mathcal{X}, & \mathcal{A}u(t) &= \mathcal{L}u(t), \\ \mathcal{B} : D(\mathcal{B}) \subset \mathcal{X} &\mapsto \mathcal{U}, & \mathcal{B}u(t) &= \mathcal{L}_\Gamma u(t)|_\Gamma, \\ \mathcal{A} : D(\mathcal{A}) &\mapsto \mathcal{X}, & \mathcal{A}u(t) &= \mathcal{A}u(t), \text{ for } u \in D(\mathcal{A}), \\ D(\mathcal{A}) &= D(\mathcal{A}) \cap \ker(\mathcal{B}) = \{u \in D(\mathcal{A}); \mathcal{L}_\Gamma u(t)|_\Gamma = 0\}, \end{aligned} \quad (2.4)$$

where the domain $D(\mathcal{A}) \subset D(\mathcal{B})$ is the set of functions in $L^2(\Omega)$ with derivatives

up to order k in $L^2(\Omega)$, defining the input and output operators as

$$\begin{aligned}\mathcal{B} : \mathbb{R}^m &\mapsto \mathcal{X}, & \mathcal{B}\phi(t) &= \mathbf{g}(\mathbf{x})\phi(t), \\ \mathcal{B}_\Gamma : \mathbb{R}^{m_\Gamma} &\mapsto \mathcal{U}, & \mathcal{B}_\Gamma\phi_\Gamma(t) &= \mathbf{g}_\Gamma(\mathbf{x})\phi_\Gamma(t), \\ \mathcal{C}_k : \mathcal{X} &\mapsto \mathbb{R}, & \mathcal{C}_k u(t) &= (\delta(\mathbf{x} - \mathbf{x}_k), \mathcal{L}_y u(t)), \\ \mathcal{Q}_i : \mathcal{X} &\mapsto \mathbb{R}, & \mathcal{Q}_i u(t) &= (h_i(\mathbf{x}), \mathcal{L}_q u(t))\end{aligned}\tag{2.5}$$

and construct an operator \mathcal{Z} such that

$$\mathcal{Z} : \mathcal{U} \mapsto \mathcal{X}, \quad \mathcal{B}\mathcal{Z}\mathcal{B}_\Gamma\phi_\Gamma(t) = \mathcal{B}_\Gamma\phi_\Gamma(t),\tag{2.6}$$

the system (2.1) can be formulated as [43, section 3.3]

$$\begin{aligned}\frac{\partial u_h(t)}{\partial t} &= \mathcal{A}u_h(t) - \mathcal{Z}\mathcal{B}_\Gamma\dot{\phi}_\Gamma(t) + \mathcal{A}\mathcal{Z}\mathcal{B}_\Gamma\phi_\Gamma(t) + \mathcal{B}\phi(t), \\ \mathbf{y}(t) &= \mathcal{C}\left(u_h(t) + \mathcal{Z}\mathcal{B}_\Gamma\phi_\Gamma(t)\right), \\ \mathbf{q}(t) &= \mathcal{Q}\left(u_h(t) + \mathcal{Z}\mathcal{B}_\Gamma\phi_\Gamma(t)\right),\end{aligned}\tag{2.7}$$

where the solution of (2.7) is related to the classical solution of (2.1) by

$$u(t) = u_h(t) + \mathcal{Z}\mathcal{B}_\Gamma\phi_\Gamma(t).\tag{2.8}$$

From (2.6) and (2.8) it follows that $u_h(t)$ can be regarded as a homogeneous solution and $\mathcal{Z}\mathcal{B}_\Gamma\phi_\Gamma(t)$ as a particular solution that satisfies the boundary conditions. Equation (2.7) can also be formulated on the extended state space $\mathcal{X}^e = \mathcal{X} \oplus \mathbb{R}^{m_\Gamma}$

$$\begin{aligned}\dot{\mathbf{u}}^e(t) &= \bar{\mathcal{A}}\mathbf{u}^e(t) + \bar{\mathcal{B}}\bar{\phi}(t), & \mathbf{u}^e(0) &= \mathbf{u}_0^e, \\ \mathbf{y}(t) &= \bar{\mathcal{C}}\mathbf{u}^e(t), \\ \mathbf{q}(t) &= \bar{\mathcal{Q}}\mathbf{u}^e(t),\end{aligned}\tag{2.9}$$

where

$$\begin{aligned}\mathbf{u}^e(t) &= [u_h^T(t) \quad \phi_\Gamma^T(t)]^T, & \bar{\phi}(t) &= [\phi^T(t) \quad \dot{\phi}_\Gamma^T(t)]^T, \\ \bar{\mathcal{A}} &= \begin{bmatrix} \mathcal{A} & \mathcal{A}\mathcal{Z}\mathcal{B}_\Gamma \\ 0 & 0 \end{bmatrix}, & \bar{\mathcal{B}} &= \begin{bmatrix} \mathcal{B} & -\mathcal{Z}\mathcal{B}_\Gamma \\ 0 & \mathbf{I} \end{bmatrix}, \\ \bar{\mathcal{C}} &= [\mathcal{C} \quad \mathcal{C}\mathcal{Z}\mathcal{B}_\Gamma], & \bar{\mathcal{Q}} &= [\mathcal{Q} \quad \mathcal{Q}\mathcal{Z}\mathcal{B}_\Gamma].\end{aligned}\tag{2.10}$$

The control objective is to synthesise an output feedback that minimises the quadratic (LQR) cost function

$$\mathcal{J} = \int_0^\infty (\mathbf{q}, \mathbf{q})_{\mathbb{R}^n} + (\bar{\phi}, \mathbf{R}\bar{\phi})_{\mathbb{R}^n} dt,\tag{2.11}$$

subject to the system dynamics (2.9) where $(\cdot, \cdot)_{\mathbb{R}^n}$ denotes the standard inner product in \mathbb{R}^n .

2.3. PRELIMINARIES ON MULTIVARIATE SPLINES

Given a bounded polygonal domain $\Omega \in \mathbb{R}^n$ and let \mathcal{T} be a triangulation of Ω . The spline space is the space of all smooth piecewise polynomial functions of degree d and smoothness r over \mathcal{T} with $0 \leq r < d$

$$S_d^r(\mathcal{T}) := s \in C^r(\Omega) : s|_{\Delta} \in \mathcal{P}_d, \forall \Delta \in \mathcal{T}, \quad (2.12)$$

where \mathcal{P}_d denotes the space of all polynomials of total degree d and Δ denotes an n -simplex (line in 1-D, triangle in 2-D, tetrahedron in 3-D) and $\Omega = \bigcup_{\Delta \in \mathcal{T}} \Delta$. In this chapter, the B-form representation of splines defined on triangulations is used [41, 42]. Only the essential theory that is necessary for the treatment of the spline model reduction framework is discussed here. We refer to Lai and Schumaker [40] for a more complete coverage.

Let $\Delta = \langle \mathbf{v}_0, \mathbf{v}_1, \dots, \mathbf{v}_n \rangle$ be an n -simplex with vertices $\mathbf{v}_i = (x_1^{(i)}, x_2^{(i)}, \dots, x_n^{(i)})$. A separate local coordinate system can be defined for each simplex in terms of barycentric weights. In this coordinate system every point $\mathbf{x} = (x_1, x_2, \dots, x_n) \in \mathbb{R}^n$ is described in terms of a unique weighted vector sum of the vertices of Δ

$$\mathbf{x} = \sum_{i=0}^n b_i \mathbf{v}_i, \quad \sum_{i=0}^n b_i = 1, \quad (2.13)$$

where $\mathbf{b} = (b_0, b_1, \dots, b_n) \in \mathbb{R}^{n+1}$ is called the barycentric coordinate of point $\mathbf{x} = (x_1, \dots, x_n)$ relative to simplex Δ . In the remainder of this chapter, we denote $b_{\Delta_j}(\mathbf{x}) : \mathbb{R}^n \rightarrow \mathbb{R}^{n+1}$ as the mapping from Cartesian coordinates to barycentric coordinates for a specific simplex with $\mathbf{b} = b_{\Delta_j}(\mathbf{x})$.

The simplex polynomials are expressed in terms of Bernstein - Bézier basis polynomials of degree d

$$B_{\kappa}^d(b_{\Delta_j}(\mathbf{x})) = \begin{cases} \frac{d!}{\kappa_0! \kappa_1! \dots \kappa_n!} b_0^{\kappa_0} b_1^{\kappa_1} \dots b_n^{\kappa_n} = \frac{d!}{\kappa!} \mathbf{b}^{\kappa} & \mathbf{x} \in \Delta_j, \\ 0 & \mathbf{x} \notin \Delta_j, \end{cases} \quad (2.14)$$

with $\kappa = (\kappa_0, \kappa_1, \dots, \kappa_n) \in \mathbb{N}^{n+1}$ a multi-index with properties $|\kappa| = \kappa_0 + \kappa_1 + \dots + \kappa_n$ and $|\kappa| = \kappa_0 + \kappa_1 + \dots + \kappa_n$. In [42] it is shown that the set

$$\mathcal{B}^d = \{B_{\kappa}^d(\mathbf{b}), |\kappa| = d\} \quad (2.15)$$

forms a unique stable local basis for \mathcal{P}_d on Δ . Hence, any simplex polynomial p^{Δ_j} of degree d defined on Δ can be uniquely written as a linear combination of basis polynomials in \mathcal{B}^d [42]

$$p^{\Delta_j}(\mathbf{x}) = \sum_{|\kappa|=d} c_{\kappa}^{\Delta_j} B_{\kappa}^d(\mathbf{b}), \quad (2.16)$$

with $c_{\kappa}^{\Delta_j}$ the B-coefficients. The total number of valid permutations of κ is $\hat{d} = (d+n)!/n!d!$ which is equal to the total number of B-coefficients per simplex. The B-coefficients have a special property in the sense that they have a unique geometric location inside their parent simplex which are referred to as the domain points. The

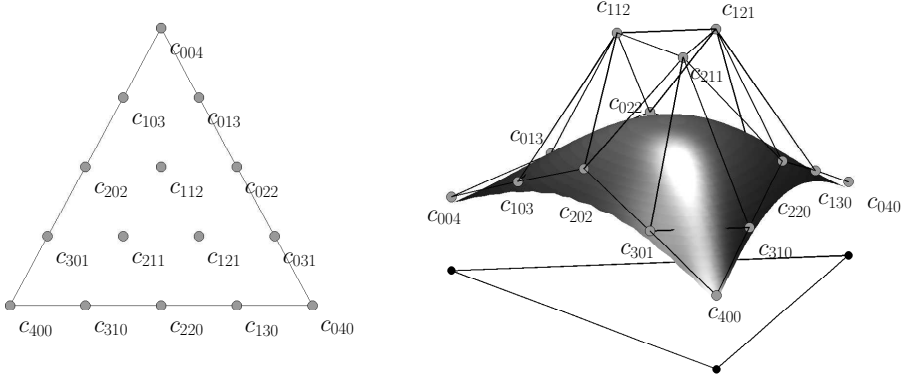


Figure 2.1: Spatial location B-coefficients for a two-dimensional simplex polynomial of degree four (left) and the B-net of the polynomial (right)

complete set of domain points ξ_κ in barycentric coordinates of a polynomial of degree d is given by

$$\mathcal{D}_d = \left\{ \xi_\kappa = \frac{\kappa}{d}, \quad |\kappa| = d \right\}, \quad (2.17)$$

which is equal to the location of the unique maximum of the Bernstein basis polynomial B_κ^d in (2.14). In figure 2.1, the domain points and the B-net are shown for a bivariate simplex polynomial of degree 4. The following theorem will be used for the spline approximation of functions over simplices.

Theorem 1. *There is a unique polynomial p in n variables of degree d that interpolates any given function f on a n -simplex over the domain points in (2.17).*

See Chung and Yao [69] for a proof. The B-form polynomial (2.16) can also be written in vector form [70]

$$p^{\Delta_j}(\mathbf{x}) = \mathbf{B}_{\Delta_j}^d(\mathbf{x}) \mathbf{c}^{\Delta_j}, \quad (2.18)$$

with $\mathbf{B}_{\Delta_j}^d(\mathbf{x}) = [B_\kappa^d(b_{\Delta_j}(\mathbf{x}))]_{|\kappa|=d} \in \mathbb{R}^{1 \times \hat{d}}$ the vector of basis polynomials and with $\mathbf{c}^{\Delta_j} := [c_\kappa^{\Delta_j}]_{|\kappa|=d} \in \mathbb{R}^{\hat{d} \times 1}$ the vector of B-coefficients. Similarly, the globally defined spline function can be written as

$$s(\mathbf{x}) = \sum_{j=1}^J \sum_{|\kappa|=d} c_\kappa^{\Delta_j} \mathbf{B}_\kappa^d(\mathbf{x}) = \mathbf{B}^d(\mathbf{x}) \mathbf{c}, \quad (2.19)$$

with $\mathbf{B}^d(\mathbf{x}) \in \mathbb{R}^{1 \times J\hat{d}}$ the global vector of vector basis polynomials and $\mathbf{c} \in \mathbb{R}^{J\hat{d} \times 1}$ the global vector of B-coefficients and J the total number of simplices. A spline function is by definition a piecewise defined polynomial with C^r continuity over the element simplex boundaries. Continuity of order C^r between two neighboring B-form simplex polynomials p^{Δ_i} , p^{Δ_j} is achieved when all m th order directional

derivatives, with $0 \leq m \leq r$ are equal at every point on the edge $\tilde{\Delta}_{i,j} = \Delta_i \cap \Delta_j$ between the two simplices Δ_i, Δ_j . This is enforced by homogeneous equality constraints of the form $\mathbf{H}^{\Delta_i, \Delta_j} [\mathbf{c}_{\Delta_i}^T, \mathbf{c}_{\Delta_j}^T]^T = 0$ which are defined for every edge of two neighbouring simplices in triangulation \mathcal{T} [62] and [40, pp.133-135]. This guarantees the existence of a matrix $\mathbf{H} \in \mathbb{R}^{R^* \times Jd}$ with $R^* = \text{rank}(\mathbf{H})$ such that $s \in C^r(\Omega)$ if and only if

$$\mathbf{H}\mathbf{c} = 0. \quad (2.20)$$

Constructing \mathbf{H} is not trivial and we refer to de Visser *et al.* [70] for a general formulation of the continuity conditions and the procedure to derive them utilising a B-net orientation rule.

We next discuss the process of computing integrals and inner product of B-form polynomials which are required for the Galerkin projection. The integral of a B-form basis polynomial of degree d and dimension n for any multi-index $|\kappa| = d$ over the volume of its simplex Δ is given by

$$\int_{\Delta} B_{\kappa}^d(\mathbf{x}) d\mathbf{x} = \frac{S_{\Delta}}{\binom{d+n}{n}}, \quad (2.21)$$

where S_{Δ} is the length (1d), area (2d), volume (3d) or hypervolume of the simplex. Equation (2.21) leads directly to inner products of any two B-form basis polynomials $B_{\gamma}^{d_1}, B_{\kappa}^{d_2}$. Using (2.14) we have

$$B_{\gamma}^{d_1} B_{\kappa}^{d_2} = \frac{d_1! d_2!}{\gamma! \kappa!} \mathbf{b}^{\kappa+\gamma}, \quad B_{\gamma+\kappa}^{d_1+d_2} = \frac{(d_1 + d_2)!}{(\gamma + \kappa)!} \mathbf{b}^{\kappa+\gamma}. \quad (2.22)$$

It follows that

$$\int_{\Delta} B_{\gamma}^{d_1} B_{\kappa}^{d_2} d\mathbf{x} = \int_{\Delta} \frac{d_1! d_2!}{\gamma! \kappa!} \frac{(\gamma + \kappa)!}{(d_1 + d_2)!} B_{\gamma+\kappa}^{d_1+d_2} d\mathbf{x}, \quad (2.23)$$

which with (2.21) results in

$$\int_{\Delta} B_{\gamma}^{d_1} B_{\kappa}^{d_2} d\mathbf{x} = \frac{d_1! d_2!}{(d_1 + d_2)!} \frac{S_{\Delta}}{\binom{d_1+d_2+n}{n}} \frac{(\gamma + \kappa)!}{\gamma! \kappa!}. \quad (2.24)$$

In the same way it can be shown that the integral of the product of three B-form basis polynomials $B_{\mu}^{d_1}, B_{\gamma}^{d_2}$ and $B_{\kappa}^{d_3}$ is given by

$$\int_{\Delta} B_{\mu}^{d_1} B_{\gamma}^{d_2} B_{\kappa}^{d_3} d\mathbf{x} = \frac{d_1! d_2! d_3!}{(d_1 + d_2 + d_3)!} \frac{S_{\Delta}}{\binom{d_1+d_2+d_3+n}{n}} \frac{(\mu + \gamma + \kappa)!}{\mu! \gamma! \kappa!}. \quad (2.25)$$

2.4. BOUNDARY CONDITIONS AS SIDE CONSTRAINTS

Similar to the continuity conditions (2.20), the boundary conditions (2.1b) are included as side constraints for the B-coefficients which are derived in this section. With standard finite element methods boundary conditions are commonly explicitly incorporated (Dirichlet type) in the finite element basis or implicitly incorporated

(Neumann type) using a suitable choice for the weak formulation of the PDE. We treat them as side constraints to simplify the construction of the spline basis that satisfies the boundary conditions. No modifications to the spline basis or to the weak formulation are required for different types of boundary conditions. This also allows us to define a model reduction scheme for the general class of linear parabolic PDEs in the next section. The side constraints constrain the spline polynomials at the boundary such that the spline solution satisfies the boundary conditions. The derivation of the constraints requires a new matrix formulation for B-spline derivatives whose image is in the same polynomial space. This allows the formulation of all differential operators in (2.2) in terms of a single degree polynomial basis which will also prove to be essential in the model reduction framework. These derivatives are completely defined in terms of a mapping acting on its B-coefficients and are derived by combining the *de Castelau* formulation for the derivatives [71] with a polynomial degree raising algorithm [63].

We start by introducing a mapping that raises the degree of a simplex polynomial $p \in \mathcal{P}_d$ to $p \in \mathcal{P}_{d+m}$. Let p be a polynomial of degree d defined on a simplex Δ written in the vector form (2.18), and let \mathbf{c} be its coefficients. Then it can also be evaluated by [63]

$$\mathbf{B}^d(\mathbf{x})\mathbf{c} = \frac{d!}{(d+m)!} \mathbf{B}^{d+m}(\mathbf{x}) \mathbf{N}_{\Delta}^{d+m,d} \mathbf{c}, \quad (2.26)$$

with $\mathbf{N}_{\Delta}^{d+m,d} \in \mathbb{R}^{\frac{(d+m+n)!}{n!(d+m)!} \times \frac{(d+n)!}{n!d!}}$ the degree raising matrix that raises the set of B-coefficients of degree d into a set of B-coefficients of degree $d+m$ [63]. The right hand side of (2.26) is again a B-form polynomial with $\mathbf{B}^{d+m}(\mathbf{x})$ the polynomial basis and $\frac{d!}{(d+m)!} \mathbf{N}_{\Delta}^{d+m,d} \mathbf{c}$ its B-coefficient vector. It follows that the mapping given by $\mathbf{c} \mapsto \frac{d!}{(d+m)!} \mathbf{N}_{\Delta}^{d+m,d} \mathbf{c}$ transforms the B-coefficient vector of $p \in \mathcal{P}_d$ to the B-coefficient vector of $p \in \mathcal{P}_{d+m}$.

We next discuss derivatives of B-form polynomials. Let $\mathbf{a} = b_{\Delta_j}(\vec{\mathbf{v}}) - b_{\Delta_j}(\mathbf{0}) = (a_0, a_1, \dots, a_n)$ be the directional coordinate of the unit vector $\vec{\mathbf{v}}$ in barycentric coordinates. Then the general k th order derivative of a polynomial p of degree $1 \leq k \leq d$ in the unit directions $\vec{\mathbf{v}}_1, \dots, \vec{\mathbf{v}}_k$ is given by [40, pp.29]

$$D_{\vec{\mathbf{v}}_k} \cdots D_{\vec{\mathbf{v}}_1} p(\mathbf{x}) = \frac{d!}{(d-k)!} \sum_{|\kappa|=d-k} c_{\kappa}^{(k)}(\mathbf{a}^{(1)}, \dots, \mathbf{a}^{(k)}) \mathbf{B}_{\kappa}^{d-k}(\mathbf{x}) \quad (2.27)$$

where $c_{\kappa}^{(k)}(\mathbf{a}^{(1)}, \dots, \mathbf{a}^{(k)})$ are the quantities obtained after carrying out k steps of the de Castelau iteration

$$c_{\kappa}^{(k)}(\mathbf{a}) = \sum_{|\gamma|=1} \mathbf{a}^{\gamma} c_{\kappa+\gamma}^{(k-1)}(\mathbf{a}), \quad |\kappa|=d-k, \quad k \leq d \quad (2.28)$$

using the directional coordinates $\mathbf{a}^{(1)}, \dots, \mathbf{a}^{(k)}$ of $\vec{\mathbf{v}}_1, \dots, \vec{\mathbf{v}}_k$ in that order. For example, if we put $d_{\kappa} = c_{\kappa}^{(1)}(\mathbf{a}^{(1)})$, then $c_{\kappa}^{(2)}(\mathbf{a}^{(1)}, \mathbf{a}^{(2)}) = d_{\kappa}^{(1)}(\mathbf{a}^{(2)})$. Equation (2.28) can be written in matrix form [71]

$$\mathbf{c}^{(k)} = \mathbf{P}^{d-k, d-k+1}(\mathbf{a}) \mathbf{c}^{(k-1)}(\mathbf{a}), \quad (2.29)$$

with $\mathbf{P}^{d-k,d-k+1} \in \mathbb{R}^{\frac{(d-k+n)!}{n!(d-k)!} \times \frac{(d-k+1+n)!}{n!(d-k+1)!}}$ the one-step de Castelau matrix [71] which reduces the set of B-coefficients of degree $d-k+1$ into a set of B-coefficients of degree $d-k$. Using the vector formulation of the B-form polynomial (2.18) and the de Castelau algorithm (2.29), the general derivative (2.27) can be written in matrix form

$$D^k p(\mathbf{x}) = \frac{d!}{(d-k)!} \mathbf{B}^{d-k}(\mathbf{x}) \mathbf{P}^{d-k,d}(\mathbf{a}^{(1)}, \dots, \mathbf{a}^{(k)}) \mathbf{c}, \quad (2.30)$$

with $D^k = D_{v_k} \cdots D_{v_1}$ and

$$\mathbf{P}^{d-k,d}(\mathbf{a}^{(1)}, \dots, \mathbf{a}^{(k)}) = \prod_{i=1}^k \mathbf{P}^{d-i,d-i+1}(\mathbf{a}^{(i)}) \quad (2.31)$$

a multi-degree de Castelau matrix. Equation (2.30) can be combined with polynomial degree raising (2.26) to construct k th-order derivatives whose image is in \mathcal{P}_{d-k+m} .

Theorem 2. *Let $p \in \mathcal{P}_d$ be a B-form polynomial of degree $1 \leq k \leq d$ relative to simplex Δ , and given a set of directions $\vec{v}_1, \dots, \vec{v}_k$ described by the directional coordinates $\mathbf{a}^{(k)} = (a_0^{(k)}, \dots, a_n^{(k)})$. The matrix form of the k th order derivative $D^k = D_{\vec{v}_k} \cdots D_{\vec{v}_1} p \in \mathcal{P}_{d-k+m}$ in the unit directions $\vec{v}_1, \dots, \vec{v}_k$ is given by*

$$D^k p(\mathbf{x}) = \frac{d!}{(d-k+m)!} \mathbf{B}^{d-k+m}(\mathbf{x}) \mathbf{N}_{\Delta}^{d-k+m,d-k} \mathbf{P}^{d-k,d}(\mathbf{a}^{(1)}, \dots, \mathbf{a}^{(k)}) \mathbf{c}. \quad (2.32)$$

Proof. The right-hand side of (2.30) is a B-form polynomial in \mathcal{P}_{d-k} with $\mathbf{B}^{d-k}(\mathbf{x})$ its polynomial basis and $\mathbf{c}^{(k)} = \frac{d!}{(d-k)!} \mathbf{P}^{d-k,d}(\mathbf{a}^{(1)}, \dots, \mathbf{a}^{(k)}) \mathbf{c}$ its coefficients. Applying the mapping $\mathbf{c}^{(k)} \mapsto \frac{(d-k)!}{(d-k+m)!} \mathbf{N}_{\Delta}^{d-k+m,d-k} \mathbf{c}^{(k)}$ to (2.30) to raise $D^k p(\mathbf{x}) \in \mathcal{P}_{d-k}$ to $D^k p(\mathbf{x}) \in \mathcal{P}_{d-k+m}$ gives the result in (2.32). \square

The spline function $s \in S_d^r(\Omega)$ is guaranteed to be r -times continuously differentiable on the domain Ω . The following corollary introduces a mapping for the B-coefficient vector to compute derivatives of s and follows directly from theorem 2.

Corollary 1. *Given the B-coefficient vector \mathbf{c} of $s \in S_d^r(\mathcal{T})$, the mapping $\mathbf{c} \mapsto \mathbb{T}_{D^k}^{d-k+m,d} \mathbf{c}$ with*

$$\mathbb{T}_{D^k}^{d-k+m,d} = \text{diag} \left(\frac{d!}{(d-k+m)!} \mathbf{N}_{\Delta}^{d-k+m,d-k} \mathbf{P}^{d-k,d}(\mathbf{a}^{(1)}, \dots, \mathbf{a}^{(k)}) \right)_{j=1}^J \quad (2.33)$$

maps the B-coefficients of $s \in S_d^r(\mathcal{T})$ to the B-coefficients of $D^k s \in S_{d-k+m}^{r-k}(\mathcal{T})$, that is

$$D^k \left[\mathbf{B}^d(\mathbf{x}) \mathbf{c} \right] = \mathbf{B}^{d-k+m}(\mathbf{x}) \mathbb{T}_{D^k}^{d-k+m,d} \mathbf{c}. \quad (2.34)$$

Hence, any spatial derivative can simply be constructed by applying the mapping (2.33) in parameter space. Note that the spatial derivative D^α (2.3) of order $|\alpha|$ is a special case of D^k . Corollary 1 is used to define a similar transformation matrix for the general linear differential operator (2.2) with constant coefficients.

Theorem 3. Let \mathcal{L} be a linear partial differential operator of order k given by (2.2) with constant coefficients and given the B-coefficient vector \mathbf{c} of $s \in S_d^r(\mathcal{T})$. Furthermore let $\mathbb{T}_{D^\alpha}^{d,d}$ be the transformation matrix that maps $s \in S_d^r(\mathcal{T})$ to $D^\alpha s \in S_d^{r-|\alpha|}(\mathcal{T})$ constructed using (2.33) with $k = m = |\alpha|$. Then the mapping $\mathbf{c} \mapsto \mathbb{T}_{\mathcal{L}}^{d,d} \mathbf{c}$ with

$$\mathbb{T}_{\mathcal{L}}^{d,d} = \sum_{|\alpha| \leq k} a_\alpha \mathbb{T}_{D^\alpha}^{d,d} \quad (2.35)$$

maps the B-coefficients of $s \in S_d^r(\mathcal{T})$ to the B-coefficients of $Ls \in S_d^{r-k}(\mathcal{T})$, that is $\mathcal{L} [\mathbf{B}^d(\mathbf{x})\mathbf{c}] = \mathbf{B}^d(\mathbf{x})\mathbb{T}_{\mathcal{L}}^{d,d} \mathbf{c}$.

Proof. Applying Corollary 1, the linear operator acting on s can be written in terms of a single degree basis polynomial

$$\begin{aligned} \mathcal{L} [\mathbf{B}^d(\mathbf{x})\mathbf{c}] &= \sum_{|\alpha| \leq k} a_\alpha D^\alpha [\mathbf{B}^d(\mathbf{x})\mathbf{c}] \\ &= \sum_{|\alpha| \leq k} a_\alpha \mathbf{B}^d(\mathbf{x}) \mathbb{T}_{D^\alpha}^{d,d} \mathbf{c}, \end{aligned} \quad (2.36)$$

which can be written in the form $\mathcal{L} [\mathbf{B}^d(\mathbf{x})\mathbf{c}] = \mathbf{B}^d(\mathbf{x})\mathbb{T}_{\mathcal{L}}^{d,d} \mathbf{c}$ where $\mathbb{T}_{\mathcal{L}}^{d,d}$ is given by (2.35). \square

This theorem is used to define the boundary constraints. The value of a B-form simplex polynomial at the edge of the simplex is uniquely determined by the values of the B-coefficients located on the edge [64] (See also Figure 2.1). This implies that there is a matrix \mathbf{D} which maps the B-coefficients of s to the B-coefficients of $s|_\Gamma$, that is $s|_\Gamma = \tilde{\mathbf{B}}^d(\mathbf{x})\mathbf{D}\mathbf{c}$, with $\tilde{\mathbf{B}}^d(\mathbf{x})$ an $n-1$ B-form vector basis [64]. Or in other words, the action $\mathbf{c} \mapsto \mathbf{D}\mathbf{c}$ selects the B-coefficients located on the boundary. Combined with theorem 3 it follows that $\mathbf{c} \mapsto \mathbf{D}\mathbb{T}_{\mathcal{L}_\Gamma}^{d,d} \mathbf{c}$ maps the B-coefficients of s to the B-coefficients of $\mathcal{L}_\Gamma s|_\Gamma$, that is $\mathcal{L}_\Gamma s|_\Gamma = \tilde{\mathbf{B}}^d(\mathbf{x})\mathbf{D}\mathbb{T}_{\mathcal{L}_\Gamma}^{d,d} \mathbf{c}$. Furthermore, by theorem 1 there is a unique $n-1$ dimensional simplex polynomial that interpolates the actuator distribution functions $g_{\Gamma,i}(\mathbf{x})$ at the domain points on the simplex face located on the boundary Γ . Denote \mathbf{g}_Γ^i as the B-coefficient vector of the $n-1$ dimensional spline function that interpolates $g_{\Gamma,i}(\mathbf{x})$ over the complete set of domain points on the boundary Γ and define $\mathbf{G}_\Gamma = [\mathbf{g}_\Gamma^1 \cdots \mathbf{g}_\Gamma^m]$, we may set

$$\mathbf{D}\mathbb{T}_{\mathcal{L}_\Gamma}^{d,d} \mathbf{c}(t) = \mathbf{G}_\Gamma \phi_\Gamma(t) \quad (2.37)$$

to enforce that the spline solution satisfies the boundary condition (2.1b) approximately. Note that in the case of homogeneous boundary conditions the B-coefficient constraints model the boundary conditions exactly since no approximations are involved.

Example 1. As an example consider the following homogeneous Robin boundary conditions

$$as + b \frac{\partial s}{\partial n} = 0 \quad \text{on } \Gamma, \quad (2.38)$$

where a and b are constants. First the left hand side of (2.38) is written as a single spline function

$$\mathbf{B}^d(\mathbf{x}) \left(a\mathbf{I} + b\mathbb{T}_{D_n}^{d,d} \right) \mathbf{c} = \mathbf{B}^d(\mathbf{x}) \mathbb{T}_{\mathcal{L}_\Gamma}^{d,d} \mathbf{c} = 0 \quad (2.39)$$

and we can set

$$\mathbf{D} \left(a\mathbf{I} + b\mathbb{T}_{D_n}^{d,d} \right) \mathbf{c} = \mathbf{D} \mathbb{T}_{\mathcal{L}_\Gamma}^{d,d} \mathbf{c} = 0 \quad (2.40)$$

to encode that the spline function satisfies (2.38) on the boundary.

2.5. MODEL REDUCTION OF LINEAR PARABOLIC PDES

In this section, the finite-dimensional state-space description of (2.1) is constructed using multivariate splines. First, the DPS is reduced to a finite set of coupled ODEs using Galerkin projection after which the complete system of equations including the side constraints for the smoothness conditions (2.20) and boundary conditions (2.37) is transformed to state-space format using a null space approach that significantly reduces the size of the system.

The spline approximation is determined through the following Galerkin-type weak formulation: Find $u(\mathbf{x}, t) \in L^2(0, T; H^k(\Omega))$ such that

$$\int_{\Omega} \frac{\partial u(\mathbf{x}, t)}{\partial t} v(\mathbf{x}) \, d\mathbf{x} = \int_{\Omega} \left(\mathcal{L}u(\mathbf{x}, t) + \mathbf{g}(\mathbf{x})\phi(t) \right) v(\mathbf{x}) \, d\mathbf{x}, \quad (2.41)$$

$$\mathcal{L}_\Gamma u(\mathbf{x}, t) = \mathbf{g}_\Gamma(\mathbf{x})\phi(t), \quad \text{on } \Gamma_T,$$

$\forall v \in V_0$ and $t \in [0, T]$, with $H^k(\Omega)$ the standard Sobolev space consisting of all functions whose spatial derivatives up to k th-order exist in the weak sense and are in $L^2(\Omega)$ and with V_0 the space associated with the test functions $v(\mathbf{x})$

$$V_0 = \{v \in H^k(\Omega) : \mathcal{L}_\Gamma v = 0\}. \quad (2.42)$$

A common approach is to apply integration by parts and the Gauss-Green theorem to (2.41) to lower the smoothness requirements and to implicitly incorporate natural (Neumann type) boundary conditions in the weak formulation. This approach is not employed here since a spline basis of higher degree and smoothness with the characteristics of the strong solution can easily be constructed.

We now define the spline approximation of (2.41). Let \mathcal{T} be the triangulation of Ω if Ω is a polygonal domain. Otherwise we choose the vertices on Γ such that \mathcal{T} becomes the approximation of Ω . Let d and r be two positive integers with $d > r$, $r \geq k - 1$ and let \mathcal{S} be a spline subspace consisting of spline functions which are C^r inside Ω . We have that $\mathcal{S} \subset S_d^{k-1}(\mathcal{T}) \subset H^k(\Omega)$. The finite-dimensional approximation of u in Ω can be represented by

$$u_N(\mathbf{x}, t) = s_u(\mathbf{x}, t) = \sum_{j=1}^J \sum_{|\kappa|=d} c_\kappa^{\Delta_j}(t) B_\kappa^d(\mathbf{x}) = \mathbf{B}^d(\mathbf{x}) \mathbf{c}(t), \quad (2.43)$$

with $s \in \mathcal{S}$, $N = J\hat{d}$ and where the B-coefficients satisfy the C^r continuity conditions (2.20). In (2.43) the B-form basis polynomials $B_\kappa^d(\mathbf{x})$ are used as spatial basis

functions and the B-coefficients as time-varying expansion coefficients. Let $\mathcal{S}_0 = \mathcal{S} \cap V_0$. The spline approximation of (2.41) with respect to the spatial variables is $s(\cdot, t) \in \mathcal{S}$ which must satisfy the approximate boundary conditions (2.37) such that

$$\int_{\Omega} \frac{\partial s_u(\mathbf{x}, t)}{\partial t} s_v(\mathbf{x}) \, d\mathbf{x} = \int_{\Omega} \left(\mathcal{L} s_u(\mathbf{x}, t) + \mathbf{g}(\mathbf{x}) \phi(t) \right) s_v(\mathbf{x}) \, d\mathbf{x} \quad (2.44)$$

$\forall s_v \in \mathcal{S}_0$ and $t \in [0, T]$. Recall from theorem 3 that the differential operator acting on s can be written in terms of a single degree basis polynomial

$$\mathcal{L} \left[\mathbf{B}^d(\mathbf{x}) \mathbf{c}(t) \right] = \sum_{|\alpha| \leq k} a_{\alpha}(\mathbf{x}) \mathbf{B}^d(\mathbf{x}) \mathbb{T}_{D^{\alpha}}^{d,d} \mathbf{c}(t), \quad (2.45)$$

with $\mathbb{T}_{D^{\alpha}}^{d,d}$ the transformation matrix that maps the B-coefficient vector of $s \in S_d^r(\mathcal{T})$ to the B-coefficients of $D^{\alpha} s \in S_d^{r-|\alpha|}(\mathcal{T})$. Let \mathbf{d} be the B-coefficient vector of the test function $s_v \in \mathcal{S}_0$ with $s_v = \mathbf{B}^d(\mathbf{x}) \mathbf{d}$, (2.44) can be written as

$$\begin{aligned} & \mathbf{d}^T \left(\int_{\Omega} \left[\mathbf{B}^d(\mathbf{x}) \right]^T \mathbf{B}^d(\mathbf{x}) \, d\mathbf{x} \right) \dot{\mathbf{c}}(t) \\ &= \mathbf{d}^T \left[\sum_{|\alpha| \leq k} \left(\int_{\Omega} a_{\alpha}(\mathbf{x}) \left[\mathbf{B}^d(\mathbf{x}) \right]^T \mathbf{B}^d(\mathbf{x}) \, d\mathbf{x} \right) \mathbb{T}_{D^{\alpha}}^{d,d} \right] \mathbf{c}(t) \\ &+ \mathbf{d}^T \left(\int_{\Omega} \left[\mathbf{B}^d(\mathbf{x}) \right]^T \mathbf{g}(\mathbf{x}) \, d\mathbf{x} \right) \phi(t), \end{aligned} \quad (2.46)$$

which must hold for all B-coefficient vectors \mathbf{d} of splines in \mathcal{S}_0 , that is for all \mathbf{d} satisfying the C^r smoothness constraints $\mathbf{H}\mathbf{d} = 0$ and the homogeneous boundary constraints $\mathbf{D}\mathbb{T}_{\mathcal{L}_T}^{d,d} \mathbf{d} = 0$. Equation (2.46) is written in terms of B-form polynomials by approximating the actuator distribution functions $g_i(\mathbf{x})$ and the PDE coefficients $a_{\alpha}(\mathbf{x})$ using B-splines. If these functions are continuous, interpolation is the obvious choice. By theorem 1 there is a unique simplex polynomial that interpolates $a_{\alpha}(\mathbf{x})$ over the simplex domain points $\{\xi_{\kappa}^{\Delta}, |\kappa| = d\}$. Let \mathbf{a}^{α} be a B-coefficient vector with $s_{a_{\alpha}}(\mathbf{x}) = \mathbf{B}^d(\mathbf{x}) \mathbf{a}^{\alpha} \in S_d^0(\mathcal{T})$ the spline interpolation of $a_{\alpha}(\mathbf{x})$ over the complete set of domain points and let \mathbf{g}^i be a B-coefficient vector with $s_{g_i}(\mathbf{x}) = \mathbf{B}^d(\mathbf{x}) \mathbf{g}^i \in S_d^0(\mathcal{T})$ the spline interpolation of $g_i(\mathbf{x})$ and define $\mathbf{G} = [\mathbf{g}^1, \mathbf{g}^2, \dots, \mathbf{g}^m]$, then the projection condition (2.46) can be approximated in terms of B-form polynomials by

$$\begin{aligned} & \mathbf{d}^T \left(\int_{\Omega} \left[\mathbf{B}^d(\mathbf{x}) \right]^T \mathbf{B}^d(\mathbf{x}) \, d\mathbf{x} \right) \dot{\mathbf{c}}(t) \\ &= \mathbf{d}^T \left[\sum_{|\alpha| \leq k} \left(\int_{\Omega} \mathbf{B}^d(\mathbf{x}) \mathbf{a}^{\alpha} \left[\mathbf{B}^d(\mathbf{x}) \right]^T \mathbf{B}^d(\mathbf{x}) \, d\mathbf{x} \right) \mathbb{T}_{D^{\alpha}}^{d,d} \right] \mathbf{c}(t) \\ &+ \mathbf{d}^T \left(\int_{\Omega} \left[\mathbf{B}^d(\mathbf{x}) \right]^T \mathbf{B}^d(\mathbf{x}) \, d\mathbf{x} \right) \mathbf{G} \phi(t). \end{aligned}$$

If $a_{\alpha}(\mathbf{x})$ and $g_i(\mathbf{x})$ are not continuous, interpolation can still be used except that the interpolation values should come from a suitable continuous approximation of

$a_\alpha(\mathbf{x})$ and $g_i(\mathbf{x})$ or one can use a piecewise discontinuous polynomial approximation using for example a least squares fit [70].

The integral over a simplex Δ of the product of two or more basis polynomials defined on different simplices is always equal to zero because of their local support. It follows that the integrals in (2.47) result in block diagonal matrices. Applying the integration gives

$$\mathbf{d}^T \mathbf{M} \dot{\mathbf{c}}(t) = \mathbf{d}^T \left(\sum_{|\alpha| \leq k} \mathbf{K}(\mathbf{a}^\alpha) \mathbb{T}_{D^\alpha}^{d,d} \right) \mathbf{c}(t) + \mathbf{d}^T \mathbf{M} \mathbf{G} \phi(t), \quad (2.47)$$

with $\mathbf{M} = \text{diag}(\mathbf{M}_\Delta)$ a mass matrix [64] with blocks

$$\mathbf{M}_\Delta = \left[\int_\Delta B_\kappa^d(\mathbf{x}) B_\gamma^d(\mathbf{x}) \, d\mathbf{x} \right]_{\substack{|\kappa|=d \\ |\gamma|=d}} \quad (2.48)$$

and $\mathbf{K}(\mathbf{a}^\alpha) = \text{diag}(\mathbf{K}_\Delta(\mathbf{a}^\alpha))$ a bending matrix with blocks

$$\begin{aligned} \mathbf{K}_\Delta(\mathbf{a}^\alpha) &= \left[\int_\Delta \mathbf{B}^d(\mathbf{x}) \mathbf{a}^\alpha B_\kappa^d(\mathbf{x}) B_\gamma^d(\mathbf{x}) \, d\mathbf{x} \right]_{\substack{|\kappa|=d \\ |\gamma|=d}} \\ &= \left[\int_\Delta \sum_{|\mu|=d} B_\mu^d(\mathbf{x}) a_\mu^\alpha B_\kappa^d(\mathbf{x}) B_\gamma^d(\mathbf{x}) \, d\mathbf{x} \right]_{\substack{|\kappa|=d \\ |\gamma|=d}}. \end{aligned} \quad (2.49)$$

Using (2.24) and (2.25) the mass and bending matrices can be explicitly calculated with

$$\mathbf{M}_\Delta = \frac{d! d!}{(2d)!} \frac{S_\Delta}{\binom{2d+n}{n}} \left[\frac{(\gamma + \kappa)!}{\gamma! \kappa!} \right]_{\substack{|\kappa|=d \\ |\gamma|=d}}, \quad (2.50)$$

$$\mathbf{K}_\Delta^\alpha = \frac{d! d! d!}{(3d)!} \frac{S_\Delta}{\binom{3d+n}{n}} \left[\sum_{|\mu|=d} a_\mu^\alpha \frac{(\mu + \gamma + \kappa)!}{\mu! \gamma! \kappa!} \right]_{\substack{|\kappa|=d \\ |\gamma|=d}}. \quad (2.51)$$

Let $\mathbf{K} = \sum_{|\alpha| \leq k} \mathbf{K}(\mathbf{a}^\alpha) \mathbb{T}_{D^\alpha}^{d,d}$ and $\mathbf{F} = \mathbf{M} \mathbf{G}$, it follows that the B-coefficient vector \mathbf{c} of the spline approximation satisfies

$$\mathbf{d}^T \mathbf{M} \dot{\mathbf{c}}(t) = \mathbf{d}^T \mathbf{K} \mathbf{c}(t) + \mathbf{d}^T \mathbf{F} \phi(t), \quad (2.52a)$$

$$\mathbf{H} \mathbf{c}(t) = \mathbf{0}, \quad (2.52b)$$

$$\mathbf{D} \mathbb{T}_{\mathcal{L}_\Gamma}^{d,d} \mathbf{c}(t) = \mathbf{G}_\Gamma \phi_\Gamma(t) \quad (2.52c)$$

for all B-coefficient vectors \mathbf{d} of splines in \mathcal{S}_0 satisfying $\mathbf{H} \mathbf{d} = \mathbf{0}$ and $\mathbf{D} \mathbb{T}_{\mathcal{L}_\Gamma}^{d,d} \mathbf{d} = \mathbf{0}$. Existence and uniqueness of \mathbf{c} can be shown by using the same argument for the existence of the weak solution satisfying (2.41) [62, 65]. We are interested in solving

(2.52) for $\dot{\mathbf{c}}$. A null-space approach is proposed which significantly reduces the size of the system by the rank of the side constraints. Let $\mathbf{L} = \begin{bmatrix} \mathbf{H}^T & (\mathbf{D}\mathbb{T}_{\mathcal{L}_\Gamma}^{d,d})^T \end{bmatrix}^T$ and $\bar{\mathbf{G}}_\Gamma = [\mathbf{0}^T \quad \mathbf{G}_\Gamma^T]^T$, the constraints (2.52b) and (2.52c) can be written as

$$\mathbf{L}\mathbf{c}(t) = \bar{\mathbf{G}}_\Gamma\phi_\Gamma(t). \quad (2.53)$$

Let \mathbf{V} be a basis for $\text{null}(\mathbf{L})$ such that $\mathbf{L}\mathbf{V} = 0$ and let $\mathbf{c}_p(t) = \mathbf{Z}\phi_\Gamma(t)$ be a particular solution of (2.53). The general solution set for (2.53) can be written as

$$\mathbf{c}(t) = \mathbf{V}\mathbf{c}_h(t) + \mathbf{Z}\phi_\Gamma(t), \quad (2.54)$$

with $\mathbf{c}_h \in \mathbb{R}^{N-R^*}$ the coordinate vector of \mathbf{c} relative to the basis for $\text{null}(\mathbf{L})$ and with R^* the rank of \mathbf{L} . Since $\mathbf{L}\mathbf{d} = 0$ for all B-coefficient vectors \mathbf{d} of splines in \mathcal{S}_0 , the solution set for \mathbf{d} can be written as $\mathbf{d} = \mathbf{V}\mathbf{d}_h$. Substituting this set for \mathbf{d} and the solution set (2.54) for \mathbf{c} in (2.52) gives

$$\mathbf{d}_h^T \mathbf{V}^T \mathbf{M} (\mathbf{V}\dot{\mathbf{c}}_h(t) + \mathbf{Z}\dot{\phi}_\Gamma(t)) = \mathbf{d}_h^T \mathbf{V}^T \mathbf{K} (\mathbf{V}\mathbf{c}_h(t) + \mathbf{Z}\phi_\Gamma(t)) + \mathbf{d}_h^T \mathbf{V}^T \mathbf{F}\phi(t), \quad (2.55)$$

which is a reduced unconstrained system of order $N - R^*$ projected on the null space of the side constraints. Since (2.55) must hold for all \mathbf{d}_h , (2.55) is equivalent to

$$(\mathbf{V}^T \mathbf{M} \mathbf{V}) \dot{\mathbf{c}}_h(t) = \mathbf{V}^T [\mathbf{K} \mathbf{V} \mathbf{c}_h(t) + \mathbf{K} \mathbf{Z} \phi_\Gamma(t) + \mathbf{F} \phi(t) - \mathbf{M} \mathbf{Z} \dot{\phi}_\Gamma(t)]. \quad (2.56)$$

The null-space method requires the construction of the null basis \mathbf{V} for \mathbf{L} . We use the sparse null-space algorithm recently introduced in Hölzel and Bernstein [72] which is particularly useful for computing the null space of large sparse matrices. The algorithm from Hölzel and Bernstein [72] is presented in appendix C and extended to compute both a basis for the null space and a particular solution for the linear equality constraints (2.53). For the measured output (2.1c) and the controlled output (2.1d), the null space Galerkin method yields

$$y_k(t) = \mathbf{B}^d(\mathbf{x}_k) \mathbb{T}_{\mathcal{L}_y}^{d,d} [\mathbf{V}\mathbf{c}_h(t) + \mathbf{Z}\phi_\Gamma(t)], \quad (2.57)$$

$$q_i(t) = (\mathbf{h}^i)^T \mathbf{M} \mathbb{T}_{\mathcal{L}_q}^{d,d} [\mathbf{V}\mathbf{c}_h(t) + \mathbf{Z}\phi_\Gamma(t)], \quad (2.58)$$

where $\mathbb{T}_{\mathcal{L}_z}^{d,d}$ maps the B-coefficient vector of s to the B-coefficient vector of $\mathcal{L}_z s$ and with \mathbf{h}^i the B-coefficient vector of the spline that interpolates $h_i(\mathbf{x})$. Finally, we obtain the system in state-space format

$$\begin{aligned} \dot{\mathbf{u}}_N^e(t) &= \mathbf{A}\mathbf{u}_N^e(t) + \bar{\mathbf{B}}\bar{\phi}(t), \\ y_k(t) &= \mathbf{C}_k \mathbf{u}_N^e(t), \\ q_i(t) &= \mathbf{Q}_i \mathbf{u}_N^e(t), \end{aligned} \quad (2.59)$$

where

$$\begin{aligned}
\mathbf{u}_N^e(t) &= [\mathbf{c}_h^T(t) \quad \phi_\Gamma^T(t)]^T, \quad \bar{\phi}(t) = [\phi^T(t) \quad \dot{\phi}_\Gamma^T(t)]^T, \\
\mathbf{A} &= \begin{bmatrix} \left(\mathbf{V}^T \mathbf{M} \mathbf{V} \right)^{-1} \mathbf{V}^T \mathbf{K} \mathbf{V} & \left(\mathbf{V}^T \mathbf{M} \mathbf{V} \right)^{-1} \mathbf{V}^T \mathbf{K} \mathbf{Z} \\ 0 & 0 \end{bmatrix}, \\
\mathbf{B} &= \begin{bmatrix} \left(\mathbf{V}^T \mathbf{M} \mathbf{V} \right)^{-1} \mathbf{V}^T \mathbf{F} & - \left(\mathbf{V}^T \mathbf{M} \mathbf{V} \right)^{-1} \mathbf{V}^T \mathbf{M} \mathbf{Z} \\ 0 & \mathbf{I} \end{bmatrix}, \\
\mathbf{C}_k &= \left[\mathbf{B}^d(\mathbf{x}_k) \mathbb{T}_{\mathcal{L}_y}^{d,d} \mathbf{V} \quad \mathbf{B}^d(\mathbf{x}_k) \mathbb{T}_{\mathcal{L}_y}^{d,d} \mathbf{Z} \right], \\
\mathbf{Q}_i &= \left[(\mathbf{h}^i)^T \mathbf{M} \mathbb{T}_{\mathcal{L}_q}^{d,d} \mathbf{V} \quad (\mathbf{h}^i)^T \mathbf{M} \mathbb{T}_{\mathcal{L}_q}^{d,d} \mathbf{Z} \right].
\end{aligned} \tag{2.60}$$

Remark 1. The approximation power of the general multivariate spline space $S_d^r(\mathcal{T})$ is not fully known. For bi-variate spline spaces full approximation power in all p-norms is achieved when $d \geq 3r + 2$ (see Lai and Schumaker [73] and Lai and Schumaker [40, pp.276-286]). The orthogonality of the Galerkin projection (2.44) ensures that the approximation \mathbf{u}_N^e is the best possible solution in the space spanned by the basis functions. Specific bounds for the L^2 norm of projections onto bi-variate spline spaces $S_d^0(\mathcal{T})$ and $S_d^d(\mathcal{T})$ with $d \geq 3r + 2$ are derived in Von Golitschek and Schumaker [74].

2.6. CONTROLLER SYNTHESIS

The reduced-order model (2.59) can be used to design any suitable linear controller. In this study a quadratic optimal design is considered where the controlled output (2.58) is used to build the objective function (2.11). The quadratic objective function (2.11) for the reduced-order model becomes

$$\mathcal{J} = \int_0^\infty (\mathbf{u}_N^e)^T \mathbf{Q}^T \mathbf{Q} \mathbf{u}_N^e + \bar{\phi}^T \mathbf{R} \bar{\phi} \, dt. \tag{2.61}$$

Assuming that (\mathbf{A}, \mathbf{B}) is stabilisable the state feedback $\bar{\phi}(t) = -\mathbf{K}_c \mathbf{x}^N(t)$ that minimises (2.61) can be computed by solving the associated algebraic Riccati equation for (2.61) (see appendix B). An output feedback controller is obtained by combining the state feedback with a state observer and takes the form

$$\begin{aligned}
\bar{\phi}(t) &= -\mathbf{K}_c \hat{\mathbf{u}}_N^e(t), \\
\dot{\hat{\mathbf{u}}}_N^e(t) &= \mathbf{A} \hat{\mathbf{u}}_N^e(t) + \mathbf{B} \bar{\phi}(t) + \mathbf{K}_o (\mathbf{y}(t) - \hat{\mathbf{y}}(t)), \\
\hat{\mathbf{y}}(t) &= \mathbf{C} \hat{\mathbf{u}}_N^e(t), \quad \hat{\mathbf{u}}_N^e(0) = \hat{\mathbf{u}}_{N,0}^e,
\end{aligned} \tag{2.62}$$

where the observer gain \mathbf{K}_o is tuned such that the closed-loop dynamics of the estimation error $(\mathbf{u}_N^e - \hat{\mathbf{u}}_N^e)$ governed by the eigenvalues of $\mathbf{A} - \mathbf{K}_o \mathbf{C}$ is asymptotically stable with a sufficient convergence rate. The closed-loop system consists of the

actual DPS (2.9) combined with the controller (2.62)

$$\begin{bmatrix} \dot{\mathbf{u}}^e \\ \dot{\hat{\mathbf{u}}}_N^e \end{bmatrix} = \begin{bmatrix} \bar{\mathbf{A}} & -\bar{\mathbf{B}}\mathbf{K}_c \\ \mathbf{K}_o\bar{\mathbf{C}} & \mathbf{A} - \mathbf{B}\mathbf{K}_c - \mathbf{K}_o\mathbf{C} \end{bmatrix} \begin{bmatrix} \mathbf{u}^e \\ \hat{\mathbf{u}}_N^e \end{bmatrix}. \quad (2.63)$$

When using reduced-order models in the design of a control system, the truncated dynamics must be taken into account in the stability analysis. Robustness with respect to the truncated dynamics of reduced-order controllers based on projections on non-modal subspaces, such as finite-element spaces and spline spaces, for the linear class of parabolic DPS treated in this chapter has been discussed in Balas [54]. In Balas [54], precise conditions are derived under which model reduction based on consistent Galerkin approximations will lead to stable infinite-dimensional control. In particular, provided that the infinite-dimensional system is exponentially stable and N sufficiently large, a controller which exponentially stabilises the closed-loop ODE system also stabilises the closed-loop parabolic PDE system. The assumption that the DPS is exponentially stable is generally required in order to prove that the estimates are bounded for all times, that is $\|u - u_N\|_2 \leq \mu(N)$, $\forall t$ with $\mu(N)$ a positive number depending on N satisfying $\lim_{N \rightarrow \infty} \mu(N) = 0$ [54, 61]. In the next section we apply the reduction method to control two unstable PDEs and analyse the closed-loop stability by computing the eigenvalues of (2.63) numerically. To compute the eigenvalues and to simulate the response of the system, an accurate high-order model is used to represent the actual DPS, that is, $\bar{\mathbf{A}}$, $\bar{\mathbf{B}}$ and $\bar{\mathbf{C}}$ in (2.63), and lower order models are used to design the control system. For a given partitioning of the domain, the degree and order of continuity of the splines basis can be chosen arbitrarily to derive these state-space models. The order of continuity is chosen equal to the continuity of the strong solution of the PDE system. For the systems considered in the next section the strong solution is C^2 smooth. The degree of the control model can subsequently be tuned to obtain a desirable trade-off between the order of the model and the accuracy of the model, and thereby closed-loop performance. We provide a closed-loop performance analysis for various degrees and select the model that gives a good balance between model order and performance to implement the controller.

2.7. DEMONSTRATION

In this section, two representative PDE control problems are presented to demonstrate the implementation and to evaluate the effectiveness of the proposed model reduction scheme. In the first case we consider stabilisation of a 1-D unstable reaction-diffusion process which is often considered as a benchmark problem (see e.g. Smyshlyaev and Krstic [46]). For this problem an analytic solution of the spatial differential operator eigenvalue problem is available which allows for a direct comparison of the eigenvalues and stability eigenfunctions of the reduced-order models with the analytic solution. In the second case, stabilisation of a 2-D reaction-convection-diffusion equation on an irregular spatial domain is considered for which analytic solutions of the spatial differential operator eigenvalue problem are not possible. This is a non-trivial example which better illustrates the potential of the spline reduction framework. We provide numerical convergence results for increasing

Table 2.1: Number of system states ($J\hat{d} - R^* + 1$).

Degree	3	4	5	6	7	8	9	10
\mathcal{T}_3	5	8	11	14	17	20	23	26
\mathcal{T}_6	8	14	20	26	32	38	44	50

polynomial degrees and show that effective feedback stabilisation can be achieved using low-order control models.

2.7.1. BOUNDARY FEEDBACK STABILISATION OF A REACTION-DIFFUSION EQUATION

In this demo boundary feedback control of an unstable reaction-diffusion equation with constant coefficients is considered

$$\left\{ \begin{array}{ll} \frac{\partial u(x,t)}{\partial t} = \mu \frac{\partial^2 u(x,t)}{\partial x^2} + au(x,t) & \text{in } (0,1) \times (0,\infty), \\ u(0,t) = 0, \quad u(1,t) = u(t) & \text{in } (0,\infty), \\ u(x,0) = \sin(\pi x) & \text{in } (0,1), \\ y(t) = \frac{\partial u(0,t)}{\partial x} & \text{in } (0,\infty), \\ q_1(t) = \int_{\Omega} \sin(\pi x) u(x,t) \, d\mathbf{x} & \text{in } (0,\infty), \\ q_2(t) = \int_{\Omega} \sin(2\pi x) u(x,t) \, d\mathbf{x} & \text{in } (0,\infty), \end{array} \right. \quad (2.64)$$

where $\frac{\partial u}{\partial x}(0,t)$ is measured and $u(1,t)$ is actuated. The coefficients are chosen as $\mu = 0.2$, $a = 4$. The complete system is converted to state-space format using a $C^2(\Omega)$ continuous spline basis of various degrees defined on a uniform partitioning of the domain consisting of three and six simplices. The dimension of the state-space systems is listed in table 2.1. For system (2.64), the differential operator is of the form $\mathcal{A}u = \mu \frac{\partial^2 u}{\partial x^2} + au$ and the exact solution of the differential operator eigenvalue problem $\mathcal{A}\tilde{u}_j(x) = \lambda_j \tilde{u}_j(x)$ is given by [43]

$$\lambda_j = a - \mu j^2 \pi^2, \quad \tilde{u}_j(x) = \sin(j\pi x), \quad (2.65)$$

with $j = 1, 2, \dots, \infty$, λ_j the eigenvalues and \tilde{u}_j the eigenfunctions. The case with $\mu = 0.2$, $a = 4$ corresponds to one unstable eigenvalue at $\lambda_1 = 4 - 0.2\pi^2 \approx 2.03$. Using this eigenfunction expansion we can directly calculate power spectral density (PSD) of the differential operator [75]

$$\|(i\omega - \mathcal{A})^{-1}\|_{HS}^2 = \|\mathcal{F}(\omega)\|_{HS}^2 = \sum_{j \in \mathbb{N}} \frac{1}{\omega^2 + \lambda_j^4}, \quad (2.66)$$

where $\|\cdot\|_{HS}$ denotes the Hilbert-Schmidt norm (generalisation of the Frobenius norm for matrices). Figure 2.2 shows the errors for the first four dominant eigenvalues of the reduced-order models and figure 2.3 compares the PSD. It can be observed that the dominant modes converge quickly up to numerical precision and that the reduced-order models only deviate at higher frequencies.

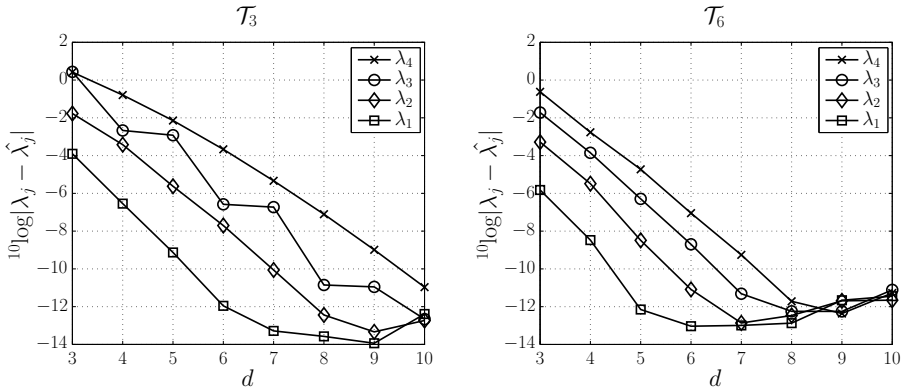


Figure 2.2: The error of the first four dominant eigenvalues of the $S_d^2(\mathcal{T}_3)$ and $S_d^2(\mathcal{T}_6)$ reduced-order models.

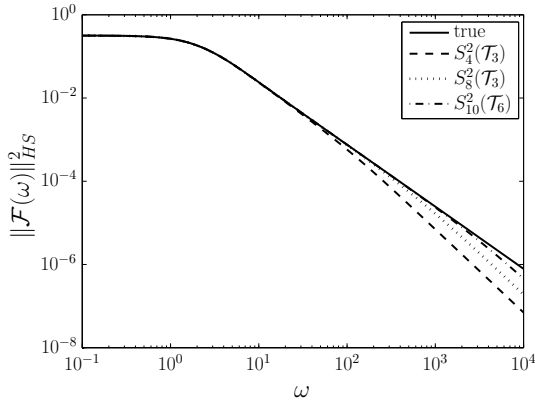


Figure 2.3: Power spectral density of the differential operator of the reduced-order models compared with the analytic solution.

Table 2.2: Real part of the two least stable eigenvalues of the closed loop system (2.63).

degree	3	4	5	6	7	8
σ_1	-1.41	-2.47	-2.62	-2.69	-2.69	-2.69
σ_2	-1.56	-3.29	-3.06	-3.09	-3.10	-3.10

The control objective is to stabilise the state at its unstable equilibrium $\bar{u} = 0$. The controller (2.62) is synthesised using $s \in S_d^2(\mathcal{T}_3)$ Galerkin models of various degrees. The controlled output is built using the first two dominant eigenfunctions $\tilde{u}_1(x), \tilde{u}_2(x)$ and the input weight is set to $R = 0.01$. Adding more eigenfunctions to the controlled output or lowering the input weight did not further improve the performance of the controller. An $s \in S_{10}^2(\mathcal{T}_6)$ Galerkin model is assumed to rep-

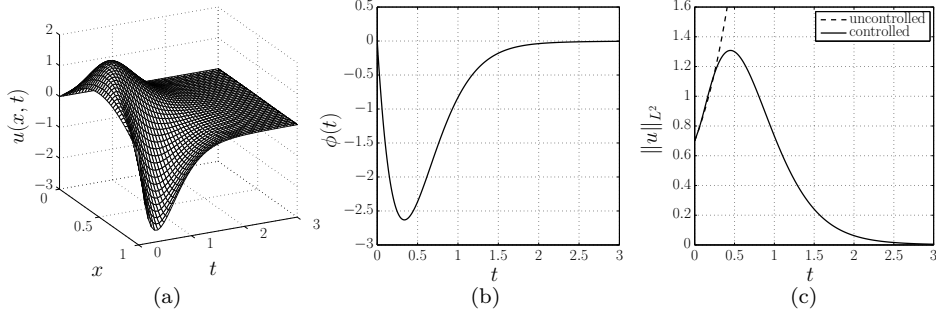


Figure 2.4: Closed-loop response of the $s \in S_4^2(\mathcal{T}_3)$ controller. An $s \in S_{10}^2(\mathcal{T}_6)$ Galerkin model is used for simulating the response. (a) Response, (b) boundary control input, (c) L^2 norm of the state.

represent the original DPS, that is $\bar{\mathcal{A}}, \bar{\mathcal{B}}, \bar{\mathcal{C}}$ in (2.63), and is used in the simulations. It is verified that a further increase of the order provided no improvement on the accuracy of the results. The real part of the two least stable eigenvalues (pairs) of the closed-loop system (2.63) is shown in table 2.2. Higher degree controllers give a faster stabilisation but no significant improvement is achieved after $d = 4$; the dominant dynamics are accurately captured by low-degree models. The closed-loop response for the $s \in S_4^2(\mathcal{T}_3)$ model-based controller is shown in figure 2.4. It can be observed that the $s \in S_4^2(\mathcal{T}_3)$ model-based controller provides a satisfactory performance and quickly stabilises the system.

2.7.2. IN-DOMAIN CONTROL OF A REACTION-CONVECTION-DIFFUSION EQUATION

In this demo in-domain feedback control of a reaction-convection-diffusion equation is considered with spatially varying coefficients

$$\left\{ \begin{array}{l} \frac{\partial u(\mathbf{x}, t)}{\partial t} = \mu(\mathbf{x}) \nabla^2 u(\mathbf{x}, t) - v(\mathbf{x}) \cdot \nabla u(\mathbf{x}, t) \\ \quad + a(\mathbf{x}) u(\mathbf{x}, t) + \mathbf{g}(\mathbf{x}) \phi(t) \quad \text{in } \Omega_T, \\ \frac{\partial u(\mathbf{x}, t)}{\partial n} = 0 \quad \text{on } \Gamma, \\ u(\mathbf{x}, 0) = 5 \cos(\pi(x_1^2 - 1)(x_1^2 - 0.09)) \\ \quad - 5 \cos(\pi(x_2^2 - 1)(x_2^2 - 0.09)), \\ y_k(t) = q_k(t) = u(x_k, t) \quad \text{for } k = 1, \dots, 4 \end{array} \right. \quad (2.67)$$

defined on a rectangular domain with a cut-out

$$\Omega = \{(x_1, x_2), (x_1, x_2) \in (-1, 1) \times (-1, 1) \setminus (-0.3, 0.3) \times (-0.3, 0.3)\}.$$

A rotating velocity field is applied with $v(\mathbf{x}) = [x_2 \quad -x_1]^T$, the diffusivity is kept constant $\mu(\mathbf{x}) = \mu = 0.05$ and the reaction rate is chosen as $a(\mathbf{x}) = 0.5 \cos(\frac{1}{2}\pi x_1) e^{x_2}$ which has a destabilising effect. The system is controlled using four actuators whose spatial distributions are modelled as Gaussian radial basis functions: $g_i(\mathbf{x}) = \exp[-(\|\mathbf{x} - \mathbf{x}_c\|_2^2)/(2\sigma^2)]$ and four in-domain Dirichlet measurements are used for

Table 2.3: Dimension state-space systems

Degree	4	5	6	7	8	9	10
(a) Number of states $J\hat{d} - R^*$							
\mathcal{T}_{56}	18	114	266	474	738	1058	1434
\mathcal{T}_{120}	32	232	552	992	1552	2232	3032
(b) State reduction R^*							
\mathcal{T}_{56}	822	1062	1302	1542	1782	2022	2262
\mathcal{T}_{120}	1768	2288	2808	3328	3848	4368	4888

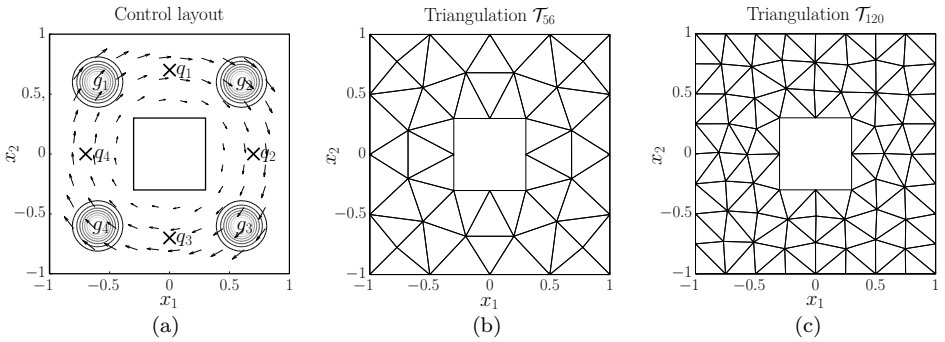


Figure 2.5: Control layout and triangulations. (a): Domain, convective field $v(\mathbf{x})$, actuator distribution contours $g_i(\mathbf{x})$ and sensor locations z_i . (b): Triangulation with 56 simplices used for control design. (c): Triangulation with 120 simplices used for simulation.

feedback. The complete geometry is shown in figure 2.5 along with the triangulations used in this study. All state-space models are derived using a C^2 continuous spline basis of various degrees defined on a triangulation consisting of 56 and 120 simplices. The dimension of the state-space systems are listed in table 2.3(a) and the size reduction R^* resulting from the null-space projection is listed in table 2.3(b).

Since no analytic solution is available, the state-space systems are validated using a manufactured solution [76]. For this, we consider the system (2.67) with manufactured solution $u^*(\mathbf{x}, t) = u(\mathbf{x}, 0)\phi^*(t)$. Since the solution is not exact, inserting this solution into the PDE results in a residual that does not cancel out. This residual is added as the source term to the right-hand side of the PDE to create a modified PDE for which the artificial solution is correct and can thus be used for comparison. A sinusoidal input is applied $\phi^*(t) = \cos(\pi t)$ and the resulting state-space models are integrated over a time span of 1 second using a low sample time of $\Delta t = 0.001$ to minimise the errors from the time integration. The maximum error of spline solutions of various degrees against the manufactured solution is shown in figure 2.6.

$S_d^2(\mathcal{T}_{56})$ state-space models for the original system are used to synthesise the controller (2.62). The measured output is also chosen as the controlled output and

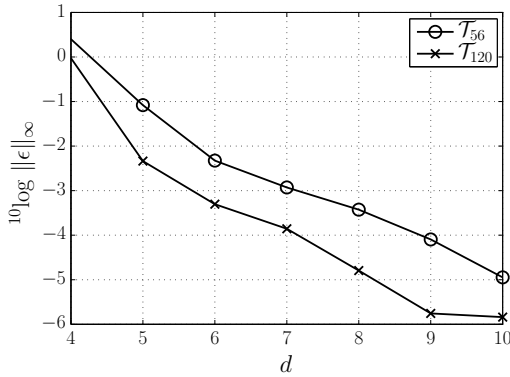


Figure 2.6: The maximum error versus degrees on \mathcal{T}_{56} and \mathcal{T}_{120} with respect to the manufactured solution.

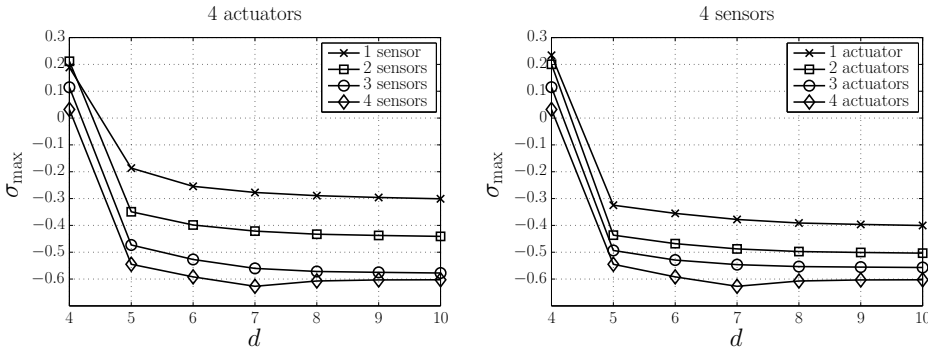


Figure 2.7: Real part of the least stable eigenvalue of the closed-loop system (2.63) with $\mathbf{R} = \text{diag}(0.01)$. An $s \in S_9^2(\mathcal{T}_{120})$ model is used as the 'true system'. Left: $s \in S_d^2(\mathcal{T}_{56})$ controllers using four actuators with one (y_1), two (y_1, y_3), three (y_1, y_2, y_3) and four sensors. Right: $s \in S_d^2(\mathcal{T}_{56})$ controllers using four sensors with one (g_1), two (g_1, g_3), three (g_1, g_2, g_3) and four actuators.

the input weight is set to $\mathbf{R} = \text{diag}(0.01)$. A high-order $s \in S_9^2(\mathcal{T}_{120})$ model is assumed to represent original DPS and is used to simulate the response. Figure 2.7 shows the real part of the most dominant eigenvalue of the closed-loop system for various sensor/actuator configurations. We were able to lower the degree to $d = 5$ after which the stabilisation effect is lost at $d = 4$ which is in accordance with the validation results in figure 2.6. The $s \in S_6^2(\mathcal{T}_{56})$ model gives a good balance between performance and model order (see Table 2.3), and is used to implement the controller. Figure 2.8 shows the dominant eigenvalues of the $s \in S_6^2(\mathcal{T}_{56})$ control model and the $s \in S_9^2(\mathcal{T}_{120})$ simulation model. It can be observed that the eigenvalues of the control and simulation model coincide well and that they only differ significantly in the highly damped region ($\text{Re } \lambda < -4.5$). As a result the controller effectively stabilises the system as can be seen in figure 2.9. As a final study, we keep the $s \in S_6^2(\mathcal{T}_{56})$ controller but vary the number of observation points used for feedback (figure 2.10(a)) and the number of actuators used for control (figure 2.10(b)). It can

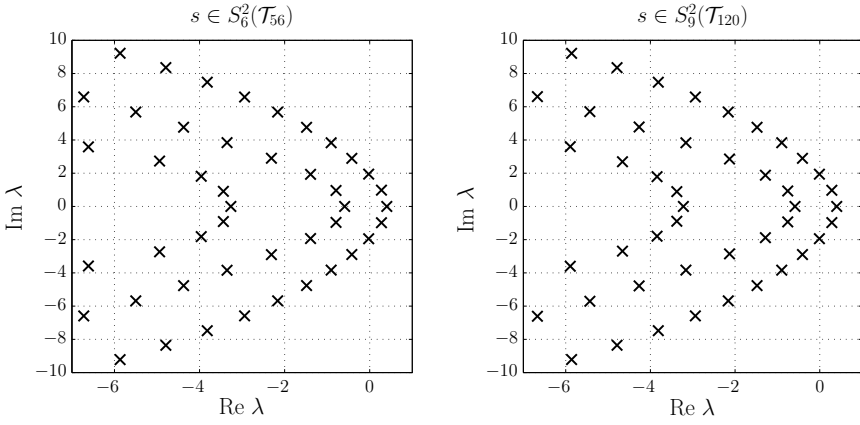


Figure 2.8: Dominant system poles of the $s \in S_6^2(\mathcal{T}_{56})$ control model (left) and of the $s \in S_9^2(\mathcal{T}_{120})$ simulation model (right).

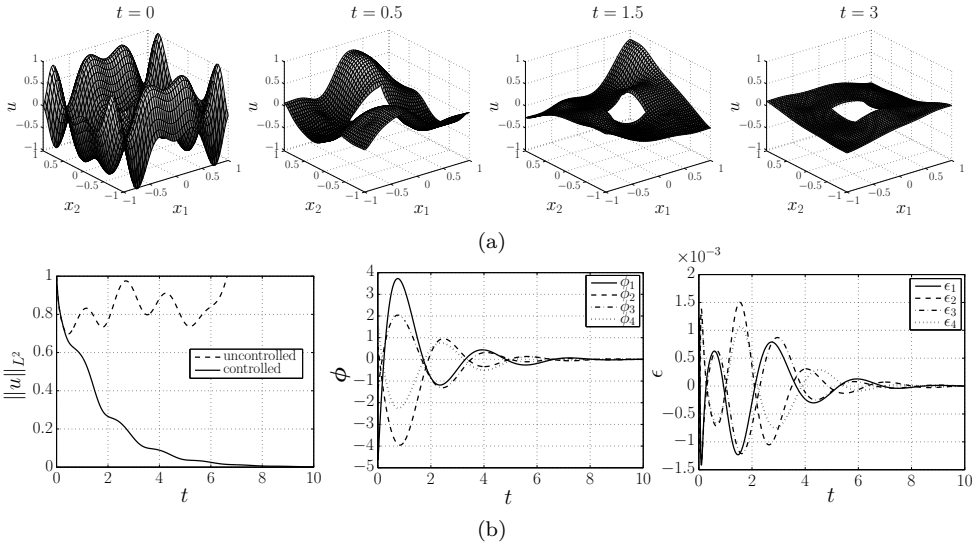


Figure 2.9: Closed-loop response of the $s \in S_6^2(\mathcal{T}_{56})$ controller using four sensors and four actuators. An $s \in S_9^2(\mathcal{T}_{120})$ Galerkin model is used for simulating the response. (a): Response at 4 time instants. (b): L_2 norm (left), control inputs (middle) and observer estimation errors (right).

be observed that effective feedback stabilisation can be achieved using a minimal amount of sensors and actuators.

2.8. CONCLUSIONS

This chapter presented a new framework for model reduction of parabolic PDEs on general geometries using multivariate B-splines of arbitrary degree and arbitrary smoothness. The method uses Galerkin projection with B-splines to derive state-

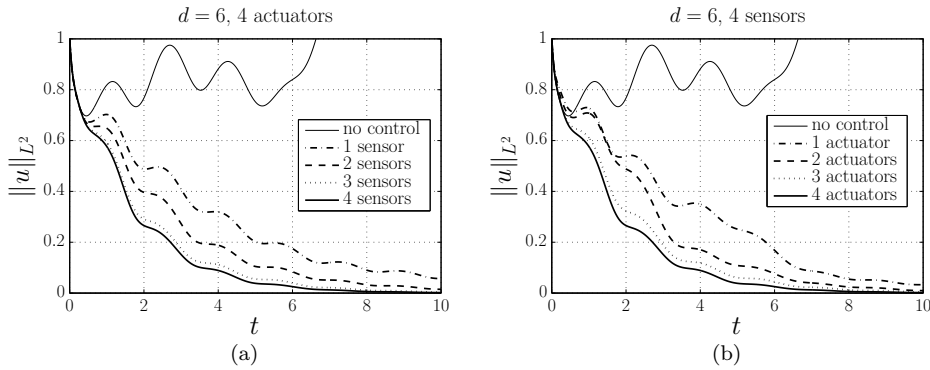


Figure 2.10: L^2 norm of the state for various controllers. An $s \in S_9^2(\mathcal{T}_{120})$ model is used as the 'true system'. (a): $s \in S_6^2(\mathcal{T}_{56})$ controller using four actuators with one (y_1), two (y_1, y_3), three (y_1, y_2, y_3), and four sensors. (b): $s \in S_6^2(\mathcal{T}_{56})$ controllers using four sensors with one (g_1), two (g_1, g_3), three (g_1, g_2, g_3) and four actuators.

space descriptions that can be used for control design. The method can be used to design both in-domain and boundary feedback controllers for PDEs. The effectiveness of the proposed reduction scheme is demonstrated using two examples, a 1-D unstable reaction-diffusion equation and a 2-D unstable reaction-convection-diffusion equation with spatially varying coefficients on an irregular domain. A fast numerical convergence of the models is demonstrated for increasing mesh resolution and degree of splines. It is shown that the proposed reduction scheme results in accurate low-order models of the PDE. The reduced-order models are successfully applied to design and implement feedback controllers for the two test cases. Order reduction is achieved by defining a triangulation and spline basis that effectively balances numerical accuracy and computational complexity for the application of control theoretic tools. The controller is subsequently designed in closed-loop with a high-order discretisation. The high-order discretisation is used as a high fidelity truth model to assure that the controller achieves closed-loop stability. Since the considered PDE control problems are unstable, no closed-loop stability guarantees are available for the original (non-discretised) infinite-dimensional system. However, the high fidelity models were converged up to numerical precision giving confidence that the controllers are robust to the truncated dynamics. A fast convergence of the closed-loop system eigenvalues is demonstrated and it is shown that the order of the model only has to be sufficiently large, e.g. 8 degrees of freedom for the 1-D control example, to achieve effective feedback stabilisation.

For more complex systems, such as Navier-Stokes systems, this method can also be used in conjunction with state-space based truncation methods, such as balanced truncation, to produce real-time capable models. In the next chapter this combination will be used for estimation and control in wall-bounded shear flows. Future work will focus on extending this method to nonlinear PDE systems to further evaluate its effectiveness for practical applications of PDE control.

3

Localised estimation and control of instabilities in shear flows

A new framework is presented for estimation and control of instabilities in wall-bounded shear flows described by the linearised Navier-Stokes equations. The control design considers the use of localised actuators/sensors to account for convective instabilities in an \mathcal{H}_2 optimal control framework. External sources of disturbances are assumed to enter the control domain through the inflow. A new inflow disturbance model is proposed for external excitation of the perturbation modes that contribute to transition. This model allows efficient estimation of the flow perturbations within the localised control region of a conceptually unbounded domain. The state-space discretisation of the infinite-dimensional system is explicitly obtained, which allows application of linear control theoretic tools. A reduced-order model is subsequently derived using exact balanced truncation that captures the input/output behaviour and the dominant perturbation dynamics. This model is used to design an \mathcal{H}_2 optimal controller to suppress the instability growth. The two-dimensional non-periodic channel flow is considered as an application case. Disturbances are generated upstream of the control domain and the resulting flow perturbations are estimated/controlled using point wall shear measurements and localised unsteady blowing and suction at the wall. The controller is able to cancel the perturbations and is robust to both unmodelled disturbances and sensor inaccuracies. For single-frequency and multiple-frequency disturbances with low sensor noise a nearly full cancellation is achieved. For stochastic forced disturbances and high sensor noise an energy reduction in perturbation wall shear stress of 96% is shown.

This chapter has been published as: H.J. Tol, M. Kotsonis, C.C. de Visser and B. Bamieh, *Localised estimation and control of linear instabilities in two-dimensional wall-bounded shear flows*, Journal of Fluid Mechanics, vol. 824, pp. 818-865, 2017

3.1. INTRODUCTION

It is widely accepted that if the initial perturbations are small, the initial phase of the laminar-turbulent transition in wall-bounded shear flows is largely governed by linear mechanisms [21, 77–79]. The application of linear control theory to fluid flows is therefore considered as a viable route to suppress instabilities and delay transition for reducing skin-friction drag [33, 37, 39, 80–85]. In particular, optimal multivariable control strategies (LQG/ \mathcal{H}_2 , \mathcal{H}_∞) [29, 86] have been successfully applied, see Kim and Bewley [6], Bagheri and Henningson [7], Sipp and Schmid [9] for an in-depth review on this subject. These control strategies can be decomposed in a state estimation problem from non-ideal (noisy) measurements and a state feedback control problem. Once the evolution of the flow perturbations is sufficiently estimated, the estimated state can subsequently be used for feedback control of the perturbations. The construction of an accurate linear state-space model describing the perturbation dynamics from all inputs to all outputs is the cornerstone of linear-model based control and is considered as a significant challenge [7, 9]. Limits related to unmodelled dynamics and nonlinearities are commonly assessed from case to case [85, 87] and/or addressed using robust design techniques such as \mathcal{H}_∞ loop shaping [15, 39]. For example, in Jones *et al.* [39] the effect of nonlinearity is attenuated by a linear feedback controller that employs high loop gain over a selected frequency range. As recently reviewed in Sipp and Schmid [9], Schmid and Sipp [28], different difficulties arise for modelling and control of globally unstable oscillator flows and convectively unstable amplifier flows. Oscillator flows, such as bluff body flows and open cavity flows, are characterised by the presence of global instabilities that oscillate at a particular frequency and are rather insensitive to upstream perturbations. Modelling the external disturbance environment is thus less of an issue for suppressing global instabilities [9, 88–90], but it raises different issues related to nonlinear saturation of global instabilities [15]. On the other hand amplifier flows, such as channel flows and boundary layer flows, are characterised by the presence of convective instabilities that amplify downstream (in space) in a broadband frequency spectrum in both space and time. Amplifier flows are highly sensitive to external disturbances and there exists only a small window in time to suppress convective instabilities. This poses great challenges for control design and accurately modelling the upstream disturbance environment is crucial since it forms the basis for estimation and control of the flow perturbations [33, 91, 92]. This chapter focuses on convective instabilities due to their strong relevance to engineering problems such as laminar-turbulent transition of flow over aerofoils. Besides the distinction in instability behaviour, two approaches with regard to the flow modelling and the controller synthesis are frequently further distinguished from each other [7], namely the wavenumber approach for distributed control design and the localised control approach using reduced-order models. The framework presented in this chapter is inspired by both approaches which are discussed next.

3.1.1. DISTRIBUTED CONTROL AND LOCALISED COMPUTATIONS

A large number of studies, including the seminal works by Joshi *et al.* [80] and Bewley and Liu [37], consider full-domain distributed sensing and actuation to derive

the control laws. Distributed control designs often exploit the spatial invariance property of parallel flows to derive low-order models of the perturbation dynamics. In the case of spatial invariance it is assumed that the base flow is invariant in the streamwise (x) and spanwise (z) directions and that the sensors and actuators are fully distributed along these coordinates. By using a Fourier-Galerkin decomposition or a Fourier transform along the spatially invariant coordinates, the system can be block diagonalised and decoupled in terms of discrete sets of wavenumbers that replace the spatially invariant coordinates [37, 80]. Analysis and design of the controller can thus be carried out on a parameterised lower-dimensional system. The resulting feedback controllers can subsequently be reconstructed in physical space by computing the so-called control convolution kernels [45, 82]. In Høpfner *et al.* [91], Chevalier *et al.* [93] stochastic models for external sources of excitation were introduced that allow the computation of well-resolved estimation convolution kernels for shear stress and pressure measurements. These estimation/control convolution kernels have a localised structure in space and it was shown in Bamieh *et al.* [45] that localisation of the convolution kernels is a universal property of spatially invariant optimal control problems. Although, strictly speaking the wavenumber approach is only applicable to spatially invariant systems, it has also been successively applied to spatially developing boundary layers [84, 94, 95] and fully turbulent flows [96–98]. The use of control/estimation convolution kernels avoids the need for online fast Fourier transforms (FFT) of the measurement vector and inverse Fourier transform (iFFT) of the control vector. While this approach introduces a controller with the same order as the system, it is shown in Högberg *et al.* [82] that spatially truncating the convolution kernels does not degrade the closed-loop performance of the control system. Since these convolution kernels are localised, the feedback controller can be implemented with only localised computations. As a result, relatively small computational domains can be considered for an effective control design. For example in Chevalier *et al.* [84] and Monokrousos *et al.* [95] all perturbations were generated upstream of the control domain and they were able to suppress Tollmien-Schlichting waves and streaks in a flat plate boundary layer using small strips of distributed sensors and actuators.

3.1.2. MODEL REDUCTION AND LOCALISED CONTROL

The exploitation of the spatial invariance property for control design, although effective for distributed feedback control, requires sensor and actuator distributions that are currently not available or cannot be manufactured in a cost effective way. Moreover, in practice efficient control can be achieved using only a few localised sensors and actuators, leading to a more cost-effective control design. This led to the use of reduced-order modelling techniques for control design that make no assumptions on the flow geometry and the shape and distribution of the actuators/sensors. This approach, also known as the reduced-order modelling approach, accounts for physically realisable localised actuators/sensors and has been validated in experiments [87, 88, 99]. Galerkin projection is commonly applied, in which a reduced-order model (ROM) is obtained by projecting the Navier-Stokes equations onto a reduced set of modes. The choice of these modes is critical and greatly determines the

effectiveness of the ROM for control application [89, 100, 101]. The global eigenfunctions (EF) of the linear operator [102], as well as different variants of proper orthogonal decomposition modes (POD) [103, 104] have been successfully applied for model reduction and control design. Another approach is the use of balanced modes, also known as balanced truncation, which typically produces models that are more robust and are better able to capture the input-output behaviour of the system [34, 89, 100, 101].

Balanced truncation is widely used for model reduction of linear systems [67] and has the advantage of having a priori error bounds and guaranteed stability of the reduced-order model. This method requires an initial model of the flow in finite-dimensional state-space format and constructs a ROM by extracting the most controllable and observable modes of the state-space system. The construction of these so-called balanced modes involves the computation of the controllability and observability Gramians of the high-order model. These Gramians are obtained by solving a set of Lyapunov equations which becomes computationally intractable for very large systems (e.g. 10^5 states or more). Furthermore this method requires a model of the flow in state-space format, which is not always available for complex flow control problems. To reduce the complexity, an approximate method is proposed by Rowley [34], called balanced POD (BPOD), in which empirical Gramians are computed directly from impulse response snapshots of the system and the related adjoint. This method is suitable for large systems as it avoids the direct computation of the Gramians and is successfully applied for modelling of the channel flow [101] and control of both boundary layer flows [7, 33, 105] and globally unstable flows [89, 106].

A limitation of BPOD is that it requires full-state snapshots and adjoint simulations to form the bi-orthogonal sets and thus cannot be applied to experimental data. Another approach is the use of system identification methods in which low-order models are obtained from a sample of input-output measurements. In particular the eigensystem realisation algorithm (ERA) [107] was recently used to construct reduced-order models for fluid flows [15, 27, 85, 90, 108, 109]. ERA is based on the impulse response measurements and does not require prior knowledge of the high-order system. It is shown in Ma *et al.* [90] that ERA can theoretically obtain the same reduced-order models as BPOD and in Flinois and Morgans [15] it is shown that ERA can also directly be applied to globally unstable flows.

3.1.3. SCOPE AND OUTLINE OF THE PRESENT STUDY

Modelling the influence of upstream disturbances is crucial for the control of convective instabilities. The disturbance sources are generally not precisely known in real experiments and modelling assumptions have to be made. For localised transition control the disturbance is commonly represented by a localised body force placed upstream of the control actuators, see e.g. Belson *et al.* [27], Bagheri *et al.* [33], Semeraro *et al.* [85, 92]. For example, in Semeraro *et al.* [92] the disturbance was modelled as a localised initial condition that provides the maximum energy amplification of the perturbation at a given final time. Different choices and placements of the disturbance model result in different spatial and temporal scales of the

perturbations in the control region. To properly account for the upstream disturbance environment, relatively large computational domains are often considered to derive the ROM. These result in high-dimensional systems and prohibit the direct state-space modelling from the governing equations. Currently, direct modelling is avoided, also due the computational challenges, and low-order linear approximations of the dynamics are obtained from snapshots through (adjoint) numerical simulations or from input-output data using system identification. Often the same disturbance that is used to synthesise the ROM and control laws is also used to evaluate the controller through numerical simulations. Robustness of the controller to unmodelled disturbances is often not shown or addressed.

In this chapter a new approach is presented for localised modelling and control of convective instabilities in two-dimensional (2-D) wall-bounded shear flows. The objective is to provide a systematic procedure to efficiently model upstream disturbance environments and to design reduced-order controllers directly from the governing equations without the use of numerical simulations or system identification. Inspired by the earlier work regarding distributed control, very large systems are avoided by focussing on localised computations. When using spatially localised actuators/sensors for feedback control, the control domain that encapsulates the actuators/sensors is much smaller than the complete physical domain. It is assumed that external sources of disturbances enter the control domain through the inflow boundary. A novel physically motivated inflow disturbance model is proposed for the external excitation, which allows efficient estimation of the flow perturbations within the localised control domain using wall shear sensors. Unlike common practices for localised control, the state-space system used for discretisation of the infinite-dimensional system is explicitly obtained. The state-space modelling in this chapter can make a large set of powerful and mature control theoretic tools for model reduction and control directly applicable to the linearised Navier-Stokes equations. In this work the modelling is combined with exact balanced truncation to reduce the order of the controller and the truncated dynamics is taken into account in the control system design.

The scope of this chapter is input-output modelling of the flow dynamics (actuators/sensors and upstream perturbations) and \mathcal{H}_2 optimal reduced-order controller design. A super-critical 2-D non-periodic channel flow is chosen as application case. This is both mathematically and physically one of the best understood geometries and allows for a rigorous verification of the modelling method and the control design using the classical linear stability theory. The formulation and the methods presented in this chapter can in principle be applied to general geometries and any actuator/sensor configuration and allow for a straightforward extension to spatially developing boundary layers. A feedforward actuator/sensor configuration [27] is considered in which upstream sensors are used to detect the incoming perturbations. Such a set-up is commonly considered for convectively unstable flows [9, 33, 85] and guarantees the best nominal performance [27]. Nonetheless a feedforward approach can be more sensitive to unmodelled disturbances/dynamics as compared to feedback configurations as argued in [27]. In this chapter closed-loop convergence is shown with respect to the truncated dynamics and the robustness to unmodelled

disturbances is assessed from case to case. The controllers are evaluated using linear simulations based on the assumption that the amplitude of the perturbations is small. In Semeraro *et al.* [85] it is verified through nonlinear simulations that a fully linear control approach can be effective in delaying transition in the presence of perturbation amplitudes up to 1% of the free stream velocity. Limitations with respect to strong nonlinear dynamics at transitional amplitudes are out of the scope of this work. However, the modelling presented in this chapter also enables the application of linear \mathcal{H}_∞ robust design strategies, of the sort presented in Flinois and Morgans [15], Jones *et al.* [39], Baramov *et al.* [83], to account for modelling uncertainties. This would require a change of control set-up to include feedback measurement information to effectively account for model uncertainty in the control design.

The outline of this chapter is as follows. Section 3.2 outlines the dynamic modelling and the problem formulation for control of convective instabilities. Section 3.3 presents the design and synthesis of the reduced-order controller. In section 3.4 the controller is evaluated using numerical simulations of the closed-loop system. All disturbances are generated upstream of the computational domain for the control model. Three different disturbance cases are considered in order to demonstrate the effectiveness and the robustness of the proposed control design. In the last section concluding remarks are given and a discussion regarding the application of this method to more complex flow geometries is laid out. This chapter is complemented with two Appendices. In appendix A the numerical scheme to derive the finite-dimensional state-space system of the flow is described. This numerical scheme is based on multivariate B-splines defined on triangulations [40–42] and is an extension of the model reduction scheme for parabolic PDEs presented in chapter 2 to fluid flows. In Appendix B the state-space formulas for the controller that solves the \mathcal{H}_2 optimal control problem are given.

3.2. DYNAMIC MODELLING AND PROBLEM FORMULATION

This section presents the dynamic modelling and a generalised problem formulation for localised control of instabilities that contribute to transition in 2-D wall-bounded shear flows. The classical route to transition is considered, in accordance with the linear stability theory (LST) [21], triggered by linear growth of convective instabilities. The 2-D non-periodic channel flow is considered as application case. First the channel geometry and the governing equations are given in section 3.2.1. In section 3.2.2 the feedforward actuator/sensor configuration used for control is presented. The new inflow disturbance model to account for upstream disturbance environments is introduced in section 3.2.3. To apply linear control theoretical tools the input-output system must be formulated into the standard state-space form. To generalise the framework the system is written as an abstract equation in operator form [43, 110] in section 3.2.4. Explicit discrete expressions are obtained for all operators and the underlying numerical method (Appendix A) is discussed in section 3.2.5. Finally the \mathcal{H}_2 optimal control problem to account for the flow perturbations is defined in section 3.2.6.

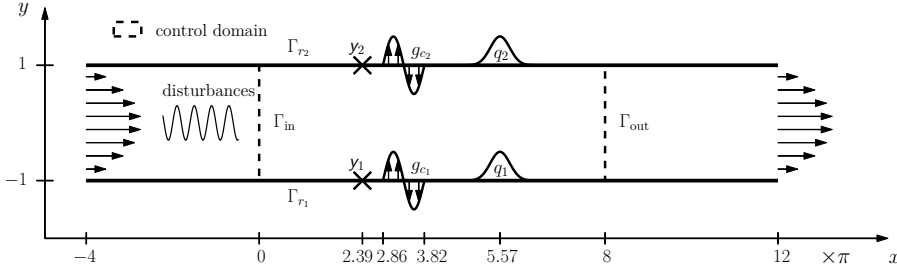


Figure 3.1: Channel flow geometry and control layout including the shear sensor locations y_i , boundary actuator distributions $g_i(x)$ and controlled output distribution $q_i(x)$.

3.2.1. GOVERNING EQUATIONS

This chapter considers a 2-D non-periodic flow between two infinite flat plates. The flow is non-dimensionalised using the maximum centreline velocity U_0 and half-height h with corresponding Reynolds number $Re = \frac{U_0 \rho h}{\mu}$ where ρ is the density and μ the dynamic viscosity of the fluid. For flow simulations a total non-dimensional length $L_{sim} = 16\pi$ is considered. This section focuses in particular on the flow model that is used for control design. For control design purposes a localised region with a length of $L_c = 8\pi$ is considered. External sources of disturbances are assumed to enter the control domain through the inflow. The geometry of the flow is shown in figure 3.1. A supercritical case is studied at $Re = 7000$ for which the flow field is convectively unstable. However, the non-periodic flow configuration is globally stable since any initial perturbation eventually leaves the computational domain. The control objective is to stabilise convective perturbations around the steady-state parabolic velocity profile $\mathbf{U}(y) = [1 - y^2, 0]^T$. The dynamics of small-amplitude perturbations in a viscous incompressible flow is governed by the Navier-Stokes equations linearised around the base flow and the continuity equation

$$\frac{\partial \mathbf{u}}{\partial t} + (\mathbf{U} \cdot \nabla) \mathbf{u} + (\mathbf{u} \cdot \nabla) \mathbf{U} - \frac{1}{Re} \Delta \mathbf{u} + \nabla p = \mathbf{f} \quad \text{in } \Omega, \quad (3.1a)$$

$$\nabla \cdot \mathbf{u} = 0 \quad \text{in } \Omega, \quad (3.1b)$$

$$\mathbf{u} = \mathbf{u}_b \quad \text{on } \Gamma_D, \quad (3.1c)$$

$$-pn + \frac{1}{Re} (\mathbf{n} \cdot \nabla) \mathbf{u} = 0 \quad \text{on } \Gamma_{out}, \quad (3.1d)$$

where $\mathbf{u}(\mathbf{x}, t) = [u(\mathbf{x}, t), v(\mathbf{x}, t)]$ and $p(\mathbf{x}, t)$ denote the velocity and pressure perturbation field, $\mathbf{x} = (x, y)$ is the spatial coordinate and $\mathbf{f}(\mathbf{x}, t)$ is an in-domain body force field per unit mass typically used for applying control. The system is closed by the boundary conditions (3.1c)-(3.1d) where $\Gamma_D = \Gamma_{in} \cup \Gamma_r$ is the Dirichlet part of the boundary, Γ_{in} the inflow part of the boundary, Γ_r are the rigid walls and Γ_{out} the Neumann outflow part of the boundary. $\mathbf{u}_b(\mathbf{x}, t)$ is a prescribed velocity input profile used for boundary control at the wall boundary Γ_r and for the external disturbances at the inflow boundary Γ_{in} . The outflow boundary condition (3.1d) is known as a no-stress condition and has proven to be well suited for unidirec-

tional outflows [111]. It is naturally satisfied by the variational formulation used in the numerical method (see appendix A). The artificial non-physical effect of this boundary condition near the outflow is investigated in section 3.3. In this study only boundary feedback control is considered, therefore the in-domain body force is set to zero ($\mathbf{f} = 0$) in the remainder of this section. However, in-domain disturbances are considered to evaluate the controller in section 3.4.

3.2.2. INPUTS AND OUTPUTS

The chosen control objective is to suppress the effect of inflow disturbances on the fluctuating wall shear stress. The control actuation is achieved by means of unsteady blowing and suction at the wall and boundary shear sensors are used to extract the measurements. A feedforward actuator/sensor configuration [27] is considered in which two point shear sensors at the walls are placed upstream of the control actuators. A schematic representation of the control layout is shown in figure 3.1. It is shown in Belson *et al.* [27] that feedforward configurations achieve the best disturbance attenuation, but can be less robust to additional disturbances not seen by the sensor. The shear sensors \mathbf{y}_m are therefore placed close to the control actuators \mathbf{g}_c . In addition a controlled shear output \mathbf{q} is defined which will be used to define the performance objective of the controller. The specifications will be discussed next. The boundary actuation is modelled through the boundary conditions (3.1c) and is decomposed into an external disturbance and a control

$$\mathbf{u}|_{\Gamma_D} = \mathbf{u}_b = \mathbf{u}_c(\mathbf{x}, t) + \mathbf{u}_d(\mathbf{x}, t), \quad (3.2)$$

with $\mathbf{u}_c(\mathbf{x}, t)$ the actuation imposed at the rigid walls and $\mathbf{u}_d(\mathbf{x}, t)$ the external disturbance imposed at the inflow. This disturbance model is discussed in detail in the next section. To manipulate the flow, localised wall-normal blowing and suction with zero-net-mass-flux is considered. It is assumed that the spatio-temporal actuator model is described by the following state-space description

$$\begin{aligned} \dot{\boldsymbol{\eta}}_c &= \tau^{-1}(\boldsymbol{\phi} - \boldsymbol{\eta}_c) = \mathcal{A}_c \boldsymbol{\eta}_c + \mathcal{B}_c \boldsymbol{\phi}, \\ \mathbf{u}_c &= \mathbf{G}_c \boldsymbol{\eta}_c = \mathcal{C}_c \boldsymbol{\eta}_c, \end{aligned} \quad (3.3)$$

with $\boldsymbol{\eta}_c(t) \in \mathbb{R}^2$ the actuator state that describes the magnitude of the blowing and suction, $\boldsymbol{\phi}(t) \in \mathbb{R}^2$ the control input and $\mathbf{u}_c(\mathbf{x}, t)$ is the actuator velocity output at the wall. The temporal dynamics is described by a first-order low-pass filter defined by $\mathcal{A}_c = -\tau^{-1}\mathbf{I}$, $\mathcal{B}_c = \tau^{-1}\mathbf{I}$ with τ the time constant of the filter. A fast actuator is assumed with $\tau = 0.1$, that is a stable approximation of a pure integrator typically used for boundary control in shear flows, see e.g. [82, 94]. The actuator output at the wall is defined by $\mathcal{C}_c = \mathbf{G}_c(\mathbf{x}) = [\mathbf{g}_{c_1}(\mathbf{x}), \mathbf{g}_{c_2}(\mathbf{x})]$ with $\mathbf{g}_{c_i} \in L^2(\Gamma_{r_i})^2$ the spatial distribution function that describes how $\eta_{c_i}(t)$ is distributed on the rigid boundary. A localised sinusoidal spatial distribution function is considered

$$\mathbf{g}_c(\mathbf{x}) = \begin{cases} \left[\begin{array}{c} 0 \\ \sin\left(\frac{2\pi(x-x_g)}{L_g}\right) \end{array} \right]^T & \text{if } x \in [x_g, x_g + L_g] \\ \left[\begin{array}{c} 0 \\ 0 \end{array} \right]^T & \text{elsewhere.} \end{cases} \quad (3.4)$$

Such a set-up is frequently considered in a fully distributed setting to control single wavenumber pairs, see e.g. Aamo and Krstic [10], Bewley and Liu [37], Jones *et al.* [39]. Here a localised distribution is considered with a spatial length of $L_g = 3 \approx 0.95\pi$ and origin at $x_g = 9 \approx 2.86\pi$. The length L_g is less than half the wavelength of the dominant spatial perturbation mode which is 2π (see next section).

Information about the perturbation field is given by two wall-normal shear stress point measurements

$$\begin{aligned} y_{m_i} &= \int_{\Gamma_{r_i}} \delta(x - x_m) \mathbf{t} \cdot (\mathbf{n} \cdot \nabla) \mathbf{u}|_{\Gamma_{r_i}} dx + w_{n_i} \\ &= \int_{\Gamma_{r_i}} \delta(x - x_m) \frac{\partial u}{\partial y}|_{\Gamma_{r_i}} dx + w_{n_i}, \end{aligned} \quad (3.5)$$

where \mathbf{n} is the inward unit normal on Γ_r and \mathbf{t} the corresponding unit tangential vector and the Dirac function δ indicates a point measurement. The term wall shear stress is used loosely here as the shear stress at the wall $\tau_{xy}|_{\Gamma_r} = (1/Re)\partial u/\partial y|_{\Gamma_r}$ also depends on the Reynolds number. It is assumed that the Reynolds number is known, so that $\partial u/\partial y|_{\Gamma_r}$ may easily be determined from measurements of $\tau_{xy}|_{\Gamma_r}$. The measurement noise $\mathbf{w}_n(t)$ is assumed to be a Gaussian stochastic process with zero means and covariances

$$E \{ \mathbf{w}_n(t) \} = 0, \quad E \{ \mathbf{w}_n(t) \mathbf{w}_n^T(\tau) \} = \mathbf{I} \sigma_n^2 \delta(t - \tau), \quad (3.6)$$

with σ_n^2 the variance of both sensors. A feedforward configuration is chosen where the sensor is placed upstream of the control actuators at $x_m = 7.5 \approx 2.39\pi$. In addition to the measured output, also two controlled outputs are defined

$$q_i = \int_{\Gamma_{r_i}} h(x) \mathbf{t} \cdot (\mathbf{n} \cdot \nabla) \mathbf{u}|_{\Gamma_{r_i}} dx, \quad (3.7)$$

where $h(x)$ is determined by the desired performance specifications in the domain. In this study we wish to stabilise the perturbations by minimising the wall shear stress downstream of the control actuators integrated over a localised region over the boundary. To this end $h(x)$ is chosen as a Gaussian distribution function

$$h(x) = e^{-\frac{(x-x_q)^2}{\sigma_x^2}}, \quad (3.8)$$

with $x_q = 17.5 \approx 5.57\pi$ the centre of the distribution and $\sigma_x = 1$ the radius. The controlled output is used to define the control objective in the \mathcal{H}_2 control framework later in this section.

3.2.3. INFLOW DISTURBANCE MODEL

2-D flow perturbations are characterised by unsteady fluctuations over a broad range of length scales and time scales. This makes the problem of estimating and controlling these perturbations inherently difficult. In particular the performance of the state estimation relies on the construction of a proper model for the external flow

disturbances [91]. In this section a new inflow disturbance model is introduced which allows for an efficient estimation of the flow perturbations within the localised control domain. To generate the external disturbances a superposition of eigenmodes from the spectrum of the Orr-Sommerfeld (OS) operator is used. These modes are calculated from the OS equation at the desired temporal frequencies. With this approach, specific modes of the flow perturbations can thus be selected and are included in the control design. In this way the most dominant modes that contribute to transition can be precisely targeted by the controller. These modes are included in the state-space model by imposing them at the inflow boundary of the control domain. Such a boundary condition has been used to introduce disturbances in DNS, e.g. for evaluating controllers [83, 112]. However, the use of such boundary conditions as a disturbance model that is included in the design of the controller has so far not been reported. We consider \mathcal{H}_2 optimal control which is a design methodology in which the external sources of excitation are stochastic. First the disturbance model is presented for the case of stochastic excitation of the modes in section 3.2.3 and in section 3.2.3 the specific modes are selected that are included in the control design.

EXTERNAL DISTURBANCES

Assuming that the perturbations are sufficiently small, a single mode of the flow perturbation in a 2-D unbounded domain takes the form

$$\mathbf{u} = \text{Real} \left[A_0 \tilde{\mathbf{u}}(y) e^{i(\alpha x - \omega t)} \right], \quad (3.9)$$

with A_0 the initial amplitude, $\tilde{\mathbf{u}}(y) = \tilde{\mathbf{u}}_r(y) + i\tilde{\mathbf{u}}_i(y) \in \mathbb{C}$ the eigenfunction, ω the radial frequency and α the non-dimensional wavenumber. The eigenfunction $\tilde{\mathbf{u}}$ for a particular frequency and wavelength can be determined from the Orr-Sommerfeld equation which will be discussed in the next section. The inflow is considered as the disturbance source which generates the perturbation (3.9) at a particular frequency that grows in space. Thus, the case $\omega \in \mathbb{R}$ and $\alpha = \alpha_r + i\alpha_i \in \mathbb{C}$ is considered and the spatial wavelength of the perturbation is given by $\lambda_x = 2\pi/\alpha_r$. At the inflow $x = 0$ a single mode of the perturbation can be described by

$$\begin{aligned} \mathbf{u}|_{\Gamma_{in}} = \mathbf{u}_d &= \text{Real} \left[A_0 \tilde{\mathbf{u}}(y) e^{-i\omega t} \right] \\ &= \tilde{\mathbf{u}}^r \underbrace{A_0 \cos(\omega t)}_{\eta_d^r} + \tilde{\mathbf{u}}^i \underbrace{A_0 \sin(\omega t)}_{\eta_d^i}. \end{aligned} \quad (3.10)$$

Equation (3.10) corresponds to a solution of a modal perturbation imposed at the inflow. The spatial content consists of the real and imaginary part of the eigenmode each excited with a persistent sinusoidal temporal input, where η_d^r is the input that excites the real part of the eigenmode and η_d^i the input that excites the imaginary part of the eigenmode. The two temporal components are not independent and for a modal perturbation the two components are 90° out of phase, that is $\angle \eta_d^r = \angle \eta_d^i + 90^\circ$. However, external disturbances are accounted for in a stochastic control framework in which the temporal disturbances are considered as independent

inputs. To effectively account for modal perturbations in the control design, η_d is not regarded as an external disturbance, but as a dynamic state in the disturbance model. The phase dependency can then be included in the model by exploiting the fact that $\eta_d^i = -\frac{1}{\omega}\dot{\eta}_d^r$ for the case of a modal perturbation with frequency ω . Let $\eta_d^r = \eta_d$ and $\eta_d^i = -\frac{1}{\omega}\dot{\eta}_d$, (3.10) can be represented in terms of a single temporal component and its derivative

$$\mathbf{u}_d = \tilde{\mathbf{u}}^r \eta_d - \frac{1}{\omega} \tilde{\mathbf{u}}^i \dot{\eta}_d, \quad (3.11)$$

where the imaginary part of the eigenfunction is scaled with the perturbation frequency to account for the phase. Accounting for the phase in the model will reduce the non-modal spatial transients introduced by the perturbation near the inflow as will be shown in section 3.3.1. To account for the inflow perturbation (3.11) in the control design a second-order low-pass filter is proposed for the temporal dynamics

$$\ddot{\eta}_d = \omega_n^2 w_d - 2\zeta\omega_n \dot{\eta}_d - \omega_n^2 \eta_d, \quad (3.12)$$

with ζ the damping ratio, ω_n the undamped natural frequency and w_d the external disturbance assumed to be an uncorrelated white Gaussian stochastic process with zero mean and variance

$$E\{w_d(t)\} = 0, \quad E\{w_d(t)w_d(\tau)\} = \sigma_d^2 \delta(t - \tau). \quad (3.13)$$

The low-pass filter (3.12) allows the frequency response shaping of \mathbf{u}_d at the inflow. The parameters are chosen such that the filter amplifies the frequencies near the frequency ω of the perturbation mode. The damping ratio is set to $\zeta = 0.25$. The natural frequency is chosen such that the peak frequency $\omega_p = \omega_n \sqrt{1 - 2\zeta^2}$, where the filter has the maximum magnitude, is equal to the frequency of the perturbation mode. The magnitude plot of the filter as a function of the normalised frequency ω/ω_p is shown in figure 3.2. With these settings the filter amplifies the disturbance magnitude by approximately a factor two at ω_p . By increasing the magnitude at the perturbation frequency the controller will be better able to target the mode. The filter attenuates the disturbance at higher frequencies which will also make the controller design more robust to unresolved dynamics [39]. Finite-dimensional representations of the system (discussed in the next section) are used for the control design which only resolve a finite number of modes, typically those with a lower temporal frequency. By suppressing the magnitude of the disturbance at higher frequencies, the situation where the disturbance excites unresolved plant dynamics is avoided. This in turn avoids that the controller, which is designed based on the disturbance model, estimates unresolved plant dynamics. This phenomenon is also known as spillover and can destabilise the infinite-dimensional system [53].

The disturbance model defined by (3.11) and (3.12) can be written in state-space

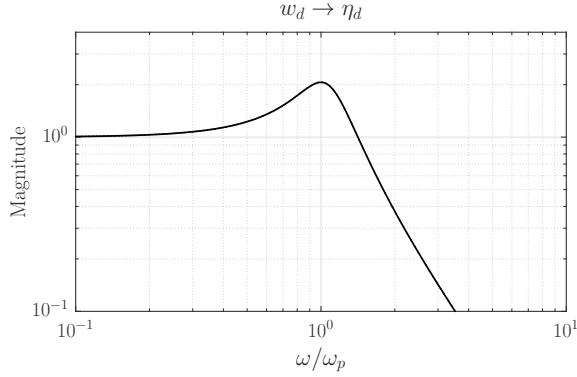


Figure 3.2: Magnitude plot of the low pass filter (3.12) used for the disturbance model. The frequency is normalized with the peak frequency ω_p .

format as

$$\left. \begin{aligned} \begin{bmatrix} \dot{\eta}_d \\ \ddot{\eta}_d \end{bmatrix} &= \underbrace{\begin{bmatrix} 0 & 1 \\ -\omega_n^2 & -2\zeta\omega_n \end{bmatrix}}_{\mathcal{A}_d} \underbrace{\begin{bmatrix} \eta_d \\ \dot{\eta}_d \end{bmatrix}}_{\bar{\eta}_d} + \underbrace{\begin{bmatrix} 0 \\ \omega_n^2 \end{bmatrix}}_{\mathcal{B}_d} w_d \\ \mathbf{u}_d &= \underbrace{\begin{bmatrix} \tilde{\mathbf{u}}^r & -\frac{1}{\omega} \tilde{\mathbf{u}}^i \end{bmatrix}}_{\mathcal{C}_d} \begin{bmatrix} \eta_d \\ \dot{\eta}_d \end{bmatrix} \end{aligned} \right\} \Rightarrow \begin{aligned} \dot{\bar{\eta}}_d &= \mathcal{A}_d \bar{\eta}_d + \mathcal{B}_d w_d \\ \mathbf{u}_d &= \mathcal{C}_d \bar{\eta}_d, \end{aligned} \quad (3.14)$$

where $\bar{\eta}_d = [\eta_d, \dot{\eta}_d]$ is the state, w_d is the external disturbance and the perturbation velocity \mathbf{u}_d at the inflow is the output. For the case when multiple N modes are accounted for in the control design, the state-space systems for the selected frequencies and wavenumbers can be combined in diagonal form as $\mathcal{A}_d = \text{diag}\{\mathcal{A}_{d_1}, \dots, \mathcal{A}_{d_N}\}$, $\mathcal{B}_d = \text{diag}\{\mathcal{B}_{d_1}, \dots, \mathcal{B}_{d_N}\}$ and $\mathcal{C}_d = [\mathcal{C}_{d_1}, \dots, \mathcal{C}_{d_N}]$.

SELECTION OF THE PERTURBATION MODES

The next step is to select the modes that contribute to the transition process to include in the disturbance model (3.14) for control design. The modes are computed from the Orr-Sommerfeld equation. Let $\tilde{\mathbf{u}} = [\partial\tilde{\psi}/\partial y, -\partial\tilde{\psi}/\partial x] = [\tilde{\psi}', -i\alpha\tilde{\psi}]^T$. The eigenfunction for the streamfunction $\tilde{\psi}$ satisfies the Orr-Sommerfeld equation

$$\begin{aligned} \left(U - \frac{\omega}{\alpha}\right) (\tilde{\psi}'' - \alpha^2 \tilde{\psi}) - U'' \tilde{\psi} &= -\frac{i}{\alpha Re} (\tilde{\psi}'''' - 2\alpha^2 \tilde{\psi}'' + \alpha^4 \tilde{\psi}), \\ \tilde{\psi}(\pm 1) = \tilde{\psi}'(\pm 1) &= 0, \end{aligned} \quad (3.15)$$

which is an eigenvalue problem with $\tilde{\psi}$ the eigenfunction of the problem and with either α or ω the eigenvalue of the problem. The prime superscript in (3.15) denotes differentiation with respect to y . The spatial amplification theory is considered to generate the modes. Thus a real frequency ω is chosen and (3.15) is solved for the complex eigenfunction and complex wavenumber α . At each frequency and Reynolds number this gives a spectrum of spatial eigenvalues. Figure 3.3 shows the spectrum

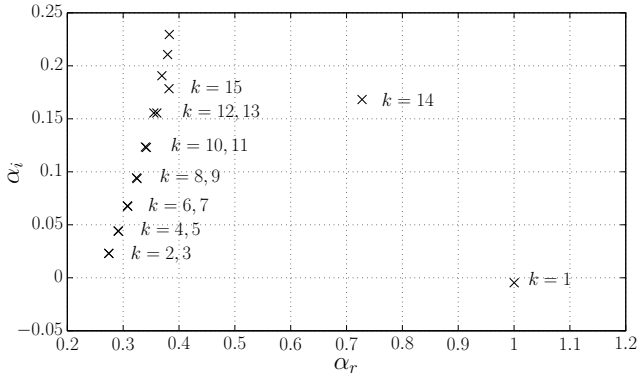


Figure 3.3: Spatial Orr-Sommerfeld spectrum for $\omega = 0.253$ and $Re = 7000$. Only the dominant eigenvalues that contribute to a physical downstream response are shown.

at the most dominant frequency that includes the mode with the maximum growth rate given by the imaginary part of the spatial eigenvalue (wavenumber). For the case $Re = 7000$ the dominant frequency is approximately $\omega = 0.253$. Only the least stable eigenvalues that contribute to a physical downstream response are shown in figure 3.3 [21, pp. 260]. The spectrum contains one spatially growing mode ($k = 1$) with a negative imaginary part. This is the leading or most unstable mode that contributes to the primary route to transition [16] in 2-D channel flows. The left branch $k = 2, \dots, k = 13, k = 15$ are ‘centre modes’ [6] with very little support near the walls and represent perturbations in the freestream. Mode $k = 14$ is highly stable and has negligible influence in the transition process. Figure 3.4 shows the spatial eigenvalue of the first or most unstable ($k = 1$) mode as a function of the temporal frequency. Although the flow is unstable over the frequency range $0.216 \leq \omega \leq 0.286$, only the leading mode calculated at the most amplified frequency $\omega = 0.253$ is included in the control design. This will be referred to as the design point in the remainder of the chapter. Figure 3.5 shows the shape of the eigenfunction for this particular mode. This mode is used to define the inflow perturbation (3.14). Note that the design frequency becomes part of the disturbance model. This model can easily be extended to include the dominant modes calculated for different temporal frequencies. However, it is found that adding more eigensolutions does not improve the performance of the control system. This is a direct result of the near-linear dependence of the leading eigenmodes for different temporal frequencies. In other words the modes are very similar. It will be shown in section 3 that also at other frequencies than the design point, the single mode inflow disturbance will quickly develop in-domain to a travelling wave with a spatial growth as predicted by the Orr-Sommerfeld equation (3.15).

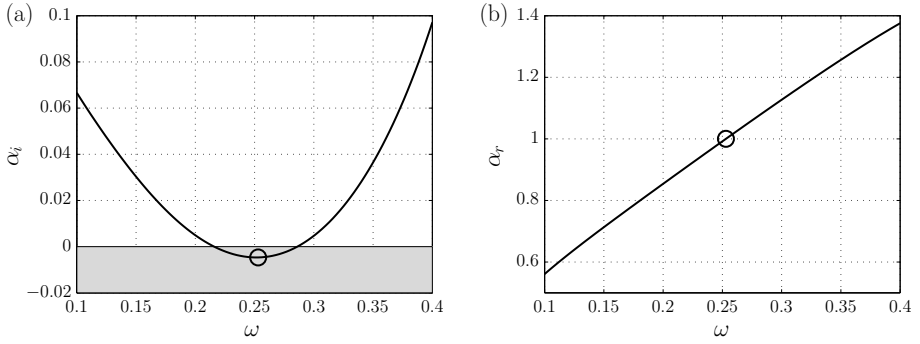


Figure 3.4: The leading or most unstable wavenumber as function of the temporal frequency ω at $Re = 7000$. (a) The imaginary part α_i . Negative values of α_i characterise unstable modes (gray region). (b) The real part α_r . The point marked by 'o' corresponds to the most amplified frequency for the investigated conditions.

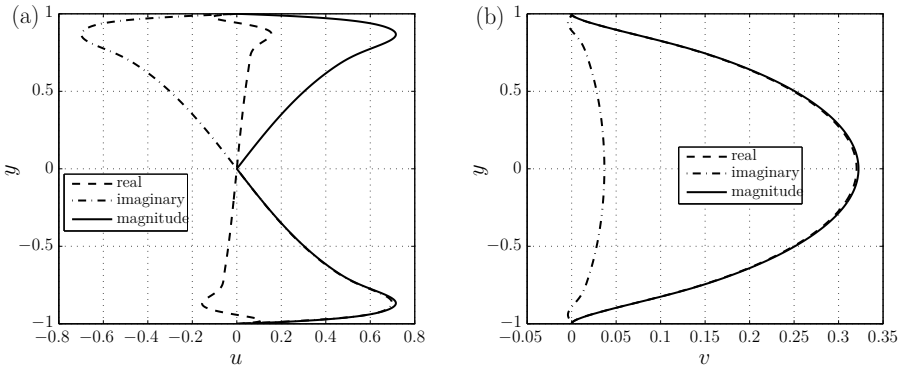


Figure 3.5: The selected eigenfunction included in the inflow disturbance model for the control design. The Orr-Sommerfeld eigenfunction for u (a) and v (b) calculated at $Re = 7000$, $\omega = 0.253$. The corresponding wavenumber for this mode is $\alpha = 1 - 0.0047i$.

3.2.4. STATE-SPACE FORMULATION

In this section the linearised Navier-Stokes equations (LNSE) including the inputs, outputs and the inflow disturbance model are written as a boundary control system in the standard state-space format ($\dot{\mathbf{u}} = \mathcal{A}\mathbf{u} + \mathcal{B}\phi$, $\mathbf{y} = \mathcal{C}\mathbf{u}$). This is required for defining the control objective and applying control theoretic tools. Boundary control systems do not fit directly into the standard form. However, we can extract the boundary controlled part of the dynamical model and rewrite the system on an extended state space in standard form. This method originates from Fattorini [113] and has been applied for boundary control of wall-bounded shear flows [82, 84, 94]. We also refer to Curtain and Zwart [43, Sec 3.3] for more information on this formulation. Let $\mathcal{X}(\Omega)$ be the space of n -dimensional divergence free functions defined on Ω with inner product $(\mathbf{u}_1, \mathbf{u}_2) = \int_{\Omega} \mathbf{u}_1 \cdot \mathbf{u}_2 d\mathbf{x}$ and norm $\|\mathbf{u}_1\|_2 = (\mathbf{u}_1, \mathbf{u}_1)^{1/2}$ where $\mathbf{u}_1, \mathbf{u}_2 \in \mathcal{X}$. Furthermore, let the trajectory segment $\mathbf{u}(\cdot, t) = \{\mathbf{u}(\mathbf{x}, t), \mathbf{x} \in \Omega\}$ be

the state and $\mathbf{u}(t)|_{\Gamma} \in \mathcal{U}$ the value of $\mathbf{u}(t)$ on the boundary defined in a separable Hilbert space \mathcal{U} . The LNSE (3.1) in $\mathcal{X}(\Omega)$, including the boundary inputs (3.2), the measurements (3.5) and the controlled output (3.7), can be written as

$$\begin{aligned}\dot{\mathbf{u}} &= \mathcal{A}\mathbf{u}, \\ \mathcal{B}\mathbf{u} &= \mathbf{u}_c + \mathbf{u}_d, \\ \mathbf{q} &= \mathcal{Q}\mathbf{u}, \\ \mathbf{y}_m &= \mathcal{C}\mathbf{u} + \mathbf{w}_n.\end{aligned}\tag{3.16}$$

The operator $\mathcal{A} : D(\mathcal{A}) \subset \mathcal{X} \mapsto \mathcal{X}$ corresponds to evaluating the linear differential operator of the LNSE. The pressure can be eliminated from the equations by using a space of velocity fields which are divergence free [110], which is also done here (see also appendix A for the variational formulation). $\mathcal{B} : \mathcal{X} \mapsto \mathcal{U}$ is a boundary operator which maps the flow field to its values on the boundary and \mathcal{C} , \mathcal{Q} are output operators, respectively defined as

$$\mathcal{B}\mathbf{u} = \mathbf{u}|_{\Gamma_D}, \quad \mathcal{C}_i\mathbf{u} = (\delta(x - x_m), \mathbf{t} \cdot (\mathbf{n} \cdot \nabla) \mathbf{u}|_{\Gamma_{r_i}}), \quad \mathcal{Q}_i\mathbf{u} = (h(x), \mathbf{t} \cdot (\mathbf{n} \cdot \nabla) \mathbf{u}|_{\Gamma_{r_i}}).\tag{3.17}$$

To extract the boundary controlled part the first step is to construct two operators \mathcal{Z}_c , \mathcal{Z}_d such that

$$\begin{aligned}\mathcal{Z}_c : \mathcal{U} &\mapsto \mathcal{X}, \quad \mathcal{B}\mathcal{Z}_c\mathbf{u}_c = \mathbf{u}_c, \\ \mathcal{Z}_d : \mathcal{U} &\mapsto \mathcal{X}, \quad \mathcal{B}\mathcal{Z}_d\mathbf{u}_d = \mathbf{u}_d.\end{aligned}\tag{3.18}$$

The boundary condition can then be removed by decomposing the state into

$$\mathbf{u} = \mathbf{u}_h + \mathcal{Z}_c\mathbf{u}_c + \mathcal{Z}_d\mathbf{u}_d.\tag{3.19}$$

The dynamics of the new state \mathbf{u}_h is governed by the following evolution equation with homogeneous boundary conditions [43]

$$\dot{\mathbf{u}}_h = \mathcal{A}\mathbf{u}_h - \mathcal{Z}_c\dot{\mathbf{u}}_c + \mathcal{A}\mathcal{Z}_c\mathbf{u}_c - \mathcal{Z}_d\dot{\mathbf{u}}_d + \mathcal{A}\mathcal{Z}_d\mathbf{u}_d,\tag{3.20}$$

where the operator $\mathcal{A} : D(\mathcal{A}) \mapsto \mathcal{X}$ is defined as

$$\begin{aligned}\mathcal{A}\mathbf{u}_h(t) &= \mathcal{A}\mathbf{u}_h(t), \text{ for } \mathbf{u}_h \in D(\mathcal{A}), \\ D(\mathcal{A}) &= D(\mathcal{A}) \cap \ker(\mathcal{B}) = \{\mathbf{u}_h \in \mathcal{X} \mid \mathbf{u}_h(t)|_{\Gamma_D} = 0\}.\end{aligned}\tag{3.21}$$

If \mathbf{u}_h is a solution of the homogeneous system (3.20), then \mathbf{u} defined by (3.19) is a solution of the original system (3.16) [43, 113]. Equation (3.20) contains both the temporal inputs and their time derivatives which is undesirable since they are not independent inputs. This can be eliminated by reformulating (3.20) on the extended state-space $\mathcal{X}^e = \mathcal{X} \oplus \mathcal{U}$

$$\begin{bmatrix} \dot{\mathbf{u}}_h \\ \dot{\mathbf{u}}_c \\ \dot{\mathbf{u}}_d \end{bmatrix} = \begin{bmatrix} \mathcal{A} & \mathcal{A}\mathcal{Z}_c & \mathcal{A}\mathcal{Z}_d \\ 0 & 0 & 0 \\ 0 & 0 & 0 \end{bmatrix} \begin{bmatrix} \mathbf{u}_h \\ \mathbf{u}_c \\ \mathbf{u}_d \end{bmatrix} + \begin{bmatrix} -\mathcal{Z}_c \\ \mathbf{I} \\ 0 \end{bmatrix} \dot{\mathbf{u}}_c + \begin{bmatrix} -\mathcal{Z}_d \\ 0 \\ \mathbf{I} \end{bmatrix} \dot{\mathbf{u}}_d.\tag{3.22}$$

The inflow perturbation velocity and the wall actuation velocity have become a state of the system in this formulation. The external input is actually the time derivative of the boundary velocity. From the actuator model (3.3) it follows that $\mathbf{u}_c = \mathcal{C}_c \boldsymbol{\eta}_c$, $\dot{\mathbf{u}}_c = \mathcal{C}_c \mathcal{A}_c \boldsymbol{\eta}_c + \mathcal{C}_c \mathcal{B}_c \phi$ and from the disturbance model (3.14) it follows that $\mathbf{u}_d = \mathcal{C}_d \boldsymbol{\eta}_d$, $\dot{\mathbf{u}}_d = \mathcal{C}_d \mathcal{A}_d \bar{\boldsymbol{\eta}}_d + \mathcal{C}_d \mathcal{B}_d w_d$. Substituting these expressions in (3.22), and combining this system with the actuator dynamics (3.3) and the disturbance dynamics (3.14), gives the following augmented system

$$\begin{aligned} \begin{bmatrix} \dot{\mathbf{u}}_h \\ \dot{\boldsymbol{\eta}}_c \\ \dot{\bar{\boldsymbol{\eta}}}_d \end{bmatrix} &= \underbrace{\begin{bmatrix} \mathcal{A} & \mathcal{A} \mathcal{Z}_c \mathcal{C}_c - \mathcal{Z}_c \mathcal{C}_c \mathcal{A}_c & \mathcal{A} \mathcal{Z}_d \mathcal{C}_d - \mathcal{Z}_d \mathcal{C}_d \mathcal{A}_d \\ 0 & \mathcal{A}_c & 0 \\ 0 & 0 & \mathcal{A}_d \end{bmatrix}}_{\bar{\mathcal{A}}} \underbrace{\begin{bmatrix} \mathbf{u}_h \\ \boldsymbol{\eta}_c \\ \bar{\boldsymbol{\eta}}_d \end{bmatrix}}_{\mathbf{u}^e} \\ &+ \underbrace{\begin{bmatrix} -\mathcal{Z}_c \mathcal{C}_c \mathcal{B}_c \\ \mathcal{B}_c \\ 0 \end{bmatrix}}_{\bar{\mathcal{B}}_c} \phi + \underbrace{\begin{bmatrix} -\mathcal{Z}_d \mathcal{C}_d \mathcal{B}_d \\ 0 \\ \mathcal{B}_d \end{bmatrix}}_{\bar{\mathcal{B}}_d} w_d, \\ \mathbf{q} &= \underbrace{\begin{bmatrix} \mathcal{Q} & \mathcal{Q} \mathcal{Z}_c \mathcal{C}_c & \mathcal{Q} \mathcal{Z}_d \mathcal{C}_d \end{bmatrix}}_{\bar{\mathcal{Q}}} \begin{bmatrix} \mathbf{u}_h \\ \boldsymbol{\eta}_c \\ \bar{\boldsymbol{\eta}}_d \end{bmatrix}, \\ \mathbf{y}_m &= \underbrace{\begin{bmatrix} \mathcal{C} & \mathcal{C} \mathcal{Z}_c \mathcal{C}_c & \mathcal{C} \mathcal{Z}_d \mathcal{C}_d \end{bmatrix}}_{\bar{\mathcal{C}}} \begin{bmatrix} \mathbf{u}_h \\ \boldsymbol{\eta}_c \\ \bar{\boldsymbol{\eta}}_d \end{bmatrix} + \mathbf{w}_n, \end{aligned} \quad (3.23)$$

where also included are the resulting output equations from the state transformation (3.19). (3.23) can be compactly written as

$$\begin{aligned} \dot{\mathbf{u}}^e &= \bar{\mathcal{A}} \mathbf{u}^e + \bar{\mathcal{B}}_c \phi + \bar{\mathcal{B}}_d w_d, \\ \mathbf{q} &= \bar{\mathcal{Q}} \mathbf{u}^e, \\ \mathbf{y}_m &= \bar{\mathcal{C}} \mathbf{u}^e + \mathbf{w}_n, \end{aligned} \quad (3.24)$$

with \mathbf{u}^e the extended state. A final remark is given about the controllability of the system. By formulating the system on the extended state space (3.20) pure integrators have been added at the system external inputs. This results in additional system poles at the origin. As a result, the system in the form (3.20) is not stabilisable, which means that not all uncontrollable modes are asymptotically stable. This is a direct result of the fact that both the control and disturbance are defined at the boundary and both appear as a state in the system. It is not possible to influence the additional poles of the disturbance dynamics by means of control and vice versa (Assumption (i) is violated, and assumptions (iii) and (iv) are violated for $\omega = 0$, see Appendix B). By including the actuator dynamics and disturbance dynamics, the uncontrollable poles at the origin are moved to the stable left half-plane to the location of the eigenvalues of \mathcal{A}_c and \mathcal{A}_d . The state-space formulation (3.23) is thus stabilisable which allows the synthesis of \mathcal{H}_2 optimal controllers.

3.2.5. FINITE-DIMENSIONAL SYSTEM

Equation (3.24) represents the continuous formulation of the flow control problem. For simulation and control design a finite-dimensional representation of (3.24) is required. In chapter 2 a framework is presented for deriving state-space descriptions for a general class of linear parabolic PDEs to which standard control theoretic tools can be applied. This method is also used in this chapter and uses multivariate B-splines of arbitrary degree and smoothness defined on triangulations [40–42] to find matrix representations of all operators in (3.23). This method has the flexibility of the finite element method to use local refinements and to cope with irregular domains, and the high approximation power of spectral methods. The triangulations used to construct the simulation model and the model that is used as a starting point for model reduction and control design are shown in figure 3.6. The use of spline spaces provides a convenient way for stating the degree and smoothness of the spline model. In addition, the approximation properties of such spline spaces have been extensively studied in the literature [40]. Let \mathcal{T} be the triangulation of Ω . The spline space is the space of all smooth piecewise polynomial functions of arbitrary degree d and arbitrary smoothness r over \mathcal{T} with $0 \leq r < d$

$$S_d^r(\mathcal{T}) := \{s \in C^r(\Omega) : s|_t \in \mathcal{P}_d, \forall t \in \mathcal{T}\}, \quad (3.25)$$

with \mathcal{P}_d the space of all polynomials of total degree d and t denotes a triangle. We construct a basis for the smooth divergence free spline subspace \mathcal{S} such that $\mathcal{S} \subset \mathcal{X}$ in conjunction with a Galerkin scheme to obtain a finite-dimensional representation of the governing equations. The pressure is eliminated from the equations by using a space of velocity fields which are divergence free and a suitable choice of the variational formulation. This will also avoid singularities in the numerical method. The Galerkin-type variational formulation through which the spline approximation is determined and the corresponding numerical method are described in detail in appendix A.1.

To derive the full-order control model a structured triangulation is used, refined near the walls to properly resolve the shear features of the flow consisting of $n_t = 960$ triangles, and the $\mathcal{S}_4^0(\mathcal{T}_{960})^2$ spline space is chosen as approximating space for the velocity field. C^0 continuous spline elements are chosen which allows an accurate interpolation of the actuator distribution function at the boundary. Degree $d = 4$ elements are chosen which allows the construction of an exactly divergence free basis and to obtain better approximation properties [40, 62]. With this degree each element t has a total of $N_t = 15$ degrees of freedom. The complete basis for $L^2(\Omega)^2$ has a total of $N = n_t \times N_t \times 2 = 28800$ degrees of freedom. This basis is used to spatially discretise the system. The resulting discrete system is transformed to state-space format using the null-space projection method. This projection employs a similar state transformation as in (3.19), but in a discrete setting, and results in a reduced number of states that have a minimal non-zero support for the smooth divergence free spline space $\mathcal{S} \subset \mathcal{X}$. The reduction is equal to the total rank R^* of the discrete divergence, boundary and smoothness operators. The order of the state-space model resulting from the null-space projection is $N - R^* = 5569$. The large reduction can be contributed to the fact that the constrained smooth divergence

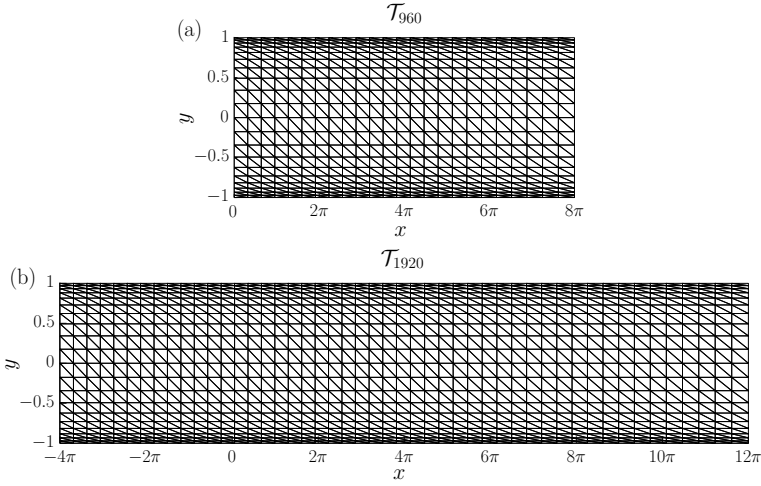


Figure 3.6: Triangulations used for the simulation model and the model that is used for model reduction and control design. (a) Triangulation with 960 triangles used for the control model. (b) Triangulation with 1920 triangles used for the simulation model.

free subspace is much smaller than the unconstrained space. The order of the model is sufficiently small to allow a direct application of balanced truncation for model reduction. For the case of spatially periodic boundary conditions the accuracy of the model can be assessed via comparison of the model spectra with the temporal spectra of the Orr-Sommerfeld equation (3.15). This comparison is demonstrated in appendix A.2. The numerical accuracy of the first 22 dominant eigenvalues varies between $2 \times 10^{-8} \leq |\lambda_k - \lambda_k^{OS}| \leq 2 \times 10^{-3}$. This is considered accurate for the purpose of control design and demonstration. A more physical validation of the model for the non-periodic case considered in this study is conducted in section 3.3. A different model is used for simulating the response of system. The simulation model is defined on a longer domain with a total length of $L_{sim} = 16\pi$. A similar triangulation consisting of 1920 triangles is used and the simulation model has approximately the same accuracy as the control model. In the next sections we focus on the control model and use the notation $(\mathcal{A}, \mathcal{B}, \mathcal{C}, \mathcal{D})$ to represent the full-order finite-dimensional system and use the notation $(\mathbf{A}, \mathbf{B}, \mathbf{C}, \mathbf{D})$ to represent a reduced-order system resulting from balanced truncation.

3.2.6. FORMULATION OF THE \mathcal{H}_2 CONTROL PROBLEM

In this section the feedback design problem for the state-space representation of the flow (3.24) is cast as an \mathcal{H}_2 optimisation problem. The state-space formulas for the optimal solution are given in Appendix B. We refer to Zhou *et al.* [29], Doyle *et al.* [30], Skogestad and Postlethwaite [86] for more detail on this control theory. The main objective of the feedback control design is to find a control input ϕ based on the output measurement \mathbf{y}_m that minimises the wall shear stress defined by \mathbf{q} in the presence of the disturbances w_d and \mathbf{w}_n . First the standard control formulation that is considered by \mathcal{H}_2 control is presented. The application of \mathcal{H}_2 control to the

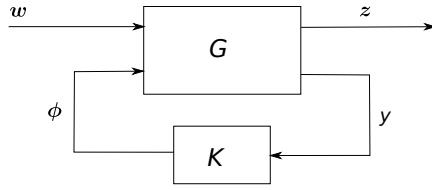


Figure 3.7: The general control configuration. System G , controller K , output measurement y , control input ϕ , performance objective z and exogenous disturbances w .

state-space representation of the flow (3.24) will follow thereafter. Let w be the vector of exogenous disturbances and z the vector of performance measures to be minimised. The \mathcal{H}_2 control problem is a disturbance rejection problem and considers the standard control configuration shown in figure 3.7 which is described by

$$\begin{bmatrix} z \\ y \end{bmatrix} = \mathbf{G}(s) \begin{bmatrix} w \\ \phi \end{bmatrix} = \begin{bmatrix} \mathbf{G}_{zw}(s) & \mathbf{G}_{z\phi}(s) \\ \mathbf{G}_{yw}(s) & \mathbf{G}_{y\phi}(s) \end{bmatrix} \begin{bmatrix} w \\ \phi \end{bmatrix}, \quad (3.26)$$

$$\phi = \mathbf{K}(s)y,$$

with $\mathbf{K}(s)$ the controller to be synthesised and $\mathbf{G}(s)$ the open-loop transfer function matrix of the generalised plant defined by

$$\mathbf{G}(s) = \mathbf{C}_p (s\mathbf{I} - \mathbf{A}_p)^{-1} \mathbf{B}_p + \mathbf{D}_p, \quad (3.27)$$

with the state-space realisation

$$\mathbf{G}(s) = \left[\begin{array}{c|cc} \mathbf{A}_p & \mathbf{B}_1 & \mathbf{B}_2 \\ \hline \mathbf{C}_1 & 0 & \mathbf{D}_{12} \\ \mathbf{C}_2 & \mathbf{D}_{21} & 0 \end{array} \right] = \left[\begin{array}{c|c} \mathbf{A}_p & \mathbf{B}_p \\ \hline \mathbf{C}_p & \mathbf{D}_p \end{array} \right], \quad (3.28)$$

To account for the state disturbances w_d and the measurement noise w_n in a \mathcal{H}_2 control framework the state-space system (3.24) is formulated as a generalised plant (3.28) and scaled in terms of two parameters which may be individually adjusted to achieve the desired closed-loop performance. A similar scaling was also presented in Bewley and Liu [37]. The control objective is to counteract the influence of the state disturbance w_d on the controlled output defined by $\mathbf{q} = \tilde{\mathbf{Q}}\mathbf{u}^e$. Therefore the controlled output is used to define the performance measure z

$$z = \begin{bmatrix} \tilde{\mathbf{Q}} \\ 0 \end{bmatrix} \mathbf{u}^e + \begin{bmatrix} 0 \\ l\mathbf{I} \end{bmatrix} \phi, \quad (3.29)$$

which also includes a penalty on the control defined by the parameter l . The parameter l determines the trade-off between a low control effort ($\phi^T \phi$) and a low controlled output energy ($\mathbf{q}^T \mathbf{q}$). For the design of the controller, decisions must be made about the expected state disturbances and measurement noise. The temporal magnitude of these disturbances in the state-space system is defined by the expected covariances of the temporal state disturbance (3.13) and the measurement

noise (3.6). In this study it is assumed that nothing is known a priori about the expected covariances. To make a parametric study for the controller design tractable, a relative magnitude of the measurement noise is defined

$$\gamma = \frac{\sigma_n}{\sigma_d}, \quad (3.30)$$

which is the ratio between the root mean square of the expected variance of respectively the sensor noise and the state disturbance. The state disturbance and measurement noise are respectively modelled as $w_d = \sigma_d w_1$ and $w_n = \sigma_n w_2$ with w_1 and w_2 defined as white noise with unit intensity. The system is parameterised in terms of γ by defining a new scaled observation that is used for feedback

$$\begin{aligned} \mathbf{y} &= \frac{\gamma}{\sigma_n} \mathbf{y}_m = \frac{\gamma}{\sigma_n} (\bar{\mathbf{C}} \mathbf{u}^e + \sigma_n \mathbf{w}_2) \\ &= \frac{\gamma}{\sigma_n} \bar{\mathbf{C}} \mathbf{u}^e + \gamma \mathbf{w}_2 \end{aligned} \quad (3.31)$$

and the system is normalised such that $\sigma_d = 1$. Using this normalisation it follows from (3.30) that $\gamma = \sigma_n$ and the observation (3.31) is obtained by a simple change of variables. For the control design γ does not represent a physical root mean square value of the measurement noise, but a relative measure with respect to the state disturbance, used to tune the controller. Defining the vector of disturbances as $\mathbf{w} = [w_1, w_2^T]^T$ and the following system matrices

$$\begin{aligned} \mathbf{A}_p &= \bar{\mathbf{A}}, \quad \mathbf{B}_1 = [\sigma_d \bar{\mathbf{B}}_d \quad 0], \quad \mathbf{B}_2 = \bar{\mathbf{B}}_c, \\ \mathbf{C}_1 &= \begin{bmatrix} \bar{\mathbf{Q}} \\ 0 \end{bmatrix}, \quad \mathbf{D}_{12} = \begin{bmatrix} 0 \\ \mathbf{I} \end{bmatrix}, \quad \mathbf{C}_2 = \frac{\gamma}{\sigma_n} \bar{\mathbf{C}}, \quad \mathbf{D}_{21} = [0 \quad \gamma \mathbf{I}], \end{aligned} \quad (3.32)$$

the system (3.24) can be written as a generalised plant with the state-space formulation (3.28), that is

$$\begin{aligned} \dot{\mathbf{u}}^e &= \mathbf{A}_p \mathbf{u}^e + \mathbf{B}_1 \mathbf{w} + \mathbf{B}_2 \phi, \\ \mathbf{z} &= \mathbf{C}_1 \mathbf{u}^e + \mathbf{D}_{12} \phi, \\ \mathbf{y} &= \mathbf{C}_2 \mathbf{u}^e + \mathbf{D}_{21} \mathbf{w}. \end{aligned} \quad (3.33)$$

The \mathcal{H}_2 control design problem for this system is to find a controller $\mathbf{K}(s)$ that, based on the measurement information \mathbf{y} , generates a control input ϕ which stabilises the system (3.33) internally and minimises

$$\|\mathbf{T}_{zw}(s)\|_2 = \sqrt{\frac{1}{2\pi} \int_{-\infty}^{\infty} \text{Trace}\{\mathbf{T}_{zw}^*(i\omega) \mathbf{T}_{zw}(i\omega)\} d\omega} \quad (3.34)$$

$$= \sqrt{\frac{1}{2\pi} \int_{-\infty}^{\infty} \sum_{i,j} |T_{zw}^{i,j}(i\omega)|^2 d\omega}. \quad (3.35)$$

Equation (3.34) is referred to as the \mathcal{H}_2 -norm of the closed-loop transfer function matrix \mathbf{T}_{zw} from the external disturbances \mathbf{w} to the control objectives \mathbf{z} and $|T_{zw}^{i,j}|$

denotes the magnitude of the closed-loop transfer function from the j -th disturbance to the i -th objective. \mathbf{T}_{zw} is given by

$$\mathbf{T}_{zw}(s) = \frac{\mathbf{z}(s)}{\mathbf{w}(s)} = \mathbf{G}_{zw}(s) + \mathbf{G}_{z\phi}(s)\mathbf{K}(s)(\mathbf{I} - \mathbf{G}_{y\phi}(s)\mathbf{K}(s))^{-1}\mathbf{G}_{yw}(s), \quad (3.36)$$

which follows from (3.26). Physically, the \mathcal{H}_2 norm in (3.34) can be interpreted as the amplification of the system from \mathbf{w} to \mathbf{z} integrated over all frequencies. In the time domain, this is equivalent to the variance amplification of stochastic disturbances [79]. By minimising the \mathcal{H}_2 norm, the controlled output power $E[\mathbf{z}^T\mathbf{z}]$ of the system, due to unit white Gaussian disturbances \mathbf{w} , is minimised. The state-space formulas for the optimal controller $\mathbf{K}(s)$ that minimise (3.34) are given in appendix B. It combines a state estimator (Kalman filter) for the flow field and a state feedback, and has a state-space description of the form

$$\begin{aligned} \dot{\mathbf{u}}_K^e &= \mathcal{A}_K\mathbf{u}_K^e + \mathcal{B}_K\mathbf{y}, \\ \phi &= \mathcal{C}_K\mathbf{u}_K^e, \end{aligned} \quad (3.37)$$

with \mathbf{u}_K^e the estimated state and $\mathcal{A}_K = \mathcal{A} + \mathcal{B}_2\mathcal{C}_K - \mathcal{B}_K\mathcal{C}_2$. The controller input matrix \mathcal{B}_K represents the estimator gain and the output matrix \mathcal{C}_K represents the state feedback gain. The controller (3.37) can be structured using the separation principle, which means that the estimator and state feedback can be tuned independently. Thus the control penalty l and the estimation parameter γ may be individually adjusted to achieve the desired characteristics for the closed-loop system \mathbf{T}_{zw} . A low value for the control penalty l results in higher gain state feedback \mathcal{C}_K . Similarly, when γ is small (high signal to noise ratio) the observation is fed back more aggressively (high observer gain \mathcal{B}_K) than when γ is high. The controller $\mathbf{K}(s)$ in (3.37) represents the full order controller. Such a high-order controller is usually not real time implementable for practical flow configurations. To synthesise a reduced-order controller $\mathbf{K}_r(s)$ for the high-order plant the so-called reduce-then-design approach [114] is used, which is discussed in detail in the next section. This section also includes a parametric study for the parameters γ and l .

3.3. CONTROLLER DESIGN AND SYNTHESIS

In this section the reduced-order controller is designed and synthesised for the problem defined in the previous section. An input-output analysis [33] is conducted in section 3.3.1 for the uncontrolled system using the spatio-temporal frequency response [79, 83] to identify the perturbation modes that are captured by the inflow disturbance model and are retained in the reduced-order model. The input-output analysis reveals the non-modal transients introduced by the inflow disturbance as well as the modal unstable perturbation modes. In section 3.3.2 a reduced-order model that captures the input-output behaviour is derived using balanced truncation. This model is used to design the optimal controller and the truncated dynamics is taken into account in the control system design. This section also includes a parametric study for the estimator and state feedback design problem. Finally, the closed-loop performance of three selected controllers is evaluated in the frequency

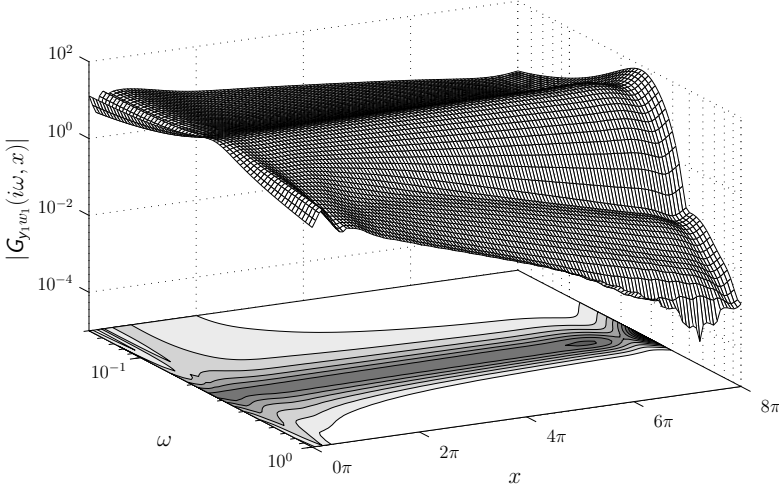


Figure 3.8: The magnitude of the spatio-temporal frequency response from the inflow disturbance w_1 to the shear along the lower wall $y_1(x, y = -1)$. The 10 contour levels lie within $|G_{y_1 w_1}| \in [6.9, 69.4]$.

domain in 3.3.3. These three controllers will also be evaluated in section 3.4 using numerical simulations of the closed-loop system.

3

3.3.1. ANALYSIS OF THE UNCONTROLLED SYSTEM

In this section the uncontrolled system from the disturbance input \mathbf{w} to the shear output \mathbf{y} , that is $\mathbf{G}_{yw} = [\mathbf{G}_{yw_1}, \mathbf{G}_{yw_2}]$ in (3.26), is analysed in the frequency domain. In particular the effect of the inflow disturbance w_1 on \mathbf{y} is investigated from an input-output viewpoint. The disturbance input w_1 excites the Orr-Sommerfeld eigenfunction calculated for the most amplified frequency ($\omega = 0.253$) at the inflow, see also section 3.2.3 and figure 3.5. The perturbation shear stress created by the disturbance along the complete lower wall, $y_1(x) = (\partial u / \partial y)(x, -1)$, is considered as output in the analysis. In this way the spatial transients created by the inflow disturbance can be evaluated and the perturbation modes that are excited can be identified. The same results hold for the upper wall due to the symmetry of the geometry. If a linear system is forced by a sinusoidal input at a particular frequency, once the initial temporal transients have died out asymptotically, the output will also be sinusoidal, at the same frequency, but with a change in amplitude and a phase shift. The magnitude amplification and phase shift of the output are equal to the magnitude and phase of the frequency response of the system. The frequency response is obtained by evaluating the transfer function on the imaginary axis, that is $s = i\omega$. The asymptotic response for the shear output along the lower wall in the spatio-temporal frequency domain is given by

$$y_1(i\omega, x) = \mathbf{G}_{y_1 w_1}(i\omega, x)w_1(i\omega), \quad (3.38)$$

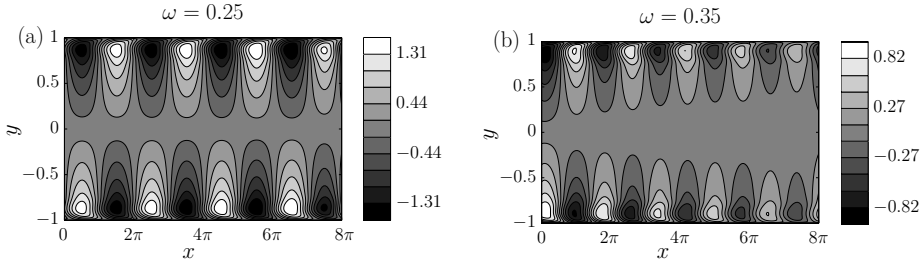


Figure 3.9: Fully developed open-loop response of the streamwise perturbation velocity for two inflow disturbance frequencies. (a) 10 levels in the range $u \in [-1.61, 1.61]$. (b) 10 levels in the range $u \in [-1.00, 1.00]$.

where $\mathbf{G}_{y_1 w_1}(i\omega, x)$ is obtained from the (1,1) element of

$$\mathbf{G}_{yw}(i\omega, x) = \mathcal{C}_2(x) (i\omega \mathbf{I} - \mathbf{A}_p)^{-1} \mathbf{B}_1. \quad (3.39)$$

$\mathbf{G}_{y_1 w_1}(i\omega, x)$ is the spatio-temporal frequency response function [79] from the inflow disturbance w_1 to the shear stress along the lower wall. It is a function of temporal frequency and streamwise direction. $\mathbf{G}_{y_1 w_1}(i\omega, x)$ is visualised using the magnitude bode plot $|\mathbf{G}_{y_1 w_1}(i\omega, x)|$ which is shown in figure 3.8. To support the interpretation of the magnitude the fully developed open-loop response for $\omega = 0.25$ and $\omega = 0.35$ is shown in figure 3.9. The effect of the low-pass filter (3.12) on the magnitude at the inflow and the amplification at the design frequency $\omega = 0.253$ can clearly be observed. After initial spatial transients near the inflow boundary, the modal perturbations are revealed and the magnitude linearly increases or decreases depending on the frequency of w_1 . At the design frequency an insignificant transient is involved for the mode to develop in the domain. Larger transients can be observed near the inflow at other frequencies than the design point. These non-modal transients do not cause a problem for control design as they have died out in the control region ($x > 2\pi$). The outflow boundary condition (3.1d) gives rise to an artificial gain near the outflow $x > 6\pi$. This does not result in reflections (wiggles) in the control domain. No special attention needs to be taken for the non-physical region as long as no measurement sensors are placed in this region. For validation purposes the exponential growth for the perturbation shear output is compared with predictions from linear stability theory. The exponential growth can be calculated using

$$\alpha_i = -\frac{1}{x_1 - x_0} \ln \frac{|\mathbf{G}_{y_1 w_1}(i\omega, x_1)|}{|\mathbf{G}_{y_1 w_1}(i\omega, x_0)|}. \quad (3.40)$$

The location of the shear sensor $x_0 = x_m = 2.39\pi$ and the location of the controlled shear output $x_1 = x_q = 5.57\pi$ are chosen to compute the growth rate. Within this region the magnitude varies linearly over a wide range of frequencies. Figure 3.10 shows the magnitude of $\mathbf{G}_{y_1 w_1}(i\omega, x)$ at the two spatial locations and the exponential growth rate of the magnitude compared with the growth rates from LST. Good agreement with LST predictions can be observed. Both the model and the OS-equation predict instability within the range $0.216 \leq \omega \leq 0.286$. The real part of the

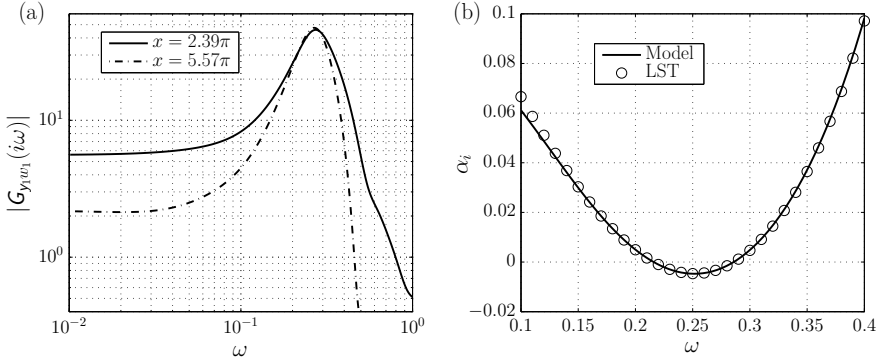


Figure 3.10: (a) Magnitude of the shear output at two x -locations and (b) resulting exponential growth (3.40) compared with the solutions of the Orr-Sommerfeld equation.

wavenumber α_r and the corresponding wavelength $\lambda_x = 2\pi/\alpha_r$ of the perturbation can be evaluated using the phase response of the system. Let $\angle \mathcal{G}_{y_1 w_1}(i\omega, x)$ be the phase in degrees for the shear output along the lower wall. The real part of the wavenumber can be calculated using

$$\alpha_r = \frac{|\angle \mathcal{G}_{y_1 w_1}(i\omega, x_1) - \angle \mathcal{G}_{y_1 w_1}(i\omega, x_0)| \frac{\pi}{180}}{x_1 - x_0}. \quad (3.41)$$

Figure 3.11 shows the phase at the two spatial locations and the resulting wavenumbers compared with the predictions from LST. It can be observed that also the wavelengths are in good agreement with LST. At $\omega = 0.25$ LST predicts a wavelength of $\lambda_x = 2\pi/\alpha_r \approx 2\pi$ and at $\omega = 0.35$ a wavelength of $\lambda_x \approx 1.6\pi$. These wavelengths can also be observed in figure 3.9.

These results verify that the single mode inflow disturbance model accurately captures the wavelengths and growth rates in a wider frequency band in the actuator/sensor region. Also at other frequencies than the design frequency, the disturbance will quickly develop in-domain to a travelling wave with a spatial wavelength and growth rate as predicted by the OS equation. It provides confidence that the followed modelling procedure allows for an efficient estimation of the dominant flow perturbations in the localised control domain using wall shear sensors. In the next section the controller is designed to reduce the magnitude of the shear downstream of the control actuators.

3.3.2. REDUCED-ORDER CONTROLLER

The reduce-then-design approach [114] is used to construct a reduced-order controller for the high-order plant. First, exact balanced truncation [67] is applied to construct a reduced-order model (ROM) of the full order system after which the ROM is used to synthesise the optimal controller. Exact balanced truncation requires dense matrix factorisations and generally results in a computational complexity of $\mathcal{O}(N^3)$ and a storage requirement of $\mathcal{O}(N^2)$. Exact balanced truncation is not computationally tractable for very large systems and approximate methods,

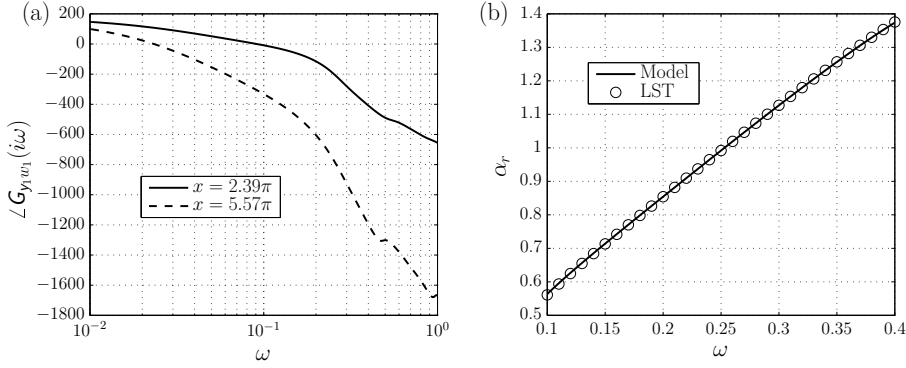


Figure 3.11: (a) Phase of the shear output at two x -locations and (b) resulting wavelength (3.41) compared with the solutions of the Orr-Sommerfeld equation.

such as proposed by Rowley [34], could be used in this case. However, the modelling approach in this chapter avoids very large systems through localised computations allowing to apply exact balanced truncation ($N = 5569$ for the control model). Since the current flow configuration is globally stable, balanced truncation can directly be applied without the need of separating the stable and unstable subspaces. Only the application of balanced truncation for model reduction and control design is discussed in this section. We refer to Moore [67] for more detail and to Kim and Bewley [6], Rowley [34] for more background in the context of flow control.

Balanced truncation extracts the most controllable and observable modes of the system and first involves creating a balanced realisation of the system such that each state has an equal measure for both controllability and observability. Let $\mathbf{G}_b(s) = (\mathcal{A}_b, \mathcal{B}_b, \mathcal{C}_b, \mathcal{D}_b)$ be a balanced realisation of the generalised plant $\mathbf{G}(s) = (\mathcal{A}_p, \mathcal{B}_p, \mathcal{C}_p, \mathcal{D}_p)$ given by (3.28) such that the controllability Gramian and observability Gramian respectively defined as

$$\mathbf{P} = \int_0^{\infty} e^{\mathcal{A}_b t} \mathcal{B}_b \mathcal{B}_b^T e^{\mathcal{A}_b^T t} dt, \quad (3.42)$$

$$\mathbf{Q} = \int_0^{\infty} e^{\mathcal{A}_b^T t} \mathcal{C}_b^T \mathcal{C}_b e^{\mathcal{A}_b t} dt \quad (3.43)$$

are given by $\mathbf{P} = \mathbf{Q} = \text{diag}(\sigma_1^H, \sigma_2^H, \dots, \sigma_N^H) =: \boldsymbol{\Sigma}$ where $\sigma_1^H \geq \sigma_2^H \geq \dots \geq \sigma_N^H \geq 0$ are the Hankel singular values of the system. An efficient algorithm for creating balanced realisations is available in Matlab (`balreal`). This algorithm computes the similarity transformation $\mathbf{u}_b^e = \mathbf{S} \mathbf{u}^e$, which balances the plant matrices through $\mathcal{A}_b = \mathbf{S} \mathcal{A}_p \mathbf{S}^{-1}$, $\mathcal{B}_b = \mathbf{S} \mathcal{B}_p$, $\mathcal{C}_b = \mathcal{C}_p \mathbf{S}^{-1}$ and $\mathcal{D}_b = \mathcal{D}_p$. The similarity transformation \mathbf{S} is obtained from the Cholesky factorisation of the Gramians [115]. The Gramians are computed by solving a set of Lyapunov equations [67]. This method is also stable if the system contains nearly uncontrollable/unobservable modes which are present in the linearised Navier-Stokes operator [6, 37]. The balanced realisation

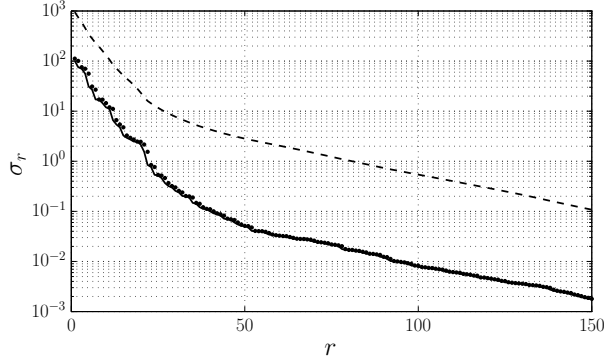


Figure 3.12: The first 150 Hankel singular values (\bullet markers), the theoretical upper bound (dashed line) and theoretical lower bound (solid line) for the maximum error of the reduced-order model.

and corresponding singular values can be partitioned as

$$\mathcal{A}_b = \begin{bmatrix} \mathcal{A}_{11} & \mathcal{A}_{12} \\ \mathcal{A}_{21} & \mathcal{A}_{22} \end{bmatrix}, \quad \mathcal{B}_b = \begin{bmatrix} \mathcal{B}_1 \\ \mathcal{B}_2 \end{bmatrix}, \quad \mathcal{C}_b = [\mathcal{C}_1 \quad \mathcal{C}_2], \quad \mathbf{\Sigma} = \begin{bmatrix} \mathbf{\Sigma}_1 & 0 \\ 0 & \mathbf{\Sigma}_2 \end{bmatrix}, \quad (3.44)$$

where $\mathbf{\Sigma}_1 = \text{diag}(\sigma_1^H, \sigma_2^H, \dots, \sigma_r^H)$ and $\mathbf{\Sigma}_2 = \text{diag}(\sigma_{r+1}^H, \sigma_{r+2}^H, \dots, \sigma_N^H)$. The reduced-order model of order r is obtained by truncating the least observable/controlable modes, that is truncating the $r+k, k=1, \dots, N-r$ modes: $\mathbf{G}_r(s) = (\mathcal{A}_{11}, \mathcal{B}_1, \mathcal{C}_1, \mathcal{D}_b) := (\mathbf{A}, \mathbf{B}, \mathbf{C}, \mathbf{D})$. Note that balanced truncation does not depend on \mathcal{D}_b and it follows that $\mathcal{D}_b = \mathcal{D}_p = \mathbf{D}$. A feature of balanced truncation is the existence of upper and lower bounds for the maximum error of the reduced-order model

$$\sigma_{r+1}^H \leq \|\mathbf{G} - \mathbf{G}_r\|_\infty < 2 \sum_{k=r+1}^N \sigma_k^H \quad (3.45)$$

with σ_{r+1}^H the first neglected Hankel singular value. Figure 3.12 shows the first 150 Hankel singular values of the system and the upper and lower bounds for the maximum error. The steep initial drop indicates that the input-output behaviour can be captured using low-order models. However, no guarantees are available about the stability and performance of a controller designed for \mathbf{G}_r on the original system \mathbf{G} and the truncated dynamics should be taken into account in the performance analysis. Therefore, instead of evaluating the performance of the ROM, the performance of the reduced-order controller in combination with the original system is evaluated for increasing order r .

The reduced-order model \mathbf{G}_r is used to synthesise the \mathcal{H}_2 optimal reduced-order controller $\mathbf{K}_r(s)$ that minimises (3.34) (See appendix B), and takes the form

$$\begin{aligned} \dot{\mathbf{u}}_K^e &= \mathbf{A}_K \mathbf{u}_K^e + \mathbf{B}_K \mathbf{y}, \\ \phi &= \mathbf{C}_K \mathbf{u}_K^e, \end{aligned} \quad (3.46)$$

with $\mathbf{u}_K^e \in \mathbb{R}^r$ the controller state. The resulting closed-loop system from the disturbance \mathbf{w} to the control objective \mathbf{z} is obtained by combining the controller

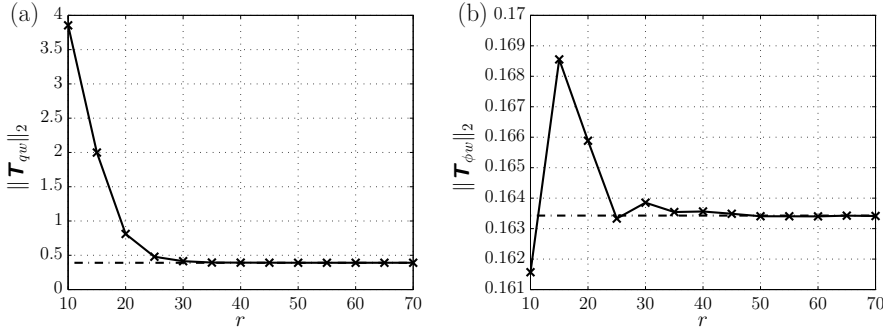


Figure 3.13: Convergence of the closed-loop system norms $\|\mathbf{T}_{qw}\|_2$ (a) and $\|\mathbf{T}_{\phi w}\|_2$ (b) versus the order r of the reduced-order controller with $l = 1$, $\gamma = 1$. The two dashed lines indicate the norms of the full order ($r = N = 5569$) controller.

(3.46) with the original system (3.33) and is given by

$$\begin{aligned} \begin{bmatrix} \dot{\mathbf{u}}^e \\ \dot{\mathbf{u}}_K^e \end{bmatrix} &= \underbrace{\begin{bmatrix} \mathbf{A}_p & \mathbf{B}_2 \mathbf{C}_K \\ \mathbf{B}_K \mathbf{C}_2 & \mathbf{A}_K \end{bmatrix}}_{\mathbf{A}_{cl}} \begin{bmatrix} \mathbf{u}^e \\ \mathbf{u}_K^e \end{bmatrix} + \underbrace{\begin{bmatrix} \mathbf{B}_1 \\ \mathbf{B}_K \mathbf{D}_{21} \end{bmatrix}}_{\mathbf{B}_{cl}} \mathbf{w}, \\ \mathbf{z} &= \underbrace{\begin{bmatrix} \mathbf{C}_1 & \mathbf{D}_{12} \mathbf{C}_K \end{bmatrix}}_{\mathbf{C}_{cl}} \begin{bmatrix} \mathbf{u}^e \\ \mathbf{u}_K^e \end{bmatrix}. \end{aligned} \quad (3.47)$$

For the design of the controller, the performance of the closed-loop system (3.47) is characterised for different combinations of control penalties l and estimation penalties γ . As in Bewley and Liu [37] a parametric study is conducted for the \mathcal{H}_2 norms of the following two closed-loop transfer functions

$$\mathbf{T}_{qw} = [\mathbf{C}_1 \quad 0] (s\mathbf{I} - \mathbf{A}_{cl})^{-1} \mathbf{B}_{cl}, \quad (3.48)$$

$$\mathbf{T}_{\phi w} = [0 \quad \mathbf{C}_K] (s\mathbf{I} - \mathbf{A}_{cl})^{-1} \mathbf{B}_{cl}, \quad (3.49)$$

which are the closed-loop transfer function matrices from the disturbance to respectively the controlled output \mathbf{q} and the control input ϕ . The definitions of the closed-loop system matrices ($\mathbf{A}_{cl}, \mathbf{B}_{cl}, \mathbf{C}_{cl}$) follow from (3.47). The \mathcal{H}_2 norms of these transfer functions are related by

$$\|\mathbf{T}_{zw}\|_2^2 = \|\mathbf{T}_{qw}\|_2^2 + l^2 \|\mathbf{T}_{\phi w}\|_2^2, \quad (3.50)$$

with $\mathbf{T}_{zw} = \mathbf{C}_{cl} (s\mathbf{I} - \mathbf{A}_{cl})^{-1} \mathbf{B}_{cl}$ the transfer function from the disturbance to the combined performance objective \mathbf{z} . A low value for $\|\mathbf{T}_{qw}\|_2$ indicates a good controller performance while a low value for $\|\mathbf{T}_{\phi w}\|_2$ indicates a low control effort. A finite value for these norms means an exponentially stable closed-loop system. Figure 3.13 shows the norms as function of the order r of the controller for the combination $\gamma = 1$, $l = 1$. The norm of the full order controller ($r = N$) is indicated by the asymptotes. It can be observed that the performance of the closed-loop

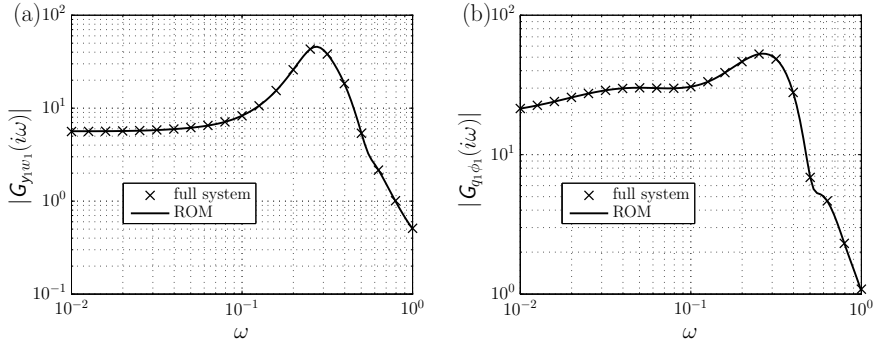


Figure 3.14: Performance of the ROM ($r = 50$). Magnitude frequency response from the state disturbance w_1 to the measured output y_1 (a) and from the control input ϕ_1 to the controlled shear output q_1 (b) at the lower wall.

system converges quickly to the case of a full order controller. Similar results were obtained for other combinations. We select $r = 50$ to design and implement the controller. With this order the performance has converged and there is no loss in performance due to the truncated dynamics. The input-output behaviour of the ROM with $r = 50$ is compared to full system in figure 3.14. Shown is the magnitude frequency response of the transfer function $G_{y_1 w_1}$ from the inflow disturbance w_1 to the measured output y_1 (a) and the transfer function $G_{q_1 \phi_1}$ from the control input ϕ_1 to the controlled output q_1 at the lower wall (b). There is a good agreement and the ROM accurately captures the input-output (disturbance and control) behaviour.

Figure 3.15 shows the contours of the \mathcal{H}_2 norms and the relative energy norm $\|\mathbf{T}_{qw}\|_2^2 / \|\mathbf{G}_{qw}\|_2^2$ for the order $r = 50$ controller. It can be observed that an energy reduction between 90% – 99% can easily be achieved by a proper choice of the design parameters. The performance for the case $l \rightarrow \infty, \gamma \rightarrow \infty$ converges to the uncontrolled case. The control penalty l can be used to tune the feedback gain \mathbf{C}_K in (3.46) and determines the trade-off between control effort and magnitude of the shear perturbation \mathbf{q} . Lower values lead to an increased controller performance (low $\|\mathbf{T}_{qw}\|_2$) at the cost of a higher control effort. It is found that choosing $l < 10$ does lead to a significantly increase in performance. The parameter γ can be used to tune the estimator, that is the output injection gain \mathbf{B}_K in (3.46). Low values for γ (high to noise ratio) lead to a higher magnitude of estimator feedback and an increased performance. However, choosing a lower value for γ leads to a reduced robustness. The role of γ is to account for uncertainties in the estimated output which also arise in the case of unmodelled dynamics and unmodelled disturbances. High estimator gain feedback can in this case result in larger overshoots which should be avoided since they can aggravate the initial stage to transition. From the contour of $\|\mathbf{T}_{qw}\|_2$ it can be observed that for a given control penalty l , the estimation penalty γ , and thus the robustness, can be increased up to the curvature of the contour level without significant loss of performance. Thus choices for l and γ on the curvature of a desired performance level can be considered as an optimal trade-off between robustness and the desired performance. In this study robustness

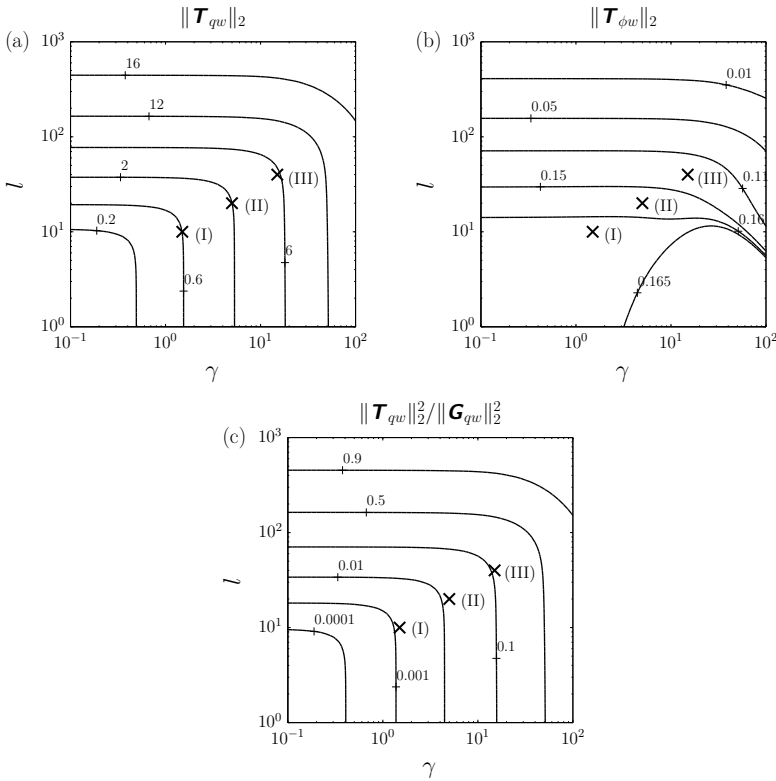


Figure 3.15: Contours of the closed-loop system norms $\|T_{qw}\|_2$ (a), $\|T_{\phi w}\|_2$ (b) and the relative energy norm $\|T_{qw}\|_2^2 / \|G_{qw}\|_2^2$ (c) with a $r = 50$ reduced-order controller for different combinations of control parameter l and estimation parameter γ ($\|G_{qw}\|_2 = 16.90$). Controllers (I) $l = 10, \gamma = 1.5$, (II) $l = 20, \gamma = 5$ and (III) $l = 40, \gamma = 15$ are considered for evaluating the closed-loop response of the system.

is valued more than control effort in determining the trade-off. Three controllers will be investigated in the next sections for evaluating the performance in the frequency domain and through numerical simulation. The design parameters for the controllers are marked in figure 3.15. The first (I) is a high gain controller with $l = 10, \gamma = 1.5$ corresponding to approximately a 99.9% energy reduction. The second (II) is an intermediate controller with $l = 20, \gamma = 5$ corresponding to a 99% energy reduction and the third (III) is a lower gain controller with $l = 40, \gamma = 15$ corresponding to a 90% energy reduction.

3.3.3. CLOSED-LOOP FREQUENCY RESPONSE

In this section the three selected controllers are evaluated in the frequency domain. The magnitude frequency response from w_1 to the controlled output q_1 (3.7) is shown in figure 3.16. The magnitude of the closed-loop system $T_{q_1 w_1}$ is compared with the magnitude of the open-loop system $G_{q_1 w_1}$. The frequency domain performance for

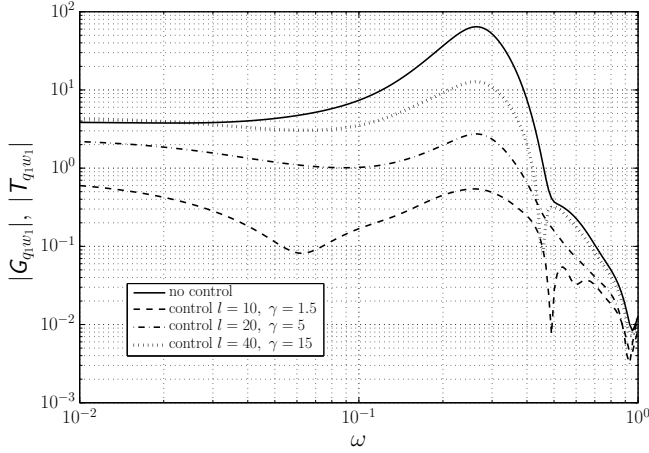


Figure 3.16: Closed-loop frequency response from the inflow disturbance w_1 to the controlled output q_1 along the lower wall.

the three controllers is in accordance with the results in figure 3.15. Controller (III) limits the control effort and takes higher levels of sensor inaccuracies into account. It is more conservative also with respect to higher frequencies. The three controllers significantly suppress the most amplified frequencies close to the design frequency $\omega = 0.253$ as well as the off-design frequencies. The peak magnitude is equal to the \mathcal{H}_∞ norm of $T_{q_1 w_1}$ which is reduced between approximately 80% – 99% for the three controllers.

The perturbation shear reduction along the complete walls, as well as spatial transients introduced by the control can be evaluated using the spatio-temporal frequency response. Figure 3.17 shows the magnitude for the shear along the lower wall for the open-loop system (a) and closed-loop (b) system with controller (II). Compared to the open-loop magnitude it can be observed that the controller significantly reduces the shear in the entire downstream region of the control actuators. The magnitude at the most dominant frequencies $0.1 \leq \omega \leq 0.4$ is significantly suppressed and only small amplifications are present in the region of the control actuator.

3.4. CLOSED-LOOP SIMULATIONS

In this section the effectiveness of the proposed control design is evaluated using linear simulations of the closed-loop system. The three controllers characterised by (I) $l = 10, \gamma = 1.5$, (II) $l = 20, \gamma = 5$ and (III) $l = 40, \gamma = 15$ are again considered, see also figure 3.15. The model defining a channel with a total length of $L_{sim} = 16\pi$, as discussed in section 3.2.5, is used for simulating the response. Disturbances are generated upstream of the control domain and propagate downstream. Three different disturbance cases are considered to demonstrate the robustness of the control design. In the first case (Case A, section 3.4.1), a single-frequency perturbation is

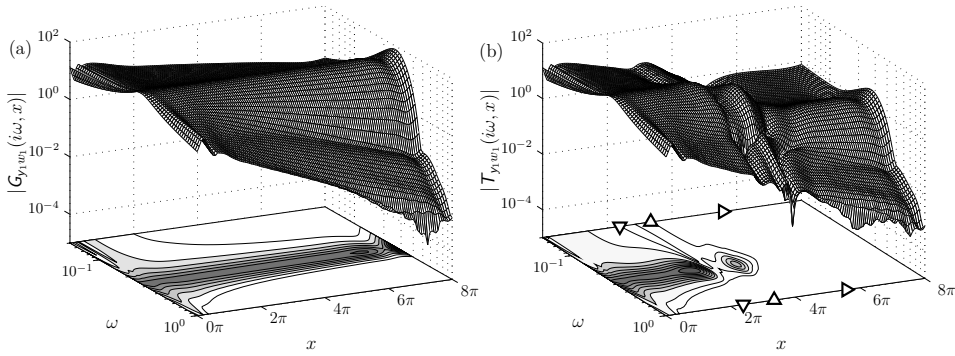


Figure 3.17: Open loop (a) and closed-loop (b) magnitude frequency response from the inflow disturbance w_1 to the shear stress ν_1 along the lower wall. The 10 contour levels lie within $|\mathcal{G}_{y_1 w_1}|, |\mathcal{T}_{y_1 w_1}| \in [6.9, 69.4]$ ($l = 20, \gamma = 5$). The triangles indicate respectively the position of the measurement sensors (∇), the actuators (\triangle) and the controlled outputs (\triangleright).

considered which is generated using the disturbance model presented in section 3.2. This case can be seen as the design case, since the same disturbance model is used for both simulation and control design. In the second test case (case B, section 3.4.2) a multiple-frequency disturbance is considered in the form of a wave-train consisting of a linear combination of Orr-Sommerfeld modes. This case is used to verify the spatio-temporal frequency domain results in the previous section and to test if the controller based on the single mode inflow disturbance model indeed allows for efficient estimation and control of perturbations in a wider frequency band. In the third test case (case C, section 3.4.3) the controller is evaluated for a stochastic excited body force located at the upper wall. Similar body forces have been used by Bagheri *et al.* [33], Dadfar *et al.* [109] to evaluate controllers for transition delay. The case is used to study the effectiveness of the controller in a transient unmodelled environment.

For simulating the response, the original unscaled system (3.24) is considered. For the design of the controller no a priori knowledge is assumed about the expected covariances σ_d^2 and σ_n^2 of respectively the state and measurement disturbances. Therefore, a scaling is introduced in terms of an expected relative magnitude of the sensor noise $\gamma = \sigma_n/\sigma_d$. γ plays a role for accounting measurement uncertainties in the control design and is not used for defining the measurement noise in the simulations. We also wish to investigate the robustness of the three controllers with respect to unmodelled measurement inaccuracies. Therefore each disturbance case is considered with both a low sensor noise $\sigma_n = 0.01$ and a high sensor noise $\sigma_n = 0.2$. In total 18 different cases were simulated: three disturbance cases (A,B,C) with three controllers and two sensor noise intensities. The cases and the results are summarised in table 3.1 and are discussed in more detail in the next three sections.

3.4.1. CASE A: SINGLE-FREQUENCY DISTURBANCE

In the first case a single-frequency modal disturbance, of the form (3.9), is considered with $\omega = 0.253$ which has the maximum growth rate for the investigated

Case	Control penalty l	estimation penalty γ	Shear energy reduction $\ q_{con}\ _2^2/\ q_{unc}\ _2^2$	control effort rms ϕ
A1.I	10	1.5	0.000088	0.002404
A2.I	10	1.5	0.001521	0.002398
A1.II	20	5	0.001940	0.002319
A2.II	20	5	0.003669	0.002312
A1.III	40	15	0.041873	0.001932
A2.III	40	15	0.044999	0.001924
B1.I	10	1.5	0.000112	0.001064
B2.I	10	1.5	0.007609	0.001091
B1.II	20	5	0.002147	0.001023
B2.II	20	5	0.007735	0.001045
B1.III	40	15	0.048270	0.000840
B2.III	40	15	0.047928	0.000855
C1.I	10	1.5	0.027664	0.001026
C2.I	10	1.5	0.038694	0.001017
C1.II	20	5	0.030085	0.000985
C2.II	20	5	0.041530	0.000972
C1.III	40	15	0.078881	0.000806
C2.III	40	15	0.092690	0.000791

Table 3.1: The controlled shear output energy reduction and the control effort for three controllers. Three disturbance cases (A, B, C) are considered with both a low sensor noise (A1, B1, C1) and with a high sensor noise (A2, B2, C2). Each case is evaluated using three controllers (A1.I, A1.II, A1.III). Disturbance case A-C corresponds respectively to the single-frequency disturbance, Multiple-frequency disturbance and stochastic in-domain forcing. (rms $\phi = \sqrt{\frac{1}{T} \int_0^T |\phi|^2 dt}$)

conditions. This disturbance is generated at the inlet $x = -4\pi$ of the simulation domain using the disturbance model presented in section 3.2.3. The shape of the disturbance corresponds to the eigenfunction calculated from the Orr-Sommerfeld equation at $\omega = 0.253$ (see figure 3.5). To mimic the transitional regime in the simulations the amplitude of the perturbation is set to $A_0 = 0.01$. First the performance of controller (II) with $l = 20$, $\gamma = 5$ and a low sensor noise $\sigma_n = 0.01$ is investigated. Figure 3.18 shows the temporal evolution of the shear measurements \mathbf{y}_m that are used for feedback, the control input ϕ (amplitude of the blowing and suction), the perturbation energy ($E = \|\mathbf{u}\|_{L^2}^2$) and the norm of the controlled output $\|\mathbf{q}\|_2$. \mathbf{q} reflects the controller performance as it is used within the control objective that is minimised by the controller, see (3.29). As the perturbation convects downstream towards the control region, the amplitude of blowing and suction increases to cancel the perturbation. The effect of the noise on the shear measurements can be observed and the resulting control input confirms the filtering and feedback of these measurements. Both control actuators at the upper and lower wall act in phase which is to be expected due to the symmetry of the geometry and the control layout. A snapshot at $t = 200$ of the flow perturbation field in the control domain $x \in [0, 8\pi]$ is shown in figure 3.19. The performance of the state estimation is best visualised without control applied. Figure 3.19(a) shows the estimated flow field without control, figure 3.19(b) shows the real flow field without control and figure 3.19(c) shows the real controlled flow. The estimated flow field is computed from the controller state \mathbf{u}_K^e through $\mathbf{u}_K^e \mapsto \mathbf{S}_r^{-1} \mathbf{u}_K^e$ where \mathbf{S}_r^{-1} are the first r columns of the inverse of the similarity transformation as discussed in section 3.3.2. It can be seen that

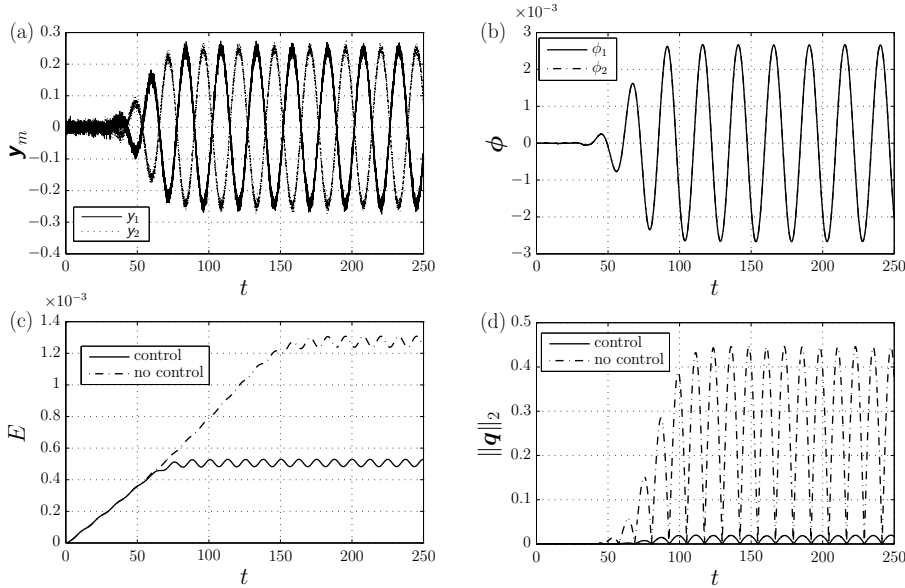


Figure 3.18: Closed-loop performance for the single-frequency disturbance case. Controller (II) with low sensor noise is considered. (a) Shear measurements \mathbf{y}_m used for feedback. (b) Control input ϕ (amplitude of the blowing and suction). (c) Perturbation energy $E = \|\mathbf{u}\|_{L^2}^2$. (d) Norm of the controlled perturbation shear output $\|\mathbf{q}\|_2$.

the flow perturbations are well reconstructed in the control region where the measurements are taken, actuation is applied and where the performance objective \mathbf{q} is defined. As a result the controller is effective in cancelling the perturbations by minimising the effect of the perturbation on \mathbf{q} . Only low-amplitude oscillations remain. The required amplitude of the blowing and suction is of the same order as the magnitude of the perturbation as can be seen in the snapshot for the wall-normal velocity component in figure 3.19(c).

To compare the performance of the three controllers, the spatial evolution of the perturbation is evaluated. We define the amplitude of the streamwise velocity perturbation as

$$A(x) = \max_{t,y} \sqrt{|u|^2}. \quad (3.51)$$

Figure 3.20 shows the amplitude for the three controllers with both low ($\sigma_n = 0.01$) and high ($\sigma_n = 0.2$) measurement noise. The amplitude reduction for the three controllers is in accordance with the frequency domain results in figure 3.16. The controllers are also robust to higher levels of sensor noise. Controller (III) takes higher sensor inaccuracies into account and the performance is preserved in the case of high sensor noise, see also table 3.1. Controllers (I) and (II) do not take such high measurement noise into account and the performance is less preserved. However, no severe deterioration can be observed. This can also be contributed to the simple structure of the perturbation.

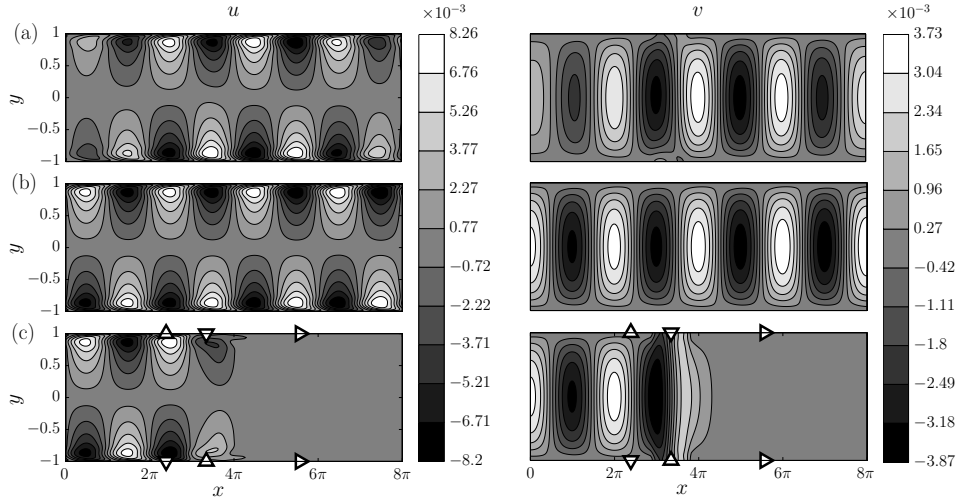


Figure 3.19: Snapshot of the perturbation velocity within the control domain $x \in [0, 8\pi]$ at $t = 200$ for the uncontrolled and controlled single-frequency ($\omega = 0.253$) disturbance. Controller (II) with low sensor noise is considered. (a) Estimated velocity without control. (b) True velocity without control. (c) True velocity with control. The triangles indicate respectively the position of the measurement sensors (∇), the actuators (Δ) and the controlled outputs (\triangleright).

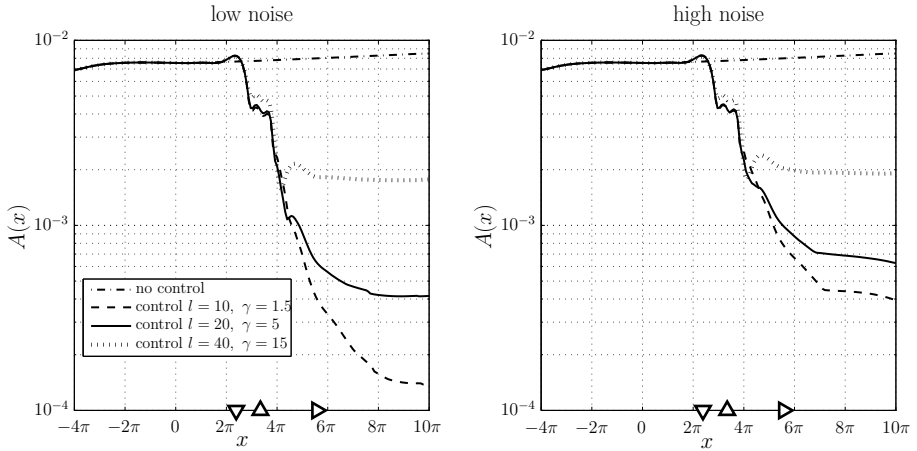


Figure 3.20: The maximum amplitude of the streamwise perturbation velocity (3.51) of the single-frequency disturbance for three controllers. (a) Feedback with low measurement noise $\sigma_n = 0.01$. (b) Feedback with high measurement noise $\sigma_n = 0.2$. The triangles indicate respectively the position of the measurement sensors (∇), the actuators (Δ) and the controlled outputs (\triangleright).

3.4.2. CASE B: MULTIPLE-FREQUENCY DISTURBANCE

In the second test case a multiple-frequency disturbance is considered. The total disturbance consists of a linear combination of Orr-Sommerfeld modes. In total 16 modes in the frequency range $\omega \in [0.1, 0.4]$ are excited. Thus the disturbance is generated using 16 eigenfunctions whose shape corresponds to the eigenfunction

Frequency ω	wavelength α_r	growth rate α_i
0.10	0.5611	0.0666
0.12	0.6247	0.0511
0.14	0.6843	0.0369
0.16	0.7418	0.0242
0.18	0.7982	0.0134
0.20	0.8541	0.0049
0.22	0.9095	0.0010i
0.24	0.9646	-0.0042
0.26	1.0193	-0.0044
0.28	1.0735	-0.0015
0.30	1.1270	0.0047
0.32	1.1797	0.0145
0.34	1.2314	0.0281
0.36	1.2817	0.0469
0.38	1.3300	0.0687
0.40	1.3757	0.0971

Table 3.2: Spectrum of the multiple-frequency wave packet for case B.

calculated from the Orr-Sommerfeld equation at the selected frequencies. The temporal frequencies, the spatial wavelengths and spatial growth rates of these modes are listed in table 3.2. The spectrum includes 3 convectively unstable modes and 13 stable modes. Each mode is given the same amplitude $A_0 = 0.002$ such that the total disturbance is in the form of a wave-train that is modulated as it propagates downstream. First the performance of controller (II) with a low sensor noise $\sigma_n = 0.01$ is again investigated. The input-output signals and the closed-loop performance are shown in figure 3.21 and a snapshot at $t = 200$ of the perturbation field in the control domain is shown in figure 3.22. The modulation of the perturbation can clearly be observed and the perturbation presents a richer structure as compared to the single-frequency case. With respect to the closed-loop performance the same observations can be made. The measurements are successfully filtered and the real flow is reconstructed well in the control domain as can be seen in figure 3.22. The controller is again able to cancel the perturbations and to suppress the perturbation wall shear stress. Although the unstable modes are dominant in the simulations, the (nearly) stable modes have not damped out and are still present as can be seen in figure 3.22. Nevertheless, the controller achieves nearly a full cancellation of the perturbations. This corroborates the findings of the input-output analysis presented in section 3.3.1 showing that the single mode disturbance model accurately captures the spatial wavelength and spatial growth of perturbations in a wider frequency band in the actuator/sensor region. As such the controller is able to effectively estimate and control a broader frequency spectrum of modes. To compare the performance of the three controllers, the spatial evolution of the perturbation is again evaluated. Since the amplitude of the perturbation also varies in time a measure for the time averaged amplitude is defined

$$\bar{A}(x) = \max_y \sqrt{\frac{1}{T} \int_0^T |u|^2 dt}, \quad (3.52)$$

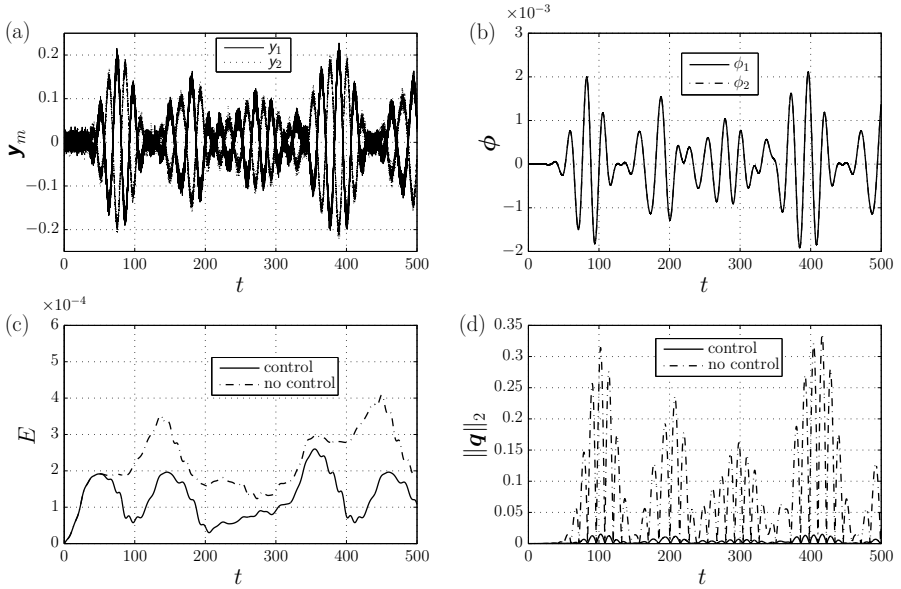


Figure 3.21: Closed-loop performance for the Multiple-frequency disturbance case. Controller (II) with low sensor noise is considered. (a) Shear measurements \mathbf{y}_m used for feedback. (b) Control input ϕ . (c) Perturbation energy $E = \|\mathbf{u}\|_{L^2}^2$. (d) Norm of the controlled perturbation shear output $\|\mathbf{q}\|_2$.

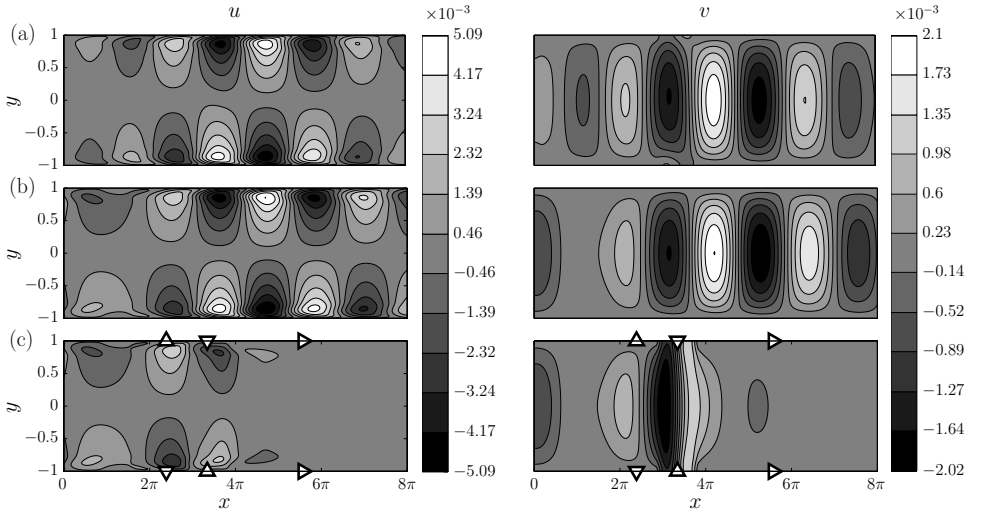


Figure 3.22: Snapshot of the perturbation velocity within the control domain $x \in [0, 8\pi]$ at $t = 200$ for the uncontrolled and controlled Multiple-frequency disturbance. Controller (II) with low sensor noise is considered. (a) Estimated velocity without control. (b) True velocity without control. (c) True velocity with control. The triangles indicate respectively the position of the measurement sensors (∇), the actuators (Δ) and the controlled outputs (\triangleright).

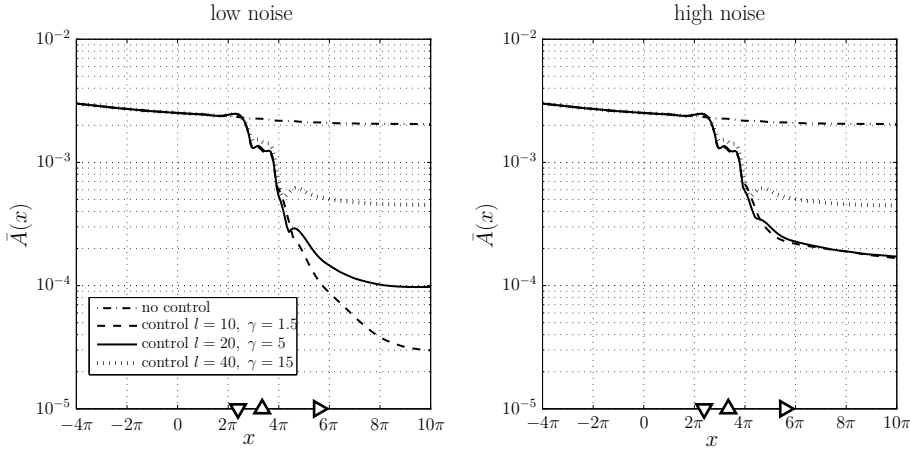


Figure 3.23: The wall-normal maximum amplitude of the rms streamwise perturbation velocity (3.52) of the Multiple-frequency disturbance for three controllers. (a) Feedback with low measurement noise $\sigma_n = 0.01$. (b) Feedback with high measurement noise $\sigma_n = 0.2$. The triangles indicate respectively the position of the measurement sensors (∇), the actuators (Δ) and the controlled outputs (\triangleright).

which is the wall-normal maximum amplitude of the root mean square (rms) streamwise velocity perturbation [116]. Figure 3.23 shows the time averaged amplitude for the three controllers with both low and high measurements noise. It can be observed that the amplitude reduction in case of high measurement noise for controller (I) is reduced more significantly. This is to be expected since the controller does not take high measurement inaccuracies into account. However, it still achieves a robust performance. Actually controller (I) and (II) have a comparable performance, see also table 3.1. This indicates that there is no large sensitivity in the choice of design parameters in case of high sensor noise. Again, the performance of controller (III) is preserved and is in accordance with its design.

3.4.3. CASE C: STOCHASTIC IN-DOMAIN FORCING

In the third most challenging test case a stochastic in-domain forcing is considered which is generated at the upper wall near the inflow. In this case the momentum equation is forced with

$$\mathbf{f}(x, y, t) = \mathbf{F}(x, y)w(t), \quad (3.53)$$

where $w(t)$ is zero mean white noise with a normal distribution at unit intensity. The spatial distribution of the 'vibrating ribbon' at the upper wall ($y = 1$) corresponds to that of Bertolotti *et al.* [117] and has the form $F_x = \partial\psi/\partial y$, $F_y = -\partial\psi/\partial x$ with

$$\psi(x, y) = \epsilon \exp\left(-\frac{(x - x_r)^2}{\sigma_x^2} - \frac{(y - 1)^2}{\sigma_y^2}\right) (y - 1)^2 \cos((x - x_r)), \quad (3.54)$$

where $\epsilon = 0.5$ is the amplitude of the force, $\sigma_x = 1$, $\sigma_y = 0.1$ the spatial lengths, $x_r = -3\pi$ the x -position of the ribbon. The spatial distribution of this force is shown

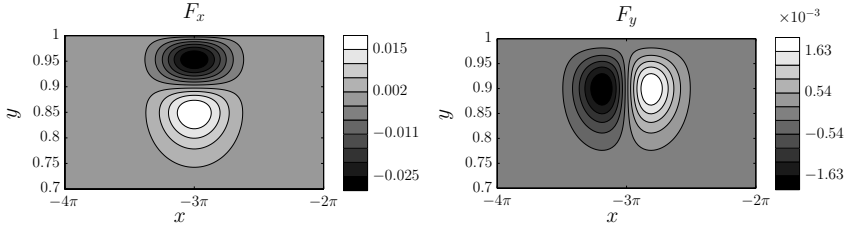


Figure 3.24: Contours of the spatial distribution $\mathbf{F} = [F_x, F_y]^T$ of the in-domain disturbance used for Case C.

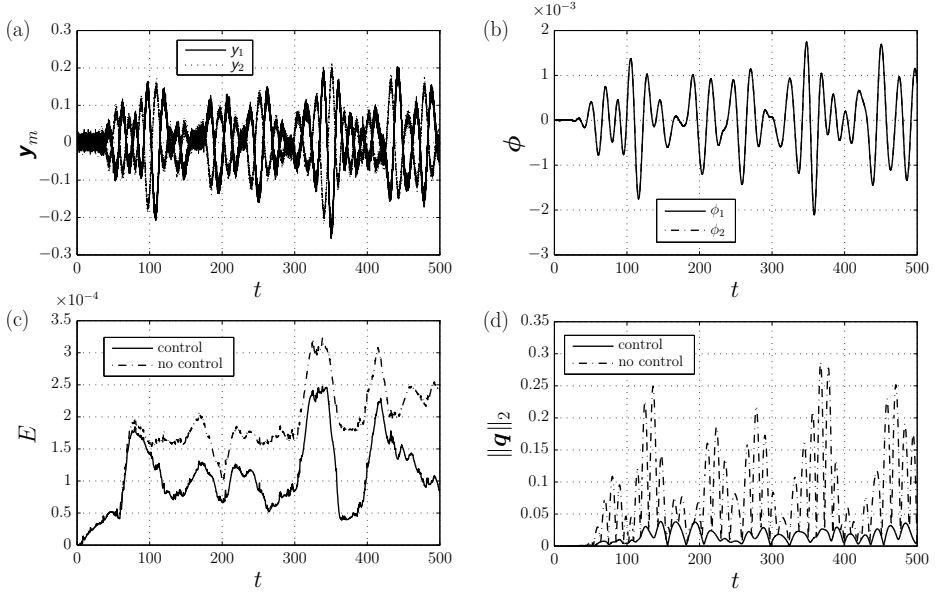


Figure 3.25: Closed-loop performance for the stochastic disturbance case. Controller (II) with low sensor noise is considered. (a) Shear measurements \mathbf{y}_m used for feedback. (b) Control input ϕ . (c) Perturbation energy $E = \|\mathbf{u}\|_{L^2}^2$. (d) Norm of the controlled perturbation shear output $\|\mathbf{q}\|_2$.

in figure 3.24. The body force (F_x, F_y) is both divergence free and satisfies the no-slip boundary conditions. First the performance of controller (II) with a low sensor noise is investigated. The input-output signals and the closed-loop performance are shown in figure 3.25 and a snapshot at $t = 350$ of the perturbation field in the control domain is shown in figure 3.26. In addition, to better visualise the evolution of the perturbation and the controller performance, the temporal evolution for the shear stress along the lower wall for the uncontrolled case and the controlled case is shown in figure 3.27.

The stochastic disturbance excites a spectrum of frequencies which results in large initial transients after which the disturbance develops in the form of wavepackets as can be seen in the energy plot in figure 3.25. The transients can also be observed

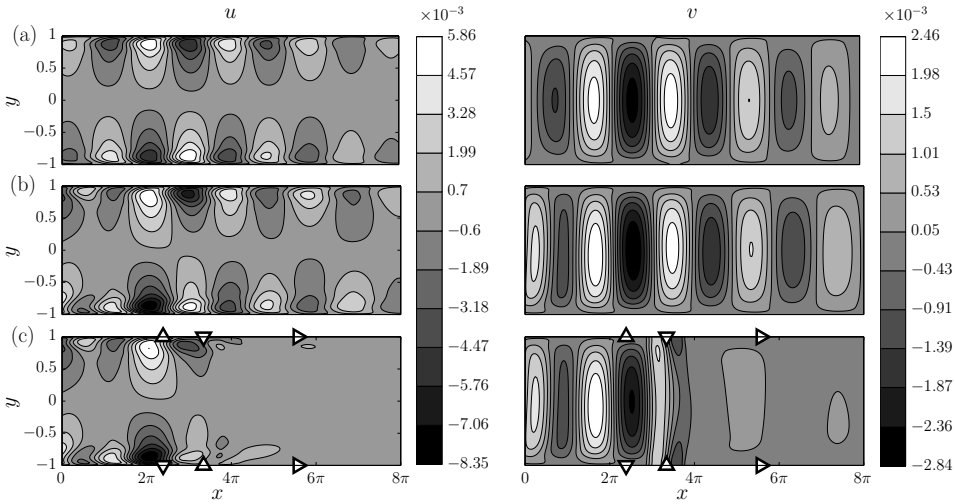


Figure 3.26: Snapshot of the perturbation velocity within the control domain $x \in [0, 8\pi]$ at $t = 350$ for the uncontrolled and controlled stochastic disturbance. Controller (II) with low sensor noise is considered. (a) Estimated velocity without control. (b) True velocity without control. (c) True velocity with control. The triangles indicate respectively the position of the measurement sensors (∇), the actuators (Δ) and the controlled outputs (\triangleright).

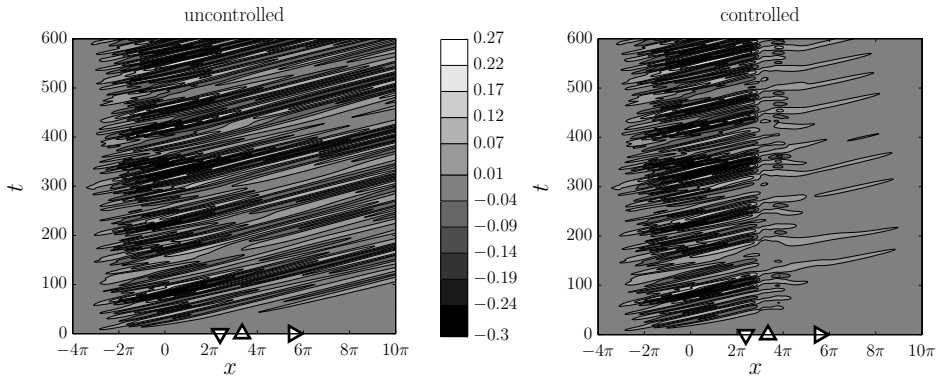


Figure 3.27: Temporal evolution of the wall shear stress $\partial u/\partial y$ along the bottom wall of the channel for the stochastic forced disturbance. The triangles indicate respectively the position of the measurement sensors (∇), the actuators (Δ) and the controlled outputs (\triangleright).

in the temporal evolution of the wall shear stress in figure 3.27 and are also present in the control region. It can be observed that the controller is still able to properly estimate the flow field and is effective in both minimising the wall shear stress and reducing the perturbation energy in the domain. Although a complete cancellation of the disturbance is not possible, the controller manages to achieve a reduction of 97% in the controlled shear output power, see also table 3.1. Note that the disturbance is completely independent of the disturbance model used to design the controller. It is defined in-domain and creates initially asymmetric developing per-

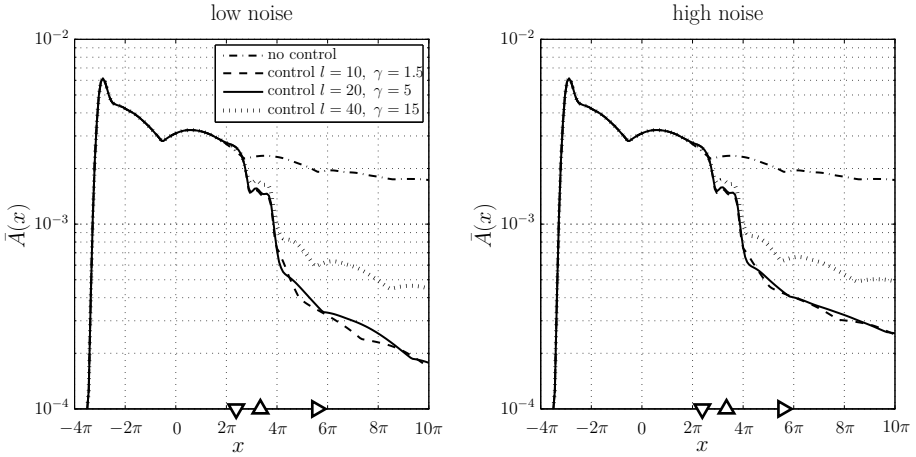


Figure 3.28: The wall-normal maximum amplitude of the rms streamwise perturbation velocity (3.52) of the stochastic forced disturbance for three controllers. (a) Feedback with low measurement noise $\sigma_n = 0.01$. (b) Feedback with high measurement noise $\sigma_n = 0.2$. The triangles indicate respectively the position of the measurement sensors (∇), the actuators (Δ) and the controlled outputs (\triangleright).

turbations while the complete input-output layout is symmetric. Furthermore the transients are not accounted for in the control design and the perturbations are not fully developed in the control domain. Nevertheless, the controller achieves a high level of robustness to unmodelled disturbances; no overshoots can be observed in the perturbation energy and the controlled output, and the controller does not aggravate the flow. This can be contributed to the fact that the controller is able to estimate and stabilise the underlying modes that are present in the disturbance as can be seen from figure 3.26.

Figure 3.28 shows the time-averaged amplitude for the three controllers with both low and high measurements noise. It can be observed that controllers (I) and (II) have comparable performance, also for the low sensor noise case. This can be contributed to the fact that uncertainties in output measurements also arise due to the unmodelled disturbances. This indicates that there is also no large sensitivity in the choice of design parameters in case of unmodelled disturbances.

3.5. CONCLUSIONS

The chapter presented a new framework to design and synthesise \mathcal{H}_2 optimal controllers for control of linear instabilities in 2-D laminar wall-bounded shear flows. The 2-D non-periodic channel flow is considered as a case study. The flow modelling accounts both for localised actuation/sensing and the dominant perturbation dynamics in physical space. A new inflow disturbance model is presented for external sources of excitation. This model allows for an efficient estimation of the flow perturbations in the localised control domain using wall shear sensors. The perturbation modes that contribute to transition can be selected and are included

in the control design. In this way the most dominant modes of the flow can be precisely targeted by the controller. A reduced-order model ($r = 50$) that captures the input-output behaviour is derived directly from the linearised Navier-Stokes equations using exact balanced truncation. No numerical simulations are required to synthesise the controller. The reduced-order model is used to design an \mathcal{H}_2 optimal controller to minimise the wall shear stress created by the perturbations. It is shown that there is no loss in performance due to the truncated dynamics and the reduced-order controller maintains the closed-loop performance as compared to the full order controller. The controller is evaluated with linear simulations of the closed-loop system. Three different disturbance cases are considered to evaluate the effectiveness and robustness of the proposed control design. It is shown that the controller is able to cancel the perturbations and is robust to both unmodelled disturbances and sensor inaccuracies.

The modelling presented in this chapter provides an efficient means to design and synthesise controllers directly from the governing equations. This can be contributed to the fact that the aim is to capture the input-output behaviour for localised sensors and actuators, and the dominant perturbation dynamics within this localised region. It is shown that with the new inflow disturbance model only minor spatial transients are involved for the perturbation modes to develop in the domain. This allows an arbitrary placement of the computational inflow boundary as it does not affect the spatial length scales of the perturbations in the control region. Small computational domains can thus be used to create the control models. Furthermore, to achieve effective control it is not required to fully resolve the flow at all length scales in the initial model. Only the dominant modes that contribute to transition and are included in the control design should be accurately resolved. These features can make the extension to three dimensions computationally feasible. Transition in 3-D flows is also governed by algebraic growth of non-modal perturbations, which bypasses the classical transition scenario considered in this study. To effectively apply this method to 3-D flows requires the inclusion of multiple perturbation modes at different wavenumbers in the disturbance model or the use of optimal inflow perturbations, e.g. of the form presented in Andersson *et al.* [116].

Significant work remains to be done to apply this method in experiments. In the next chapter this method is extended for control of Tollmien-Schlichting waves in spatially developing boundary layer flows, which is the first step towards the experimental validation of this method in the wind tunnel (Chapter 5). Future work will focus on the application for efficient modelling and control of 3-D disturbances. This chapter focussed on optimal control and no other model uncertainties, such as input/actuator uncertainties and uncertainties in the Reynolds number were addressed. Recently in Fabbiane *et al.* [87] it is shown through experiments that deviations from the design conditions can destabilise optimal controllers. Future work will also focus on addressing model uncertainties by integrating this method in a \mathcal{H}_∞ robust control framework.

4

Estimation and control of TS waves in Falkner-Skan boundary layers

This chapter investigates the use of point wall pressure measurements for dynamic estimation and control of Tollmien-Schlichting (TS) waves in Falkner-Skan boundary layers. A new approach is presented for input-output modelling of the linear dynamics of the fluid system and the integration with \mathcal{H}_2 /LQG reduced-order control design. The input-output relation between the external velocity perturbations and the pressure fluctuation at the wall is derived directly from the governing equations. A Kalman filter is used to obtain time-resolved estimates of the velocity field using pressure information at a single point on the wall. The estimated field is in turn used to calculate an optimal feedback control to suppress the instabilities. The controllers are evaluated for localised optimal perturbations that convect downstream (TS waves). Robustness to variations in the Reynolds number and pressure gradient is analysed. It is shown that the controller is able to reduce the peak energy with more than 99% for the nominal designed case. In the case of small parameter variations (< 25%) a reduction of more than 90% is shown and in case of large parameter variations (> 50%) a reduction of more than 50% is shown.

This chapter is under review in AIAA journal as: H.J. Tol, M. Kotsonis and C.C. de Visser, *Estimation and control of TS waves in Falkner-Skan boundary layers*, 2018

4.1. INTRODUCTION

Advances in actuator and sensor technologies that can sense/manipulate fluid flows on very short time and length scales have motivated the field of closed-loop flow control. In closed-loop control real-time sensor information is used to devise controls that alter the flow towards a desired state. In practice, measurements are non-ideal (noisy) and available only in a small portion of the system. Dynamic estimation strategies filter the available information using the governing equations, to extract the signal and to reconstruct the state of the system. The estimated state can subsequently be used within a state feedback control law. The combination of model-based estimation and control has gained significant attention for flow control [6, 7, 9] and is commonly referred to as an output feedback controller or a dynamic compensator [33, 82, 84, 109, 118]. In this study, pressure-based compensators are designed to delay laminar-turbulent transition triggered by two-dimensional Tollmien-Schlichting (TS) wavepackets in laminar Falkner-Skan flows. The compensator approach in this study can be classified as a white box/gray box approach in which the model is a-priori based on the physics of the system, in this case the linearised Navier-Stokes equations (LNSE). Such model-based techniques provide important insights into the instability mechanisms that have to be addressed and potentially lead to the best possible performance with stability guarantees. For a recent and extensive review on control of transition and turbulence, also including so-called black-box and model-free approaches, the reader is referred to Brunton and Noack [8].

Two crucial aspects to achieve practical implementation of compensators are the computational cost for real-time application and the integration of physically realizable actuators/sensors that are localised in space. To address these aspects, reduced-order models (ROM) have been extensively used in the design of compensators. Many techniques are available for model reduction of fluid flows which commonly involve the projection of the high-order system on a lower dimensional subspace. We refer to [32] for a recent review on model reduction methods for flow analysis and control. It is accepted that for control design purposes, projection on controllable and observable subspaces, formed by so-called balanced modes, produces the most reliable models with superior performance [32, 89, 100, 101]. Balanced truncation [67] is widely used in control theory to extract the most controllable and observable modes of the system. However, exact balanced truncation is computationally intractable for high-order systems, e.g. if $n > 10^5$. For flow control purposes snapshot-based (white box) balanced truncation [34] and input-output-based (black-box) truncation using the eigensystem realization algorithm (ERA) [90, 107] are widely used. Both aim to construct approximate balanced reduced-order models that capture the input-output behavior of the system, similar to exact balanced truncation.

To account for spatially localised actuators/sensors in the control design, Bagheri *et al.* [33] were the first to rigorously combine balanced model reduction with \mathcal{H}_2 /LQG closed-loop control for convective instabilities in 2-D boundary layer flows. The control design considered the use of in-domain volume forcing actuation and in-domain velocity measurements. This approach was extended in Bagheri *et al.*

[105] to include wall shear measurement and wall actuation by means of localised suction and blowing. A generalization of the work of Bagheri *et al.* [33] to 3-D flows is presented in Semeraro *et al.* [92] and was applied by Semeraro *et al.* [85] in fully non-linear simulations to verify the possibility of delaying transition to turbulence using velocity measurements and volume forcing actuation. Limitations related to a more realistic set-up were addressed by Dadfar *et al.* [109, 119] for 2-D boundary layer flows. They integrated experimentally identified models of plasma actuators and physical actuator constraints were taken into account in the control design. Using plasma actuators and hot-wire velocity measurements Fabbiane *et al.* [87] demonstrated, for the first time, suppression of disturbances in wind-tunnel experiments using 2-D model-based LQG compensators, without any model fitting or system identification.

Currently, localised (white/gray) model-based compensators for transition delay have either used velocity measurements or shear measurements for estimation of the perturbation field. Although, hot wire anemometry and hot film sensors can be effective for closed-loop control [87, 120], they can become problematic in practice. Hot wires are intrusive and the wires can break easily. Wall shear stress sensors are placed on the wall, but generally have a low signal to noise ratio, are not robust (temperature dependent, high mechanical stresses) and uncertainties are hard to quantify [121]. Pressure measurements on the other hand generally have a high signal-to-noise ratio and can be extracted remotely from the surface, e.g. using microphones embedded within a small cavity. The cavity does result in a loss of amplitude and phase and gives rise to Helmholtz resonances, which has to be accounted for.

Pressure measurements are commonly considered for control of global instabilities in free shear layer flows involving flow-induced noise/vibrations and flow-structure interaction. We refer to Cattafesta *et al.* [5] for an extensive review on control of flow-induced cavity oscillations. Different variants (linear, quadratic, higher order) of static estimators, also known as stochastic estimation (SE) as originally introduced by Adrian [122], have been successfully applied for control in cavity flows [88, 123] and axisymmetric jets [124]. We refer to Lasagna *et al.* [125] for a recent overview of the SE technique, both for investigating the flow physics and the control applications. With SE the state estimate is represented by a static function of the sensors and the state estimate depends only on the measurements at the present time. This technique does not require a model, but requires a larger number of sensors, and is more sensitive to noise than dynamic model-based observers, such as the Kalman filter [5, 34, 124, 126]. Owing to the need for a ROM of the flow dynamics, preferably balanced, that relate the point pressure measurements with the model variables, dynamic state estimation is challenging. Models used for dynamic estimation/control which are based solely on the physics of the system have been obtained through POD/Galerkin projection in Sinha *et al.* [124], Rowley and Juttijudata [127], and balanced models from input-output data (black-box) using ERA have been obtained in Illingworth *et al.* [108, 128] for feedback control of flow resonances.

Pressure sensors provide significant advantages over velocity or shear stress sen-

sors in experimental applications. However, no attempt has yet been made to integrate point pressure measurements in the framework of (white/gray) model-based estimation and control for convective instabilities in boundary layer flows. This is the goal of the present study. The main contribution of this chapter is a new approach for the input-output modelling of the *linear* dynamics and the integration with \mathcal{H}_2 /LQG reduced-order controller design. To the best of our knowledge this is the first time that a localised pressure-based compensator is derived directly from the governing equations which is used to control instabilities in boundary layer flows. The use of pressure measurements for dynamic flow estimation is not trivial. Two fundamental challenges have been identified and addressed in this study.

1) For modelling of wall-bounded shear flows, the pressure is commonly eliminated from the state equations (also in this study) by formulating the linearised Navier-Stokes equations in a divergence free state-space, see e.g. Bagheri *et al.* [33], Semeraro *et al.* [92], Bagheri *et al.* [105] and we refer Bewley *et al.* [129] for a general framework. Due to the fact that pressure is eliminated from the model, estimation for correlating the model variables to the pressure measurements becomes less trivial.

2) Wall-bounded shear flows behave as noise amplifiers that support convective instabilities in broadband frequency spectrum. Amplifier flows are highly sensitive to upstream external disturbances and there is only a small window in time to suppress the convective instabilities. Accurately modelling the effect of upstream disturbances is crucial as it forms the basis for estimation and control of the flow perturbations in the control domain [33, 130]. Since the fluctuating pressure at a given point on the wall is related to the global information of the associated flow field (e.g. through the pressure-Poisson equation), additional unmodelled disturbances as well as dynamic uncertainties inherent in any ROM, can result in high uncertainties in the modelled pressure output.

Accurately modelling the effect of upstream disturbances in 2-D wall bounded shear flows has been addressed in chapter 3. It was shown that the use of physically motivated inflow disturbance models allows for efficient estimation and control of the perturbations within a localised region that encapsulates the actuators and sensors. Very large systems are subsequently avoided by synthesizing the controller within a localised computational domain. The synthesis approach combines direct state-space modelling from the governing equations with exact balanced truncation to design low-order controllers. In chapter 3 flow perturbations in a channel flow are estimated/controlled using wall shear measurements and localised suction and blowing at the wall. In this chapter the framework from chapter 3 is applied to Falkner-Skan flows and is extended by introducing point wall pressure measurements for the flow estimation. This study provides the first step towards applying the controller for transition delay in experiments. As stated earlier, the objective is to enable the use of point pressure sensors for dynamic flow estimation because of their practical advantages, rather than improving the performance as compared to other measurement strategies. In order to provide physical insights in how, and if, the aforementioned additional modelling challenges affect the controller performance, the results with pressure sensing are compared with the results of shear sensing,

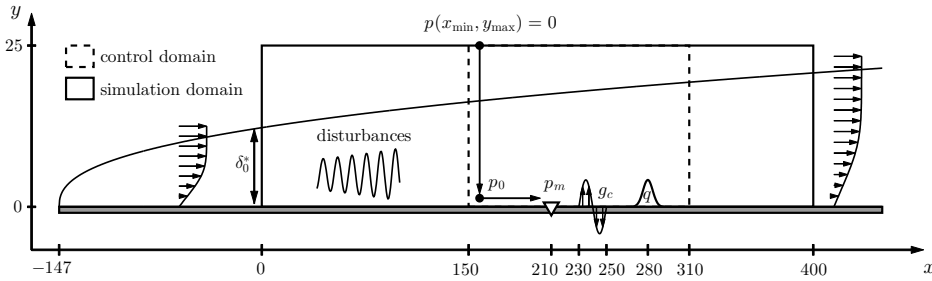


Figure 4.1: Simulation domain, control domain and input-output configuration for the control of perturbations in a 2-D flat plate geometry. Reference displacement thickness δ_0^* , pressure measurement p_m , controlled output q , actuator distribution g_c and $p_0 = p(x_{min}, y_{min})$ with p the fluctuating pressure. The two dot (•) connected arrows indicate the spatial integration paths along the inflow and wall boundary to derive the output equation for p_m in section 4.5.

which has been typically used in previous studies. In addition, the robustness of the modelling and control approach to variations in the Reynolds number and the pressure gradient is investigated.

The outline of this chapter is as follows. In section 4.2 the governing equations are presented. In section 4.3 the equations are written in state-space form and the finite-dimensional approximation is discussed. Section 4.4 presents the inflow disturbance model, which is linked to the relevant flow physics, and is of importance for the estimation problem. The pressure is eliminated from the state equations by formulating the state equations in a divergence free basis. In section 4.5 a new pressure output equation is derived which relates the upstream disturbances and the velocity perturbation field with the pressure at the measurement location at the wall. The output equation is required to dynamically estimate the velocity field using a Kalman filter. In section 4.6 the reduced-order controller/estimator is designed within an \mathcal{H}_2 /LQG optimal control framework. The controllers are evaluated in section 4.7 followed by conclusions in section 4.8.

4.2. GOVERNING EQUATIONS

2-D perturbations in an incompressible boundary layer flow over a flat plate are considered. The flow configuration, including the inputs-outputs, used in this study is shown in figure 4.1. The chosen control objective is to suppress the effect of inflow disturbances on the wall shear stress defined by the controlled output $q(t)$. The control actuation is achieved by localised wall-normal suction and blowing at the wall characterised by the distribution $g_c(x)$ and a pressure sensor is used to extract the measurement information $p_m(t)$ at the wall. A feedforward actuator/sensor configuration [27] is considered in which the sensors are placed upstream of the actuators to detect the upcoming perturbation. Such a setup is recommended for \mathcal{H}_2 /LQG optimal control of convective instabilities as reviewed by Sipp and Schmid [9], Schmid and Sipp [28]. It guarantees robust stability in amplifier flows and the best nominal performance [9, 27, 28]. Due to the convective nature of the flow, this setup dynamically corresponds to disturbance feedforward control, which is a special

case of output feedback control within the optimal control framework formalised by Doyle *et al.* [30]. In this section the flow domain and the governing equations are presented. The inputs and outputs will be discussed in the next sections.

The dynamics of the perturbations are obtained by linearising the Navier-Stokes equations around the steady boundary layer. The boundary layer is approximated by a profile from the family of Falkner-Skan similarity solutions. It is assumed that the outer free-stream velocity is given by $U_\infty^* = U_0^*(x^*/x_0^*)^m$ with x_0^* a fixed physical position from the virtual leading edge of the plate and U_0^* the free-stream velocity at that position. The asterisk (*) is used to denote a dimensional variable. The parameter m characterizes the pressure gradient, both favourable ($m > 0$) and adverse pressure gradients ($m < 0$) can be accounted for. The boundary layer displacement thickness δ_0^* and the free-stream velocity U_0^* at $x^* = x_0^*$ are chosen as reference variables to non-dimensionalise the flow with corresponding Reynolds number $Re = Re_0 = \frac{U_0^* \delta_0^*}{\nu}$ where ν is the kinematic viscosity. For the nominal simulation case and control design case we select $Re = 500$, $m = -0.02$ which corresponds to a distance of $x_0^* = 147\delta_0^*$ from the virtual leading edge. The computational domain is also scaled with δ_0^* and the non-dimensional coordinates are defined as $x = (x^* - x_0^*)/\delta_0^*$, $y = y^*/\delta_0^*$. For flow simulations the domain $x_{sim} \in [0, 400]$, $y_{sim} \in [0, 25]$ is considered. The controller is synthesised using localised computations within the domain $x_c \in [150, 310]$, $y_c \in [0, 25]$. Based on the following similarity variable $\xi(x^*) = y^* \sqrt{U_\infty^*/\nu x^*}$, the boundary layer in these domains is obtained by solving the Falkner-Skan equation

$$\begin{aligned} f''' + \frac{m+1}{2} f f'' + m(1-f^2) &= 0, \\ f(0) = f'(0) &= 0, \quad f'(\infty) = 1. \end{aligned} \quad (4.1)$$

The solutions for $f(\xi)$ and $f'(\xi)$ are combined into the non-dimensional velocity profiles

$$U(\mathbf{x}) = \frac{U^*}{U_0^*} = U_\infty f'(\xi), \quad (4.2)$$

$$V(\mathbf{x}) = \frac{V^*}{U_0^*} = \frac{1}{2\varrho} \sqrt{\frac{U_\infty}{(x+x_0)x_0}} \left((1-m)\xi f'(\xi) - (1+m)f(\xi) \right), \quad (4.3)$$

with $\xi(\mathbf{x}) = \varrho \sqrt{U_\infty \frac{x_0}{x+x_0}} y$, $\varrho = \int_0^\infty (1-f') d\xi$ and $U_\infty = U_\infty^*/U_0^* = (x/x_0 + 1)^m$. The displacement thickness for this boundary layer is given by $\delta^* = \int_0^\infty (1 - U^*/U_\infty^*) dy^* = \sqrt{\nu x^*/U_\infty^*} \varrho$, and the local Reynolds number Re_δ at a particular x station can subsequently be computed using

$$Re_\delta = Re \sqrt{\left(1 + \frac{\varrho^2 x}{Re} \right) U_\infty}. \quad (4.4)$$

Figure 4.2 shows the boundary layer (4.2)-(4.3) along with the local Reynolds numbers (4.4). Small perturbations to the boundary layer are governed by the linearised

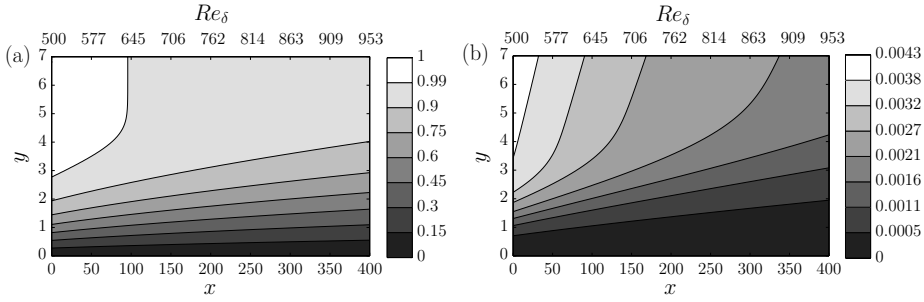


Figure 4.2: Falkner-Skan boundary layer ($m = -0.02$, $Re_0 = 500$) used for the linearization. (a) streamwise component U . (b) wall-normal component V .

Navier-Stokes equations (LNSE). Let $\mathbf{U}(\mathbf{x}) + \mathbf{u}(\mathbf{x}, t)$ be the perturbed velocity field. The linearised non-dimensional equations, including the boundary conditions used in this study, are given by

$$\frac{\partial \mathbf{u}}{\partial t} = - \underbrace{(\mathbf{U} \cdot \nabla) \mathbf{u} - (\mathbf{u} \cdot \nabla) \mathbf{U}}_{\mathcal{L}\mathbf{u}} + \frac{1}{Re} \Delta \mathbf{u} - \nabla p + \mathbf{f}, \quad (4.5a)$$

$$0 = \nabla \cdot \mathbf{u}, \quad (4.5b)$$

$$\mathbf{u}|_{\Gamma_D} = \mathbf{u}_b, \quad (4.5c)$$

$$0 = -\mathbf{n}p|_{\Gamma_{out}} + \frac{1}{Re} (\mathbf{n} \cdot \nabla) \mathbf{u}|_{\Gamma_{out}}, \quad (4.5d)$$

where \mathcal{L} is the linearised Navier-Stokes operator, $\mathbf{u}(\mathbf{x}, t) = [u(\mathbf{x}, t), v(\mathbf{x}, t)]$ and $p(\mathbf{x}, t)$ denote the velocity and pressure perturbation field and $\mathbf{f}(\mathbf{x}, t)$ is body force field per unit mass. In-domain body forces are typically used for applying control. In this study only wall-actuation is considered, which is modelled through the boundary condition. Without loss of generality the body force will be set to zero in the remainder of the chapter. The system is closed by the boundary conditions (4.5c)-(4.5d), where Γ_{out} is the outflow part of the boundary and Γ_D is the Dirichlet part of the boundary, which includes the rigid wall Γ_{wall} , the computational inflow Γ_{in} and the outer free-stream boundary Γ_{fs} . \mathbf{u}_b is the prescribed velocity input profile at the boundary, which is used to model the wall-actuation (see next section) and to account for external disturbances in the control design. The inflow boundary condition used to impose the external disturbances in the control model is discussed in section 4.4 and is an integral part of the control design. An unperturbed flow is assumed at the computational inflow of the simulation domain ($\mathbf{u}(0, y) = 0$). For both cases it is assumed that the perturbations vanish at the upper boundary ($\mathbf{u}(x, 25) = 0$). A standard outflow boundary condition (4.5d) is prescribed, which has proven to be well suited for uni-directional outflows [111]. The outflow condition is implicitly satisfied by the variational formulation used to discretise the LNSE and does not need to be explicitly taking into account.

4.3. STATE-SPACE FORMULATION

In order to apply linear control theoretic tools the flow equations must be formulated into the standard state-space form. To generalise the modelling approach and control system design the equations are written as an abstract equation in operator form [43, 110]. Explicit discrete expressions are obtained for all operators which are discussed afterwards.

4.3.1. ABSTRACT FORM

The pressure term, along with the divergence equation can be eliminated by the projection of the equations onto the divergence free space [110]. This avoids singularities resulting from the assumption of incompressibility. Control and disturbance are introduced through the boundary which renders the system in-homogeneous. By a standard lifting procedure [94, 110] the effect of the boundary condition can be represented by a volume forcing in a modified state-space system with homogeneous boundary conditions. We also refer to Curtain and Zwart [43, section 3.3] for more information about this formulation. The boundary condition is decomposed into an external disturbance and a control $\mathbf{u}_b = \mathbf{u}_d + \mathbf{u}_c$ with $\mathbf{u}_c(x, t)$ the suction and blowing imposed at the rigid wall and $\mathbf{u}_d(y, t)$ the perturbation velocity imposed at the inflow. Both actuation and disturbance are mathematically equivalent. The boundary condition can be lifted by setting

$$\mathbf{u} = \mathbf{u}_h + \mathcal{Z}\mathbf{u}_b = \mathbf{u}_h + \mathcal{Z}_c\mathbf{u}_c + \mathcal{Z}_d\mathbf{u}_d, \quad (4.6)$$

where \mathbf{u}_h is a solution of the homogeneous problem and \mathcal{Z} ‘lifts’ the boundary condition to the interior of the domain and must be defined such that $(\mathcal{Z}\mathbf{u}_b)|_{\Gamma_D} = \mathbf{u}_b$ and $\nabla \cdot (\mathcal{Z}\mathbf{u}_b) = 0$ [43, 110]. Let $\mathcal{X} = \{\mathbf{u} \in L^2(\Omega)^2 \mid \nabla \cdot \mathbf{u} = 0\}$ and let \mathcal{P} be an orthogonal projector from $L^2(\Omega)^2 \mapsto \mathcal{X}$ satisfying $\mathcal{P}\mathbf{u} = \mathbf{u}$ and $\mathcal{P}(\nabla p) = 0$. Applying the projection \mathcal{P} to (4.5a) and substituting the change of variables (4.6) gives the following homogeneous equation in operator form

$$\dot{\mathbf{u}}_h = \mathcal{A}\mathbf{u}_h + \mathcal{A}\mathcal{Z}\mathbf{u}_b - \mathcal{Z}\dot{\mathbf{u}}_b, \quad (4.7)$$

where $\mathcal{A}\mathbf{u} = \mathcal{P}\mathcal{L}\mathbf{u}$, $\mathcal{A}\mathbf{u} = \mathcal{A}\mathbf{u}$ for $\mathbf{u} \in \mathcal{D}(\mathcal{A})$ and the domain $\mathcal{D}(\mathcal{A})$ includes homogeneous boundary conditions $\mathcal{D}(\mathcal{A}) = \{\mathbf{u} \in \mathcal{X} \mid \mathbf{u}|_{\Gamma_D} = 0\}$. The external input in (4.7) is actually the time derivative of the prescribed velocity at the boundary \mathbf{u}_b . The spatio-temporal boundary actuator/disturbance model for \mathbf{u}_b can be described by

$$\begin{aligned} \dot{\boldsymbol{\eta}}_b &= \mathcal{A}_b\boldsymbol{\eta}_b + \mathcal{B}_b^c\phi(t) + \mathcal{B}_b^d w_d, \\ \mathbf{u}_b &= \mathcal{C}_b\boldsymbol{\eta}_b, \end{aligned} \quad (4.8)$$

where $\boldsymbol{\eta}_b(t)$ is the temporal state at the boundary, $\phi(t)$ the control input, $w_d(t)$ the external disturbance input and $\mathbf{u}_b(\mathbf{x}, t)$ is the output velocity at the boundary. Since actuation and disturbance are independent of each other, the state-space (4.8) has the form $\mathcal{A}_b = \text{diag}\{\mathcal{A}_c, \mathcal{A}_d\}$, $\mathcal{B}_b^c = [\mathcal{B}_c, 0]^T$, $\mathcal{B}_b^d = [0, \mathcal{B}_d]^T$, $\mathcal{C}_b = [\mathcal{C}_c, \mathcal{C}_d]$. The inflow disturbance model $(\mathcal{A}_d, \mathcal{B}_d, \mathcal{C}_d)$ is discussed in detail in the next section.

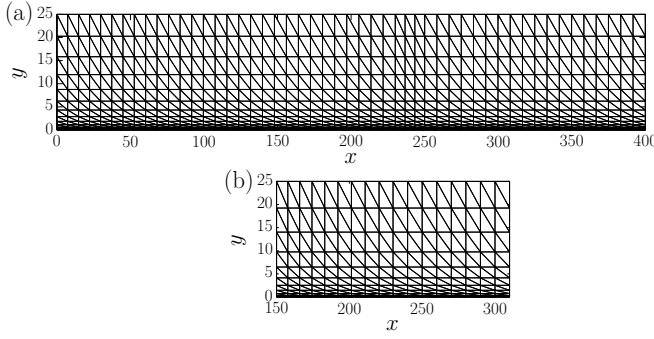


Figure 4.3: Triangulations used for the simulation model and control model. (a) Triangulation with 1200 elements used for the simulation model. (b) Triangulation with 340 elements used for the control model.

To manipulate the flow, localised unsteady blowing and suction is considered that influences the wall-normal component at the wall. It is assumed that the actuator dynamics are described by

$$\begin{aligned}\dot{\eta}_c &= \tau^{-1}(\phi - \eta_c) = \mathcal{A}_c \eta_c + \mathcal{B}_c \phi, \\ \mathbf{u}_c &= \mathbf{g}_c \eta_c = \mathcal{C}_c \eta_c,\end{aligned}\tag{4.9}$$

with $\eta_c(t)$ the temporal actuator state that describes the amplitude of the blowing and suction. The temporal dynamics are governed by a simple first order lag filter with τ the time constant. The time constant is set equal to the sampling time of the simulations. In this case the filter corresponds to a stable approximation of a pure integrator commonly used for boundary control [80, 84]. A localised spatial distribution is considered with $\mathbf{g}_c(x) = [0, g_{c_v}]^T$ where $g_{c_v} = \sin(2\pi(x - x_g)/L_g)$ if $x_g \leq x \leq x_g + L_g$ and $g_{c_v} = 0$ elsewhere. The spatial length is set to $L_g = 20$ starting at $x_g = 230$. The spatial length is chosen to be less than the spatial wavelengths of the dominant TS waves (see next section) and allows for effective control over a broad frequency spectrum. Combining the boundary dynamics (4.8) with the dynamics in the interior of the domain (4.7) and using $\dot{\mathbf{u}}_b = \mathcal{C}_b \mathcal{A}_b \boldsymbol{\eta}_b + \mathcal{C}_c \mathcal{B}_c \phi + \mathcal{C}_d \mathcal{B}_d w_d$ it is straightforward to express (4.7) in the (extended) state-space form

$$\dot{\mathbf{u}}^e = \bar{\mathcal{A}} \mathbf{u}^e + \bar{\mathcal{B}}_c \phi + \bar{\mathcal{B}}_d w_d,\tag{4.10}$$

$$\begin{aligned}\mathbf{u}^e &= \begin{bmatrix} \mathbf{u}_h \\ \boldsymbol{\eta}_b \end{bmatrix}, \quad \bar{\mathcal{A}} = \begin{bmatrix} \mathcal{A} & \mathcal{Z} \mathcal{C}_b - \mathcal{Z} \mathcal{C}_b \mathcal{A}_b \\ 0 & \mathcal{A}_b \end{bmatrix}, \quad \mathcal{A}_b = \begin{bmatrix} \mathcal{A}_c & 0 \\ 0 & \mathcal{A}_d \end{bmatrix}, \quad \mathcal{C}_b = [\mathcal{C}_c \quad \mathcal{C}_d], \\ \bar{\mathcal{B}}_c &= \begin{bmatrix} -\mathcal{Z}_c \mathcal{C}_c \mathcal{B}_c \\ \mathcal{B}_b^c \end{bmatrix}, \quad \bar{\mathcal{B}}_d = \begin{bmatrix} -\mathcal{Z}_d \mathcal{C}_d \mathcal{B}_d \\ \mathcal{B}_b^d \end{bmatrix}, \quad \mathcal{B}_b^c = \begin{bmatrix} \mathcal{B}_c \\ 0 \end{bmatrix}, \quad \mathcal{B}_b^d = \begin{bmatrix} 0 \\ \mathcal{B}_d \end{bmatrix},\end{aligned}$$

where \mathbf{u}^e denotes an extended state. The output equation for the wall pressure measurements will be derived in section 4.5. This equation is less trivial since the pressure is eliminated from the state equations.

4.3.2. FINITE-DIMENSIONAL APPROXIMATION

Equation (4.10) represents the continuous formulation of the system. For simulation and control design a finite-dimensional approximation of (4.10) is required. The method of Galerkin projection with multivariate splines presented in chapter 2 is used to find matrix representations of all operators in (4.10). The pressure is eliminated from the equations by using a space of velocity fields which is divergence free and a suitable choice of variational formulation (see appendix A.1). By expanding the solution in the null basis of the discrete divergence operator a minimal support basis is obtained for a divergence free spline space $\mathcal{S} \subset \mathcal{X}$. The system is projected on this basis through the variational formulation to obtain the finite-dimensional system. The triangulations used to construct the simulation model and the initial model that is used for model reduction and control design are shown in figure 4.3. To derive the simulation model a structured triangulation consisting of 1200 elements is used. It is refined near the wall using a hyperbolic stretching function to properly resolve the shear features. C^0 continuous elements and high degree, fifth order B-form polynomials are chosen which allow for better approximation properties [64]. The simulation model has a total of 11501 states. The model order already includes a large initial reduction resulting from the elimination of the divergence free constraint through the null basis expansion, which is equal to rank of the discrete divergence operator. It is verified with a mesh convergence analysis that higher resolutions did not provide an improved accuracy of the simulation results. To construct the initial model that is used for model reduction and control design a lower order discretisation is used. Again C^0 , $d = 5$ elements are chosen, but a coarser mesh consisting of 340 elements is used. The control model has 3231 states which allows efficient application of control theoretic tools for model reduction and control design. In the next sections the notation $(\mathcal{A}, \mathcal{B}, \mathcal{C}, \mathcal{D})$ is used to denote the full order finite-dimensional system and the notation $(\mathbf{A}, \mathbf{B}, \mathbf{C}, \mathbf{D})$ is used to denote a reduced-order model.

4.4. INFLOW DISTURBANCES

The state-space description (4.10) also includes a disturbance model, defined by $(\mathcal{A}_d, \mathcal{B}_d, \mathcal{C}_d)$, to account for external disturbances in the control design. In particular the performance of the state estimation relies on the model for the external disturbances as the estimation error is minimised in the presence of these disturbances. The spatio-temporal structures that can be estimated in the control (actuators/sensors) domain depend on the spatial-temporal structures that are excited by the external disturbances. External disturbances are introduced through the inflow boundary $\mathbf{u}|_{\Gamma_{in}} = \mathbf{u}_d$ with \mathbf{u}_d the inflow perturbation velocity. The inflow perturbation is computed such that it allows for efficient estimation of the dominant perturbations that contribute to transition. The primary route to transition [16] is considered, triggered by linear growth of the primary modes as described by the classical linear stability theory (LST) [21]. LST assumes a locally parallel flow in which the primary modes take the form

$$\mathbf{u} = \text{Real} \left[\tilde{\mathbf{u}} e^{i(\alpha x - \omega t)} \right], \quad (4.11)$$

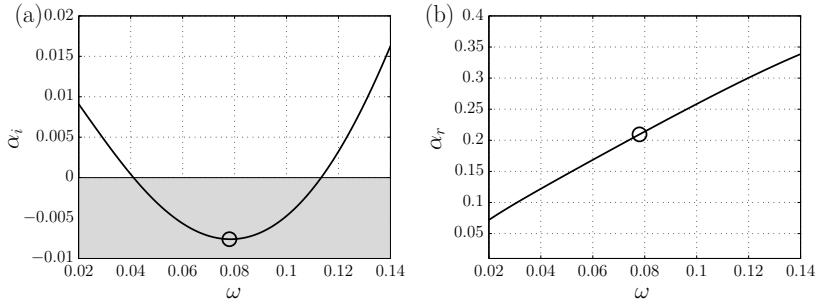


Figure 4.4: The leading or most unstable wavenumber as function of temporal frequency at $Re_0 = 500$, $x = 150$, $m = -0.02$. (a) The imaginary part. Negative values characterize unstable modes (gray region). (b) The real part. The point marked by ‘o’ corresponds to the most amplified frequency for the investigated conditions.

with $\tilde{\mathbf{u}}(y) = \tilde{\mathbf{u}}_r(y) + i\tilde{\mathbf{u}}_i(y)$ the complex eigenfunction of the mode, $\alpha = \alpha_r + i\alpha_i$ the complex wave-number and ω the real frequency of the mode. The inflow is considered as the disturbance source which generates the perturbation (4.11) at a particular frequency ω . The modes are computed as solutions of the Orr-Sommerfeld equation using a local parallel spatial stability analysis at the inflow of the control domain, that is at $Re_0 = 500$ and $x = 150$ ($Re_\delta = 706$). Figure 4.4 shows the wavenumber (spatial eigenvalue) of the primary mode as function of the temporal frequency. Negative values for α_i characterize unstable modes. Although the spectrum of the Orr-Sommerfeld operator is continuous and unstable over a broad range of frequencies, only the most unstable primary mode is included in the model for control design. The motivation for this will be explained later in this section. For the nominal investigated conditions, the most amplified frequency is found at $\omega = \omega_d = 0.078$, see figure 4.4. This frequency will be referred to as the design frequency. Note that this frequency is not necessarily the most amplified frequency for the spatially developing boundary layer and a discrepancy between the parallel theory and the non-parallel theory is to be expected [131]. Nevertheless, it is found that the design frequency selected from parallel theory provides a good estimate. The shape of the eigenfunction at this frequency is shown in figure 4.5. The eigenfunction is normalised such that the maximum magnitude of the streamwise component is equal to one. At the inflow, this perturbation mode (4.11) can be described by

$$\mathbf{u}|_{\Gamma_{in}} = \mathbf{u}_d = \underbrace{\tilde{\mathbf{u}}_r \cos(\omega_d t)}_{\eta_d} + \underbrace{\tilde{\mathbf{u}}_i \sin(\omega_d t)}_{-\frac{1}{\omega_d} \dot{\eta}_d}. \quad (4.12)$$

Equation (4.12) employs an ansatz in time and the two temporal components are 90° out of phase. To account for the perturbation modes in a stochastic control

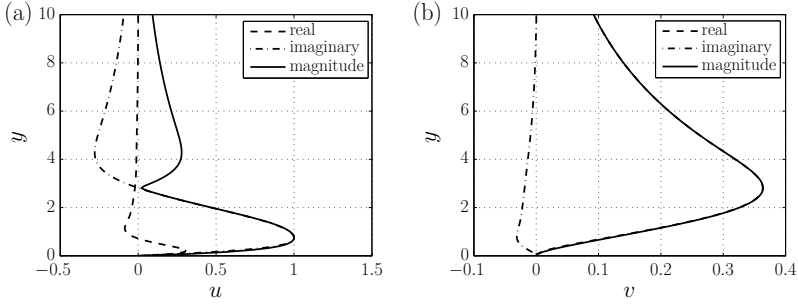


Figure 4.5: The Orr-Sommerfeld eigenfunction for u (a) and v (b) calculated at $Re_0 = 500$, $x = 150$, $\omega = 0.078$, $m = -0.02$.

design, the following dynamic disturbance model is proposed in section 3.2.3

$$\begin{bmatrix} \dot{\eta}_d \\ \dot{\eta}_d \end{bmatrix} = \underbrace{\begin{bmatrix} 0 & 1 \\ -\omega_n^2 & -2\zeta\omega_n \end{bmatrix}}_{\mathcal{A}_d} \underbrace{\begin{bmatrix} \eta_d \\ \dot{\eta}_d \end{bmatrix}}_{\tilde{\eta}_d} + \underbrace{\begin{bmatrix} 0 \\ \omega_n^2 \end{bmatrix}}_{\mathcal{B}_d} w_d, \quad (4.13a)$$

$$\mathbf{u}_d = \underbrace{\begin{bmatrix} \tilde{\mathbf{u}}_r - \frac{1}{\omega_d} \tilde{\mathbf{u}}_i \end{bmatrix}}_{\mathcal{C}_d} \begin{bmatrix} \eta_d \\ \dot{\eta}_d \end{bmatrix}. \quad (4.13b)$$

The temporal dynamics (4.13a) of the perturbation mode \mathbf{u}_d is given by a second order low-pass filter with ω_n the undamped natural frequency, ζ the damping ratio, $\tilde{\eta}_d = [\eta_d, \dot{\eta}_d]^T$ the temporal state and w_d the external disturbance input. The low-pass filter allows the magnitude shaping of \mathbf{u}_d depending on the input frequency of w_d . We choose $\zeta = 0.15$ and $\omega_n = 0.08$ such the filter has a peak frequency $\omega_p = \sqrt{1 - 2\zeta^2} = \omega_d$ at the design frequency and amplifies the magnitude of the disturbance w_d at this frequency with approximately a factor of 3.5. By increasing the magnitude of the disturbance around the design frequency, the controller will be better able to target the most unstable frequencies that contribute to transition, while at the same time achieving robustness at the off-design frequencies.

For the control design the external disturbance is assumed to be zero-mean Gaussian white noise with unit root mean square (rms) intensity. This scaling was discussed in detail in section 3.2.6. The temporal state is distributed at the inflow boundary through the output equation (4.13b), where η_d excites the real part of the eigenfunction and $\dot{\eta}_d$ excites the imaginary part of the eigenfunction scaled with the perturbation frequency to account for the phase. This model can easily be extended to include the excitation of Orr-Sommerfeld eigenfunctions calculated at different temporal frequencies. However, it was shown in chapter 3 that a single mode disturbance model is effective for estimation of multiple frequency wavepackets, which is also observed for the application case considered in this study. This can be contributed to the fact that the eigenfunction is excited over all frequencies in case of stochastic excitation. Also at other frequencies than the design frequency, the inflow perturbation will develop spatially to modal perturbations with different

wavelengths and growth rates. The computational inflow is placed sufficiently far from the sensor location such that the non-modal and possible non-physical spatial transient behaviour near the inflow does not significantly contribute to the input-output behaviour. The sensitivity of the controller performance with respect to the location of the computational inflow boundary will be investigated in section 4.7.

4.5. PRESSURE OUTPUT EQUATION

Information about the perturbations is extracted from pressure measurements at a single point on the wall. In this section the pressure output equation is derived which relates the model variables, i.e. the upstream disturbances and the velocity perturbation field, with the fluctuating pressure at the measurement location at the wall. The output equation is required to estimate the velocity field using a Kalman filter. The output equation is derived from the LNSE which describes the fluctuation pressure uniquely up to an arbitrary additive constant in space. To fix this constant it is assumed that the fluctuating pressure is zero at the intersection point of the outer free-stream boundary and the inflow boundary ($p(x_{min}, y_{max} = 0) = 0$), see also figure 4.1). The formulation of the output equation utilizes the formal inverse of the pressure gradient at the inflow and wall boundaries. The use of spatial integration along the boundaries avoids additional computational challenges which would arise when considering the 2-D pressure-Poisson equation, such as higher order derivatives and non-homogeneous Neumann boundary conditions. The practice of integrating the governing equations to obtain the pressure can also be found in literature. For example, to obtain the pressure field from experimental velocity field data [132]. However, the application for dynamic flow estimation has so far not been reported. Two spatial integration paths are considered to formulate the output equation, see also figure 4.1. The first path is along the inflow boundary from the freestream boundary, with $p(x_{min}, y_{max}, t) = 0$, to the pressure at the wall $p(x_{min}, 0, t) = p_0(t)$. The second path is along the wall, with $p_0(t)$ as boundary condition, to the pressure at the measurement location $p(x_m, 0, t) = p_m(t)$. First the second integration path is considered.

The pressure at the wall is related with the perturbation velocity through

$$\partial_x p|_{\Gamma_{wall}} = \frac{1}{Re} \partial_{yy} u|_{\Gamma_{wall}}, \quad p(x_{min}, t)|_{\Gamma_{wall}} = p_0(t). \quad (4.14)$$

Equation (4.14) is obtained by evaluating the x -momentum equation (4.5a) at the wall. The boundary condition at x_{min} can be lifted through the following linear change of variables $p|_{\Gamma_{wall}} = p_h + \mathcal{I}p_0$ where p_h is the solution with homogeneous boundary conditions and with $\mathcal{I}(x)p_0 = p_0$ for all x satisfying $\mathcal{I}p_0|_{x_{min}} = p_0$ and $\partial_x \mathcal{I} = 0$. Note that $\mathcal{I}(x)p_0(t)$ represents the constant in space to uniquely define the pressure at the wall. The pressure at the wall is subsequently given by

$$\begin{aligned} p|_{\Gamma_{wall}} &= p_h + \mathcal{I}p_0 \\ &= \tilde{\partial}_x^{-1} \frac{1}{Re} \partial_{yy} u|_{\Gamma_{wall}} + \mathcal{I}p_0, \end{aligned} \quad (4.15)$$

where $\tilde{\partial}_x^{-1}$ denotes the formal inverse of $\tilde{\partial}_x$ which is defined as $\tilde{\partial}_x p = \partial_x p$ for $p \in \mathcal{D}(\tilde{\partial}_x)$ with $\mathcal{D}(\tilde{\partial}_x) = \{p \in L^2(\Gamma_{wall}) \mid p(x_{min}, t) = 0\}$. $\tilde{\partial}_x$ is simply the restriction of ∂_x with the homogeneous boundary condition to allow the inversion of the operator. The measured pressure is obtained by evaluating (4.15) at the measurement location and can be written as

$$p_m = p(x = x_m, t)|_{\Gamma_{wall}} = \mathcal{C}_{wall} \mathbf{u} + p_0, \quad (4.16)$$

where the output operator \mathcal{C}_{wall} is formally defined as

$$\mathcal{C}_{wall} \mathbf{u} = \frac{1}{Re} \int_{\Gamma_{wall}} \delta(x - x_m) \tilde{\partial}_x^{-1} \partial_{yy} u |_{\Gamma_{wall}} dx. \quad (4.17)$$

The Dirac function indicates a point measurement at x_m . Equation (4.16) still contains the unknown boundary condition p_0 . The equation for p_0 is obtained similarly by considering the first integration path. This path is defined by the y -momentum equation at the inflow boundary

$$\partial_y p |_{\Gamma_{in}} = \mathbf{e}_2^T (\mathcal{L} - \partial_t) \mathbf{u} |_{\Gamma_{in}}, \quad p(y_{max}, t) |_{\Gamma_{in}} = 0, \quad (4.18)$$

where $\mathbf{e}_2 = [0 \ 1]^T$ selects the wall-normal component of the equation. Defining $\tilde{\partial}_y p = \partial_y p$ for $p \in \mathcal{D}(\tilde{\partial}_y)$ with $\mathcal{D}(\tilde{\partial}_y) = \{p \in L^2(\Gamma_{in}) \mid p(y_{max}) = 0\}$, (4.18) can be solved for the pressure at the inflow boundary

$$p |_{\Gamma_{in}} = \tilde{\partial}_y^{-1} \mathbf{e}_2^T (\mathcal{L} - \partial_t) \mathbf{u} |_{\Gamma_{in}}. \quad (4.19)$$

From the disturbance model (4.13) it follows that $\partial_t \mathbf{u} |_{\Gamma_{in}} = \dot{\mathbf{u}}_d = \mathcal{C}_d \mathcal{A}_d \bar{\boldsymbol{\eta}}_d + \mathcal{C}_d \mathcal{B}_d w_d$ and substituting this expression in (4.19) gives

$$p |_{\Gamma_{in}} = \tilde{\partial}_y^{-1} \mathbf{e}_2^T (\mathcal{L} \mathbf{u} |_{\Gamma_{in}} - \mathcal{C}_d \mathcal{A}_d \bar{\boldsymbol{\eta}}_d - \mathcal{C}_d \mathcal{B}_d w_d). \quad (4.20)$$

Defining the output operators as

$$\begin{aligned} \mathcal{C}_{in} \mathbf{u} &= \int_{\Gamma_{wall}} \delta(y) \tilde{\partial}_y^{-1} \mathbf{e}_2^T \mathcal{L} \mathbf{u} |_{\Gamma_{in}} dx, \\ \mathcal{C}_{in}^\eta \bar{\boldsymbol{\eta}}_d &= - \int_{\Gamma_{wall}} \delta(y) \tilde{\partial}_y^{-1} \mathbf{e}_2^T \mathcal{C}_d \mathcal{A}_d \bar{\boldsymbol{\eta}}_d dx, \\ \mathcal{D}_{in} w_d &= - \int_{\Gamma_{wall}} \delta(y) \tilde{\partial}_y^{-1} \mathbf{e}_2^T \mathcal{C}_d \mathcal{B}_d w_d dx, \end{aligned} \quad (4.21)$$

the output equation for p_0 can be written as

$$p_0 = p(0, t) |_{\Gamma_{in}} = \mathcal{C}_{in} \mathbf{u} + \mathcal{C}_{in}^\eta \bar{\boldsymbol{\eta}}_d + \mathcal{D}_{in} w_d. \quad (4.22)$$

Substituting (4.22) for p_0 in (4.16) gives

$$p_m = (\mathcal{C}_{wall} + \mathcal{C}_{in}) \mathbf{u} + \mathcal{C}_{in}^\eta \bar{\boldsymbol{\eta}}_d + \mathcal{D}_{in} w_d. \quad (4.23)$$

Applying the linear change of variables from (4.6) for \mathbf{u} and using $\mathbf{u}_c = \mathcal{C}_c \eta_c$, $\mathbf{u}_d = \mathcal{C}_d \bar{\eta}_d$ finally gives the output equation for the pressure at the measurement location.

$$\begin{aligned} p_m &= \begin{bmatrix} \mathcal{C}_{wall} + \mathcal{C}_{in} & (\mathcal{C}_{wall} + \mathcal{C}_{in}) \mathcal{Z}_c \mathcal{C}_c & (\mathcal{C}_{wall} + \mathcal{C}_{in}) \mathcal{Z}_d \mathcal{C}_d + \mathcal{C}_{in}^\eta \end{bmatrix} \begin{bmatrix} \mathbf{u}_h \\ \eta_c \\ \bar{\eta}_d \end{bmatrix} + \mathcal{D}_{in} w_d \\ &= \bar{\mathcal{C}}_p \mathbf{u}^e + \bar{\mathcal{D}}_d w_d. \end{aligned} \quad (4.24)$$

Again, discrete expressions are obtained for all operators in (4.24) using Galerkin projection where the pressure at the boundaries is approximated by a univariate spline basis for $L^2(\Gamma)$. Note that the uncertain state dynamics due to the unknown constant is accounted for in the output equation as a direct feed-through of the state disturbances. To also account for sensor inaccuracies it also assumed that the measurement is corrupted by zero-mean Gaussian white noise w_n which modifies (4.24) to

$$p_m = \bar{\mathcal{C}}_p \mathbf{u}^e + \bar{\mathcal{D}}_d w_d + \gamma_p w_n, \quad (4.25)$$

where γ_p reflects the magnitude of the uncertainty which can be tuned to design the controller. The gradient approach to derive (4.25) results in uncertainties in the output equation. Firstly, $p_0(t)$ defined in (4.22) is uncertain due to the assumption of zero fluctuation pressure at the freestream boundary. Secondly, the pressure output p_m is obtained by integrating the governing equations and the associated global flow field from the inflow to the measurement location. As a result, additional unmodelled disturbances and dynamic uncertainties can accumulate in high output uncertainties. To investigate whether this affects the robustness and performance of the controller, a second measurement case is considered which is based on the wall shear stress

$$\tau_m = \tau_{xy}(x_m, t)|_{\Gamma_{wall}} = \bar{\mathcal{C}}_\tau \mathbf{u}^e + \gamma_\tau w_n, \quad (4.26)$$

where

$$\bar{\mathcal{C}}_\tau \mathbf{u}^e = \frac{1}{Re} \int_{\Gamma_{wall}} \delta(x - x_m) \partial_y u|_{\Gamma_{wall}} dx. \quad (4.27)$$

4.6. \mathcal{H}_2 /LQG REDUCED-ORDER CONTROL DESIGN

The reduced-order controller is designed within an \mathcal{H}_2 /LQG optimal control framework to account for the inflow disturbances and measurement noise. The controller is designed for the state-space system defined by the state equation (4.10) and the output equations (4.25) and (4.26). In addition a controlled output q is defined which is used as control objective to synthesise the controller. The complete input-output system can be formulated as

$$\begin{aligned} \dot{\mathbf{u}}^e &= \bar{\mathcal{A}} \mathbf{u}^e + \bar{\mathcal{B}}_c \phi + \bar{\mathcal{B}}_d w_d, \\ q &= \bar{\mathcal{C}}_1 \mathbf{u}^e, \\ y_m &= \bar{\mathcal{C}}_2 \mathbf{u}^e + \bar{\mathcal{D}}_d w_d + \gamma w_n, \end{aligned} \quad (4.28)$$

where y_m is either the measured pressure or the wall shear stress. The controlled output is defined by

$$\begin{aligned}
 q &= \bar{C}_1 \mathbf{u} = \int_{\Gamma_{wall}} h(x) \tau_{xy}|_{\Gamma_{wall}} dx \\
 &= \frac{1}{Re} \int_{\Gamma_{wall}} h(x) \partial_y u|_{\Gamma_{wall}} dx,
 \end{aligned} \tag{4.29}$$

where $h(x)$ is chosen as a Gaussian distribution function $h(x) = \exp[-((x - x_q)/r_x)^2]$ with $x_q = 280$ the center of the distribution and $r_x = 5$ the radius. The wall shear stress in (4.29) is found to be an effective and robust performance indicator for the input-output configuration considered in this study. The controlled output is placed sufficiently far from the actuator (see also figure 4.1) such that the actuator has no direct influence on q and minimization of q is achieved by minimizing the effect of inflow perturbations alone. However, it is found that there is not much sensitivity with respect to the choice of the position x_q and the radius r_x of the distribution, as long as it is placed sufficiently far from the actuator.

\mathcal{H}_2 optimal control defines the cost function in the frequency domain, while LQG control is the time-domain equivalent and is considered in this section. The control objective is to suppress the wall shear stress defined by q . The LQG cost function to design the controller is defined by

$$\begin{aligned}
 \mathcal{J}_{LQG} &= E \left\{ \lim_{T \rightarrow \infty} \frac{1}{T} \int_0^T \mathbf{z}^T \mathbf{z} dt \right\} \\
 &= E \left\{ \lim_{T \rightarrow \infty} \frac{1}{T} \int_0^T q^2 + l^2 \phi^2 dt \right\},
 \end{aligned} \tag{4.30}$$

with $\mathbf{z}(t) = [q(t), l\phi(t)]^T$ the performance measure to be minimised. Equation (4.30) also includes a penalty on the control input defined by the parameter l which determines the trade-off between a low controlled output power q^2 and a low control effort ϕ^2 in the design of the controller. The reduced-order controller that minimises (4.30) is derived in two steps. First, a reduced-order model (ROM) is derived using balanced truncation [67]. Secondly, the ROM is used to synthesize the controller and the truncated dynamics are taken into account in the control system design. Balanced truncation extract the most controllable and observable modes of the system. It first involves a similarity transformation of the form $\mathbf{u}^e \mapsto \mathbf{S}\mathbf{u}^e$, which balances the system matrices through $\bar{\mathbf{A}} \mapsto \mathbf{S}\bar{\mathbf{A}}\mathbf{S}^{-1}$, $\bar{\mathbf{B}} \mapsto \mathbf{S}\bar{\mathbf{B}}$ and $\bar{\mathbf{C}} \mapsto \bar{\mathbf{C}}\mathbf{S}^{-1}$, $\bar{\mathbf{D}} \mapsto \bar{\mathbf{D}}$, such that each state has an equal measure for both controllability and observability. The reduced-order model of order r described by the matrices $\mathbf{A}, \mathbf{B}, \mathbf{C}$ and \mathbf{D} is obtained from the balanced matrices by retaining the rows and columns corresponding to most controllable and observable states. The optimal controller based on the ROM combines a state estimator and a state feedback, and can be written as a dynamic system in the form

$$\begin{aligned}
 \dot{\hat{\mathbf{u}}}_r &= \mathbf{A}\hat{\mathbf{u}}_r + \mathbf{B}_c\phi + \mathbf{L}(y_m - \mathbf{C}\hat{\mathbf{u}}_r), \\
 \phi &= -\mathbf{F}\hat{\mathbf{u}}_r,
 \end{aligned} \tag{4.31}$$

with $\hat{\mathbf{u}}_r \in \mathbb{R}^r$ the estimated state and where \mathbf{F} , \mathbf{L} are respectively the state feedback gain and the estimator (Kalman) gain to be optimised. Due to the well known separation property [29, pp. 388-390] of the optimal solution the state feedback and the state estimator can be designed and synthesised independently. The state feedback gain is obtained by minimizing (4.30) when noise is ignored. For the ROM this means to find \mathbf{F} that minimizes

$$\mathcal{J} = \lim_{T \rightarrow \infty} \frac{1}{T} \int_0^T \mathbf{u}_r^T \mathbf{C}_1^T \mathbf{C}_1 \mathbf{u}_r + l^2 \phi^2 \, dt \quad (4.32)$$

subject to the closed-loop system dynamics $\dot{\mathbf{u}}_r = (\mathbf{A} - \mathbf{B}_c \mathbf{F}) \mathbf{u}_r$. The Kalman gain \mathbf{L} is subsequently obtained by minimizing the covariance of the estimated state

$$E \{ (\mathbf{u}_r - \hat{\mathbf{u}}_r)^T (\mathbf{u}_r - \hat{\mathbf{u}}_r) \} = E \{ \tilde{\mathbf{u}}_r^T \tilde{\mathbf{u}}_r \} \quad (4.33)$$

subject to the error dynamics $\dot{\tilde{\mathbf{u}}}_r = (\mathbf{A} - \mathbf{L}\mathbf{C}) \tilde{\mathbf{u}}_r + (\mathbf{B}_d - \mathbf{L}\mathbf{D}_w) w_d - \mathbf{L}\gamma w_n$. Note that \mathbf{L} is optimised to provide an optimal estimate in the presence of external disturbances w_d and w_n . For the control design the external disturbances are assumed to be Gaussian white noise with unit intensity. As a result the estimation problem is parameterised in terms of γ which reflects the uncertainty in the measurement. It can be shown that with this parameterisation γ also reflects a rms value for the sensor noise relative to the state disturbances [37], see also section 3.2.6. The optimal solutions for the control and estimation problem can be obtained independently by solving the associated algebraic Riccati equations for (4.32) and (4.33) (see appendix B), which together form the compensator (4.31). In the design of the compensator the parameters l and γ can independently be adjusted to achieve the desired closed-loop performance. However, no guarantees are available about the performance of the controller designed for the ROM on the original system. Therefore the truncated dynamics are taken into account by evaluating the performance of the controller in combination with the original system. Combining the compensator (4.31) with the original system (4.28) gives the following closed-loop system from the external disturbances to the performance measure $\mathbf{z}(t) = [q(t), l\phi(t)]^T$

$$\begin{aligned} \begin{bmatrix} \dot{\mathbf{u}}^e \\ \dot{\hat{\mathbf{u}}}_r \end{bmatrix} &= \underbrace{\begin{bmatrix} \bar{\mathbf{A}} & -\bar{\mathbf{B}}_c \mathbf{F} \\ \mathbf{L}\bar{\mathbf{C}} & \mathbf{A} - \mathbf{B}_c \mathbf{F} - \mathbf{L}\mathbf{C} \end{bmatrix}}_{\mathcal{A}_{cl}} \begin{bmatrix} \mathbf{u}^e \\ \hat{\mathbf{u}}_r \end{bmatrix} + \underbrace{\begin{bmatrix} \bar{\mathbf{B}}_d & 0 \\ \mathbf{L}\bar{\mathbf{D}}_w & \mathbf{L}\gamma \end{bmatrix}}_{\mathcal{B}_{cl}} \begin{bmatrix} w_d \\ w_n \end{bmatrix}, \\ \mathbf{z} &= \underbrace{\begin{bmatrix} \bar{\mathbf{C}}_1 & 0 \\ 0 & -l\mathbf{F} \end{bmatrix}}_{\mathcal{C}_{cl}} \begin{bmatrix} \mathbf{u}^e \\ \hat{\mathbf{u}}_r \end{bmatrix}. \end{aligned} \quad (4.34)$$

The \mathcal{H}_2 system norm of the following two closed-loop transfer functions

$$\mathbf{T}_{qw} = [\bar{\mathbf{C}}_1 \quad 0] (s\mathbf{I} - \mathcal{A}_{cl})^{-1} \mathcal{B}_{cl}, \quad (4.35)$$

$$\mathbf{T}_{\phi w} = [0 \quad -\mathbf{F}] (s\mathbf{I} - \mathcal{A}_{cl})^{-1} \mathcal{B}_{cl}, \quad (4.36)$$

will be used as performance metric to design the controller. $\|\mathbf{T}_{qw}\|_2$ is the \mathcal{H}_2 closed-loop system norm from the external disturbances to the controlled output

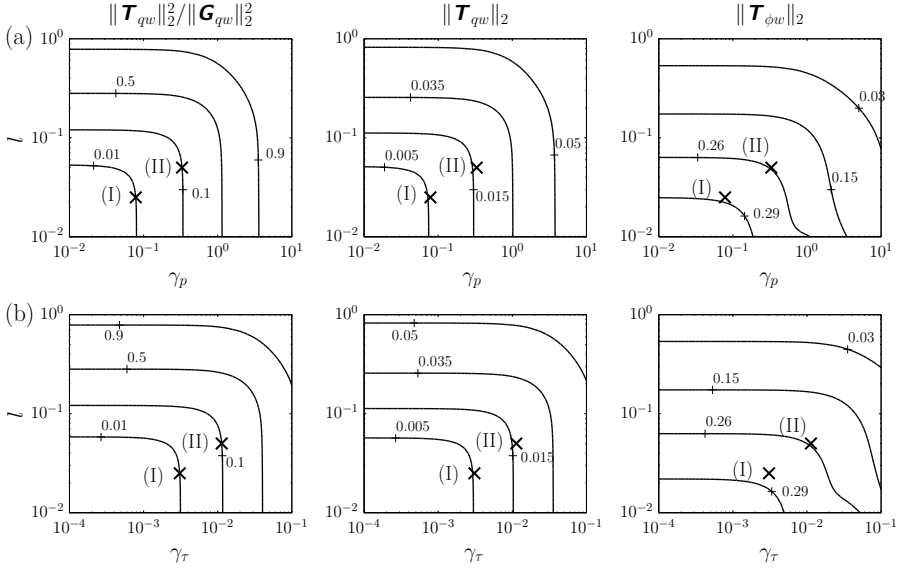


Figure 4.6: Contours of the closed-loop system norms $\|\mathbf{T}_{qw}\|$ (4.35), $\|\mathbf{T}_{\phi w}\|_2$ (4.36) and the relative energy norm $\|\mathbf{T}_{qw}\|_2^2/\|\mathbf{G}_{qw}\|_2^2$ ($\mathbf{G}_{qw} = 0.0525$). (a) pressure-based estimation. (b) shear-based estimation.

and is a measure for the control performance. $\|\mathbf{T}_{\phi w}\|_2$ is the closed-loop system norm from the external disturbances to the control input and is a measure for the control effort. These norms are related to the LQG cost function (4.30) through

$$\mathcal{J}_{LQG} = \|\mathbf{T}_{zw}\|_2^2 = \|\mathbf{T}_{qw}\|_2^2 + l^2 \|\mathbf{T}_{\phi w}\|_2^2, \quad (4.37)$$

where $\mathbf{T}_{zw} = \mathcal{C}_{cl}(sI - \mathcal{A}_{cl})^{-1} \mathcal{B}_{cl}$. Based on a convergence analysis for the system norms the order of the ROM and corresponding controller is chosen as $r = 50$. With this order the norms have converged sufficiently to the norms of the closed-loop system with the full-order controller and there is no loss in performance due to the truncated dynamics. Figure 4.6 shows the contours of the \mathcal{H}_2 system norms and the relative energy norm with both pressure-based estimation (a) and shear-based estimation (b) as function of the design parameters (γ, l) for the order $r = 50$ controller. A low value for the control penalty l gives an improved performance at the cost of a higher control effort (higher state feedback gain \mathbf{F}). A low value for γ reflects a low output uncertainty. This gives an improved estimator performance at the cost of a reduced robustness in case of unmodelled measurement inaccuracies. Due to the separation principle of the control design, the output equation (pressure or shear) only affects the performance of the state estimator which can be tuned through γ . Note that γ models a relative magnitude of the sensor noise, a convenient means to account for inaccuracies in the control design. The true magnitude of the noise will be substantially different for actual shear and pressure sensors, which typically measure in Volts. Any sensor calibration, e.g. Volts to Pascal, will also change the

magnitude of the noise. Therefore no conclusions can be drawn regarding robustness to sensor inaccuracies based on the magnitudes of γ_τ and γ_p compared to each other in figure 4.6. To make a fair comparison between the two measurement cases, γ is adjusted such that both have the same performance from a design perspective. It can be observed that, through proper selection of γ , the same performance can be achieved for a given l from an \mathcal{H}_2 design perspective, with both pressure and shear measurements. Two performance levels are chosen, those corresponding to a 99% (Design point (I)) and a 90% (Design point (II)) controlled output energy reduction. The pressure-based controllers are characterised by (I) $l = 0.025, \gamma_p = 0.0785$, (II) $l = 0.05, \gamma_p = 0.3306$ and the shear-based controllers by (I) $l = 0.025, \gamma_\tau = 0.0031$, (II) $l = 0.05, \gamma_\tau = 0.0113$. These design points are on the curvature of the performance level which provides a good trade-off between performance, control effort and robustness. For the selected controllers, robustness to output uncertainties is given priority in determining this trade-off.

4.7. RESULTS

The selected controllers are evaluated using linear simulations of the closed-loop system. The model defining a plate with a total length of $L_{sim} = 400$ as discussed in section 4.3 is used for simulating the response of the closed-loop system. All simulations are performed with a sampling time of $\Delta t = \Delta t^* \delta_0^* / U_0^* = 0.2$. The performance is studied for exponentially growing perturbations introduced using optimal initial conditions. The initial condition is optimised to provide the maximum energy growth

$$G(t) = \frac{E(t)}{E(0)} = \max_{\mathbf{u}_0} \frac{\|\mathbf{u}\|_{L^2}^2}{\|\mathbf{u}_0\|_{L^2}^2} = \max_{\|\mathbf{u}_0\|_{L^2}^2=1} \|\mathbf{u}\|_{L^2}^2 \quad (4.38)$$

at the given final time $t_{max} = 700$. At this final time the initial condition is spatially localised upstream of the control region. The initiation of the perturbations is independent of the disturbance model used to design the controller and provides a good benchmark to evaluate the effectiveness of the proposed control design [105]. In addition this perturbation case allows the proper evaluation of the estimator performance as the perturbations convect through the control domain. For the design of the estimator the problem is scaled in terms of γ . The role of γ is to account for uncertainties in the control design and is not used to define the measurement noise in the simulations. First the nominal performance without uncertainties is evaluated in section 4.7.1. The estimated pressure output $\hat{p} = \mathbf{C}\hat{\mathbf{u}}$ of the Kalman filter can be sensitive to non-physical estimated velocities near the inflow boundary of the control domain if these contribute significantly to the output behaviour. Therefore the sensitivity of the location of the computational inflow boundary, and thus the inflow disturbance model, on the controller performance is investigated in section 4.7.2. The effect of sensor noise, uncertainties in the Reynolds number and the pressure gradient is discussed in section 4.7.3.

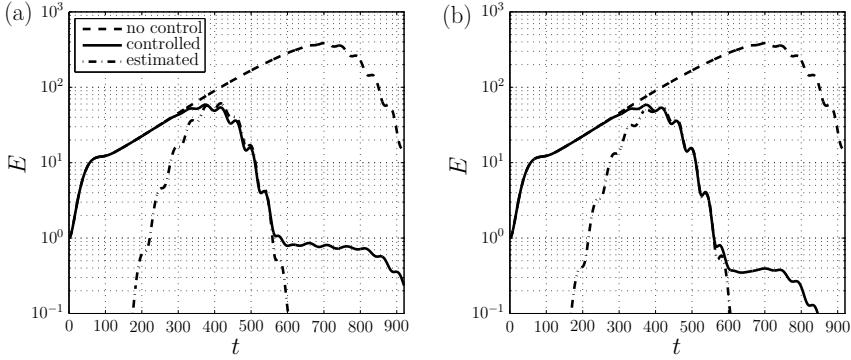


Figure 4.7: Uncontrolled, controlled and estimated energy for the optimal perturbation at $Re_0 = 500$, $m = -0.02$. Controller (I) is considered. (a) pressure-based. (b) shear-based.

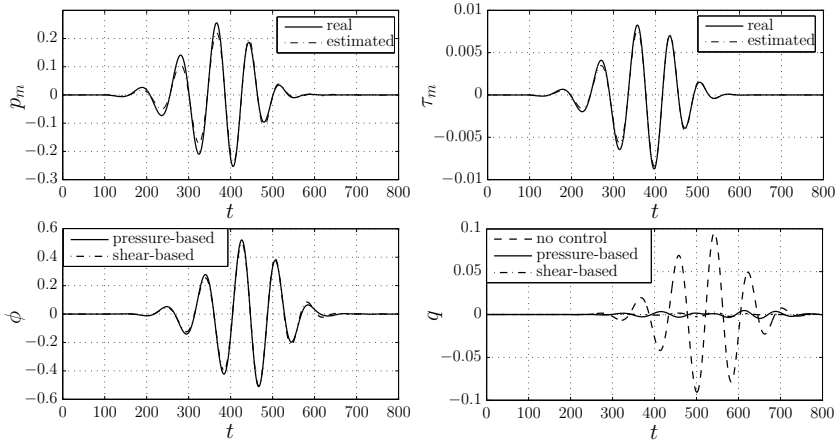


Figure 4.8: Input-output signals for control of the optimal perturbation at $Re_0 = 500$, $m = -0.02$. Controller (I) is considered.

4.7.1. NOMINAL PERFORMANCE

First the performance of controller (I) is evaluated for the nominal simulation case ($Re_0 = 500$, $m = -0.02$). Figure 4.7 shows the perturbation energy growth as function of time with both pressure-based estimation (a) and shear-based estimation (b). The input-output signals, which are the pressure measurement $p_m(t)$, the shear measurement $\tau_m(t)$, the amplitude of the blowing and suction $\phi(t)$ and the controlled output $q(t)$, are shown in figure 4.8. The controlled output $q(t)$ reflects the controller performance as it is used within the control objective that is minimised by the controller. Snapshots of the uncontrolled and controlled streamwise perturbation field with pressure-based estimation at $t = 200$, $t = 330$, $t = 450$ and $t = 600$ are shown in figure 4.9.

The initial perturbation for the uncontrolled case leads to an energy amplification of $G(t_{max}) \approx 3 \times 10^2$. After an initial transient growth the perturbation quickly

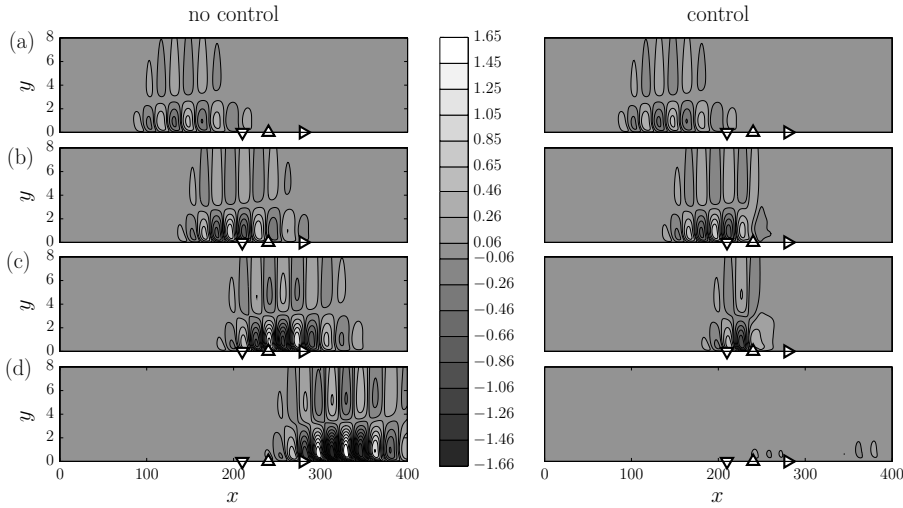


Figure 4.9: Snapshots of the uncontrolled and controlled streamwise perturbation field at $t = 200$ (a), $t = 330$ (b) $t = 450$ (c) and $t = 600$ (d). Pressure-based controller (I) is considered. The triangles indicate respectively the position of the measurement sensor (∇), the actuator (Δ) and the controlled output (\triangleright).

develops into an exponentially growing wavepacket that propagates downstream. The energy of the uncontrolled wavepacket reaches a maximum at $t = 700$ after which it decays again as the wavepacket leaves the computational domain $x_{sim} \in [0, 400]$. After the wavepacket passes the sensor ($t > 100$) the estimated perturbation energy quickly aligns with the energy of the actual state. The estimated state is used to determine the control input and the perturbation grows only until it reaches the actuator position after which it begins to decay due to the control action of unsteady blowing and suction. An energy reduction of more than two orders of magnitude is subsequently achieved. The estimated perturbation goes to zero again, while the remaining perturbation leaves the localised control domain $x_c \in [150, 310]$ after roughly $t = 550$, see also snapshot (d) in figure 4.9. The estimated energy does not align exactly due to the non-physical effect of the boundary conditions near the inflow and outflow of the control domain. The non-physical effect at the off-design frequencies near the inflow boundary contributes more to the pressure output behaviour, resulting in a slightly reduced performance as compared to the shear-based controller.

A larger over-estimation can be observed with pressure measurements, which can be contributed to the additional output uncertainty as discussed in section 4.5. The over-estimation decays over time as the perturbations propagate away from the computational inflow of the control model. This can also be viewed through the real and estimated pressure at the sensor location in figure 4.8. Note that the pressure $p_m(t)$ and shear measurements $\tau_m(t)$ are very similar. They have a negligible shift in phase compared to each other, but the pressure is amplified more with approximately a factor of 30. This is in accordance with the choice of the design parameter γ to

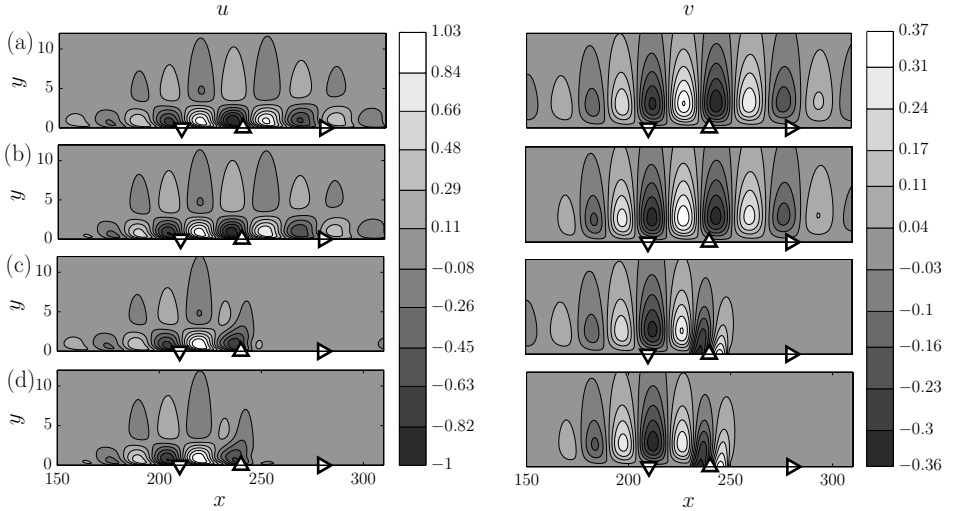


Figure 4.10: Snapshots of the perturbation velocity within the control domain $x_c \in [150, 310]$ at $t = 390$ for the uncontrolled and controlled optimal perturbation. Pressure-based controller (I) is considered. (a) Estimated velocity without control. (b) True velocity without control. (c) Estimated velocity with control. (d) True velocity with control. The triangles indicate respectively the position of the measurement sensor (∇), the actuator (Δ) and the controlled output (\triangleright).

achieve the same performance from an \mathcal{H}_2 design perspective. The control input confirms the filtering of the measurement and the wave cancellation to minimize the wall shear stress defined by q . By minimizing q the energy is reduced in the entire region upstream of the control domain. Both controllers are able to attenuate the energy with more than two orders of magnitude.

The performance of the state estimator is also visualised in figure 4.10, which shows a snapshot of the reconstructed and true flow field at $t = 390$ in the control domain $x \in [150, 310]$ with pressure-based estimation. Figure 4.10(a) shows the estimated flow field without control, figure 4.10(b) shows the real flow field without control, figure 4.10(c) shows the estimated flow field with control and figure 4.10(d) shows the true flow field with control. The estimated field without actuation applied is also shown to visualize the reconstruction in the downstream region where the controlled output is defined. The perturbations are very well reconstructed in the input-output region. As a result the control is able to effectively dampen the incoming perturbations and the effect of the suction and blowing on the flow field can clearly be observed.

Figure 4.11 shows the wall normal maximum amplitude of the rms streamwise velocity perturbation [116]

$$u_{\text{rms,max}}(x) = \max_y \sqrt{\frac{1}{T} \int_0^T |u|^2 dt} \quad (4.39)$$

for the uncontrolled and controlled case. The performance of controller (I) is compared with controller (II). The amplitude of the perturbation grows exponentially

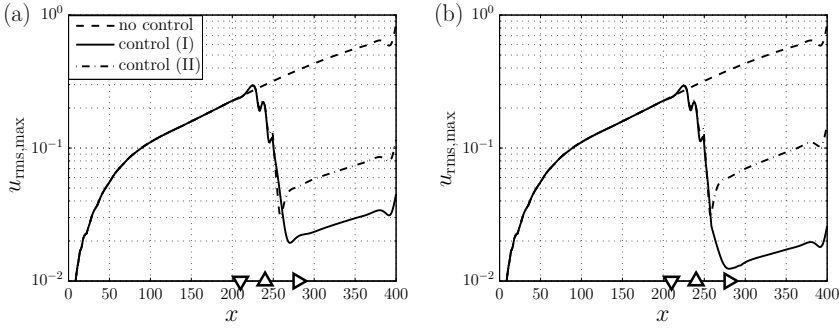


Figure 4.11: The rms streamwise perturbation velocity. (a) pressure-based. (b) shear-based. The triangles indicate respectively the position of the measurement sensor (∇), the actuator (Δ) and the controlled output (\triangleright)

until it reaches the actuator position at which it begins to decay due to the action of blowing and suction. Only a small amplification is present in the region of the control actuator ($230 \leq x \leq 250$). Controller (I) is able to reduce the amplitude with more than one order of magnitude at the location of the controlled output q ($x_q = 280$). Controller (II) is more conservative as it takes higher output uncertainties into account. It can be observed that controller (II) with pressure-based estimation achieves a better performance as compared with shear-based estimation and the additional output uncertainty no longer influences the performance. From these results it can be concluded that in the nominal case a comparable performance can be achieved with both pressure-based and shear-based control.

4.7.2. EFFECT OF DOMAIN TRUNCATION

In this section the sensitivity of the controller performance with respect to domain truncation is investigated. More specifically, the effect of the location of the computational inflow of the control domain, and thus the location of the inflow disturbance model is investigated. A controller is considered synthesised within the domain $x_c \in [180, 310]$. Compared to the nominal case in the previous section, the inflow is placed $\Delta x = 30$ closer to the location of the measurement sensor at $x_m = 210$. This corresponds to approximately one spatial wavelength $\lambda_x = 2\pi/\alpha_r$ of the most amplified perturbation mode for the investigated condition, see figure 4.4. The control design as presented in section 6 is performed with the truncated model and the design parameters are again selected such that controller (I) and (II) achieve respectively a 99% and 90% energy reduction from an \mathcal{H}_2 design perspective. Figure 4.12 shows the temporal energy growth with controller (I). Figure 4.13 shows the amplitude of the rms streamwise velocity (4.39) of controllers (I) and (II). It can be observed that the performance of pressure-based controller (I) has deteriorated as a result of the domain truncation. This can be contributed to the fact that the domain truncation results in higher pressure output uncertainties. Nevertheless, no severe deterioration can be observed. Higher output uncertainties are taking into account in the design of controller (II) and the performance is preserved in the

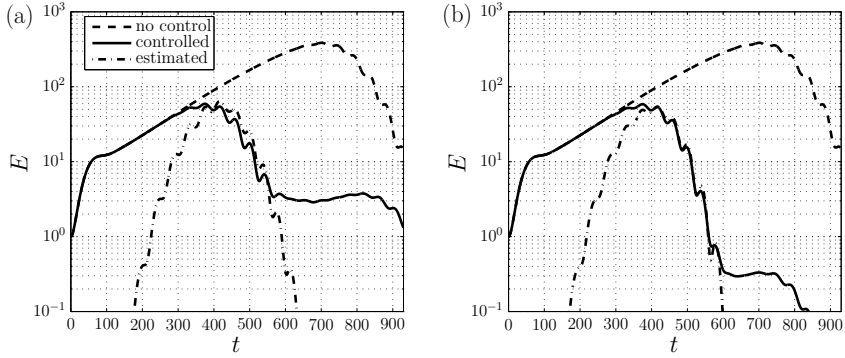


Figure 4.12: Results with the truncated control domain $x_c \in [180, 310]$. Perturbation energy for the optimal perturbation at $Re_0 = 500$, $m = -0.02$. Controller (I) is considered. (a) pressure-based. (b) shear-based.

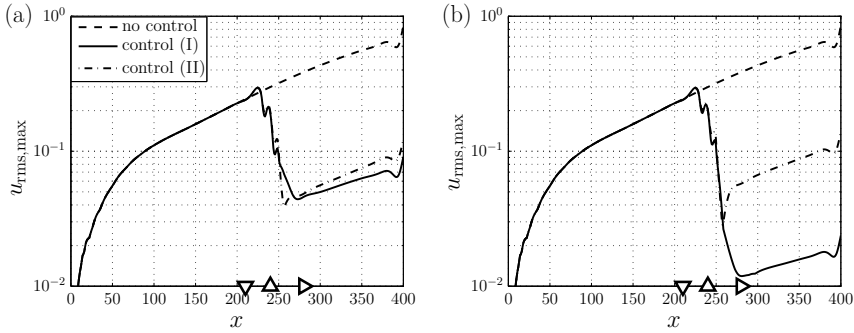


Figure 4.13: Results with the truncated control domain $x_c \in [180, 310]$. The rms streamwise perturbation velocity. (a) pressure-based. (b) shear-based.

case of a truncated domain. Actually pressure-based controllers (I) and (II) have comparable performance as can be seen from figure 4.13. The performance of both shear-based controllers has been completely preserved, as compared to the nominal case in figure 4.7(b), and the domain truncation has no effect. This illustrates the effectiveness of using the inflow disturbance model for estimation of the perturbations in the control domain.

4.7.3. ROBUSTNESS

When applying the controller in a real application, modelling uncertainties are unavoidable and deteriorate the nominal performance. The controller is designed in an optimal control framework and uncertainties are not directly taken into account as would be the case for a robust controller. In this section the controller is evaluated in off-design conditions. Both uncertainties in the pressure gradient characterised by the parameter m and the Reynolds number are considered. In addition the effect of sensor noise for the nominal case is investigated. The results for pressure-based estimation are summarised in Table 4.1. The results with shear-based estimation are

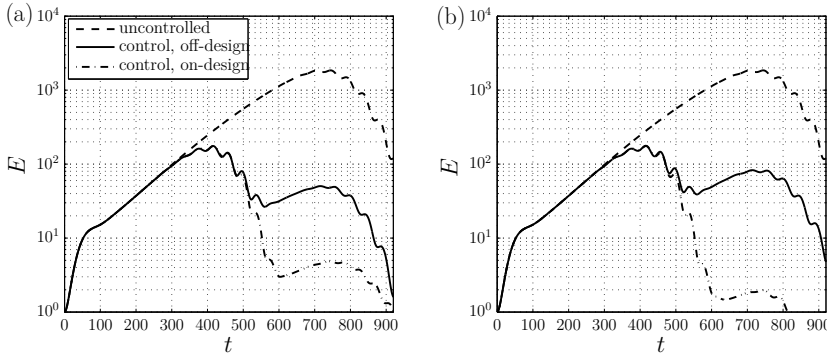


Figure 4.14: The perturbations energy with pressure-based estimation (a) and shear-based estimation (b) for an optimal perturbation at the off-design condition $Re_0 = 500$, $m = -0.03$. Controller (I) is considered and compared with the same controller acting on the designed conditions.

omitted in table 4.1 as they provide no significant difference with respect to performance, similar to what has been observed in the previous section. For example, the effect of a variation in pressure gradient with $m = -0.03$ is shown in figure 4.14. To illustrate the loss in performance, controller (I) designed for $m = -0.02$ is compared with a controller acting at the simulation conditions. In accordance to the linear stability theory the flow is more unstable and the optimal initial condition provides a larger amplification $G(t) = E(t_{max})/E(0) \approx 2 \times 10^3$. The controllers designed for $m = -0.02$ still provide an acceptable performance. Similar results are obtained with variations in the Reynolds number, see Table 4.1. In case of small variations the controller is still able to reduce the energy peak between one and two orders of magnitude. A progressive loss of performance is observed for larger deviations from the design conditions. This can be contributed to the different speed, spatial wave-length and growth of the wavepacket. This makes the control out of phase with the perturbations. Nevertheless, the controller provides an energy reduction and does not destabilize the flow in case of large uncertainties. For example, for the case $Re_0 = 800$, $m = -0.04$ the controller reduces the peak energy with approximately 65%. There is also no large sensitivity in the choice of the design parameters. Controller (II) takes higher levels of uncertainties into account in the design and the performance is more preserved. Nevertheless, controller (I) still achieves a better performance in most simulation cases.

Additional simulations have been performed in which the measurement is corrupted with Gaussian white noise with rms intensity σ_n . The effect of noise on the performance depends on the relative magnitude of the noise with respect to the measurement information (signal to noise ratio). Therefore the effect of noise is only considered for the nominal case as the amplification from the initial condition to the pressure measurement varies significantly between the simulation conditions (Energy amplification between $10^2 - 10^7$). Higher noise intensities give a reduced performance, but the effect is less significant as compared with parameter variations. In case of realistic relative noise intensities the controller is properly able to filter the measurement information and to preserve the performance. This is to be

Simulation settings			Design point	Controlled output reduction	Energy reduction
Re_0	m	σ_n		$\frac{\text{rms } q_{con}}{\text{rms } q_{unc}}$	$\frac{E(t_{max})_{con}}{E(t_{max})_{unc}}$
500	0	0	(I)	0.4212	0.1808
500	0	0	(II)	0.3102	0.0841
500	-0.02	0	(I)	0.0553	0.0021
500	-0.02	0	(II)	0.1328	0.0189
500	-0.03	0	(I)	0.1754	0.0264
500	-0.03	0	(II)	0.2622	0.0692
500	-0.04	0	(I)	0.3502	0.1149
500	-0.04	0	(II)	0.4120	0.1642
500	-0.06	0	(I)	0.6558	0.4255
500	-0.06	0	(II)	0.6850	0.4549
400	-0.02	0	(I)	0.1993	0.0381
400	-0.02	0	(II)	0.2548	0.0666
600	-0.02	0	(I)	0.1521	0.0184
600	-0.02	0	(II)	0.1547	0.0185
800	-0.02	0	(I)	0.4128	0.1600
800	-0.02	0	(II)	0.3688	0.1159
400	-0.03	0	(I)	0.1861	0.0334
400	-0.03	0	(II)	0.2925	0.0945
600	-0.03	0	(I)	0.2700	0.0630
600	-0.03	0	(II)	0.3095	0.0851
800	-0.04	0	(I)	0.5957	0.3412
800	-0.04	0	(II)	0.5937	0.3266
500	-0.02	0.02	(I)	0.0575	0.0023
500	-0.02	0.02	(II)	0.1378	0.0209
500	-0.02	0.05	(I)	0.0645	0.0022
500	-0.02	0.05	(II)	0.1431	0.0221
500	-0.02	0.15	(I)	0.1446	0.0082
500	-0.02	0.15	(II)	0.1959	0.0284

Table 4.1: Performance parameters to evaluate the robustness ($\text{rms } q = \sqrt{\frac{1}{T} \int_T |q|^2 dt}$).

expected as sensor noise is taken into account in the control design. Note that for the case $\sigma_n = 0.15$ the pressure measurement is corrupted with approximately 100% with respect to its magnitude, see figure 4.8 for the input-output signals.

4.8. CONCLUSIONS

In practical flow control applications, real-time measurements can only be obtained via sensors at discrete locations at the wall. Especially pressure-based sensors are technically attractive by ensuring that the associated costs of active flow control are positively balanced by net power savings. However, in past studies, implementation of pressure sensing in control design has not been treated in a systematic way as part of the control design methodology. In this chapter the problem of point pressure output feedback control of 2-D boundary layer instabilities is addressed. A new approach is presented to design and synthesize reduced-order compensators for estimation and control directly from the governing equations. The use of pressure

measurements for dynamic flow estimation gives rise to additional modelling difficulties and output uncertainties as the pressure at a single point is related to global information of the flow field. These uncertainties are accounted for by accurately modelling the effect of upstream perturbations on the output. The input-output behaviour, which forms the basis for the estimation strategy, between the external flow perturbations and the pressure at wall is obtained using a novel method based on spatial integration of the governing equations. The results show that the dynamic estimation strategy is capable of obtaining accurate time-resolved estimates of the convective perturbation field in the localised control domain from pressure measurements at a single location at the wall. As a result the controller is able to significantly suppress the perturbation growth, also in case of model uncertainties in both the Reynolds number and pressure gradient.

The controller is also compared against an equivalent controller formulation based on shear stress measurements. It is shown that, through proper selection of the controller design parameters, which parameterise the estimation and the state feedback control problem, a comparable performance and robustness can be achieved with both pressure and shear output feedback control. The comparison is conducted assuming an “all else equal” perspective to investigate whether the additional modelling challenges related to pressure measurement affect the maximum attainable performance. However, pressure sensors are commonly better than shear stress sensors from the viewpoint of signal to noise ratio. Accurate damping of TS waves requires highly sensitive sensors, which are able to detect low amplitude TS waves in their early linear stage. In the next chapter the controllers are applied in experiments. This work has addressed important issues related to this next step, including modelling of the input-output dynamics and obtaining experimentally feasible low-order controllers, and thus provides an important step forwards for transition delay in boundary layer flows.

5

Experimental estimation and control of natural TS waves

A compensator strategy that incorporates a model based on the linearised Navier-Stokes equations, aimed to suppress Tollmien-Schlichting waves naturally occurring in low freestream turbulence conditions is experimentally demonstrated. Experiments have been conducted on a flat plate geometry under the influence of an externally imposed adverse pressure gradient. A Kalman filter is used to estimate the effect of upstream disturbances based on pressure information from a single wall-embedded microphone. This information is used by the controller to cancel the incoming perturbations using a surface DBD plasma actuator. The estimates obtained from the Kalman filter are compared with experimental data obtained using Particle Image Velocimetry (PIV). It is shown that the Kalman filter is able to estimate the spatio-temporal behaviour of the perturbation field even though it relies on a priori assumptions on the upstream disturbance environment. The performance of the controller and its robustness to varying freestream velocities is analysed in comparison with open-loop continuous forcing. It is shown that the controller is able to additionally reduce the fluctuating pressure power at the most amplified frequencies with more than one order of magnitude and is capable of reducing the standard deviation of the downstream sensor signal between 30-60% for a range of off-design free-stream velocities.

This chapter is under review in AIAA journal as: H.J. Tol, C.C. de Visser and M. Kotsonis, *Experimental model-based estimation and control of natural Tollmien-Schlichting waves*, 2018

5.1. INTRODUCTION

Tollmien-Schlichting (TS) waves play an important role in the process of laminar-turbulent transition on unswept wings in low freestream turbulence conditions ($< 1\%$). By suppressing the growth of TS waves in their early linear stage it is possible to delay the transition process, extend laminar flow and reduce skin friction drag. Active control can be performed in an open-loop manner in which the actuator settings have been predetermined and do not depend on measurements, e.g. steady operation of plasma actuators [133]. Open-loop control typically involves changing the mean flow conditions to achieve stabilisation of the flow, which requires relative high power consumption. Reactive control strategies (i.e. closed-loop) on the other hand aim at directly targeting the inherent instability mechanism and potentially lead to a better performance and lower power consumption. Early closed-loop applications based on the wave-superposition principle [134–136] such as phase control and opposition control successfully attenuated deterministically generated TS waves. However, naturally occurring TS waves exhibit a bounded but non-deterministic spectrum of phases and frequencies. Several studies have treated the cancellation of natural and non-deterministically excited TS waves using adaptive control methods and model-free control methods, such as the filtered x-LMS algorithm [137–140] and extremum seeking control [141]. In addition, the application of model-based control theory provides a solid framework for model identification and controller design, which showed promising results in both numerical studies [85, 100, 109] and experiments [87, 120, 142, 143]. The present study follows the latter approach by developing and implementing a model-based estimator and controller for the attenuation of TS waves in an experimental framework.

Laminar boundary layers behave as noise amplifiers of upstream disturbances and are in particular challenging to control. Convective instabilities that appear as distinct wavepackets, such as TS waves, are generally uncorrelated to each other. Furthermore, there exists only a small window of opportunity to suppress these instabilities, between the time they are large enough to be detected by sensors and the time they become nonlinear. The convective nature of the flow and the lack of a physical downstream-to-upstream feedback mechanism favour a feedforward actuator-sensor configuration. In this case a sensor located upstream of the actuator measures the incoming perturbations, while the controller can use a model of the perturbation evolution to devise an actuator signal that cancels the perturbations. While such disturbance feedforward systems result in the best nominal performance, it is well known that they rely on an accurate model of the flow, including an accurate representation of the upstream disturbance environment [9, 27, 87].

The model can be obtained either from the governing equations of fluid flow (white-box) or from a sample of input-output measurements using systems identification techniques (black-box). Numerical studies commonly focus on optimal and robust estimation and control laws based on a Galerkin state-space formulation of the linearised Navier-Stokes equations [33, 37]. Such white-box model-based controllers provide important physical insights and give the best possible (i.e. optimal) performance for a given set of inputs-outputs. However, this approach requires the use of empirical model reduction methods [32] to synthesise experimentally feasi-

ble controllers. Furthermore, this approach requires a priori assumptions on the source and distribution of the external disturbances, which is not precisely known in real flow environments. Hervé *et al.* [144] and Sipp and Schmid [9] argued that Galerkin models are inappropriate due to the challenges in obtaining an accurate representation of the upstream disturbance environment. To mitigate these challenges, they recommended data-based system identification techniques for experimental control of amplifier flows. In this case the input-output relation is directly identified from a sample of input-output measurements. This approach avoids the need for a predefined disturbance model by processing information from an upstream sensor, which approximates the influence of the upstream disturbances. For example, this is achieved by incorporating this information in an auto-regressive design [142] or finite impulse response filters [120]. A drawback on the other hand is that system-identified linear models can present challenges when nonlinearities and stochastic velocity components are present in the flow, such as the presently considered case of natural TS waves cancellation.

The present work investigates the practical feasibility and performance of a white-box model-based compensator for estimation and control of TS waves in an experimental environment where the instabilities appear and grow naturally. Of the previous works, the approach taken in this study follows the guidelines set by the work of Fabbiane *et al.* [87]. Fabbiane *et al.* [87] were the first to demonstrate the suppression of artificially induced perturbations in experiments based on a DNS model of the flow. To the author's knowledge, the present study provides the first experimental demonstration of model-based control of natural TS waves in an experimental framework. This work makes use of the combined framework presented in chapters 2-4, to synthesize reduced-order controllers directly from the governing equations without the use of prior numerical data or empirical model reduction. The approach combines state-space discretisation of the linearised Navier-Stokes equations using multivariate splines with exact balanced truncation to design experimentally feasible low-order controllers. It was shown that the use of physically motivated inflow disturbance models allows for efficient estimation of the perturbations within localised computational domains, also in the case of unknown/unmodelled upstream disturbances. This framework is applied in this study for estimation and control of Tollmien-Schlichting waves. For the experimental realisation of the control objectives, wind tunnel experiments have been conducted in an anechoic, low-turbulence facility. A two-dimensional laminar boundary layer is established on a flat plate geometry under the influence of an externally imposed adverse pressure gradient. A high-sensitivity surface microphone that measures the fluctuating pressure at the wall and a Dielectric Barrier Discharge (DBD) plasma actuator are used as actuator/sensor pair. The model-based estimator and controller are implemented in a real-time FPGA-based digital signal processor. Particle Image Velocimetry (PIV) measurements are used to compare the spatio-temporal estimates obtained from the state estimator with the natural perturbation fields to validate the modelling methodology. The experimental control performance of the combined estimation/feedforward control approach is investigated in both nominal designed conditions and in off-design conditions to evaluate the robustness.

5.2. EXPERIMENTAL SET-UP

5.2.1. FLOW FACILITY AND PIV SET-UP

A schematic of the experimental set-up is shown in figure 5.1. The experiment is performed in the newly constructed Anechoic Vertical Tunnel (AVT) at TU Delft, enabling a free-stream turbulence intensity under 0.04% at the tested conditions. The test section features a square cross-section of 0.5 m on each side. Positioned at a distance of 0.1 m from the centreline, a flat plate of 1 m length and 0.5 m width features a super-elliptical leading edge and a movable flap at the trailing edge to control the stagnation point, which ensures a smooth development of the boundary layer. The freestream velocity is measured with a pitot-static tube located upstream of the leading edge and is set at $U_\infty = 9.4$ m/s as design condition for the control design. Natural two-dimensional boundary layer instabilities (i.e. TS waves) are introduced at the leading edge via boundary layer receptivity to acoustic and vortical disturbances in the freestream flow and amplify as they convect downstream. An adjustable flexible wall opposite to the flat plate controls the pressure gradient to increase the amplification rate of the perturbations and to promote transition at the relative low freestream velocities. A streamwise array of 24 surface pressure taps, positioned mid-span, is used to determine the pressure distribution (C_p) and to characterise the mean flow (see next section).

For the current study two independent experimental campaigns were performed. The first was performed using the set-up in figure 5.1, in an uncontrolled and clean setting, where the actuator was not present on the flat plate. The primary objective of this first campaign was to characterise the base flow and the stability properties of the laminar boundary layer, which are crucial for control design. In addition, the preliminary study provided the necessary experimental base to validate the modelling methodology for the dynamic flow estimation. The objective of the second campaign was the application and demonstration of reactive control, which is presented in section 5.4. Care was taken to ensure identical flow conditions between the two experimental campaigns. The C_p distributions with the 2σ bounds for both experiments are shown in figure 5.2. It can be observed that the distributions match closely in the actuator-sensor region up to $x = 0.4$ m. The kink in the pressure and corresponding increase of standard deviation after $x = 0.4$ m is an indication of laminar-turbulent transition of the boundary layer.

A two-component planar Particle Image Velocimetry (2C-PIV) system was employed to investigate the flow field in the $x-y$ plane and to compare the modelled/estimated velocity perturbation fields with the experimental perturbation fields. Illumination was provided by a Quantel EverGreen dual-pulse Nd:YAG laser of average pulse energy of 200 mJ. The laser beam (wavelength 532 nm) was arranged into a light sheet of approximately 1 mm thickness, aligned with the $x-y$ plane at the midspan of the flat plate. A 16 MPx LaVision Imager LX Pro CCD camera equipped with a Nikkor 105 mm Macro objective set at aperture of $f/5.6$ was employed to register the particle images. A cropped sensor resolution of 4920×750 pixels was used to image a Field Of View (FOV) of $130 \text{ mm} \times 20 \text{ mm}$, arriving to a magnification factor of approximately 0.2. The flow was seeded by a Safex fog generator producing water/glycol-based particles of average diameter of $1 \mu\text{m}$. Raw

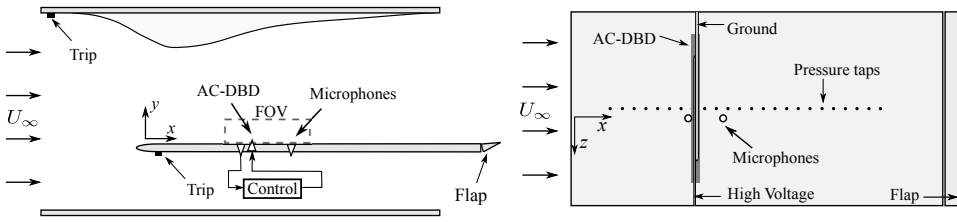


Figure 5.1: Schematic of the experimental set-up (not up to scale).

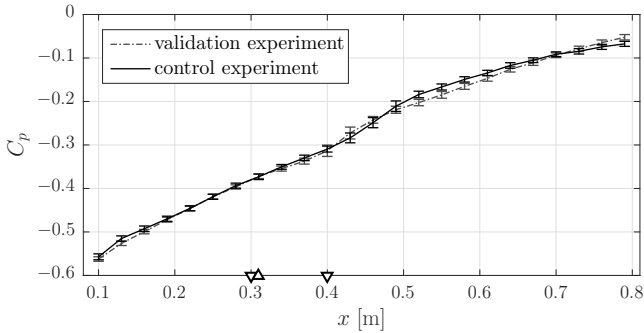


Figure 5.2: C_p distribution for the two experimental campaigns. The triangles indicate the position of the microphones (∇) and the plasma actuator (\triangle).

particle image pairs were captured at a frequency of 2.2 Hz with an interframe time interval (Δt) of 26 μs . Velocity vector fields were computed using the multi-step interrogation algorithm [145] with a final interrogation window of 12×12 pixels with a 50% overlap. The velocity vectors were returned on a grid of 9 vectors per mm. A total of 500 velocity snapshots were obtained for each measurement case. For the experimental data presented in this work, uncertainty is quantified using the correlation statistics method [146]. The local error for instantaneous velocity measurements is estimated to be $\epsilon u \approx 1\%$.

5.2.2. CONTROL SYSTEM ELEMENTS

The flow is controlled using an Alternating Current Dielectric Barrier Discharge (AC-DBD) plasma actuator. It consists of a 10 mm wide grounded and encapsulated copper electrode of 30 μm thickness and a 5 mm wide exposed electrode connected to a high voltage amplifier (Trek 20/20C). No streamwise gap is formed between the electrodes. The interface of the two electrodes is chosen as the reference position of the actuator, which is placed at $x_{\text{act}} = 0.31$ m. The active length of actuator (along which plasma is formed) has a length of 0.3 m in the spanwise direction. Two layers of dielectric polyimide tape (Kapton) with a total thickness of approximately 100 μm separate the two electrodes. Preliminary measurements verified that the geometric protrusion of the actuator has no influence on the transition process.

The actuator is driven by an amplitude modulated voltage signal formed by a

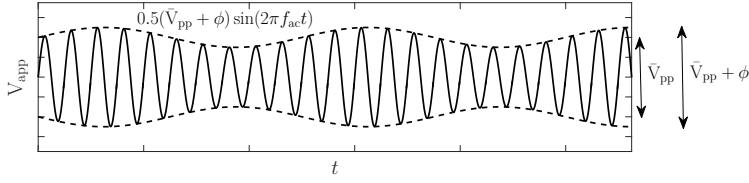


Figure 5.3: Example of an applied voltage signal visualising the operation mode of the plasma actuator. Carrier frequency f_{ac} , mean applied peak-to-peak voltage \bar{V}_{pp} and the unsteady amplitude modulation ϕ specified by the controller.

carrier sinusoidal wave and an unsteady amplitude modulation that is specified by the controller. An example of an applied voltage signal illustrating the actuator operation is shown in figure 5.3. The carrier signal is required to form the plasma. The carrier frequency of the actuator is set to 2 kHz, which is one order of magnitude higher than the most unstable TS waves for the investigated conditions. The amplitude of the applied voltage signal determines the strength of the plasma formation. For this actuator an operating range from $V_{pp} = 6$ kV to $V_{pp} = 16$ kV has to be maintained in order to produce a stable discharge [147]. The voltage is the peak-to-peak voltage (V_{pp}) of the applied waveform. To account for the threshold a constant mean forcing is applied, whereas the compensator can modulate the amplitude of the high-voltage supply through the control signal ϕ [87, 109, 141]. The mean forcing also naturally accounts for the unidirectional forcing constraint of the actuator in the control design [109]. The compensator will be discussed in detail in section 5.3. A mean voltage supply of $\bar{V}_{pp} = 8$ kV and $\bar{V}_{pp} = 9$ kV is investigated in this study. The applied voltage signal to the actuator is thus given by $V_{app} = 0.5(\bar{V}_{pp} + \phi) \sin(2\pi f_{ac} t)$ where ϕ is supplied by the compensator.

Two LinearX M53 microphones were employed to measure the fluctuation pressure at the wall. The microphones have an uncorrected frequency response of ± 5 dBspl (reference level $20 \mu\text{Pa}$) in the range 20 Hz - 20 kHz and an acoustic sensitivity of 140 mV / 94 dBspl (140 mV / Pa). The primary microphone located at $x = 0.3$ m provides the compensator with the required feedforward information. Additionally, a second microphone is placed at $x = 0.4$ m to monitor the performance of the compensator. The microphones were embedded in a cavity, within the body of the plate connected to the surface through a small pinhole of 0.1 mm in diameter. Care was taken in the design of the cavities in order to sufficiently separate the inherent cavity resonance frequency from the dominant TS wave frequencies. The microphones are calibrated in-situ to provide unsteady pressure measurements in Pascals using a GRAS 42AA pistonphone, outputting a root mean square (rms) pressure level of 114 dBspl (10 Pa) at a frequency of 250 Hz.

Software and hardware from National Instruments is used for the experimental implementation of the controller. LabView routines are constructed to control the input-output logic, process the measurement data from the microphone and generate the control input. The control logic is compiled and executed on a field-programmable gate array (FPGA) architecture using a NI 9022 CompactRIO digital signal processor. 16-bit A/D and D/A input/output modules are used for commu-

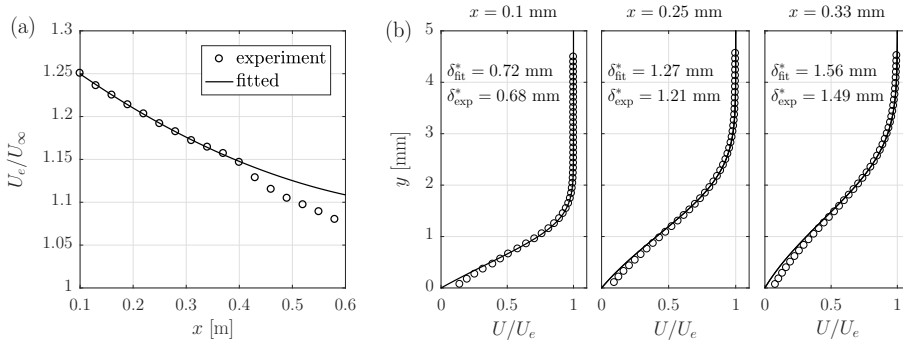


Figure 5.4: (a) Inviscid external velocity obtained from the static pressure taps and corresponding fit obtained with a second order polynomial using the data up to $x = 0.4$ m. (b) Comparison of the computed base flow with experimental data.

nication with the microphones and the plasma actuator. The control logic consists of two parallel loops. The first loop filters the measurement information (i.e. microphone readings) using a second order bandpass filter (50-800 Hz) and executes at a clock frequency of 100 kHz. The bandpass filter eliminates the DC component, the low frequency background noise and the high frequency electromagnetic noise due to the plasma actuator. The first loop is additionally responsible for the generation of the final plasma signal by producing the carrier signal and subsequently modulating it with the control signal. The second loop contains the actual compensator, in the form of vectors and two-dimensional state-space matrices (see section 5.3), which calculates the necessary amplitude modulation of the applied voltage signal and executes at 20 kHz.

5.2.3. BASE FLOW AND STABILITY

The base flow is obtained as a steady (i.e. time invariant) numerical solution of the boundary layer equations. The external freestream boundary condition is matched with the external inviscid velocity obtained from the measured C_p distributions, $U_e = U_\infty \sqrt{1 - C_p}$. To obtain a sufficiently smooth solution, the inviscid velocity distribution is fitted with a second order polynomial using the C_p data up to $x = 0.4$ m, just upstream of the kink in the pressure distribution, which is illustrated in figure 5.4(a). An analytical Falkner-Skan inflow profile based on the local approximation of $U_e(x) \propto x^m$ is assumed at the location of the first pressure tap $x_0 = 0.1$ m where m is calculated from the inviscid velocity distribution $m = (x_0/U_e)(dU_e/dx) = -0.032$. Figure 5.4(b) shows a comparison of numerically estimated and experimentally measured local velocity profiles at three locations in the considered domain. It can be observed that the mean flow fits the experimental data well, except near the wall where PIV becomes less accurate due to wall reflections and high flow shears, inherently corrupting the particle cross-correlation. It should be noted that PIV data has only been used for validation purposes and has not been used for computing the base flow for the control design.

Linear stability theory (LST) calculations for the base flow are shown in fig-

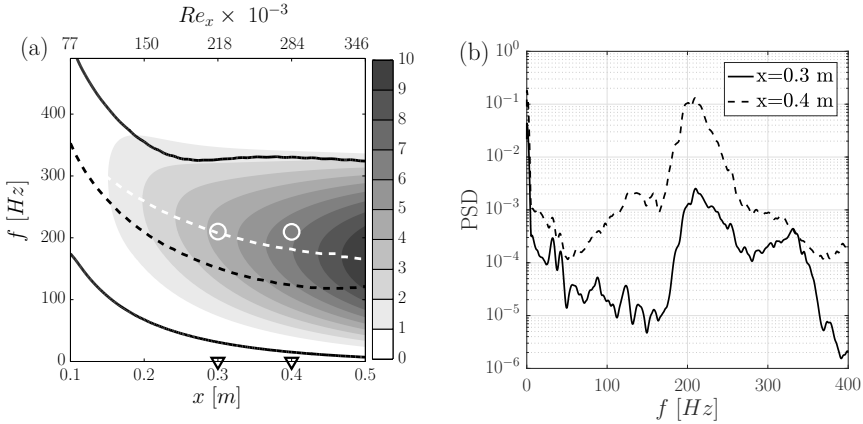


Figure 5.5: Neutral stability curve (black solid line) and integrated amplification (N) factor contours. The dashed black line shows the local most unstable frequency and the dashed white line shows the local maximum N-factor. The circles indicate the most amplified frequency measured by the pressure sensors.

ure 5.5(a) and the power spectral density (PSD) for the natural perturbations measured by the two pressure sensors is shown in figure 5.5(b). Based on the empirical N-factor method [148], LST predicts the location of transition at $x = 0.47$ m where the integrated amplification factor reaches $N \approx 9$. This estimation agrees well with the experimentally detected transition location at $x = 0.43$ m as observed from the kink in the C_p measurements in figure 5.2. The most amplified frequency measured at $x = 0.3$ m is 210 Hz which closely matches the LST predictions (dashed white line). In addition, background noise measurements have revealed that the peak at 330 Hz corresponds to noise caused by the wind tunnel power supply. The power at 210 Hz increases with two orders of magnitude between $x = 0.3$ m and $x = 0.4$ m. The slight mismatch with the LST prediction of the most amplified frequency at $x = 0.4$ m can be contributed to strong flow nonlinearities due to the larger perturbation amplitude further downstream. The good agreement between the theoretical predictions and the experimental results in the actuator/sensor region indicates that linear control based on a 2-D model of the flow can be effective for this set-up.

5.3. THE LINEAR COMPENSATOR

A disturbance feedforward controller is designed using the framework from chapter 3. The synthesis approach combines state-space discretisation of the governing equations using spline elements (chapter 2) with balanced truncation [67] to synthesize low order controllers. The computational domain and input-output layout used for control design is shown in figure 5.6. A localised computational domain $x_c \in [0.22 \text{ m}, 0.41 \text{ m}]$ is considered to avoid very large systems. The local Reynolds number at the beginning of the domain is $Re = U_0 \delta_0^* / \nu = 835$ with $U_0 = 11.3$ m/s and $\delta_0^* = 1.16$ mm, matching the experimentally measured flow parameters. The height of the domain is set to $H = 20$ mm $\approx 17\delta_0^*$. The finite-dimensional approx-

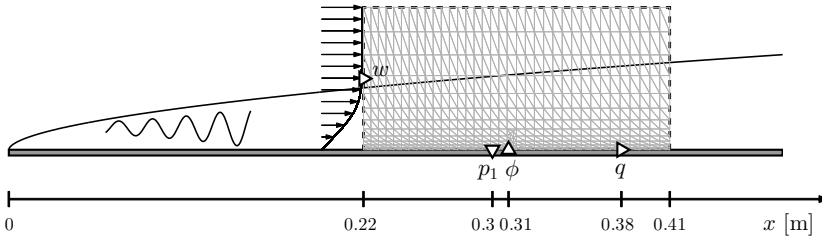


Figure 5.6: Computational domain (dashed line), mesh used for the discretisation (triangulation), and input-output configuration used for control design. The computational domain extends $164\delta_0^*$ in streamwise direction and $17\delta_0^*$ in the wall-normal direction, with $\delta_0^* = 1.16$ mm. Measurement p_1 , plasma actuator ϕ , controlled output q and inflow disturbance w .

imation of the system in state-space format is obtained using Galerkin projection of the linearised Navier-Stokes equations (LNSE) around the base flow with fifth order bivariate spline elements [40]. This system is in turn used to synthesise the reduced-order compensator. This gives rise to the following two systems

$$\dot{\mathbf{u}} = \mathbf{A}\mathbf{u} + \mathbf{B}_1\mathbf{w} + \frac{1}{k}\mathbf{B}_2\phi, \quad p_1 = \mathbf{C}\mathbf{u} + \mathbf{D}\mathbf{w} \quad (5.1)$$

$$\left. \begin{aligned} \hat{\mathbf{u}}_r &= \mathbf{A}\hat{\mathbf{u}}_r + \mathbf{B}_2\tilde{\phi} + \mathbf{L}(p_1 - \hat{p}_1), & \hat{p}_1 &= \mathbf{C}\hat{\mathbf{u}}_r \\ \tilde{\phi} &= \frac{1}{k}\phi - \mathbf{F}\hat{\mathbf{u}}_r \end{aligned} \right\} \quad (5.2)$$

Equation (5.1) is the full order system with $(\mathbf{A}, \mathbf{B}, \mathbf{C}, \mathbf{D})$ the state-space matrices resulting from the discretisation, \mathbf{u} the full order state vector, ϕ the control input that specifies the amplitude modulation of the actuator voltage signal, p_1 the upstream sensor signal and $\mathbf{w} = (w_d, w_n)$ the vector of state disturbances and measurement noise to account for uncertainties in the control design. The role of the gain k , and the underlying continuous models of the actuator \mathbf{B}_2 , sensor \mathbf{C} and the external disturbances \mathbf{B}_1 will be described later in this section. System (5.1) is balanced and reduced to retain the r most controllable/observable modes in the reduced-order model (ROM) defined by $(\mathbf{A}, \mathbf{B}, \mathbf{C}, \mathbf{D})$. Based on the available memory on the FPGA of the real-time controller the order of the ROM was set to $r = 40$. The ROM is subsequently used to design the compensator defined by (5.2) with \mathbf{L} and \mathbf{F} respectively the estimator (Kalman) gain and state-feedback gain to be optimized. The compensator combines a Kalman filter, which constructs a low-dimensional approximation from the upstream measurements p_1 and a state-feedback, which computes the control signal ϕ from the estimated state. An LQG design is employed to synthesise the compensator by solving two independent optimisation problems based on the ROM [29, Chapter 14]. In the following sections, the state-estimator and controller are discussed respectively.

5.3.1. STATE ESTIMATOR

The Kalman filter is designed to minimize the covariance of the difference between the reduced order state \mathbf{u}_r and the estimate state $\hat{\mathbf{u}}_r$ assuming that the system is

excited by Gaussian white noise. This requires a priori assumptions on the source and distribution of the upstream disturbance environment modelled by \mathcal{B}_1 and an output equation which relates the upstream perturbations with the pressure fluctuations at the measurement location at the wall. The derivation of the output equation is not trivial as the pressure is initially eliminated by formulating the LNSE on a divergence-free state-space to avoid singularities. In chapter 4 a novel method is presented to retrieve the output equation based on spatial integration of LNSE along the inflow and wall boundaries in a separate step, independently of the derivation of the state equations. Mathematically, the output operator \mathcal{C} represents the formal inverse of the pressure gradient along the inflow and wall boundaries. The disturbance model forms the basis for the model reduction and is crucial to allow an accurate reduction of the dynamics and capturing of the relevant flow physics. When model reduction is used in the design of the compensator, the spatio-temporal dynamics which are retained in the ROM and can be estimated depend on the spatio-temporal dynamics that are excited by the external disturbance model. It is shown in chapter 3, through a spatio-temporal frequency response analysis, that the use of inflow disturbance models allows for efficient estimation of the dominant flow perturbations in broad temporal and spatial bandwidth. The external disturbance model consists of a second-order low pass filter which accounts for the temporal dynamics of the most amplified Orr-Sommerfeld eigenfunction (in the present case corresponding to a TS wave). For the investigated conditions, the most amplified eigenfunction at the inflow $x = 0.22$ m is found at $f = 240$ Hz, see also figure 5.5.

To gain a more physical insight in the estimator performance and validate the modelling methodology, the estimates obtained from the estimator are compared with experimental data obtained from PIV. For this, an experiment under natural (i.e. non-actuated) conditions was performed in which the timestamps of the PIV snapshots were synchronised with the microphone-based unsteady pressure measurements. In total 500 PIV snapshots were obtained, sampled at a rate of 2.2 Hz. The upstream sensor signal p_1 was used as input to the estimator

$$\hat{\mathbf{u}}_r = \mathbf{A}\hat{\mathbf{u}}_r + \mathbf{L}(p_1 - \mathbf{C}\hat{\mathbf{u}}_r), \quad \hat{\mathbf{u}}_r(0) = 0, \quad (5.3)$$

which filters the data and reconstructs the state \mathbf{u}_r in the process. The state \mathbf{u}_r is the vector of reduced-order expansion coefficients, which is related to the full order coefficients through $\mathbf{u} = \mathbf{S}_r^{-1}\mathbf{u}_r$, where \mathbf{S}_r^{-1} are the first r columns of the inverse of the similarity transformation $\mathbf{u} \mapsto \mathbf{S}\mathbf{u}$ used to balance the system required for model reduction. In this way the flow field could be reconstructed from the reduced-order estimates and compared with experimental data at the corresponding PIV timestamps. A POD reconstruction of the PIV data was necessary in order to measure TS waves in the control region, since the measurement noise overlays the TS waves that have a low amplitude. The PIV data was reconstructed in the domain $x \in [0.285 \text{ m}, 0.345 \text{ m}]$, which encapsulates both the actuator and sensor used for control, using the first seven POD modes, which capture 30% of the total energy. It was verified that the further inclusion of additional low-energy modes was only adding more uniform noise to the reconstruction.

Figure 5.7 illustrates the comparison of the experimentally measured and esti-

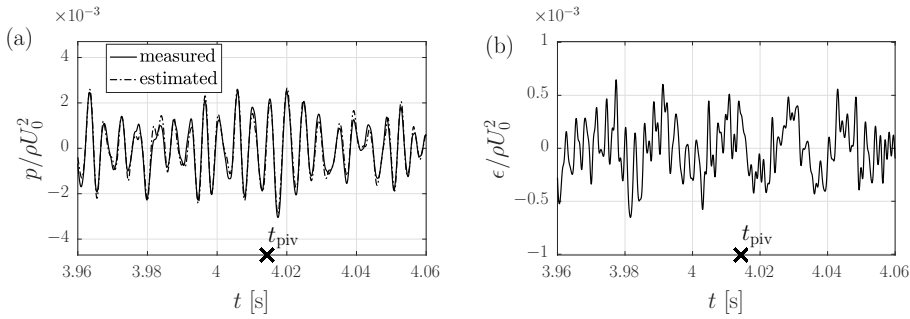


Figure 5.7: Filtering of the upstream sensor signal. (a) The measured pressure and estimated pressure. (b) the estimation error. The PIV snapshot corresponding to figure 5.8 is taken at $t = t_{\text{piv}}$.

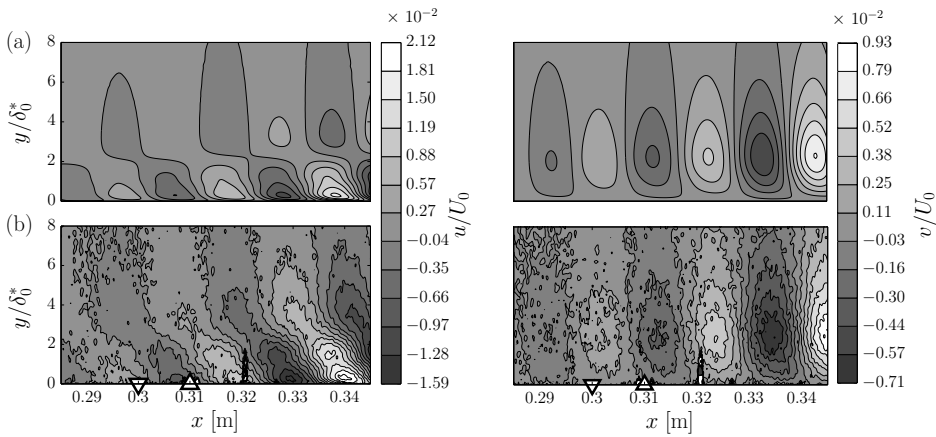


Figure 5.8: Snapshot of the perturbation velocity in the control region at $t = t_{\text{piv}}$ (see figure 5.7). (a) Estimated velocity field. (b) Experimental velocity field from POD reconstruction. The triangles indicate the position of the microphone (∇) and the plasma actuator (Δ).

mated pressure measurements for a time sample of 0.1 s. Respectively, figure 5.8 shows the instantaneous estimated velocity perturbation field and corresponding instantaneous POD reconstructed field at $t = t_{\text{piv}}$. Similar agreement was obtained for other timestamps were the TS waves were of sufficient amplitude. Figure 5.9 shows the root-mean-square (rms) value of the estimated and measured streamwise and wall-normal velocity components at four different streamwise locations. It should be noted that this is a temporal statistical quantity, while the PIV data is not time-resolved. Furthermore, the PIV data is less accurate near the wall and more noisy upstream, where the TS waves have a lower amplitude. Nonetheless important observations can be made from these results. The Kalman filter is able to reconstruct the signal and to obtain spatial-temporal estimates of the perturbation field. The shape, magnitude and phase of the perturbations match well in particular for the wall-normal component. The wall-normal component also has a simpler spatial structure and is less pronounced at the wall allowing for a better reconstruct-

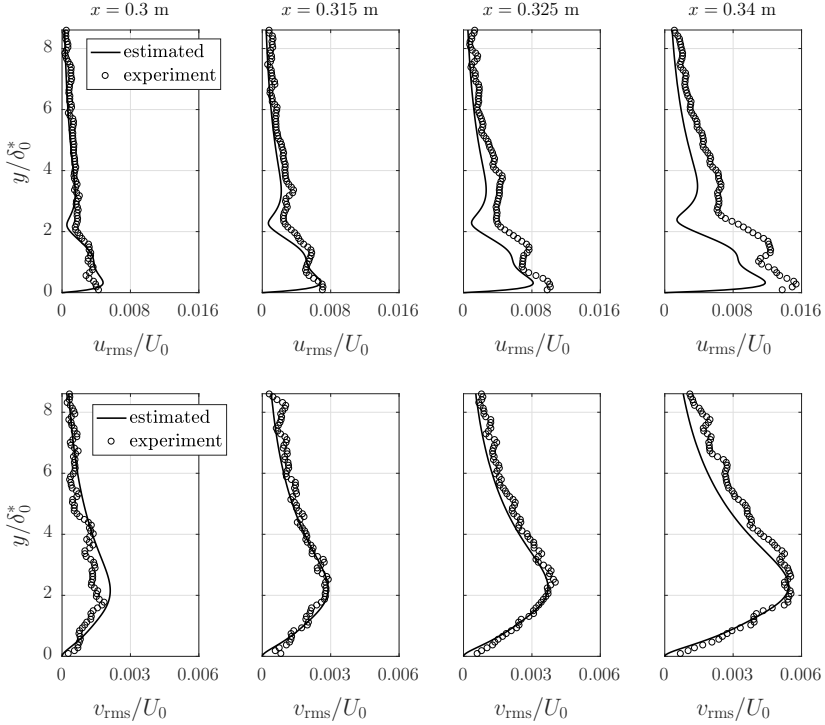


Figure 5.9: The estimated and experimentally measured rms value of the streamwise and wall-normal velocity components at four different streamwise locations.

tion with POD. The largest disagreement between the measured and reconstruct signal as well as between the measured and reconstructed perturbation field is in the maximum amplitude. The estimates deteriorate further downstream from the measurement sensor due to model uncertainties and nonlinearities. Note that the rms of the perturbation grows with a factor 3 between $0.3 \text{ m} \leq x \leq 0.34 \text{ m}$. Therefore, to achieve sufficient robustness the actuator is placed close to the feedforward sensor.

To the best of the authors's knowledge, this is the first time that model-based estimates of the perturbation field are matched with experimental data. The results indicate that model-based control theory, that makes a priori assumptions on the external disturbances, is able to predict the linear dynamics of natural flow perturbations.

5.3.2. CONTROLLER

The state feedback is designed to minimise the fluctuating wall-shear stress defined by $q = \int h(x)(\partial u / \partial y) dx$ where $h(x)$ is a Gaussian function centred at $x_q = 0.38$ with a width of 1 cm. The actuator is modelled as an in-domain body force with \mathcal{B}_2 the spatial distribution of the force, which is shown in figure 5.10. The body force

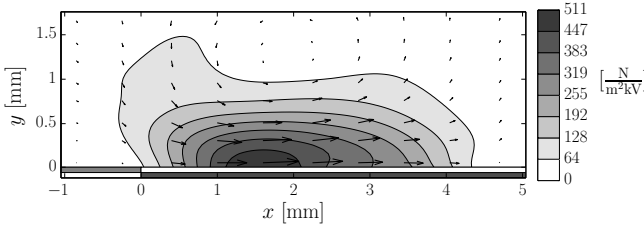


Figure 5.10: Spatial distribution of the linear plasma body force model used for controller design. Grey horizontal bars indicate the position of the exposed and covered electrodes.

is assumed to be linear in the unsteady modulation ϕ of the applied voltage signal $V_{\text{app}} = 0.5(V_0 + \phi) \sin(2\pi f_{\text{act}}t)$. The body force is obtained by fitting a linear model through experimentally derived body force distributions obtained by Kotsonis *et al.* [147], with the assumption that the body force is zero at and below the minimum discharge threshold of $V_{\text{pp}} = 6$ kV (i.e. prior to plasma ignition). It is assumed that the body force distribution gives a sufficient representation of the actual actuator effect, but the magnitude of the body force is assumed to be influenced by inherent uncertainties. The effective body force magnitude depends highly on the actuator fabrication, while the dielectric barrier degrades over time resulting in an increased power consumption and modified force magnitudes [149]. To make the control design tractable, an online tuning gain k is included to account for magnitude uncertainties in the body force model. This tuning gain scales the magnitude of the body force, or more convenient for control design, scales the magnitude of the control input $(1/k)\mathcal{B}_2\phi = \mathcal{B}_2\tilde{\phi}$. The controller is optimized for $\tilde{\phi}$ based on the nominal model and is multiplied with the tuning gain $\phi = k\tilde{\phi}$ when applied in real-time. The voltage signal to the actuator is thus given by $V_{\text{app}} = 0.5(V_0 + k\tilde{\phi}) \sin(2\pi f_{\text{act}}t)$ where $\tilde{\phi}$ is supplied by the compensator. Note that this tuning is consistent with the optimal control design since this change of coordinate not only scales the magnitude of \mathcal{B}_2 , but also changes the control penalty in the well known LQR control objective

$$\mathcal{J} = \lim_{T \rightarrow \infty} \frac{1}{T} \int_0^T q^2 + \left(\frac{l}{k} \phi \right)^2 dt = \lim_{T \rightarrow \infty} \frac{1}{T} \int_0^T q^2 + (l\tilde{\phi})^2 dt \quad (5.4)$$

that is minimized by the controller. The control penalty l is tuned such that the complete compensator reduces the energy q^2 with two orders of magnitude for the nominal case $k = 1$. While this is a rather aggressive tuning, the gain can be easily detuned online to not aggravate the flow.

To study the maximum attainable performance that can be achieved by the compensator, offline simulations have been performed in which the linearised equations are forced with a uniform stochastic disturbance, as an approximation to the inherent disturbance environment in the wind tunnel. The spatial distribution of the disturbance is modelled as a divergence free Gaussian body force distribution placed upstream of the control domain [33]. The base flow distortion introduced by the average constant forcing of the plasma actuator is taken into account in the computation of the base flow used for the linear simulations. Note that the control

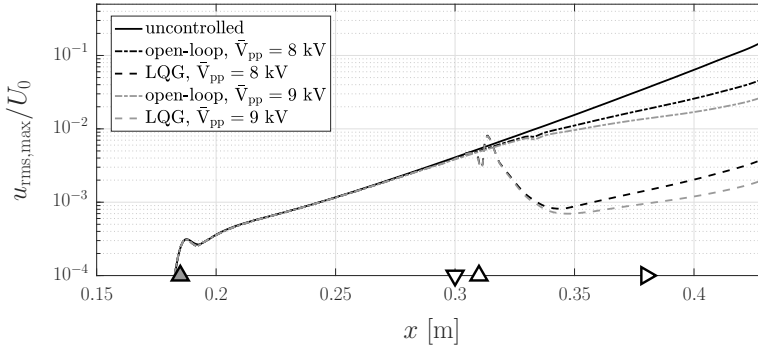


Figure 5.11: Offline simulation of a uniform white disturbance. Shown is the wall-normal maximum of the rms streamwise velocity. The triangles indicate the location the disturbance source (dark \triangle), the sensor (∇), the actuator (\triangle) and the control objective (\triangleright).

model is based on the nominal undistorted base flow which introduces a difference between modelled flow and the simulated flow (and experimental flow in the next section). Figure 5.11 shows the wall-normal maximum amplitude of the rms streamwise velocity perturbation without control, with continuous forcing at $\bar{V}_{pp} = 8$ kV and $\bar{V}_{pp} = 9$ kV, and with LQG control at these two offset voltages. The spatial growth of the uncontrolled perturbation in the control domain is in accordance with the growth observed in figure 5.9. The constant forcing has a significant stabilising effect on the flow which accumulates over some distance from the location of the actuator due to the generated streamwise jet. Nonetheless, the LQG controller achieves an additional one order of magnitude reduction as compared to continuous forcing both for the 8 kV and 9 kV offset case.

5.4. EXPERIMENTAL CONTROL PERFORMANCE

In this section the nominal performance as well as the robust performance in off-design conditions of the compensator is evaluated in the experimental context. All results contain a comparison between an 8 kV and a 9 kV mean peak-to-peak voltage supply. The performance of the compensator is in particular compared against the performance with open-loop continuous forcing to properly evaluate the contribution of the unsteady actuation. The control objective is evaluated based on the downstream microphone signal p_2 , which is recorded for periods of 20 s sampled at 30 kHz for each test case. Evaluation of the time domain performance is based on the standard deviation of the signal. To compute the standard deviation, the signal is filtered between 50-800 Hz to filter out the low frequency background noise (see also figure 5.5(b)) and the high frequency electromagnetic noise at 2 kHz due to the plasma actuator carrier signal. During preliminary tests it was found that the actuator was stronger than assumed in the control design. Additionally it was observed that strong actuation can in fact promote transition due to nonlinear effects and control spillover [150], which should be avoided. Therefore the controller had to be detuned to achieve an effective stabilisation. For the nominal designed case,

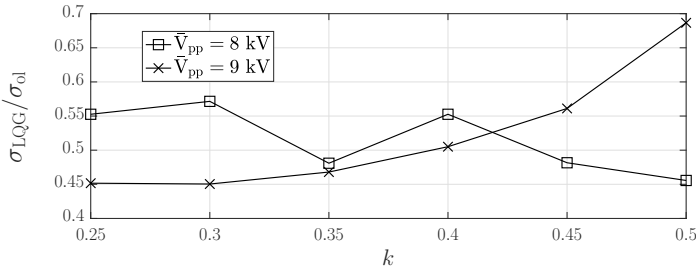


Figure 5.12: Effect of the online tuning gain on the standard deviation of the downstream sensor signal. Shown is the ratio between the LQG controlled case and the open-loop forcing case. ($\sigma_{unc} = 1.987$, $\sigma_{ol}^{8kV} = 0.766$, $\sigma_{ol}^{9kV} = 0.239$)

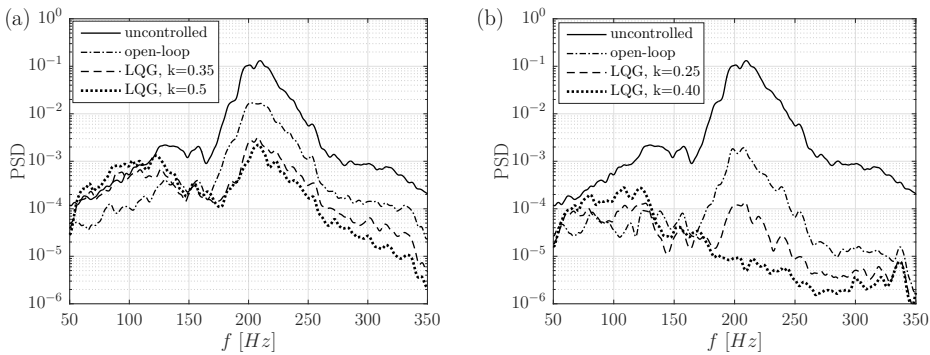


Figure 5.13: Power spectral density of the downstream sensor signal without control, with open-loop control and LQG control. (a) $\bar{V}_{pp} = 8$ kV. (b) $\bar{V}_{pp} = 9$ kV.

the data was recorded for $k \in [0.25 \ 0.5]$ with steps of $\Delta k = 0.05$. The effect of the tuning gain on the standard deviation for the nominal designed case is shown in figure 5.12. With the proper tuning, a reduction of 50-55% in standard deviation compared to open-loop forcing has been measured. The effect of the tuning gain is best observed in the frequency domain. Figure 5.13 compares the power spectral density for the 8 kV, $k = (0.35, 0.5)$ control cases (Figure 5.13(a)) and for the 9 kV, $k = (0.3, 0.4)$ control cases (Figure 5.13(b)). At these values the effect of the tuning gain was best observed. A higher gain might give a better attenuation of the most amplified frequencies, but in turn results in more spillover at the lower frequencies. For example, for the 9 kV, $k = 0.4$ control case the energy at the most amplified frequencies is reduced with two orders of magnitude (40 dB), while the $k = 0.3$ controller reduces the peak with 20 dB. Nevertheless, the standard deviation at $k = 0.4$ is higher as the amplitude at the spillover frequencies ($f < 130$ Hz) dominate the stabilised bandwidth. A similar observation can be made for the 8 kV control cases. However, the effect is more pronounced for the 9 kV cases as it achieves a better open-loop stabilisation of the most amplified frequencies. The 8 kV open-loop forcing gives a reduction of $1 - \sigma_{ol}/\sigma_{unc} = 65\%$, whereas the 9 kV

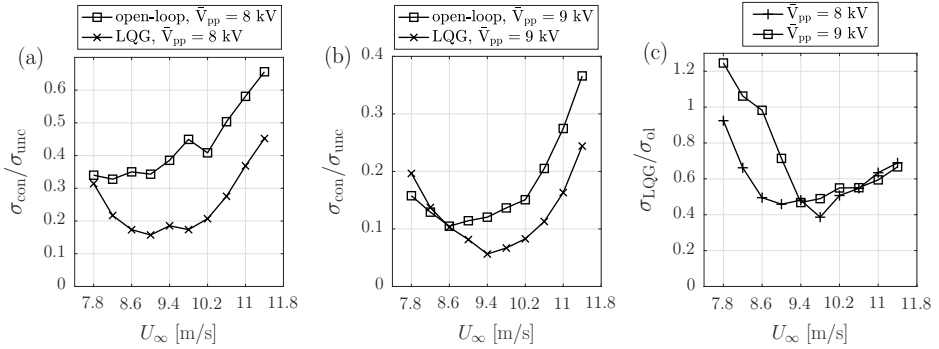


Figure 5.14: Effect of wind-tunnel speed variation on the standard deviation of the downstream sensor signal ($k = 0.35$). Ratio between the controlled (LQG and open-loop) and the uncontrolled case with $\bar{V}_{pp} = 8$ kV (a) and $\bar{V}_{pp} = 9$ kV (b). (c) Ratio between the LQG controlled and open-loop forcing case.

open-loop forcing gives an 88% reduction. This significant stabilisation can also be contributed to the low free-stream velocity as discussed in the previous section. In fact, 9 kV open-loop forcing gives a better performance than the 8 kV LQG control performance. Therefore the main benefit for the investigated conditions is a reduced power consumption. However, at higher freestream velocities, the jet added by the plasma actuators becomes less dominant and open-loop control becomes less effective, see also figure 5.14.

Figure 5.14 shows the effect of the wind tunnel speed on the standard deviation of the downstream pressure signal for $k = 0.35$. The PSD at two off-design wind tunnel speeds is shown in figure 5.15. Variations in the freestream velocity from the design condition at $U_\infty = 9.4$ m/s give a reduced performance. Nevertheless, the controller provides a reduction as compared to open-loop forcing in particular in the higher range of freestream velocities. The controller is still able to significantly reduce the spectral density at the most amplified frequencies in off-design conditions. However, at lower free-stream velocities the spillover becomes more dominant as can be seen from figure 5.15, resulting in reduced effectiveness.

In summary, the most amplified frequencies are successfully reduced by the compensator. However, the effectiveness as compared to open-loop forcing is reduced as the mean applied forcing already provides a significant stabilisation. As a result the spillover at lower frequencies introduced by the unsteady actuation becomes more dominant. The compensator is able to achieve a robust reduction in standard deviation between 30-60% within the range $U_\infty = 8.4 - 11.4$ m/s as compared to open-loop forcing.

5.5. CONCLUSIONS

An experimental implementation of a compensator strategy, based on a Galerkin discretisation of the linearised Navier-Stokes equations, has been applied in a natural TS-wave dominated flow over a flat plate subject to an adverse pressure gradient.

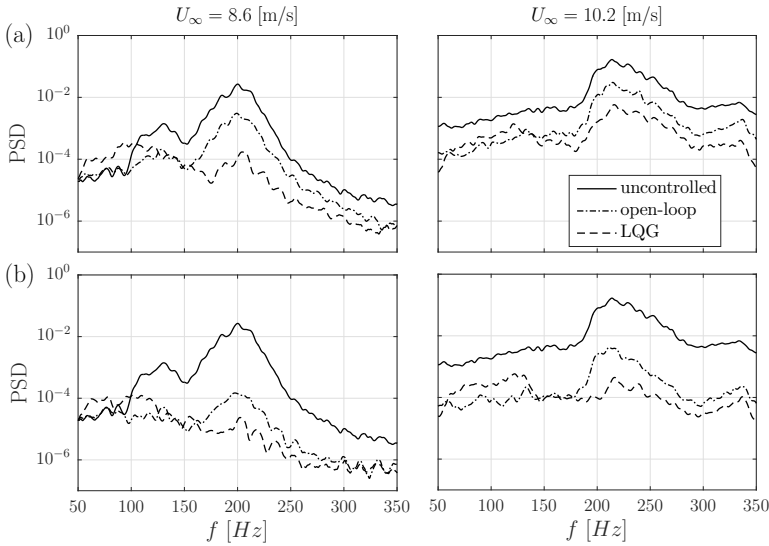


Figure 5.15: Power spectral density of the downstream sensor signal at two off-design freestream velocities. (a) $\bar{V}_{pp} = 8$ kV. (b) $\bar{V}_{pp} = 9$ kV.

Such white-box methods are not yet considered competitive in an applied setting due to their difficulty in obtaining an accurate representation of the upstream disturbance environment. However, it is experimentally verified that the Kalman filter, which makes a priori assumptions on the noise characteristics, is able to predict the effect of upstream disturbances and to estimate TS waves naturally occurring in a low freestream turbulence environment. This leads to the following conclusions: (1) it is the effect of upstream disturbances that is important to model and not the disturbances itself (which is more complex than assumed) and (2) the effect of external disturbances can be properly modelled by an inflow disturbance model.

A single DBD plasma actuator is used to simultaneously increase the local stability of the boundary layer and to attenuate the TS waves through unsteady modulation of the actuator voltage signal. The performance and robustness of the controller is compared to the case of continuous actuation. Results show that the controller is able to additionally reduce the spectral density at the most amplified frequencies with more than one order of magnitude and is capable of reducing the standard deviation of the unsteady pressure signal between 30-60% for a range of off-design freestream velocities. While this reduction is less than the respective reduction in numerical simulations, it is of the same order as what has been achieved in recent experimental studies using system identification techniques. To the best of our knowledge, the best performance (for a comparable flow scenario) was reported by Goldin *et al.* [143], who achieved a maximum localised reduction of 85% of the downstream sensor signal in a natural TS-wave dominated boundary layer flow. Juillet *et al.* [120] achieved an average localised reduction of 45% in a convective dominated channel flow and Gautier and Aider [142] achieved a 35% reduction in turbulent kinetic energy fluctuations in a convective backward-facing step flow. It

should be noted that the maximum attainable performance also depends on the choice of the actuator/sensor set-up and the disturbance scenario (TS-dominated, streak dominated, intensity, amplitude, etc.). Furthermore, the spatial extent of the reduction should be contrasted to length scales of the perturbations and the placement of the objective sensor. A similar experimental set-up and white-box approach was considered by Fabbiane *et al.* [87] to suppress TS waves in a boundary layer flow using a single plasma actuator, but introduced the upstream disturbances artificially. For uniform random disturbances they achieved a maximum reduction in standard deviation of 60%, compared to the uncontrolled case, measured 5 cm downstream of the actuator.

Fabbiane *et al.* [87] also stressed the robustness issues of disturbance feedforward optimal controllers for transition delay. The framework used in this study also shows promise for the development of robust feedback controllers to guarantee both robust stability and robust performance in off-design conditions, e.g. using \mathcal{H}_∞ and μ -synthesised techniques. It was shown in [27] that in case of feedback actuator/sensor configurations, the sensor has to be placed closely behind the actuator (less than one wave-length of the perturbations) and that such configurations are highly sensitive to neglected/truncated dynamics resulting from the model reduction step. By synthesising the reduced-order compensator directly from the governing equations, both the need for data-driven empirical model reduction and system-identification are avoided, allowing for an accurate reduction of the dynamics also for feedback actuator/sensor configurations. In this study the sensor was also placed 1 cm upstream of the actuator, which is less than half the wave-length of the most amplified perturbation. It became evident that the compensator was resilient to upstream influence of the actuator on the sensor as well as to electromagnetic inference introduced by the actuator.

Based on the presented results it can be concluded that the linear control approach presented in this chapter is a competitive technique in an applied experimental setting. It provides an efficient mean to synthesise compensators directly from the governing equations without the use of prior numerical data or experimental data. It is able to estimate and control natural flow perturbations and provides a promising direction for control of convective instabilities in wall-bounded shear flows. The question whether the modelling/synthesis approach in this study is more viable than the empirical model reduction tools and system-identification techniques currently available in the community should be carefully investigated in future works.

6

Conclusions and outlook

6.1. CONCLUSIONS

This dissertation has introduced a new approach for finite-dimensional approximation and control of wall-bounded shear flow systems. The research performed in this dissertation can be divided in three parts. Chapter 2 focussed on deriving finite-dimensional state-space representations from the governing equations. Chapter 3 concentrated on modelling, estimation and control of convective instabilities. Chapter 4 and chapter 5 were concerned with the integration of practical actuators and sensors, and to investigate the practical feasibility in experiments.

6.1.1. FINITE-DIMENSIONAL APPROXIMATION

In the first part, a new framework has been presented to obtain finite-dimensional state-space descriptions from the governing equations using multivariate splines. Multivariate splines have the desired accuracy and geometric flexibility for practical applications of PDE control. They are defined on triangular meshes allowing approximation of any domain with local refinements in the control region, i.e. the region with the sensors and actuators, and extraction of the key features of the system. Secondly, they are general in terms of smoothness and degree allowing for a high ‘spectral like’ resolving power. The degree and order of continuity of splines are simply input variables for creating the state-space models. These properties allow for the construction of models that effectively balance accuracy and computational complexity required for application of systems theoretical tools.

The main challenge in using Galerkin’s method for finite-dimensional approximation is the construction of a spatial basis for the infinite-dimensional state space, which is the space of smooth divergence-free functions which satisfies the boundary conditions. If this is not done with care, the resulting system of equations may be overdetermined or may not have a unique solution. In this case, the system matrix will be ill-conditioned and may contain non-physical spurious eigenmodes (which may even be controllable). Multivariate splines are unique in the sense that they

achieve modularity for the construction of the smooth divergence-free spatial basis. They consist of discontinuous piecewise polynomial functions over a triangulation and any desired smoothness conditions in the domain as well as the boundary conditions and the divergence-free conditions can be flexibly treated as side constraints for the polynomial expansion coefficients. This modularity allowed the generalisation of the framework for arbitrary boundary conditions and general geometries. By expanding the solution in the null basis of the side constraints results in a minimal support basis for the infinite-dimensional state space and naturally produces a system free of spurious eigenmodes. Also, a new differentiation matrix has been proposed, which greatly simplifies the computation of the partial derivatives as well as the derivation of the discrete projection matrices to obtain the finite-dimensional approximation of the differential operators. These new tools are now part of a Matlab differentiation matrix and projection suite, which can theoretically (in case of unlimited computational resources) be used for obtaining state-space descriptions of any linear PDE system, but also for solving steady partial differential equations and boundary value problems. This suite can complement existing Matlab differentiation matrix suites such as the spectral collocation software suite developed by Weideman and Reddy [151].

6.1.2. MODELLING, ESTIMATION AND CONTROL

The second part focussed on modelling, estimation and control of convective instabilities. Convective instabilities appear in a frequency broadband in both space and time and are driven by unknown upstream disturbances. Accurately modelling the effect of upstream disturbances is crucial as it forms the basis for the measured unsteadiness. The objective of the modelling was to have a desirable trade-off between model order and the spatial-temporal resolution of the model relative to the external disturbances. The objective of the control design was to avoid a disturbance specific design, i.e. to make the controller robust to unmodelled disturbances and to achieve robustness with respect to the truncated dynamics. The central design philosophy to avoid a disturbance specific control design is the following: Any perturbation field can be decomposed into a range of instability modes/eigenmodes with a temporal frequency and a spatial wavelength. Rather than making a specific assumption on the source and spatial structure of the external disturbance, the instability modes that physically contribute to the transition process are selected and included in the disturbance model. In this way the compensator is able to estimate and stabilise the underlying modes that are present in any perturbation field.

To realise this philosophy a new inflow disturbance model is proposed that consists of a second-order low-pass filter which accounts for the temporal dynamics of a combination of flow perturbation modes. The motivation for using inflow disturbance models is that the modes can be efficiently computed using a local linear stability analysis at the computational inflow. Furthermore, the spectrum at a given streamwise location reflects the broadband noise present in the upstream flow. This allowed for efficient modelling of the effect of the upstream disturbance environment using localised computational domains, which naturally prevents the creation of very large systems. Furthermore, the second-order low-pass filter allows the fre-

quency response shaping at the computational inflow to physically comply with the LST predictions, to precisely target the most unstable modes, while at the same time achieving robustness for higher, possibly unresolved frequencies. By means of a spatio-temporal frequency response analysis of the full order system it is shown that the use of inflow disturbance models allows for efficient modelling of the instabilities in a broad spatial and temporal bandwidth.

The full-order system is coupled with balanced truncation to reduce the order of the system and the corresponding controller. The full-order system is used as higher fidelity truth model to assure that the reduced-order controller maintains the closed-loop performance as compared with the full-order controller. This is crucial to assure that the controller does not exploit any weaknesses of the neglected dynamics. A fast closed-loop convergence is demonstrated with respect to the truncated dynamics and it is shown that convergence can be achieved with low-order ($r \approx 50$) controllers. The fast convergence can be contributed to the use of a mathematical Galerkin model combined with the efficient modelling of the instabilities. The effectiveness of the control design is demonstrated through three different unmodelled disturbance cases. The simulation results corroborate the presented ideas and it is shown that the controllers are capable of achieving their objectives in the presence of unmodelled disturbances.

6.1.3. ACTUATORS, SENSORS AND EXPERIMENTAL DEMONSTRATION

The third and final part focussed on the practical demonstration of the controllers. Motivated by their practical advantages, a surface microphone and a plasma actuator were chosen as the actuator/sensor pair used for control. Particularly the use of microphones for dynamic flow estimation proved to be a challenge. The pressure is initially eliminated from the state equations to avoid singularities. As a result, estimation for correlating the model variables with the pressure measurements becomes less trivial. A novel solution is proposed based on spatial integration of the pressure gradient along the boundaries. This resulted in new output operators that relate the external inflow disturbances and the perturbation field with the fluctuation pressure at the wall. The output operators were integrated in the optimal control design and proved to be successful in both simulation and experiment. The experimental study considered a natural laminar flow over a flat plat in low freestream turbulence conditions. One of the main results of the experiment is the comparison of the estimated perturbation fields with the measured data from PIV. This validated the modelling philosophy and more importantly, validated that model-based controllers, which make a priori assumptions on the noise and disturbance statistics, are able to estimate the spatio-temporal behaviour of natural flow perturbations. The external disturbance field is generally very complex. It includes freestream turbulence, sound, vorticity and wall surface roughness, which is very difficult to characterise and not included in the external disturbance model. It can therefore be concluded that it is the effect of the external disturbances that is important to characterise and not the disturbances itself. Furthermore, the effect of the external disturbances can be properly modelled with the proposed inflow disturbance model. A similar conclusion can be drawn for the actuator. It was found

that accurately modelling the effect of the plasma actuator was very difficult. The properties highly depend on the actuator fabrication and the actuator deteriorated/broke quickly during operation. To mitigate the effect of actuator uncertainties a simple online gain tuning approach is proposed, which proved to be effective in achieving attenuation of TS-waves. An additional maximum reduction of 60% as compared to open-loop forcing has been achieved. However, the gain tuning can be considered as a ‘band-aid’ solution and a better performance is anticipated in future experiments. To achieve a better performance significant efforts should be directed at the development of durable actuators along with corresponding models. This requires close collaboration with the actuator community.

6.1.4. FINAL DISCUSSION

This work showed that it is possible to synthesise experimentally feasible controllers from the governing equations without the use of empirical techniques. The main advantages are low costs for obtaining the model, fast convergence of the model and the availability of a higher fidelity truth model. The truth model can be used to gain physical insights and to assure that the reduced-order controllers are naturally robust to the truncated dynamics. Based on what has been achieved in literature it can be concluded that the proposed approach is a competitive approach also in an applied setting. However, several (severe) analytical and computational challenges had to be addressed and many more are expected to follow when continuing the development of the presented approach. Also no comparison studies have been performed with respect to the current state of the art. Therefore, no conclusions can be drawn whether the presented approach is more viable or better performing than the current tools/frameworks available in the community. This should be carefully investigated in future works before continuing the development of the presented approach.

There are still many open problems to be solved to make the approach work on for example aircraft wings or the roof of cars. Practically, this work is still limited to two-dimensional linear flow configurations. However, the examples and demonstrations in this work have not reached their computational limits. While for more complex and three-dimensional flow configurations this approach may currently be closely tied with the available computational resources, it may not be in the future considering continuing advancements in multivariate spline theory, linear algebra, microprocessors and scientific computing. It is anticipated that this approach can also significantly contribute to the understanding and control of more complex flows and is worth pursuing in future works.

6.2. OUTLOOK AND OPEN PROBLEMS

The methods presented in this dissertation provide a starting point towards more complex estimation and control problems. The following open questions and possible directions of research that extend the results in this dissertations are given:

- The practical feasibility of the framework for control of three-dimensional instabilities such as streaks should be investigated. Three-dimensional prob-

lems typically require a lot of memory for matrix storage and computations ($\mathcal{O}((n_x n_y n_z)^3)$) and this study does not make an exception to that. However, the system model should be good enough for control design and not necessary for accurate numerical simulation. The equations to be controlled are linear, the flow to be modelled is laminar and the instability mechanisms can be exploited to capture the relevant flow physics. Furthermore, it is not required to fully resolve the flow at all length and time scales to achieve effective control. By considering localised computational domains combined with focussing on resolving the dominant length scales of the perturbations, this approach can be made computationally feasible. Early systematic approaches for flow control were already able to compute three-dimensional spatially localised estimation/control convolution kernels for distributed feedback control, showing that these computational challenges can be overcome.

- Chapter 4 identified the problems related to the use of pressure measurements for dynamic flow estimation. A solution was proposed based on spatial integration of the pressure gradient along the boundaries. While effective for the considered flow configuration, it does not trivially extend to general geometries and general actuator/sensor configurations. Particularly, if a feedback actuator/sensor configuration is considered the integration path to derive the output equation passes through the streamwise location of the actuator. In this case the use of spatial integration is only robust if the actuator model is divergence free and satisfies the boundary conditions. This was not the case for the identified plasma actuator model considered in the experiments. As a result the divergence-free projection of the body force results in thin shear layers at the wall, which get integrated in the output equation, degrading the numerical accuracy and affecting the input-output behaviour significantly. This was the main reason to only investigate a feedforward actuator/sensor configuration in the experimental study. Pressure based dynamic flow estimation for general geometries is still an open problem. A possible solution is to use the pressure Poisson equation for deriving the output equation, which should be investigated in future works.
- The actuator and sensor placement that leads to good performance in convective systems results in a disturbance feedforward control system. While robust stability is guaranteed in this case, such systems suffer from a poor robust performance in case of model mismatch and uncertainties. To account for model uncertainties in the control design, a change of set-up to include feedback measurement information is required. However, convective instabilities that appear in distinct wavepackets, such as TS-waves, are generally uncorrelated to each other. As a result, to achieve effective feedback control in this case, the feedback sensor has to be placed very close behind the control actuator giving rise to an almost collocated control system. This poses severe restrictions on accurately modelling the effect of the actuator on the sensor. Such systems are more sensitive to truncated and neglected dynamics, requiring the need for robust control design techniques such as \mathcal{H}_∞ -control or μ -synthesis. Robust

reduced-order feedback control for convective systems is still an open problem. Preliminary results [152] based on the Kuramoto-Sivashinsky equation, a simplified benchmark model for convective systems, show that it is indeed possible to guarantee both robust stability and robust performance for a wide range of off-design conditions.

- One source of uncertainty in flow control is parametric uncertainty in the external freestream velocity and the Reynolds number. The Reynolds number in turn affects the base flow used for the linearisation, which acts as a spatially distributed parameter on the linearised equations. Instead of viewing the Reynolds number as source of uncertainty it can also be viewed as a nonlinearity acting on the system. A simple method to account for this nonlinearity in the control design would be the use of classical gain scheduling, for example with the external free-stream velocity as scheduling parameter, which can be measured online with a pitot-tube. This would require the design and synthesis of controllers for a family of linearisations, which spans the envelope of operation. The family of controller gains can subsequently be combined through online gain interpolation. More rigorous methods such as velocity-based linearisation along a trajectory or robust linear parameter varying techniques [153, 154] might also be worth investigating in future works, also to account for nonlinearities in actuator models.
- The flow control problem is essentially nonlinear; however, the equations were linearised in order to apply linear control theoretic tools. Although the effectiveness of linear control is physically motivated, it is anticipated that nonlinear control methods such as nonlinear dynamic inversion [155] and backstepping [156] can improve the performance at higher perturbation amplitudes and can extend the effectiveness region. This would require the use of nonlinear model reduction techniques for the (finite-dimensional) design of control systems. The method of Galerkin projection, as presented in chapter 2, also applies to nonlinear systems, and in the case of fluids leads to state-space descriptions with quadratic nonlinearities [32]. To avoid high-order systems, the system can be projected on a reduced set of modes, e.g. balanced modes of the equivalent linear system [157]. The methods presented in the dissertation can provide a new route to obtain nonlinear models using mathematical modes, rather than empirical modes.
- In this work a single actuator/sensor pair was used for estimation and control. In theory this is sufficient to achieve more than one order of magnitude reduction and also works in controlled experimental conditions. However, for future non-academic applications, e.g. aircraft wings, requires the use of spanwise and streamwise distributed actuator/sensor grids in order to achieve a profitable drag reduction and extended delay of transition. The future ‘smart’ wings require multi-input-multi-output modelling and control design. The techniques in this work naturally account for any number of actuators/sensors allowing for this extension without an increase in difficulty with respect to obtaining the model. However, the costs with respect to the experimental

feasibility, i.e. the wiring and communication needs, increase rapidly with the number of inputs and outputs. A possible route to reduce the communication needs is the use of streamwise repeated control [137] and decentralised control [158]. This involves the implementation of independent controllers at different streamwise and spanwise locations. The localised modelling approach presented in chapter 3 can provide new routes to efficiently decentralise the controllers along with their computational domain.

- This work has focussed on convective instabilities in wall-bounded flows. The application to global instabilities in more complex geometries should be investigated. Complex and irregular geometries are very tractable by the spline-Galerkin method. Preliminary results on global stability analysis of a cylinder flow, see also figure 1.2, indicate that the numerical tools are viable for resolving the global modes. The global mode in figure 1.2 was obtained as eigenmode of the system matrix, rather than as a numerical solution of an eigenvalue problem, making extension to a control application by including actuators/sensors rather straightforward. A suitable academic test case would be the control of vortex shedding for a flow over a rotating cylinder, with hot-wire sensors placed in the wake and a controller that specifies the direction and speed of the rotation.
- A final recommendation is to explore other areas involving distributed parameter systems that model physical systems. Examples are flexible structures in civil engineering applications, wavefronts for turbulence induced aberration compensation in the field of adaptive optics, chemical processes in process industries, flight envelope prediction for fault-tolerant flight control, the Einstein field equation for relativistic systems and finally quantum mechanical systems.

A

A state-space representation for incompressible fluid flows

In this appendix the finite-dimensional state-space system of the linearised Navier-Stokes equations is derived. In Awanou and Lai [64] a variational approach is presented for approximating steady Navier-Stokes equations in velocity pressure formulation using multivariate splines. This approach is combined with the framework from chapter 2 to derive state-space descriptions for the linearised Navier-Stokes equations and is presented in section A.1. The state-space system for the case of the non-periodic channel flow was validated in section 3.3 by comparing the spatial stability with the predictions from LST. For completeness and to mathematically verify the numerical method, the state-space system for the case of the periodic channel flow is verified using the temporal stability theory in section A.2.

A.1. NUMERICAL METHOD

Let Ω denote the domain in \mathbb{R}^n with $n = 2$ or 3 and Γ its boundary. In this appendix the forced LNSE are considered which are given by

$$\frac{\partial \mathbf{u}}{\partial t} + (\mathbf{U} \cdot \nabla) \mathbf{u} + (\mathbf{u} \cdot \nabla) \mathbf{U} - \frac{1}{Re} \Delta \mathbf{u} + \nabla p = \mathbf{f} \quad \text{in } \Omega, \quad (\text{A.1a})$$

$$\nabla \cdot \mathbf{u} = 0 \quad \text{in } \Omega, \quad (\text{A.1b})$$

$$\mathbf{u} = \mathbf{u}_b \quad \text{on } \Gamma_D, \quad (\text{A.1c})$$

$$-pn + \frac{1}{Re} (\mathbf{n} \cdot \nabla) \mathbf{u} = 0 \quad \text{on } \Gamma_{out}, \quad (\text{A.1d})$$

where \mathbf{u} denotes the velocity field, p the pressure, \mathbf{U} the steady base flow used for linearisation and \mathbf{f} the body force. The body force is used for control and is assumed to be of the form $\mathbf{f} = [f_i(\mathbf{x})]_{i=1}^n \phi(t)$ with $f_i(\mathbf{x})$ the spatial distribution of i th component of the body force and $\phi(t)$ the in-domain temporal control input. The system is closed by the boundary conditions (A.1c)-(A.1d) with Γ_D the Dirichlet part

of the boundary and Γ_{out} the outlet boundary. For control applications the boundary condition is of the form $\mathbf{u}|_{\Gamma_D} = \mathbf{u}_b(\mathbf{x}, t) = [g_i(\mathbf{x})]_{i=1}^n \phi_\Gamma(t)$ with $g_i(\mathbf{x})$ the spatial distribution for the i th velocity component and $\phi_\Gamma(t)$ the temporal boundary control input. In this appendix only the state-equations are considered. The reader is referred to chapter 2 for the derivation of the output equations (3.5) and (3.7). First the Galerkin-type variational formulation through which the spline approximation is determined is presented. In order to introduce the variational formulation some functions spaces need to be defined. Let $L^2(\Omega)$ be the space of square-integrable functions over Ω . We define the following Sobolev spaces

$$H^1(\Omega) = \left\{ u \in L^2(\Omega), \frac{\partial u}{\partial x_i} \in L^2(\Omega) \text{ for } i = 1, \dots, n \right\}, \quad (\text{A.2})$$

$$H_0^1(\Omega) = \{ u \in H^1(\Omega), u|_{\Gamma_D} = 0 \}. \quad (\text{A.3})$$

$H^1(\Omega)$ consists of square integrable functions whose first order derivative exists in the weak sense and $H_0^1(\Omega)$ is the subspace in which the functions vanish on the Dirichlet portion of the boundary Γ_D . For vector valued functions the notation $\mathbf{H}^1(\Omega) = H^1(\Omega)^n$ is used. We define the bilinear form

$$a(\mathbf{v}, \mathbf{u}) = \frac{1}{Re} \int_{\Omega} \nabla \mathbf{v} : \nabla \mathbf{u} \, d\Omega =: \frac{1}{Re} \int_{\Omega} \sum_{i=1}^n \sum_{j=1}^n \frac{\partial u_i}{\partial x_j} \frac{\partial v_i}{\partial x_j} \, d\Omega \quad \forall \mathbf{v}, \mathbf{u} \in \mathbf{H}^1(\Omega) \quad (\text{A.4})$$

and the trilinear form

$$b(\mathbf{v}, \mathbf{u}, \mathbf{w}) = \int_{\Omega} \mathbf{v} \cdot (\mathbf{u} \cdot \nabla) \mathbf{w} \, d\Omega = \int_{\Omega} \sum_{i=1}^n \sum_{j=1}^n v_i u_j \frac{\partial w_i}{\partial x_j} \, d\Omega \quad \forall \mathbf{v}, \mathbf{u}, \mathbf{w} \in \mathbf{H}^1(\Omega). \quad (\text{A.5})$$

Also the inner product for functions belonging to $\mathbf{L}^2(\Omega)$ is given by

$$(\mathbf{v}, \mathbf{u}) = \int_{\Omega} \mathbf{v} \cdot \mathbf{u} \, d\Omega. \quad (\text{A.6})$$

Equation (A.1) has no dynamic equation for the pressure that can be utilised for control. To avoid singularities the pressure is eliminated from the equations by using a space of velocity fields which are exactly divergence free. Let

$$\mathbf{V}_0 = \{ \mathbf{v} \in \mathbf{H}_0^1(\Omega), \nabla \cdot \mathbf{v} = 0 \}, \quad (\text{A.7})$$

$$\mathbf{V}_g = \{ \mathbf{u} \in \mathbf{H}^1(\Omega), \mathbf{u}|_{\Gamma_D} = \mathbf{u}_b, \nabla \cdot \mathbf{u} = 0 \}. \quad (\text{A.8})$$

The weak form of A.1 can be obtained by taking the inner product of the first equation (A.1a) with $\mathbf{v} \in \mathbf{V}_0$

$$\int_{\Omega} \left\{ \mathbf{v} \cdot \frac{\partial \mathbf{u}}{\partial t} - \frac{1}{Re} \mathbf{v} \cdot \Delta \mathbf{u} + \mathbf{v} \cdot (\mathbf{U} \cdot \nabla) \mathbf{u} + \mathbf{v} \cdot (\mathbf{u} \cdot \nabla) \mathbf{U} + \mathbf{v} \cdot \nabla p \right\} \, d\Omega = \int_{\Omega} \mathbf{v} \cdot \mathbf{f} \, d\Omega. \quad (\text{A.9})$$

Applying integration by parts and the divergence theorem to the diffusion term and the pressure gradient term gives

$$\begin{aligned} & \int_{\Omega} \left\{ \mathbf{v} \cdot \frac{\partial \mathbf{u}}{\partial t} + \frac{1}{Re} \nabla \mathbf{v} : \nabla \mathbf{u} + \mathbf{v} \cdot (\mathbf{U} \cdot \nabla) \mathbf{u} + \mathbf{v} \cdot (\mathbf{u} \cdot \nabla) \mathbf{U} - p (\nabla \cdot \mathbf{v}) \right\} d\Omega \\ & - \int_{\Gamma_D} \mathbf{v} \cdot \left(-p \mathbf{n} + \frac{1}{Re} (\mathbf{n} \cdot \nabla) \mathbf{u} \right) d\Gamma - \int_{\Gamma_{out}} \mathbf{v} \cdot \left(-p \mathbf{n} + \frac{1}{Re} (\mathbf{n} \cdot \nabla) \mathbf{u} \right) d\Gamma \\ & = \int_{\Omega} \mathbf{v} \cdot \mathbf{f} d\Omega. \end{aligned} \quad (\text{A.10})$$

The Neumann outflow boundary condition [A.1d](#) occurs in [\(A.10\)](#) as a boundary integral term and can therefore naturally be imposed by setting it to zero. Furthermore, $\nabla \cdot \mathbf{v} = 0$ and $\mathbf{v}|_{\Gamma_D} = 0$ for all $\mathbf{v} \in \mathbf{V}_0$. The variational formulation of the problem [\(A.1\)](#) can thus be stated as: Find $\mathbf{u} \in L^2(0, T; \mathbf{V}_g)$ such that

$$\left(\mathbf{v}, \frac{\partial \mathbf{u}}{\partial t} \right) + a(\mathbf{v}, \mathbf{u}) + b(\mathbf{v}, \mathbf{U}, \mathbf{u}) + b(\mathbf{v}, \mathbf{u}, \mathbf{U}) = (\mathbf{v}, \mathbf{f}) \quad \forall \mathbf{v} \in \mathbf{V}_0. \quad (\text{A.11})$$

The multivariate spline space is used as approximating space for the velocity. Let \mathcal{T} be the triangulation of the domain Ω . The spline space is the space of all smooth piecewise polynomial functions of arbitrary degree d and arbitrary smoothness r over \mathcal{T} with $0 \leq r < d$

$$S_d^r(\mathcal{T}) := \{s \in C^r(\Omega), s|_{\Delta} \in \mathcal{P}_d, \forall \Delta \in \mathcal{T}\}, \quad (\text{A.12})$$

with \mathcal{P}_d the space of all polynomials of total degree d and Δ denotes a triangle. To approximate the velocity vector \mathbf{u} we use $\mathbf{s}_{\mathbf{u}} = [s_i]_{i=1}^n \in \mathbf{S}_g$ with $\mathbf{S}_g = S_d^r(\mathcal{T})^n \cap \mathbf{V}_g$. The spline approximation of [\(A.11\)](#) is to seek $\mathbf{s}_{\mathbf{u}}(\cdot, t) \in \mathbf{S}_g \subset \mathbf{V}_g$ such that

$$\left(\mathbf{s}_v, \frac{\partial \mathbf{s}_{\mathbf{u}}}{\partial t} \right) + a(\mathbf{s}_v, \mathbf{s}_{\mathbf{u}}) + b(\mathbf{s}_v, \mathbf{U}, \mathbf{s}_{\mathbf{u}}) + b(\mathbf{s}_v, \mathbf{s}_{\mathbf{u}}, \mathbf{U}) = (\mathbf{s}_v, \mathbf{f}) \quad \forall \mathbf{s}_v \in \mathbf{S}_0. \quad (\text{A.13})$$

After constructing a basis for \mathbf{S}_0 and \mathbf{S}_g , [\(A.13\)](#) is equivalent to a system of ordinary differential equations. However, the implementation of such divergence free spline elements of arbitrary degree and smoothness is very complicated. Awanou and Lai [\[64\]](#) streamlined this process by skipping the construction of smooth divergence-free finite elements. Instead, they used discontinuous piecewise polynomial functions over a triangulation and treated desired smoothness properties together with the boundary conditions and the incompressibility condition as side constraints. This approach is also applied here to the time dependent problem [\(A.13\)](#). Recall from section [2.3](#) that the multivariate spline function can be represented in the vector form

$$s_i(\mathbf{x}, t) = \mathbf{B}^d(\mathbf{x}) \mathbf{c}_i(t), \quad (\text{A.14})$$

with $\mathbf{B}^d(\mathbf{x}) \in \mathbb{R}^{1 \times J \hat{d}}$ the global vector of B-form basis polynomials, J the number of elements in \mathcal{T} and $\hat{d} = \binom{n}{n+d}$ the number of basis polynomials per element. The spline function is identified by its B-coefficient vector $\mathbf{c}_i(t) \in \mathbb{R}^{J \hat{d} \times 1}$ which are used

as the time-varying expansion coefficients. As described in section 2.3, since s has a certain smoothness, the smoothness conditions can be expressed by a linear system. That is $s \in C^r$ if and only if

$$\mathbf{H}\mathbf{c}_i = 0. \quad (\text{A.15})$$

The Dirichlet boundary condition (A.1c) provides additional constraints on the B-coefficient vector. Also recall from section 2.4 that the discrete constraints for this condition can be given by a linear system

$$\mathbf{D}\mathbf{c}_i = \mathbf{g}^i \phi_\Gamma, \quad (\text{A.16})$$

where \mathbf{g}^i is a vector of B-coefficients that interpolates $g_i(\mathbf{x})$ at the boundary Γ_D . The spline approximation $\mathbf{s}_u = [s_i]_{i=1}^n$ is identified with B-coefficients $\mathbf{c} = [\mathbf{c}_i]_{i=1}^n$. Hence the discrete equivalent of $\nabla \cdot \mathbf{u} = 0$ is given by [64]

$$\sum_{i=1}^n \mathbb{T}_{\partial_{x_i}}^{d-1,d} \mathbf{c}_i = \mathbb{T}_{\nabla}^{d-1,d} \mathbf{c} = 0, \quad (\text{A.17})$$

with $\mathbb{T}_{\partial_{x_i}}^{d-1,d}$ is the differentiation matrix, which maps the B-coefficient vector $s \in S_d^r(\mathcal{T})$ to the B-coefficient vector of $\frac{\partial}{\partial x_i} s \in S_{d-1}^{r-1}(\mathcal{T})$, see theorem 2 in section 2.4. Let $\bar{\mathbf{H}}$ and $\bar{\mathbf{D}}$ be the matrices that encode the smoothness conditions and the boundary conditions for the complete discrete velocity field. Furthermore let

$$\mathbf{L} = \left[\bar{\mathbf{H}}^T \quad \bar{\mathbf{D}}^T \quad \left(\mathbb{T}_{\nabla}^{d-1,d} \right)^T \right]^T, \quad \bar{\mathbf{G}} = [0 \quad \mathbf{G}^T \quad 0]^T, \quad (\text{A.18})$$

then for all spline vector functions \mathbf{s} with B-coefficient \mathbf{c} satisfying

$$\mathbf{L}\mathbf{c} = \bar{\mathbf{G}}\phi_\Gamma \quad (\text{A.19})$$

we have that $\mathbf{s} \in \mathbf{S}_g$, and can thus be used to approximate the variational formulation. The inner products, bilinear form and trilinear forms in (A.13) are computed using the mass and bending matrices derived section 2.5. Let \mathbf{d} denote the B-coefficient vector of the test function \mathbf{s}_v . Furthermore, let \mathbf{U}^i be a vector of B-coefficients of the spline function that interpolates $\mathbf{U}_i(\mathbf{x})$ in the domain, and let \mathbf{f}^i be a vector of B-coefficients that interpolates the spatial distribution of i th component of the body force $f_i(\mathbf{x})$. Then the inner products, the bilinear form and the trilinear forms can be approximated in terms of B-form polynomials and be computed using

$$\begin{aligned} \left(\mathbf{s}_v, \frac{\partial \mathbf{s}_u}{\partial t} \right) &= \int_{\Omega} \mathbf{s}_v \cdot \frac{\partial \mathbf{s}_u}{\partial t} \\ &= \int_{\Omega} \sum_{i=1}^n \mathbf{d}_i^T \left[\mathbf{B}^d(\mathbf{x}) \right]^T \mathbf{B}^d(\mathbf{x}) \dot{\mathbf{c}}_i \, d\Omega \\ &= \sum_{i=1}^n \mathbf{d}_i^T \mathbf{M} \dot{\mathbf{c}}_i, \end{aligned} \quad (\text{A.20})$$

$$\begin{aligned}
(\mathbf{s}_v, \mathbf{f}) &= \int_{\Omega} \mathbf{s}_v \cdot \mathbf{f} \\
&= \int_{\Omega} \sum_{i=1}^n \mathbf{d}_i^T \left[\mathbf{B}^d(\mathbf{x}) \right]^T \mathbf{B}^d(\mathbf{x}) \mathbf{f}^i \phi \, d\Omega \\
&= \sum_{i=1}^n \mathbf{d}_i^T \mathbf{M} \mathbf{f}^i \phi,
\end{aligned} \tag{A.21}$$

$$\begin{aligned}
a(\mathbf{s}_v, \mathbf{s}_u) &= \frac{1}{Re} \int_{\Omega} \nabla \mathbf{s}_v : \nabla \mathbf{s}_u \, d\Omega \\
&= \frac{1}{Re} \int_{\Omega} \sum_{i=1}^n \sum_{j=1}^n \mathbf{d}_i^T \left[\mathbb{T}_{\partial x_j}^{d,d} \right]^T \left[\mathbf{B}^d(\mathbf{x}) \right]^T \mathbf{B}^d(\mathbf{x}) \mathbb{T}_{\partial x_j}^{d,d} \mathbf{c}_i \, d\Omega \\
&= \frac{1}{Re} \sum_{i=1}^n \sum_{j=1}^n \mathbf{d}_i^T \left[\mathbb{T}_{\partial x_j}^{d,d} \right]^T \mathbf{M} \mathbb{T}_{\partial x_j}^{d,d} \mathbf{c}_i \\
&= \frac{1}{Re} \sum_{i=1}^n \mathbf{d}_i^T \left(\sum_{j=1}^n \left[\mathbb{T}_{\partial x_j}^{d,d} \right]^T \mathbf{M} \mathbb{T}_{\partial x_j}^{d,d} \right) \mathbf{c}_i,
\end{aligned} \tag{A.22}$$

$$\begin{aligned}
b(\mathbf{s}_v, \mathbf{U}, \mathbf{u}) &= \int_{\Omega} \mathbf{s}_v \cdot (\mathbf{U} \cdot \nabla) \mathbf{s}_u \, d\Omega \\
&= \int_{\Omega} \sum_{i=1}^n \sum_{j=1}^n \mathbf{d}_i^T \left[\mathbf{B}^d(\mathbf{x}) \right]^T \left(\mathbf{B}^d(\mathbf{x}) \mathbf{U}^j \right) \mathbf{B}^d(\mathbf{x}) \mathbb{T}_{\partial x_j}^{d,d} \mathbf{c}_i \, d\Omega \\
&= \sum_{i=1}^n \sum_{j=1}^n \mathbf{d}_i^T \mathbf{K}(\mathbf{U}^j) \mathbb{T}_{\partial x_j}^{d,d} \mathbf{c}_i \\
&= \sum_{i=1}^n \mathbf{d}_i^T \left(\sum_{j=1}^n \mathbf{K}(\mathbf{U}^j) \mathbb{T}_{\partial x_j}^{d,d} \right) \mathbf{c}_i,
\end{aligned} \tag{A.23}$$

$$\begin{aligned}
b(\mathbf{s}_v, \mathbf{s}_u, \mathbf{U}) &= \int_{\Omega} \mathbf{s}_v \cdot (\mathbf{s}_u \cdot \nabla) \mathbf{U} \, d\Omega \\
&= \int_{\Omega} \sum_{i=1}^n \sum_{j=1}^n \mathbf{d}_i^T \left[\mathbf{B}^d(\mathbf{x}) \right]^T \left(\mathbf{B}^d(\mathbf{x}) \mathbf{c}_j \right) \mathbf{B}^d(\mathbf{x}) \mathbb{T}_{\partial x_j}^{d,d} \mathbf{U}^i \, d\Omega \\
&= \sum_{i=1}^n \sum_{j=1}^n \mathbf{d}_i^T \mathbf{K} \left(\mathbb{T}_{\partial x_j}^{d,d} \mathbf{U}^i \right) \mathbf{c}_j,
\end{aligned} \tag{A.24}$$

with $\mathbb{T}_{\partial x_j}^{d,d}$ the differentiation matrix which maps the B-coefficients of $s \in S_d^r(\mathcal{T})$ to the B-coefficient vector $\frac{\partial}{\partial x_j} s \in S_d^{r-1}(\mathcal{T})$, with \mathbf{M} a block diagonal mass matrix

whose blocks are given by (2.48) and $\mathbf{K}(\mathbf{a})$ a block diagonal bending matrix for the B-coefficient vector \mathbf{a} (e.g. $\mathbf{a} = \mathbb{T}_{\partial x_j}^{d,d} \mathbf{U}^i$) whose blocks are given by (2.49). Using these expressions, the variational formulation (A.13) can be translated to: Find \mathbf{c} satisfying (A.19) such that

$$\mathbf{d}^T \bar{\mathbf{M}} \dot{\mathbf{c}} + \mathbf{d}^T \bar{\mathbf{K}} \mathbf{c} = \mathbf{d}^T \mathbf{F} \phi \quad \forall \mathbf{d} \text{ with } \mathbf{L} \mathbf{d} = 0, \quad (\text{A.25})$$

where $\bar{\mathbf{M}}$ is a stacked velocity mass matrix and $\bar{\mathbf{K}}$ denotes the discretisation of the linear diffusion term and the two linear convective terms. The right hand side matrix \mathbf{F} contains the contribution of the in-domain forcing model.

The side constraints are commonly enforced through Lagrange multipliers [64, 65]. In section 2.5 a null space approach is proposed to transform (A.25) to state-space format. This approach result in a reduced set of coefficients with minimal non-zero support for \mathbf{S}_g which makes the resulting state-space model suitable for control applications. Let \mathbf{V} be a basis for $\text{null}(\mathbf{L})$ such that $\mathbf{L} \mathbf{V} = 0$ and let $\mathbf{c}_p = \mathbf{Z} \phi_\Gamma$ be a particular solution of (A.19). The general solution set for (A.19) can be written as

$$\mathbf{c} = \mathbf{V} \mathbf{c}_h + \mathbf{Z} \phi_\Gamma, \quad (\text{A.26})$$

with $\mathbf{c}_h \in \mathbb{R}^{N-R^*}$ the coordinate vector of \mathbf{c} relative to the basis for $\text{null}(\mathbf{L})$ and with R^* the rank of \mathbf{L} . Since $\mathbf{L} \mathbf{d} = 0$ for all B-coefficient vectors \mathbf{d} of splines in \mathbf{S}_0 , the solution set for \mathbf{d} can be written as $\mathbf{d} = \mathbf{V} \mathbf{d}_h$. Substituting this set for \mathbf{d} and the solution set (A.26) for \mathbf{c} in (A.25) gives

$$\mathbf{d}_h^T \mathbf{V}^T \bar{\mathbf{M}} (\mathbf{V} \dot{\mathbf{c}}_h + \mathbf{Z} \dot{\phi}_\Gamma) + \mathbf{d}_h^T \mathbf{V}^T \bar{\mathbf{K}} (\mathbf{V} \mathbf{c}_h + \mathbf{Z} \phi_\Gamma) = \mathbf{d}_h^T \mathbf{V}^T \mathbf{F} \phi, \quad (\text{A.27})$$

which is a reduced unconstrained system of order $N - R^*$ projected on the null space of the side constraints. Since (A.27) must hold for all \mathbf{d}_h , (A.27) is equivalent to

$$(\mathbf{V}^T \bar{\mathbf{M}} \mathbf{V}) \dot{\mathbf{c}}_h = \mathbf{V}^T [-\bar{\mathbf{K}} \mathbf{V} \mathbf{c}_h - \bar{\mathbf{K}} \mathbf{Z} \phi_\Gamma + \mathbf{F} \phi - \bar{\mathbf{M}} \mathbf{Z} \dot{\phi}_\Gamma]. \quad (\text{A.28})$$

Defining the following matrices

$$\begin{aligned} \mathbf{A} &= -(\mathbf{V}^T \bar{\mathbf{M}} \mathbf{V})^{-1} \mathbf{V}^T \bar{\mathbf{K}} \mathbf{V}, & \mathbf{A}_\Gamma &= -(\mathbf{V}^T \bar{\mathbf{M}} \mathbf{V})^{-1} \mathbf{V}^T \bar{\mathbf{K}} \mathbf{Z}, \\ \mathbf{B}_\Omega &= (\mathbf{V}^T \bar{\mathbf{M}} \mathbf{V})^{-1} \mathbf{V}^T \mathbf{F}, & \mathbf{B}_\Gamma &= -(\mathbf{V}^T \bar{\mathbf{M}} \mathbf{V})^{-1} \mathbf{V}^T \bar{\mathbf{M}} \mathbf{Z}, \end{aligned} \quad (\text{A.29})$$

(A.28) can be written as

$$\dot{\mathbf{c}}_h = \mathbf{A} \mathbf{c}_h + \mathbf{A}_\Gamma \phi_\Gamma + \mathbf{B}_\Gamma \dot{\phi}_\Gamma + \mathbf{B}_\Omega \phi. \quad (\text{A.30})$$

Finally we obtain the system in state-space format

$$\begin{bmatrix} \dot{\mathbf{c}}_h \\ \dot{\phi}_\Gamma \end{bmatrix} = \begin{bmatrix} \mathbf{A} & \mathbf{A}_\Gamma \\ 0 & 0 \end{bmatrix} \begin{bmatrix} \mathbf{c}_h \\ \phi_\Gamma \end{bmatrix} + \begin{bmatrix} \mathbf{B}_\Gamma \\ 1 \end{bmatrix} \dot{\phi}_\Gamma + \begin{bmatrix} \mathbf{B}_\Omega \\ 0 \end{bmatrix} \phi \quad (\text{A.31})$$

A.2. VERIFICATION

In this section the numerical method is validated using the temporal stability theory. By considering the channel flow (figure 5.6) with spatially periodic boundary conditions the eigenvalues of the state-space model (A.31) can be compared with the temporal eigenvalues of the Orr-Sommerfeld equation (3.15). The channel with length $L = 8\pi$ is considered for the case $Re = 7000$. The $S_4^0(\mathcal{T}_{960})$ state-space model which is used for the controller synthesis is again considered but now with periodic boundary conditions. Periodic boundary conditions can be applied in the numerical method by simply extending the inter-element continuity between the inflow and outflow. The open-loop uncontrolled system is represented by $\dot{\mathbf{c}}_h = \mathbf{A}\mathbf{c}_h$. We wish to compare the eigenvalues λ of \mathbf{A} with the eigenvalues ω of the Orr-Sommerfeld equation. The eigenvalues of \mathbf{A} correspond to fundamental solutions $e^{\lambda t}$ in the time domain. From (3.9) it follows that the temporal frequencies of the Orr-Sommerfeld equation can be related to system eigenvalues by $\lambda^{OS} = -i\omega^{OS}$. Furthermore, the wavelengths that fit in a periodic channel of box size L are given by $\lambda_x = L/j$, $j \in \mathbb{N}^+$. Hence the corresponding wavenumbers are given by $\alpha_j = 2\pi j/L = j\alpha_0$, $j \in \mathbb{N}^+$ with α_0 the fundamental wavelength. To compare the eigenvalues of the state-space model we solve the Orr-Sommerfeld equation for a set of integer multiples of the fundamental wavenumber and apply the conversion $\lambda^{OS} = -i\omega^{OS}$ to relate the frequencies ω to system eigenvalues λ . The dominant eigenvalues of the Orr-Sommerfeld equation and the spline model are listed in table A.1. The spline model accurately captures the dominant dynamics of the flow.

k	Orr-Sommerfeld λ^{OS}	spline λ	$ \lambda - \lambda^{OS} $
1	0.00171539 - 0.25292937i	0.00171537 - 0.25292939i	0.00000003
2	-0.00759183 - 0.16438997i	-0.00759179 - 0.16439009i	0.00000013
3	-0.01182921 - 0.34340007i	-0.01183063 - 0.34339614i	0.00000418
4	-0.01747563 - 0.03476212i	-0.01747563 - 0.03476210i	0.00000002
5	-0.01806727 - 0.10889122i	-0.01806702 - 0.10889070i	0.00000058
6	-0.02099365 - 0.22879485i	-0.02099071 - 0.22879873i	0.00000487
7	-0.02111395 - 0.22887111i	-0.02111549 - 0.22886843i	0.00000309
8	-0.02144973 - 0.08601143i	-0.02144968 - 0.08601153i	0.00000011
9	-0.02973214 - 0.47006733i	-0.02975512 - 0.47005252i	0.00002734
10	-0.02982088 - 0.47011896i	-0.02982758 - 0.47015029i	0.00003204
11	-0.03010486 - 0.18403967i	-0.03010637 - 0.18403908i	0.00000162
12	-0.03639968 - 0.71336680i	-0.03574655 - 0.71362950i	0.00070398
13	-0.03646103 - 0.71340240i	-0.03643618 - 0.71340606i	0.00002512
14	-0.03770525 - 0.21175241i	-0.03763012 - 0.21170367i	0.00008956
15	-0.03799777 - 0.21196786i	-0.03804988 - 0.21203181i	0.00008249
16	-0.04198552 - 0.95771911i	-0.04124565 - 0.95600997i	0.00186241
17	-0.04201606 - 0.95773859i	-0.04200127 - 0.95779573i	0.00005902
18	-0.04238220 - 0.24852281i	-0.04238296 - 0.24852450i	0.00000185
19	-0.04672358 - 0.41404472i	-0.04669017 - 0.41400991i	0.00004825
20	-0.04686574 - 1.20274634i	-0.04683349 - 1.20289856i	0.00015560
21	-0.04687263 - 1.20274602i	-0.04810140 - 1.20071794i	0.00237128
22	-0.04951767 - 0.08897461i	-0.04951630 - 0.08896558i	0.00000913

Table A.1: Dominant eigenvalues of the $S_4^0(\mathcal{T}_{960})$ spline model compared with the solution of the Orr-Sommerfeld equation for $\alpha_j = \frac{2\pi j}{L}$, $j \in \mathbb{N}^+$. The channel with a length $L = 8\pi$ is considered for the case $Re = 7000$ with spatially periodic boundary conditions

B

Solution of the \mathcal{H}_2 /LQG optimal control problem

This appendix presents the state-space formulas for the controller that solves the \mathcal{H}_2 optimal control problem. The reader is referred to Doyle *et al.* [30] and Zhou *et al.* [29, chapter 14] for the derivation of the formulas and more information about this control theory. The \mathcal{H}_2 control problem considers the generalised plant with state-space realisation

$$\begin{aligned}\dot{\mathbf{u}} &= \mathbf{A}\mathbf{u} + \mathbf{B}_1\mathbf{w} + \mathbf{B}_2\phi, \\ z &= \mathbf{C}_1\mathbf{u} + \mathbf{D}_{12}\phi \\ \mathbf{y} &= \mathbf{C}_2\mathbf{u} + \mathbf{D}_{21}\mathbf{w}\end{aligned}$$

The output feedback $\phi(s) = \mathbf{K}(s)\mathbf{y}(s)$ must internally (exponentially) stabilise the system and minimise the \mathcal{H}_2 norm of the closed-loop map \mathbf{T}_{zw} defined by

$$\|\mathbf{T}_{zw}(s)\|_2 = \sqrt{\frac{1}{2\pi} \int_{-\infty}^{\infty} \text{Trace}\{\mathbf{T}_{zw}^T(i\omega)\mathbf{T}_{zw}(i\omega)\}d\omega} = \sqrt{\frac{1}{2\pi} \int_{-\infty}^{\infty} \sum_{i,j} |T_{zw}^{i,j}(i\omega)|^2 d\omega}.$$

This problem has a unique solution provided that

1. $(\mathbf{A}, \mathbf{B}_2, \mathbf{C}_2)$ is stabilisable and detectable
2. \mathbf{D}_{12} and \mathbf{D}_{21} have full rank.
3. $\begin{bmatrix} \mathbf{A} - i\omega\mathbf{I} & \mathbf{B}_2 \\ \mathbf{C}_1 & \mathbf{D}_{12} \end{bmatrix}$ has full column rank for all ω
4. $\begin{bmatrix} \mathbf{A} - i\omega\mathbf{I} & \mathbf{B}_1 \\ \mathbf{C}_2 & \mathbf{D}_{21} \end{bmatrix}$ has full row rank for all ω

The state-space realisation of the optimal controller $\mathbf{K}(s)$ is then given by

$$\begin{aligned}\dot{\mathbf{u}}_K &= \mathbf{A}_K \mathbf{u}_K + \mathbf{B}_K \mathbf{y} \\ \phi &= \mathbf{C}_K \mathbf{u}_K\end{aligned}$$

where

$$\begin{aligned}\mathbf{C}_K &= -\left(\mathbf{D}_{12}^T \mathbf{D}_{12}\right)^{-1} \left(\mathbf{B}_2^T \mathbf{X} + \mathbf{D}_{12}^T \mathbf{C}_1\right) \\ \mathbf{B}_K &= \left(\mathbf{Y} \mathbf{C}_2^T + \mathbf{B}_1 \mathbf{D}_{21}^T\right) \left(\mathbf{D}_{21}^T \mathbf{D}_{21}\right)^{-1} \\ \mathbf{A}_K &= \mathbf{A} + \mathbf{B}_2 \mathbf{C}_K - \mathbf{B}_K \mathbf{C}_2\end{aligned}$$

and where \mathbf{X} and \mathbf{Y} are the unique solution of the following algebraic Riccati equations

$$\begin{aligned}(\mathbf{A} - \mathbf{B}_2 \left(\mathbf{D}_{12}^T \mathbf{D}_{12}\right)^{-1} \mathbf{D}_{12}^T \mathbf{C}_1)^T \mathbf{X} + \mathbf{X} \left(\mathbf{A} - \mathbf{B}_2 \left(\mathbf{D}_{12}^T \mathbf{D}_{12}\right)^{-1} \mathbf{D}_{12}^T \mathbf{C}_1\right) - \\ \mathbf{X} \mathbf{B}_2 \left(\mathbf{D}_{12}^T \mathbf{D}_{12}\right)^{-1} \mathbf{B}_2^T \mathbf{X} + \mathbf{C}_1^T \mathbf{C}_1 - \mathbf{C}_1^T \mathbf{D}_{12} \left(\mathbf{D}_{12}^T \mathbf{D}_{12}\right)^{-1} \mathbf{D}_{12}^T \mathbf{C}_1 = 0, \\ (\mathbf{A} - \mathbf{B}_1 \mathbf{D}_{21}^T \left(\mathbf{D}_{21}^T \mathbf{D}_{21}\right)^{-1} \mathbf{C}_2) \mathbf{Y} + \mathbf{Y} \left(\mathbf{A} - \mathbf{B}_1 \mathbf{D}_{21}^T \left(\mathbf{D}_{21}^T \mathbf{D}_{21}\right)^{-1} \mathbf{C}_2\right)^T - \\ \mathbf{Y} \mathbf{C}_2^T \left(\mathbf{D}_{21}^T \mathbf{D}_{21}\right)^{-1} \mathbf{C}_2 \mathbf{Y} + \mathbf{B}_1 \mathbf{B}_1^T - \mathbf{B}_1 \mathbf{D}_{21}^T \left(\mathbf{D}_{21}^T \mathbf{D}_{21}\right)^{-1} \mathbf{D}_{21} \mathbf{B}_1^T = 0\end{aligned}$$

Linear Quadratic Gaussian (LQG) control is a special of \mathcal{H}_2 which considers the following stochastic system

$$\begin{aligned}\dot{\mathbf{u}} &= \mathbf{A} \mathbf{u} + \mathbf{B} \phi + \mathbf{w}_d, \\ \mathbf{y} &= \mathbf{C} \mathbf{u} + \mathbf{w}_n,\end{aligned}$$

where \mathbf{w}_d is a disturbance and \mathbf{w}_n is measurements noise assumed to be uncorrelated Gaussian stochastic processes with zero means and covariances

$$\begin{aligned}E \left\{ \mathbf{w}_d(t) \mathbf{w}_d^T(\tau) \right\} &= \mathbf{W} \delta(t - \tau), \text{ and} \\ E \left\{ \mathbf{w}_n(t) \mathbf{w}_n^T(\tau) \right\} &= \mathbf{V} \delta(t - \tau).\end{aligned}$$

The LQG problem is to find $\phi(s) = \mathbf{K}(s) \mathbf{y}$ that minimises

$$\mathcal{J} = E \left\{ \lim_{T \rightarrow \infty} \frac{1}{T} \int_0^T \mathbf{u}^T \mathbf{Q} \mathbf{u} + \phi^T \mathbf{R} \phi \, dt \right\}.$$

This problem can be cast as an \mathcal{H}_2 optimisation problem by defining $\mathbf{B}_1 = \mathbf{W}^{\frac{1}{2}}$, $\mathbf{D}_{21} = \mathbf{V}^{\frac{1}{2}}$, $\mathbf{C}_1 = \mathbf{Q}^{\frac{1}{2}}$, $\mathbf{D}_{12} = \mathbf{R}^{\frac{1}{2}}$.

C

A null space algorithm for linear systems

The null space approach to transform the discrete system of equations to state-space format, as presented in chapter 2 and appendix A, relies on the availability of a general solution set for the side constraints for the smoothness conditions, boundary conditions and divergence-free condition. This requires both a null space and a particular solution for a large sparse linear system of equations. In this appendix an efficient algorithm is presented to construct a general solution set in $n^3/3 + \mathcal{O}(n^2)$ multiplications. It can be applied to both full rank and deficient rank, determined and underdetermined linear systems of the form

$$\mathbf{A}\mathbf{x} = \mathbf{b}, \tag{C.1}$$

where $\mathbf{A} \in \mathbb{R}^{m \times n}$ with $\text{rank}(\mathbf{A}) = r \leq m \leq n$. Without loss of generality it is assumed that there exists a solution set of the form

$$\mathbf{x} = \mathbf{V}\mathbf{x}_h + \mathbf{p}, \tag{C.2}$$

with $\mathbf{V} \in \mathbb{R}^{n \times (n-r)}$ a basis for the null space of \mathbf{A} , $\mathbf{x}_h \in \mathbb{R}^{n-r}$ free to choose and $\mathbf{p} \in \mathbb{R}^n$ a particular solution. The calculation of the null space is equivalent to the algorithm recently presented in Hölzel and Bernstein [72] to construct a basis for the null space of large sparse matrices. The algorithm from Hölzel and Bernstein [72] is extended in this appendix to compute both a basis for the null space and a particular solution for linear systems. The described approach represents a special case of the ABS class of algorithms introduced by Abaffy, Broyden and Spedicato [159].

C.1. ALGORITHM

The algorithm computes a basis for the null space and a particular solution in m stages such that $\mathbf{x}^{(m)}$ solves the system at stage m , that is

$$\mathbf{A}\mathbf{x}^{(m)} = \mathbf{b}, \quad (\text{C.3})$$

where the solution is expressed as

$$\mathbf{x}^{(m)} = \mathbf{V}^{(m)}\mathbf{x}_h^{(m)} + \mathbf{p}^{(m)}. \quad (\text{C.4})$$

Starting with $\mathbf{V}^{(0)} = \mathbf{I}_n$, $\mathbf{p}^{(0)} = 0$, at the k th stage we wish to update the basis for the null space and the particular solution such that

$$\mathbf{A}^{(k)} = \mathbf{A}\mathbf{V}^{(k-1)} = \begin{matrix} n-k+1 \\ \left[\begin{array}{cc} 0 & k-1 \\ \mathbf{A}_2^{(k)} & m-k+1 \end{array} \right] \end{matrix}, \quad (\text{C.5a})$$

$$\mathbf{b}^{(k)} = \mathbf{b} - \mathbf{A}\mathbf{p}^{(k-1)} = \begin{matrix} \left[\begin{array}{cc} 0 & k-1 \\ \mathbf{b}_2^{(k)} & m-k+1 \end{array} \right] \end{matrix}. \quad (\text{C.5b})$$

In other words $\mathbf{V}^{(k)} \in \mathbb{R}^{n \times (n-k)}$ is a basis for the null space of the first k rows of \mathbf{A} and $\mathbf{p}^{(k)} \in \mathbb{R}^n$ a particular solution of the first k equations of $\mathbf{A}\mathbf{x} = \mathbf{b}$. At the end of the m th stage we have $\mathbf{A}\mathbf{V}^{(m)} = 0$ and $\mathbf{A}\mathbf{p}^{(m)} = \mathbf{b}$ such that (C.4) is a solution of the system (C.1). The equations are eliminated by successively substituting a solution for each equation of the form (C.4). The expressions for $\mathbf{V}^{(k)}$, $\mathbf{p}^{(k)}$ are based on the following proposition.

Proposition 1. *Let $\mathbf{A} \in \mathbb{R}^{m \times n}$, $\mathbf{a} \in \mathbb{R}^{1 \times n}$, $\mathbf{b} \in \mathbb{R}^m$ and $b_1 \in \mathbb{R}$. Also let $\mathbf{V} \in \mathbb{R}^{n \times (n-1)}$ be a basis for $\text{null}(\mathbf{a})$, $\mathbf{M} \in \mathbb{R}^{(n-1) \times (n-m-1)}$ a basis for $\text{null}(\mathbf{A}\mathbf{V})$, $\mathbf{p} \in \mathbb{R}^n$ a particular solution of $\mathbf{a}\mathbf{p} = b_1$ and $\mathbf{q} \in \mathbb{R}^{n-1}$ a particular solution of $\mathbf{A}\mathbf{V}\mathbf{q} = \mathbf{b} - \mathbf{A}\mathbf{p}$. Then*

1) $\mathbf{V}' = \mathbf{V}\mathbf{M}$ is basis for the null space of $\mathbf{A}' := \begin{bmatrix} \mathbf{a} \\ \mathbf{A} \end{bmatrix}$;

2) $\mathbf{p}' = \mathbf{V}\mathbf{q} + \mathbf{p}$ is particular solution for $\mathbf{A}'\mathbf{p}' = \mathbf{b}'$ where $\mathbf{b}' := \begin{bmatrix} b_1 \\ \mathbf{b} \end{bmatrix}$.

Proof. A proof for 1) is given in [72] and is also included here for completeness. Let $\mathbf{y} \in \text{null}(\mathbf{A}')$ such that $\mathbf{a}\mathbf{y} = 0$ and $\mathbf{A}\mathbf{y} = 0$. Since $\mathbf{y} \in \text{null}(\mathbf{a})$ there exists $\mathbf{w} \in \mathbb{R}^{n-1}$ such that $\mathbf{y} = \mathbf{V}\mathbf{w}$. Then $\mathbf{A}\mathbf{y} = \mathbf{A}\mathbf{V}\mathbf{w} = 0$ and since \mathbf{M} is a basis for $\text{null}(\mathbf{A}\mathbf{V})$ there exists $\mathbf{z} \in \mathbb{R}^{n-m-1}$ such that $\mathbf{w} = \mathbf{M}\mathbf{z}$. Then we have $\mathbf{y} = \mathbf{V}\mathbf{M}\mathbf{z}$ and hence $\mathbf{V}' = \mathbf{V}\mathbf{M}$ is a basis for $\text{null}(\mathbf{A}')$. Statement 2) is proved in the similar way. Let \mathbf{p}' be a particular solution of $\mathbf{A}'\mathbf{p}' = \mathbf{b}'$ such that $\mathbf{a}\mathbf{p}' = b_1$ and $\mathbf{A}\mathbf{p}' = \mathbf{b}$. Since also $\mathbf{a}\mathbf{p} = b_1$ and \mathbf{V} is a basis for $\text{null}(\mathbf{a})$, there exists $\mathbf{q} \in \mathbb{R}^{n-1}$ such that $\mathbf{p}' = \mathbf{V}\mathbf{q} + \mathbf{p}$. Then $\mathbf{A}\mathbf{p}' = \mathbf{A}(\mathbf{V}\mathbf{q} + \mathbf{p}) = \mathbf{b}$ which shows that \mathbf{q} must be a particular solution of $\mathbf{A}\mathbf{V}\mathbf{q} = \mathbf{b} - \mathbf{A}\mathbf{p}$. \square

From this proposition it follows that following recurrence for $\mathbf{V}^{(k)}$ and $\mathbf{p}^{(k)}$ result in the forms (C.5a) and (C.5b).

$$\mathbf{V}^{(k)} = \mathbf{V}^{(k-1)} \mathbf{M}_k, \quad (\text{C.6})$$

$$\mathbf{p}^{(k)} = \mathbf{V}^{(k-1)} \mathbf{q}_k + \mathbf{p}^{(k-1)}, \quad (\text{C.7})$$

with $\mathbf{M}_k \in \mathbb{R}^{(n-k+1) \times (n-k)}$ a basis for the null space of the k th equation of the reduced system, that is

$$\mathbf{a}_k^{(k)} \mathbf{M}_k = 0, \quad (\text{C.8})$$

and $\mathbf{q}_k \in \mathbb{R}^{n-k+1}$ a particular solution of k th equation of the reduced system, that is

$$\mathbf{a}_k^{(k)} \mathbf{q}_k = \mathbf{b}_k^{(k)}, \quad (\text{C.9})$$

where $\mathbf{a}_k^{(k)}$ denotes the k th row of $\mathbf{A}^{(k)}$. Constructing a basis for a null space and a particular solution of a single equation is trivial. Let $\mathbf{a}_k^{(k)} = [a_{k,1}^{(k)}, \dots, a_{k,n-k+1}^{(k)}]$ and let s be an index such that $a_{k,s}^{(k)} \neq 0$ and define the column vector of multipliers $\mathbf{m}_k \in \mathbb{R}^{n-k}$ as

$$\mathbf{m}_k = \left[\frac{a_{k,1}^{(k)}}{a_{k,s}^{(k)}}, \dots, \frac{a_{k,s-1}^{(k)}}{a_{k,s}^{(k)}}, \frac{a_{k,s+1}^{(k)}}{a_{k,s}^{(k)}}, \dots, \frac{a_{k,n-k+1}^{(k)}}{a_{k,s}^{(k)}} \right]^T \quad (\text{C.10})$$

then

$$\mathbf{M}_k = \begin{bmatrix} \mathbf{I}_{s-1} & \mathbf{0}_{(s-1) \times (n-k-s+1)} \\ \mathbf{0}_{1 \times (s-1)} & \mathbf{0}_{1 \times (n-k-s+1)} \\ \mathbf{0}_{(n-k-s+1) \times (s-1)} & \mathbf{I}_{n-k-s+1} \end{bmatrix} - \mathbf{e}_s \mathbf{m}_k^T, \quad (\text{C.11})$$

is a basis for the null space of $\mathbf{a}_k^{(k)}$ and

$$\mathbf{q}_k = \left[\mathbf{0}_{1 \times (s-1)}, \mathbf{b}_k^{(k)} / a_{k,s}^{(k)}, \mathbf{0}_{1 \times (n-k-s+1)} \right]^T \quad (\text{C.12})$$

a solution of (C.9). For stability reasons the index s is chosen such that it is the index of the largest absolute element in $\mathbf{a}_k^{(k)}$ where

$$|a_{k,s}^{(k)}| = \max_{1 \leq j \leq n-k+1} |a_{k,j}^{(k)}|. \quad (\text{C.13})$$

The complete algorithm is summarised below.

input : $\mathbf{A} \in \mathbb{R}^{m \times n}$ with $\text{rank}(\mathbf{A}) = r \leq m \leq n$ and $\mathbf{b} \in \mathbb{R}^{m \times 1}$.
output: Basis matrix $\mathbf{V} \in \mathbb{R}^{n \times n-r}$ for the null space of \mathbf{A} and a particular solution \mathbf{p} of $\mathbf{Ax} = \mathbf{b}$.

- 1 initialization; $\mathbf{V}^{(0)} = \mathbf{I}$, $\mathbf{p}^{(0)} = \mathbf{0}$.
- 2 **for** $k = 1 : m$ **do**
- 3 compute $\mathbf{a}_k^{(k)} = \mathbf{a}_k \mathbf{V}^{(k-1)}$, $b_k^{(k)} = b_k - \mathbf{a}_k \mathbf{p}^{(k-1)}$.
- 4 Find the column index s of the largest absolute element in $\mathbf{a}_k^{(k)}$;
- 5 **if** $a_{k,s}^{(k)} = 0$ **then**
- 6 $\mathbf{V}^{(k)} = \mathbf{V}^{(k-1)}$, $\mathbf{p}^{(k)} = \mathbf{p}^{(k-1)}$
- 7 **else**
- 8 Construct \mathbf{M}_k (C.11) and \mathbf{q}_k (C.12).
- 9 Update the basis for the null space $\mathbf{V}^{(k)} = \mathbf{V}^{(k-1)} \mathbf{M}_k$.
- 10 Update the particular solution $\mathbf{p}^{(k)} = \mathbf{V}^{(k-1)} \mathbf{q}_k + \mathbf{p}^{(k-1)}$.
- 11 **end**
- 12 **end**
- 13 **return** $\mathbf{V} = \mathbf{V}^{(k)}$, $\mathbf{p} = \mathbf{p}^{(k)}$

Algorithm 1: ABS nullspace algorithm

All computations in algorithm 1 are of the order n^2 except for the update of the null space matrix (line 9) which requires $n^3/3$ calculations.

C.2. AN ILLUSTRATIVE EXAMPLE

Consider the following linear system $\mathbf{Ax} = \mathbf{b}$

$$\begin{bmatrix} 1 & -2 & -1 \\ -3 & 2 & 3 \end{bmatrix} \begin{bmatrix} x_1 \\ x_2 \\ x_3 \end{bmatrix} = \begin{bmatrix} -1 \\ 2 \end{bmatrix}. \quad (\text{C.14})$$

For the first iteration we have $\mathbf{a}_1^{(1)} = \mathbf{a}_1$ and $b_1^{(1)} = b_1$. The second element $a_{1,2}^{(1)}$ is the largest absolute element of $\mathbf{a}_1^{(1)}$. The null space and particular solution of the first equation with $s = 2$ are given by

$$\mathbf{M}_1 = \begin{bmatrix} 1 & 0 \\ \frac{1}{2} & -\frac{1}{2} \\ 0 & 1 \end{bmatrix}, \quad \mathbf{q}_1 = \begin{bmatrix} 0 \\ \frac{1}{2} \\ 0 \end{bmatrix}. \quad (\text{C.15})$$

For the first iteration we have $\mathbf{V}^{(1)} = \mathbf{M}_1$ and $\mathbf{p}^{(1)} = \mathbf{q}_1$. Continuing to the second iteration, the second equation of the reduced system is defined by

$$\mathbf{a}_2^{(2)} = \mathbf{a}_2 \mathbf{V}^{(1)} = \begin{bmatrix} -3 & 2 & 3 \end{bmatrix} \begin{bmatrix} 1 & 0 \\ \frac{1}{2} & -\frac{1}{2} \\ 0 & 1 \end{bmatrix} = \begin{bmatrix} -2 & 2 \end{bmatrix}, \quad (\text{C.16})$$

$$b_2^{(2)} = b_2 - \mathbf{a}_2 \mathbf{p}^{(1)} = 2 - \begin{bmatrix} -3 & 2 & 3 \end{bmatrix} \begin{bmatrix} 0 \\ \frac{1}{2} \\ 0 \end{bmatrix} = 1. \quad (\text{C.17})$$

The first element is the largest absolute element of $\mathbf{a}_2^{(2)}$. The null space and particular solution with $s = 1$ of the second equation of the reduced system are given by

$$\mathbf{M}_2 = \begin{bmatrix} 1 \\ 1 \end{bmatrix}, \quad \mathbf{q}_2 = \begin{bmatrix} -\frac{1}{2} \\ 0 \end{bmatrix}. \quad (\text{C.18})$$

The null space and particular solution for the original system (C.14) are then given by

$$\mathbf{V}^{(2)} = \mathbf{V}^{(1)} \mathbf{M}_2 = \begin{bmatrix} 1 & 0 \\ \frac{1}{2} & -\frac{1}{2} \\ 0 & 1 \end{bmatrix} \begin{bmatrix} 1 \\ 1 \end{bmatrix} = \begin{bmatrix} 1 \\ 0 \\ 1 \end{bmatrix}, \quad (\text{C.19})$$

$$\mathbf{p}^{(2)} = \mathbf{V}^{(1)} \mathbf{q}_2 + \mathbf{p}^{(1)} = \begin{bmatrix} 1 & 0 \\ \frac{1}{2} & -\frac{1}{2} \\ 0 & 1 \end{bmatrix} \begin{bmatrix} -\frac{1}{2} \\ 0 \end{bmatrix} + \begin{bmatrix} 0 \\ \frac{1}{2} \\ 0 \end{bmatrix} = \begin{bmatrix} -\frac{1}{2} \\ \frac{1}{4} \\ 0 \end{bmatrix}. \quad (\text{C.20})$$

The expressions can be verified by substituting $\mathbf{x} = \mathbf{V}^{(2)} \mathbf{x}_h + \mathbf{p}^{(2)}$ in (C.14).

Bibliography

- [1] J. C. Lin, E. A. Whalen, J. L. Eppink, E. J. Siochi, M. G. Alexander, and M. Y. Andino, *Innovative flow control concepts for drag reduction*, AIAA SciTech (2016).
- [2] H. Choi, W.-P. Jeon, and J. Kim, *Control of flow over a bluff body*, Annual Review Fluid Mechanics **40**, 113–139 (2008).
- [3] D. Sipp, O. Marquet, P. Meliga, and A. Barbagallo, *Dynamics and control of global instabilities in open-flows: a linearized approach*, Applied Mechanics Reviews **63**, 030801 (2010).
- [4] C. W. Rowley and D. R. Williams, *Dynamics and control of high-Reynolds-number flow over open cavities*, Annual Review of Fluid Mechanics **38**, 251–276 (2006).
- [5] L. N. Cattafesta, Q. Song, D. R. Williams, C. W. Rowley, and F. S. Alvi, *Active control of flow-induced cavity oscillations*, Progress in Aerospace Sciences **44**, 479–502 (2008).
- [6] J. Kim and T. R. Bewley, *A linear systems approach to flow control*, Annual Review Fluid Mechanics **39**, 383–417 (2007).
- [7] S. Bagheri and D. S. Henningson, *Transition delay using control theory*, Philosophical Transactions of the Royal Society of London A: Mathematical, Physical and Engineering Sciences **369**, 1365–1381 (2011).
- [8] S. L. Brunton and B. R. Noack, *Closed-loop turbulence control: progress and challenges*, Applied Mechanics Reviews **67**, 050801 (2015).
- [9] D. Sipp and P. J. Schmid, *Linear closed-loop control of fluid instabilities and noise-induced perturbations: A review of approaches and tools*, Applied Mechanics Reviews **68**, 020801 (2016).
- [10] O. M. Aamo and M. Krstic, *Flow control by feedback*, edited by Springer (Springer, 2002).
- [11] P. Huerre, *Local and global instabilities in spatial developing flows*, Annual Review Fluid Mechanics **22**, 473–537 (1990).
- [12] V. Theofilis, *Global linear instability*, Annual Review of Fluid Mechanics **43**, 319–352 (2011).

- [13] V. Kitsios, D. Rodríguez, V. Theofilis, A. Ooi, and J. Soria, *Biglobal stability analysis in curvilinear coordinates of massively separated lifting bodies*, Journal of Computational Physics **228**, 7181–7196 (2009).
- [14] K. Taira, S. L. Brunton, S. Dawson, C. W. Rowley, T. Colonius, B. J. McKeon, O. T. Schmidt, S. Gordeyev, V. Theofilis, and L. S. Ukeiley, *Modal analysis of fluid flows: An overview*, AIAA journal **55**, 4013–4040 (2017).
- [15] T. L. B. Flinois and A. S. Morgans, *Feedback control of unstable flows: a direct modelling approach using the eigensystem realization algorithm*, Journal of Fluid Mechanics **793**, 41–78 (2016).
- [16] W. S. Saric, H. L. Reed, and E. J. Kerschen, *Boundary-layer receptivity to freestream disturbances*, Annual review of fluid mechanics **34**, 291–319 (2002).
- [17] Y. S. Kachanov, *Physical mechanisms of laminar-boundary-layer transition*, Annual review of fluid mechanics **26**, 411–482 (1994).
- [18] S. C. Reddy and D. S. Henningson, *Energy growth in viscous channel flows*, Journal of Fluid Mechanics **252**, 209–238 (1993).
- [19] P. Andersson, L. Brandt, A. Bottaro, and D. S. Henningson, *On the breakdown of boundary layer streaks*, Journal of Fluid Mechanics **428**, 29–60 (2001).
- [20] B. F. Farrell, *Optimal excitation of perturbations in viscous shear flow*, The Physics of fluids **31**, 2093–2102 (1988).
- [21] P. J. Schmid and D. S. Henningson, *Stability and Transition in Shear Flows*, edited by Springer (Springer, 2001).
- [22] S. A. Orszag, *Accurate solution of the Orr-Sommerfeld stability equation*, Journal of Fluid Mechanics **50**, 689–703 (1971).
- [23] P. J. Bridges, T. J. and Morris, *Differential eigenvalue problems in which the parameter appear nonlinearly*, Journal of Computational Physics **55**, 437–460 (1984).
- [24] M. Kotsonis and S. Ghaemi, *Forcing mechanisms of dielectric barrier discharge plasma actuators at carrier frequency of 625 Hz*, Journal of Applied Physics **110**, 113301 (2011).
- [25] L. N. Cattafesta III and M. Sheplak, *Actuators for active flow control*, Annual Review of Fluid Mechanics **43**, 247–272 (2011).
- [26] K. K. Chen and C. W. Rowley, *\mathcal{H}_2 optimal actuator and sensor placement in the linearised complex Ginzburg–Landau system*, Journal of Fluid Mechanics **681**, 241–260 (2011).
- [27] B. A. Belson, O. Semeraro, C. W. Rowley, and D. S. Henningson, *Feedback control of instabilities in the two-dimensional blasius boundary layer: The role of sensors and actuators*, Physics of Fluids (1994-present) **25**, 054106 (2013).

- [28] P. J. Schmid and D. Sipp, *Linear control of oscillator and amplifier flows*, Phys. Rev. Fluids **1**, 040501 (2016).
- [29] K. Zhou, J. C. Doyle, and K. Glover, *Robust and optimal control*, edited by P. H. N. Jersey (Prentice hall New Jersey, 1996).
- [30] J. C. Doyle, K. Glover, P. P. Khargonekar, and B. Francis, *State-space solutions to standard H_2 and H_∞ control problems*, Automatic Control, IEEE Transactions on **34**, 831–847 (1989).
- [31] N. Wiener, *Cybernetics or Control and Communication in the Animal and the Machine*, Vol. 25 (MIT press, 1961).
- [32] C. W. Rowley and S. T. M. Dawson, *Model reduction for flow analysis and control*, Annual Review of Fluid Mechanics **49**, 387–417 (2017).
- [33] S. Bagheri, L. Brandt, and D. S. Henningson, *Input–output analysis, model reduction and control of the flat-plate boundary layer*, Journal of Fluid Mechanics **620**, 263–298 (2009).
- [34] C. W. Rowley, *Model reduction for fluids, using balanced proper orthogonal decomposition*, International Journal of Bifurcation and Chaos **15**, 997–1013 (2005).
- [35] B. R. Noack, M. Morzynski, and G. Tadmor, *Reduced-order modelling for flow control*, Vol. 528 (Springer Science & Business Media, 2011).
- [36] O. A. Ladyzhenskaya, *The mathematical theory of viscous incompressible flow*, Vol. 12 (Gordon & Breach New York, 1969).
- [37] T. R. Bewley and S. Liu, *Optimal and robust control and estimation of linear paths to transition*, Journal of Fluid Mechanics **365**, 305–349 (1998).
- [38] J. McKernan, G. Papadakis, and J. F. Whidborne, *A linear state-space representation of plane poiseuille flow for control design: a tutorial*, International Journal of Modelling, Identification and Control **1**, 272–280 (2006).
- [39] B. L. Jones, P. H. Heins, E. C. Kerrigan, J. F. Morrison, and A. S. Sharma, *Modelling for robust feedback control of fluid flows*, Journal of Fluid Mechanics **769**, 687–722 (2015).
- [40] M. J. Lai and L. L. Schumaker, *Spline functions on triangulations*, 110 (Cambridge University Press, 2007).
- [41] G. Farin, *Triangular Bernstein-Bézier patches*, Computer Aided Geometric Design **3**, 83–127 (1986).
- [42] C. de Boor, *B-form basics*, in *Geometric Modeling: Algorithms and New Trends*, edited by G. Farin (SIAM, Philadelphia, 1987) pp. 131–148.

- [43] R. F. Curtain and H. J. Zwart, *An introduction to infinite-dimensional linear systems theory* (Springer-Verlag, New York, 1995).
- [44] I. Lasiecka and R. Triggiani, *Control theory for partial differential equations: Volume 1, Abstract parabolic systems: Continuous and approximation theories*, Vol. 1 (Cambridge University Press, Cambridge, UK, 2000).
- [45] B. Bamieh, F. Paganini, and M. Dahleh, *Distributed control of spatially invariant systems*, IEEE Transactions on Automatic Control **47**, 1091–1107 (2002).
- [46] A. Smyshlyaev and M. Krstic, *Closed-form boundary state feedbacks for a class of 1-D partial integro-differential equations*, IEEE Transactions on Automatic Control **49**, 2185–2201 (2004).
- [47] G. Hagen, I. Mezić, and B. Bamieh, *Distributed control design for parabolic evolution equations: application to compressor stall control*, Automatic Control, IEEE Transactions on **49**, 1247–1258 (2004).
- [48] A. Smyshlyaev and M. Krstic, *Backstepping observers for a class of parabolic PDEs*, Systems and Control Letters **54**, 613–625 (2005).
- [49] A. Baccoli, A. Pisano, and Y. Orlov, *Boundary control of coupled reaction-diffusion processes with constant parameters*, Automatica **54**, 80 – 90 (2015).
- [50] R. Vazquez and M. Krstic, *Control of turbulent and magnetohydrodynamic channel flows: boundary stabilization and state estimation* (Springer Science & Business Media, 2007).
- [51] R. Vazquez and M. Krstic, *A closed-form feedback controller for stabilization of the linearized 2-D Navier-Stokes Poiseuille system*, IEEE Transactions on Automatic Control **52**, 2298–2312 (2007).
- [52] H.-X. Li and C. Qi, *Modeling of distributed parameter systems for applications—a synthesized review from time-space separation*, Journal of Process Control **20**, 891–901 (2010).
- [53] M. J. Balas, *Feedback control of linear diffusion processes*, International Journal of Control **29**, 523–534 (1979).
- [54] M. J. Balas, *The galerkin method and feedback control of linear distributed parameter systems*, Journal of Mathematical Analysis and Applications **91**, 527–546 (1983).
- [55] M. J. Balas, *Stability of distributed parameter systems with finite-dimensional controller-compensators using singular perturbations*, Journal of Mathematical Analysis and Applications **99**, 80–108 (1984).
- [56] A. Armaou and P. D. Christofides, *Robust control of parabolic PDE systems with time-dependent spatial domains*, Automatica **37**, 61–69 (2001).

- [57] P. D. Christofides, *Nonlinear and robust control of PDE systems: Methods and applications to transport-reaction processes* (Springer Science & Business Media, New York, 2001).
- [58] P. D. Christofides and J. Baker, *Robust output feedback control of quasi-linear parabolic PDE systems*, *Systems and Control Letters* **36**, 307–316 (1999).
- [59] A. Armaou and P. D. Christofides, *Finite-dimensional control of nonlinear parabolic PDE systems with time-dependent spatial domains using empirical eigenfunctions*, *Applied Mathematics and Computer Science* **11**, 287–318 (2001).
- [60] A. Armaou and P. D. Christofides, *Dynamic optimization of dissipative PDE systems using nonlinear order reduction*, *Chemical Engineering Science* **57**, 5083–5114 (2002).
- [61] J. Baker, A. Armao, and P. D. Christofides, *Finite-dimensional approximation and control of non-linear parabolic PDE systems*, *International Journal of Control* **73**, 439–456 (2000).
- [62] G. Awanou, M. J. Lai, and P. Wenston, *The multivariate spline method for scattered data fitting and numerical solutions of partial differential equations*, in *Wavelets and Splines*, edited by G. Chen and M. J. Lai (Nashboro Press, Brentwood, TN, Athens, 2005) pp. 24–75.
- [63] X. L. Hu, D. F. Han, and M. J. Lai, *Bivariate splines of various degrees for numerical solution of partial differential equations*, *SIAM Journal on Scientific Computing* **29**, 1338–1354 (2007).
- [64] G. Awanou and M. J. Lai, *Trivariate spline approximations of 3D Navier-Stokes equations*, *Mathematics of computation* **74**, 585–601 (2004).
- [65] M. J. Lai and P. Wenston, *Bivariate splines for fluid flows*, *Computers & fluids* **33**, 1047–1073 (2004).
- [66] N. Govindarajan, C. C. de Visser, and K. Krishnakumar, *A sparse collocation method for solving time-dependent HJB equations using multivariate B-splines*, *Automatica* **50**, 2234–2244 (2014).
- [67] B. C. Moore, *Principal component analysis in linear systems: Controllability, observability, and model reduction*, *IEEE Transactions on Automatic Control* **26**, 17–32 (1981).
- [68] P. D. Christofides and P. Daoutidis, *Finite-dimensional control of parabolic PDE systems using approximate inertial manifolds*, *Journal of Mathematical Analysis and Applications* **216**, 398–420 (1997).
- [69] K. C. Chung and T. H. Yao, *On lattices admitting unique lagrange interpolations*, *SIAM Journal on numerical analysis* **13**, 735–743 (1977).

- [70] C. C. de Visser, Q. P. Chu, and J. A. Mulder, *A new approach to linear regression with multivariate splines*, *Automatica* **45**, 2903–2909 (2009).
- [71] C. C. de Visser, Q. P. Chu, and J. A. Mulder, *Differential constraints for bounded recursive identification with multivariate splines*, *Automatica* **47**, 2059–2066 (2011).
- [72] M. S. Hölzel and D. S. Bernstein, *A matrix nullspace approach for solving equality-constrained multivariable polynomial least-squares problems*, *Automatica* **50**, 3030 – 3037 (2014).
- [73] M.-J. Lai and L. L. Schumaker, *On the approximation power of bivariate splines*, *Advances in Computational Mathematics* **9**, 251–279 (1998).
- [74] M. Von Golitschek and L. L. Schumaker, *Bounds on projections onto bivariate polynomial spline spaces with stable local bases*, *Constructive approximation* **18**, 241–254 (2002).
- [75] M. R. Jovanović and B. Bamieh, *A formula for frequency responses of distributed systems with one spatial variable*, *Systems & control letters* **55**, 27–37 (2006).
- [76] P. J. Roache, *Code verification by the method of manufactured solutions*, *Journal of Fluids Engineering* **124**, 4–10 (2002).
- [77] K. M. Butler and B. F. Farrell, *Three-dimensional optimal perturbations in viscous shear flow*, *Physics of Fluids A: Fluid Dynamics* (1989-1993) **4**, 1637–1650 (1992).
- [78] L. N. Trefethen, A. E. Trefethen, S. C. Reddy, and T. A. Driscoll, *Hydrodynamic stability without eigenvalues*, *Science* **261**, 578–584 (1993).
- [79] M. R. Jovanovic and B. Bamieh, *Componentwise energy amplification in channel flows*, *Journal of Fluid Mechanics* **534**, 145–183 (2005).
- [80] S. S. Joshi, J. L. Speyer, and J. Kim, *A systems theory approach to the feedback stabilization of infinitesimal and finite-amplitude disturbances in plane Poiseuille flow*, *Journal of Fluid Mechanics* **332**, 157–184 (1997).
- [81] L. Cortelezzi and J. L. Speyer, *Robust reduced-order controller of laminar boundary layer transitions*, *Physical Review E* **58**, 1906–1910 (1998).
- [82] M. Högberg, T. R. Bewley, and D. S. Henningson, *Linear feedback control and estimation of transition in plane channel flow*, *Journal of Fluid Mechanics* **481**, 149–175 (2003).
- [83] L. Baramov, O. R. Tutty, and E. Rogers, *H_∞ control of nonperiodic two-dimensional channel flow*, *Control Systems Technology, IEEE Transactions on* **12**, 111–122 (2004).

- [84] M. Chevalier, J. Hoepffner, E. Åkervik, and D. S. Henningson, *Linear feedback control and estimation applied to instabilities in spatially developing boundary layers*, *Journal of Fluid Mechanics* **588**, 163 (2007).
- [85] O. Semeraro, S. Bagheri, L. Brandt, and D. S. Henningson, *Transition delay in a boundary layer flow using active control*, *Journal of Fluid Mechanics* **731**, 288–311 (2013).
- [86] S. Skogestad and I. Postlethwaite, *Multivariable Feedback Control: Analysis and Design* (John Wiley & Sons, 2005).
- [87] N. Fabbiane, B. Simon, F. Fischer, S. Grundmann, S. Bagheri, and D. S. Henningson, *On the role of adaptivity for robust laminar flow control*, *Journal of Fluid Mechanics* **767**, R1 (2015).
- [88] M. Samimy, M. Debiasi, E. Caraballo, A. Serrani, X. Yuan, J. Little, and J. H. Myatt, *Feedback control of subsonic cavity flows using reduced-order models*, *Journal of Fluid Mechanics* **579**, 315–346 (2007).
- [89] A. Barbagallo, D. Sipp, and P. J. Schmid, *Closed-loop control of an open cavity flow using reduced-order models*, *Journal of Fluid Mechanics* **641**, 1–50 (2009).
- [90] Z. Ma, S. Ahuja, and C. W. Rowley, *Reduced-order models for control of fluids using the eigensystem realization algorithm*, *Theoretical and Computational Fluid Dynamics* **25**, 233–247 (2011).
- [91] J. Hoepffner, M. Chevalier, T. R. Bewley, and D. S. Henningson, *State estimation in wall-bounded flow systems. part 1. perturbed laminar flows*, *Journal of Fluid Mechanics* **534**, 263–294 (2005).
- [92] O. Semeraro, S. Bagheri, L. Brandt, and D. S. Henningson, *Feedback control of three-dimensional optimal disturbances using reduced-order models*, *Journal of Fluid Mechanics* **677**, 63–102 (2011).
- [93] M. Chevalier, J. Hoepffner, T. R. Bewley, and D. S. Henningson, *State estimation in wall-bounded flow systems. part 2. turbulent flows*, *Journal of Fluid Mechanics* **552**, 167–187 (2006).
- [94] M. Högberg and D. S. Henningson, *Linear optimal control applied to instabilities in spatially developing boundary layers*, *Journal of Fluid Mechanics* **470**, 151–179 (2002).
- [95] A. Monokrousos, L. Brandt, P. Schlatter, and D. S. Henningson, *DNS and LES of estimation and control of transition in boundary layers subject to free-stream turbulence*, *International Journal of Heat and Fluid Flow* **29**, 841–855 (2008).

- [96] K. H. Lee, L. Cortelezzi, J. Kim, and J. Speyer, *Application of reduced-order controller to turbulent flows for drag reduction*, *Physics of Fluids* **13**, 1321–1330 (2001).
- [97] M. Högberg, T. R. Bewley, and D. S. Henningson, *Relaminarization of $Re_\tau = 100$ turbulence using gain scheduling and linear state-feedback control*, *Physics of Fluids (1994-present)* **15**, 3572–3575 (2003).
- [98] A. S. Sharma, J. F. Morrison, B. J. McKeon, D. J. N. Limebeer, W. H. Koberg, and S. J. Sherwin, *Relaminarisation of $Re_\tau = 100$ channel flow with globally stabilising linear feedback control*, *Physics of Fluids (1994-present)* **23**, 125105 (2011).
- [99] M. Pastoor, L. Henning, B. R. Noack, R. King, and G. Tadmor, *Feedback shear layer control for bluff body drag reduction*, *Journal of Fluid Mechanics* **608**, 161–196 (2008).
- [100] S. Bagheri, D. S. Henningson, J. Hoepffner, and P. J. Schmid, *Input-output analysis and control design applied to a linear model of spatially developing flows*, *Applied Mechanics Reviews* **62**, 020803 (2009).
- [101] M. Ilak and C. W. Rowley, *Modeling of transitional channel flow using balanced proper orthogonal decomposition*, *Physics of Fluids (1994-present)* **20**, 034103 (2008).
- [102] E. Åkervik, J. Hoepffner, U. Ehrenstein, and D. S. Henningson, *Optimal growth, model reduction and control in a separated boundary-layer flow using global eigenmodes*, *Journal of Fluid Mechanics* **579**, 305–314 (2007).
- [103] B. R. Noack, K. Afanasiev, M. Morzynski, G. Tadmor, and F. Thiele, *A hierarchy of low-dimensional models for the transient and post-transient cylinder wake*, *Journal of Fluid Mechanics* **497**, 335–363 (2003).
- [104] S. G. Siegel, J. Seidel, C. Fagley, D. M. Luchtenburg, K. Cohen, and T. McLaughlin, *Low-dimensional modelling of a transient cylinder wake using double proper orthogonal decomposition*, *Journal of Fluid Mechanics* **610**, 1–42 (2008).
- [105] S. Bagheri, E. Åkervik, L. Brandt, and D. S. Henningson, *Matrix-free methods for the stability and control of boundary layers*, *AIAA journal* **47**, 1057–1068 (2009).
- [106] S. Ahuja and C. W. Rowley, *Feedback control of unstable steady states of flow past a flat plate using reduced-order estimators*, *Journal of fluid mechanics* **645**, 447–478 (2010).
- [107] J. N. Juang and R. S. Pappa, *An eigensystem realization algorithm for modal parameter identification and model reduction*, *Journal of guidance, control, and dynamics* **8**, 620–627 (1985).

- [108] S. J. Illingworth, A. S. Morgans, and C. W. Rowley, *Feedback control of cavity flow oscillations using simple linear models*, *Journal of Fluid Mechanics* **709**, 223–248 (2012).
- [109] R. Dadfar, O. Semeraro, A. Hanifi, and D. S. Henningson, *Output feedback control of blasius flow with leading edge using plasma actuator*, *AIAA journal* **51**, 2192–2207 (2013).
- [110] T. R. Bewley, R. Temam, and M. Ziane, *A general framework for robust control in fluid mechanics*, *Physica D: Nonlinear Phenomena* **138**, 260–392 (2000).
- [111] R. Rannacher, S. Turek, and J. G. Heywood, *Artificial boundaries and flux and pressure conditions for the incompressible Navier-Stokes equations*, *International Journal for Numerical Methods in Fluids* **22**, 325–352 (1996).
- [112] M. Kotsonis, R. Giepmans, S. Hulshoff, and L. Veldhuis, *Numerical study of the control of Tollmien–Schlichting waves using plasma actuators*, *AIAA journal* **51**, 2353–2364 (2013).
- [113] H. O. Fattorini, *Boundary control systems*, *SIAM Journal on Control* **6**, 349–385 (1968).
- [114] B. D. O. Anderson and Y. Liu, *Controller reduction: concepts and approaches*, *IEEE Transactions on Automatic Control* **34**, 802–812 (1989).
- [115] A. J. Laub, M. T. Heath, C. C. Paige, and R. C. Ward, *Computation of system balancing transformations and other applications of simultaneous diagonalization algorithms*, *IEEE Transactions on Automatic Control* **32**, 115–122 (1987).
- [116] P. Andersson, M. Berggren, and D. S. Henningson, *Optimal disturbances and bypass transition in boundary layers*, *Physics of Fluids (1994–present)* **11**, 134–150 (1999).
- [117] F. P. Bertolotti, T. Herbert, and P. R. Spalart, *Linear and nonlinear stability of the blasius boundary layer*, *Journal of Fluid Mechanics* **242**, 441–474 (1992).
- [118] M. Högberg, M. Chevalier, and D. S. Henningson, *Linear compensator control of a pointsource induced perturbation in a Falkner–Skan–Cooke boundary layer*, *Physics of Fluids* **15**, 2449–2452 (2003).
- [119] R. Dadfar, A. Hanifi, and D. S. Henningson, *Feedback control for laminarization of flow over wings*, *Flow, Turbulence and Combustion* **94**, 43–62 (2015).
- [120] F. Juillet, B. J. McKeon, and P. J. Schmid, *Experimental control of natural perturbations in channel flow*, *Journal of Fluid Mechanics* **752**, 296–309 (2014).

- [121] M. Sheplak, L. Cattafesta, T. Nishida, and C. McGinley, *MEMS shear stress sensors: promise and progress*, in *24th AIAA Aerodynamic Measurement Technology and Ground Testing Conference* (2004) p. 2606.
- [122] R. J. Adrian, *On the role of conditional averages in turbulence theory*, *Turbulence in Liquids* **1**, 323–332 (1977).
- [123] N. E. Murray and L. S. Ukeiley, *Estimation of the flowfield from surface pressure measurements in an open cavity*, *AIAA journal* **41**, 969–972 (2003).
- [124] A. Sinha, A. Serrani, and M. Samimy, *Development of empirical estimators for feedback control of high-speed axisymmetric jets*, *AIAA journal* **49**, 1971–1987 (2011).
- [125] D. Lasagna, M. Orazi, and G. Iuso, *Multi-time delay, multi-point linear stochastic estimation of a cavity shear layer velocity from wall-pressure measurements*, *Physics of Fluids* **25**, 017101 (2013).
- [126] L. Ukeiley, N. Murray, Q. Song, and L. Cattafesta, *Dynamic surface pressure based estimation for flow control*, in *IUTAM Symposium on Flow Control and MEMS* (Springer, 2008) pp. 183–189.
- [127] C. W. Rowley and V. Juttijudata, *Model-based control and estimation of cavity flow oscillations*, in *Decision and Control, 2005 and 2005 European Control Conference. CDC-ECC'05. 44th IEEE Conference on* (IEEE, 2005) pp. 512–517.
- [128] S. J. Illingworth, A. S. Morgans, and C. W. Rowley, *Feedback control of flow resonances using balanced reduced-order models*, *Journal of Sound and Vibration* **330**, 1567–1581 (2011).
- [129] T. R. Bewley, P. Moin, and R. Temam, *DNS-based predictive control of turbulence: an optimal benchmark for feedback algorithms*, *Journal of Fluid Mechanics* **447**, 179–225 (2001).
- [130] H. J. Tol, M. Kotsonis, C. C. de Visser, and B. Bamieh, *Localised estimation and control of linear instabilities in two-dimensional wall-bounded shear flows*, *Journal of Fluid Mechanics* **824**, 818–865 (2017).
- [131] H. Fasel and U. Konzelmann, *Non-parallel stability of a flat-plate boundary layer using the complete Navier-Stokes equations*, *Journal of Fluid Mechanics* **221**, 311–347 (1990).
- [132] B. W. van Oudheusden, *PIV-based pressure measurement*, *Measurement Science and Technology* **24**, 032001 (2013).
- [133] S. Grundmann and C. Tropea, *Experimental transition delay using glow-discharge plasma actuators*, *Experiments in Fluids* **42**, 653–657 (2007).

- [134] A. S. Thomas, *The control of boundary-layer transition using a wave-superposition principle*, *Journal of Fluid Mechanics* **137**, 233–250 (1983).
- [135] H. W. Liepmann, G. L. Brown, and D. M. Nosenchuck, *Control of laminar-instability waves using a new technique*, *Journal of Fluid Mechanics* **118**, 187–200 (1982).
- [136] H. W. Liepmann and D. M. Nosenchuck, *Active control of laminar-turbulent transition*, *Journal of Fluid Mechanics* **118**, 201–204 (1982).
- [137] D. Sturzebecher and W. Nitsche, *Active cancellation of Tollmien-Schlichting instabilities on a wing using multi-channel sensor actuator systems*, *International Journal of Heat and Fluid Flow* **24**, 572 – 583 (2003).
- [138] M. Kotsonis, R. K. Shukla, and S. Pröbsting, *Control of natural Tollmien-Schlichting waves using dielectric barrier discharge plasma actuators*. *International Journal of Flow Control* **7** (2015).
- [139] R. Erdmann, A. Pätzold, M. Engert, I. Peltzer, and W. Nitsche, *On active control of laminar–turbulent transition on two-dimensional wings*, *Philosophical Transactions of the Royal Society of London A: Mathematical, Physical and Engineering Sciences* **369**, 1382–1395 (2011).
- [140] B. Simon, N. Fabbiane, T. Nemitz, S. Bagheri, D. S. Henningson, and S. Grundmann, *In-flight active wave cancelation with delayed-x-LMS control algorithm in a laminar boundary layer*, *Experiments in Fluids* **57**, 160 (2016).
- [141] A. Kurz, N. Goldin, R. King, C. Tropea, and S. Grundmann, *Hybrid transition control approach for plasma actuators*, *Experiments in fluids* **54**, 1610 (2013).
- [142] N. Gautier and J.-L. Aider, *Feed-forward control of a perturbed backward-facing step flow*, *Journal of Fluid Mechanics* **759**, 181–196 (2014).
- [143] N. Goldin, R. King, A. Pätzold, W. Nitsche, D. Haller, and P. Woias, *Laminar flow control with distributed surface actuation: damping tollmien-schlichting waves with active surface displacement*, *Experiments in fluids* **54**, 1478 (2013).
- [144] A. Hervé, D. Sipp, P. J. Schmid, and M. Samuelides, *A physics-based approach to flow control using system identification*, *Journal of Fluid Mechanics* **702**, 26–58 (2012).
- [145] F. Scarano and M. L. Riethmuller, *Advances in iterative multigrid PIV image processing*, *Experiments in Fluids* **29**, S051–S060 (2000).
- [146] B. Wieneke, *PIV uncertainty quantification from correlation statistics*, *Measurement Science and Technology* **26**, 074002 (2015).
- [147] M. Kotsonis, S. Ghaemi, L. Veldhuis, and F. Scarano, *Measurement of the body force field of plasma actuators*, *Journal of Physics D: Applied Physics* **44**, 045204 (2011).

- [148] J. Van Ingen, *The e^N method for transition prediction: Historical review of work at TU Delft*, in *Proceedings of the 38th AIAA Fluid Dynamics Conference and Exhibit*. (AIAA, 2008).
- [149] R. E. Hanson, N. M. Houser, and P. Lavoie, *Dielectric material degradation monitoring of dielectric barrier discharge plasma actuators*, *Journal of Applied Physics* **115**, 043301 (2014).
- [150] M. J. Balas, *Feedback control of flexible systems*, *IEEE Transactions on Automatic Control* **23**, 673–679 (1978).
- [151] J. A. Weideman and S. C. Reddy, *A matlab differentiation matrix suite*, *ACM Trans. Math. Softw.* **26**, 465–519 (2000).
- [152] R. J. Baaij, *Robust control of the Kuramoto-Sivashinsky equation*, Master's thesis, TU Delft Aerospace Engineering (2017).
- [153] W. J. Rugh and J. S. Shamma, *Research on gain scheduling*, *Automatica* **36**, 1401–1425 (2000).
- [154] D. J. Leith and W. E. Leithead, *Survey of gain-scheduling analysis and design*, *International journal of control* **73**, 1001–1025 (2000).
- [155] J. Slotine and W. Li, *Applied Nonlinear Control* (Prentice-Hall, 1991).
- [156] M. Krstic, I. Kanellakopoulos, and P. V. Kokotovic, *Nonlinear and Adaptive Control* (Wiley and Sons, 1995).
- [157] M. Ilak, S. Bagheri, L. Brandt, C. W. Rowley, and D. S. Henningson, *Model reduction of the nonlinear complex Ginzburg–Landau equation*, *SIAM Journal on Applied Dynamical Systems* **9**, 1284–1302 (2010).
- [158] R. Dadfar, N. Fabbiane, S. Bagheri, and D. S. Henningson, *Centralised versus decentralised active control of boundary layer instabilities*, *Flow, turbulence and combustion* **93**, 537–553 (2014).
- [159] J. Abaffy, C. Broyden, and E. Spedicato, *A class of direct methods for linear systems*, *Numerische Mathematik* **45**, 361–376 (1984).

Acknowledgements

First I would like to acknowledge the members of my doctoral committee as a whole for their expertise and investing time in reading this document. My gratitude goes to the flow and control team Dr. Marios Kotsonis, Dr. Coen de Visser, Prof. Fulvio Scarano and Prof. Max Mulder for giving me the opportunity and freedom to pursue this scientific adventure. I thank my supervisors Coen and Marios for their guidance and enthusiasm these years. I also would like to thank Dr. Marc Gerritsma for helping me with the numerical framework and for his comments on chapter 2. I thank Prof. Bassam Bamieh for his contributions to chapter 3. I thank Dr. Erik-Jan van Kampen and Dr. Qiping Chu for their contributions, also to the SANDI project. Many thanks to Dr. Koen Groot for the many discussions on stability theory and the great time in Rio. Many thanks to Dr. Theo Michelis for using his experimental model set-up and the great time in Portland. Thanks to Andre Kil, Robin Baai and Gerson Desouza for joining this project during their Master graduation and whom I had the pleasure to supervise. I also would like to thank Leo Molenwijk and Stefan Bernardy for making my first independent experiment a safe one. Thanks to Colette Russo and Bertine Markus for making my PhD a smooth process.

Finally, I like to thank my family for all their support and especially my wife Lydia and our son Rob for putting everything in perspective.

Curriculum Vitæ

Henry Tol

29-05-1988 Born in Volendam, The Netherlands.

EDUCATION

2007–2011 Bachelor Aviation Engineering
Amsterdam University of Applied Sciences

2011–2013 Master Aerospace Engineering (Cum Laude)
Specialisation: Control & Simulation
Delft University of Technology

2014–2018 PhD Aerospace Engineering
Delft University of Technology



PROFESSIONAL EXPERIENCE

2012–2014 Simulation Software Developer
SIMTEQ - Vijfhuizen, The Netherlands

2018–present Design Engineer
Bright Society - Eindhoven, The Netherlands

List of Publications

JOURNAL ARTICLES

H. J. Tol, M. Kotsonis and C. C. de Visser, Experimental model-based estimation and control of natural Tollmien-Schlichting waves, *under review in AIAA journal*, 2018.

H. J. Tol, M. Kotsonis and C. C. de Visser, Estimation and control of TS waves in Falkner-Skan boundary layers, *under review in AIAA journal*, 2018.

H. J. Tol, M. Kotsonis, C. C. de Visser and B. Bamieh, Localised estimation and control of linear instabilities in two-dimensional wall-bounded shear flows, *Journal of Fluid Mechanics*, 824 pp. 818–865, 2017.

H. J. Tol, C. C. de Visser and M. Kotsonis, Model reduction of parabolic PDEs using multivariate splines, *International journal of control*, 2016.

H. J. Tol, C. C. de Visser, L. G. Sun, E. van Kampen and Q. P. Chu, Multivariate spline based adaptive control of high performance aircraft with aerodynamic uncertainties, *AIAA journal of Guidance, Control and Dynamics*, 39(4) pp. 781–800, 2016.

H. J. Tol, C. C. de Visser, E. van Kampen and Q. P. Chu, Nonlinear multivariate spline based control allocation for high performance aircraft, *AIAA journal of Guidance, Control and Dynamics*, 37(6) pp. 1840–1862, 2014.

BOOK CHAPTERS

¹**H. J. Tol**, C. C. de Visser, E. van Kampen and Q. P. Chu, Nonlinear and fault-tolerant flight control using multivariate splines, *In: Advances in Aerospace Guidance, Navigation and Control*, pp. 187–204, 2015.

CONFERENCE PROCEEDINGS

H. Mehmood, **H. J. Tol** and C. C. de Visser, Multivariate spline-based adaptive control for high performance aircraft in the presence of atmospheric turbulence,

¹Use the version from the TU Delft repository or Researchgate. The edited version does not include any figure labels

AIAA Guidance, Navigation, and Control Conference, 2018, Florida, USA.

H. J. Tol, C. C. de Visser and M. Kotsonis, Control of fluid flows using multivariate spline reduced order models, *54th AIAA Aerospace Sciences Meeting, AIAA SciTech Forum*, 2016 San Diego, USA.

H. J. Tol, C. C. de Visser, E. van Kampen and Q.P. Chu, Multivariate simplex spline based nonlinear dynamic inversion control of high performance aircraft, *AIAA Guidance, Navigation, and Control Conference*, 2013, Boston, USA.